SURFACE SCIENCE OF LOW-DIMENSIONAL MATERIALS

Controlling Chemical and Optoelectronic Structure, Connecting Dissimilar Materials, and Improving Atmospheric Stability

WPI

Julia L. Martin

In partial requirements for the
Degree of Doctor of Philosophy, Ph.D. in Chemistry
submitted on 25 April 2023 to the Faculty of

WORCESTER POLYTECHNIC INSTITUTE
100 Institute Road, Worcester, Massachusetts 01609

Committee: Professors Anita E. Mattson, Ph.D. (CBC, chair);
N. Aaron Deskins, Ph.D. (Chem. E.); Pratap M. Rao, Ph.D. (Mech. E.);
Ronald L. Grimm, Ph.D. (CBC, advisor)

CONTENTS

LIST OF FIGURES

LIST OF TABLES

PREFACE

Materials engineering for improving the quality of life and tackling global issues is largely driven by surface chemistry approaches. Such strategies aim to solve not only seemingly inconsequential concerns like protection from the elements and non-stick cookware but also more critically pervasive challenges associated with atmospheric pollution, climate change, chemical warfare threats, cost-scalability factors of industrial processes, among others. For many traditional, widely-applied materials such as silicon or graphene, a diverse breadth of knowledge exists surrounding covalent derivatization strategies to impart chemical or optoelectronic tunability, achieve surface passivation, improve dispersibility in organic solvents or incorporation into polymers, among others. This thesis work aims to borrow from such established covalent derivatization techniques and exploit them for new and emerging materials for applications in solar energy and photocatalysis, sensing, electromagnetic shielding, protective barrier materials, and others. The studies herein primarily surround two classes of low-dimensional materials, bismuth-based oxyhalides and titanium-based carbides and oxides. In the case of BiOI(001), to bridge the gap between the cleanliness of a freshly cleaved surface and that available from purely chemical etching means, we explore a combination of wet chemical treatments and quantify the resulting in-

terfacial chemical states and electronic structure. Ultimately, in combination with overlayer models of idealized oxide-terminated or iodide-terminated BiOI 2D surfaces, angle-resolved X-ray photoelectron spectroscopy, ARXPS, demonstrate an oxide-dominated surface for nascent BiOI and an iodide-dominated surface for BiOI following tape exfoliation or following sequential HF etching and sonication in acetone which each demonstrate distinct electronic structure. Beyond BiOI, we present the first report of the optical properties and electronic band structure for a recently discovered one-dimensional lepidocrocite (1DL) titania that we believe to be highly quantum confined based on a comparably high band-gap energy compared to other lepidocrocite titania structures. Transient absorption, TA, spectroscopy further demonstrate broadband, long-lived sub-gap photoexcitations that we postulate to originate from Ti^{3+} defects and oxygen vacancies based on reports surrounding optically "black" TiO_2. Nonetheless, significant work remains to better understand the nature of these transient state dynamics and the implications for realizing highly efficient applications in photocatalysis and Li-based battery systems. For studies surrounding $Ti_3C_2T_x$ MXene, we derivatize the material with covalent organosilanes and ultraviolet photoelectron spectroscopy, UPS, demonstrate ~500 meV shifts in work-function values resulting from relative surface dipoles. The magnitude and direction of the interfacial dipoles are tunable based on the chemical functionality of the derivatizing molecules, and we discuss these results in the context of shielding, sensing, and battery applications. Beyond the studies herein, our derivatization strategies should broadly inform present approaches for covalently connecting dissimilar materials to enhance carrier transport and conductivities, improve atmospheric stability, design highly sensitive and selective sensors, and more.

ACKNOWLEDGMENTS

Firstly, I'd like to thank my advisor Ron Grimm for teaching me everything I know about UHV techniques, electronics, mechanics, and more. I am grateful to have gained not only a broad range of technical skills from wearing so many hats in this group, but also the interpersonal skills based on Grimm's approach to both advising and teaching. I especially want to thank Alex for being the best mentor I could have asked for and always sparking my curiosity to problem solve and not be afraid to spend hours with manuals when things aren't working. Above anything else, I'm happy to have gained a great friend in him. I'd like to thank all of the Grimmgroup members who have come through the lab during my time here: it has been a pleasure to do science with you all, and our offline chats about who-even-knows-what truly kept me sane. To my grad student friends in the department: thank you for always making the time to let me pick your brain about experimental roadblocks and always being up for a lunch break field trip. I want to especially thank Nick for being one of the strongest shoulders to lean on as well as Becca and Anna for their friendship and helping me finish out my time here on a true high note. Thank you to my friends outside of the program for the unwavering support, love, and much needed comedic relief. I'd also like to thank Prof. Titova for her mentorship as well as group members Erika,

Drew, and Katy for their optical work and collaboration. Thank you as well to Prof. Barsoum at Drexel and group members Hussein, Kiana, Mary for their collaboration and sharing of material and synthesis recipes. Lastly, I'd like to thank my other committee members: Anita Mattson, Pratap Rao, and Aaron Deskins.

I especially need to thank my family—Mom, Matt, Gia, Nana, and Papa especially—for your unconditional love and support throughout my academic career. I would not have gotten this far without you and I feel so blessed to share in this success and happiness with you all. I love you so much, always.

J. L. M.

GLOSSARY

Spiro-OMeTAD

PEDOT:PSS

APTES	3-(aminopropyl)triethoxysilane 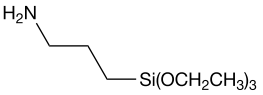
APTMS	3-(aminopropyl)trimethoxysilane 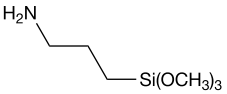
ARXPS	Angle-resolved-XPS
EELS	Electron-energy loss spectroscopy
ED	Electron donating
EW	Electron withdrawing

FEM	Field-emission microscopy
FTIR	Fourier-transform infrared (spectroscopy)
IC, ICs	Integrated circuit(s)
INS	Ion neutralization spectroscopy
IPES	Inverse photoemission spectroscopy
IRRAS	Infrared reflection-absorption spectroscopy
NEXAFS	Near-edge X-ray adsorption fine structure
PL	Photoluminescence
SEM	Scanning electron microscopy
SFG	Sum frequency generation
STM	Scanning tunneling microscopy
SERS	Surface-enhanced Raman spectroscopy
TEM	Tunneling electron microscopy
TPD	Temperature-programmed desorption
TA	Transient absorption (spectroscopy)
UHV	Ultrahigh vacuum
UPS	Ultraviolet photoelectron spectroscopy
XANES	X-ray absorption near-edge structure
XPS	X-ray photoelectron spectroscopy
XRD	X-ray diffraction
XRF	X-ray fluorescence

SYMBOLS

	Energy terms:
KE	Kinetic energy
BE	Binding energy
Φ	Work function (general material, capital Phi)
Φ_D	Work function (spectrometer)
Φ_S	Work function (surface)
ϕ_S	Surface dipole (lowercase phi) (Not to be confused with a spectrometer angle term below)
$\mathbf{E}_f$	Fermi energy or Fermi level
$\mathbf{E}_{VBM}$	Valence-band maximum energy
$\mathbf{E}_{CBM}$	Conduction-band minimum energy
$\mathbf{E}_{vac}$	Vacuum-level energy
$\mathbf{E}_{SEC}$	Seconday-electron cutoff energy

Photoelectron overlayer model terms and spectrometer geometries:

$\langle A \rangle$	Average atomic mass
d	Depth or distance into material
$D\,(E_{\mathrm{A}})$	Detector efficiency at energy E of A*th* overlayer component
E	Photoelectron kinetic energy
I	Photoelectron intensity
I_0	X-ray flux
h	Planck's constant
N_{A}	Volumetric number density of A*th* overlayer component
SF	Sensitivity Factor
$T\,(E_{\mathrm{A}})$	Analyzer transmission function at energy E of A*th* overlayer component
$\langle Z \rangle$	Average atomic number
$\mathbf{\Phi}$	Fractional (surface) coverage (bold capital Phi)
λ	Attenuation length
ν	Frequency of light
ρ	Density
σ_{A}	Surface number density of A*th* overlayer component
θ	Angle of detector collection with respect to surface normal
δ	Angle of incoming radiation with respect to surface normal (Not to be confused with a surface dipole energy term above)
γ	Angle of detector collection with respect to incoming radiation
ϕ	Angle of offset between detector collection vs plane containg δ

CHAPTER 1

INTRODUCTION

Materials engineering for the purpose of improving quality of life and tackling global issues is largely driven by surface chemistry approaches. Interfacial functionalization presents an opportunity to solve critically pervasive challenges associated with atmospheric pollution, climate change, chemical warfare threats, cost-scalability factors of industrial processes, among many others. This thesis explores a range of surface chemistry techniques for various low-dimensional materials in the context of atmospheric stability, connecting materials, and imparting selectivity and tunability. This surface science work encompasses two classes of low-dimensional materials: bismuth-based oxyhalides and titanium-based carbides and oxides. Nonetheless, our derivatization strategies should broadly inform present approaches for covalently connecting dissimilar materials to enhance carrier transport and conductivities, improve atmospheric stability, design highly sensitive and selective sensors, among others.

Chapter 2 of this thesis details the history, syntheses, chemical configurations, and derivatization strategies for conventional materials like silicon and graphene, as well as for emerging, low-dimensional materials that may

present more favorable cost-stability factors, atmospheric stability, or optoelectronic properties as compared to traditional materials. Since the rediscovery of graphene and its derivatives,[1–2] 2D layered materials have garnered remarkable interest across a range of applications for their unique physical, chemical, and optoelectronic properties.[3–6] Through our explorations of emerging 2D materials, we were particularly interested in bismuth oxyiodide (BiOI) for its oxidative stability, non-toxic and abundant precursors, and its energetic alignment to silicon in the context of tandem-junction photovoltaics. Chapter 2 details our explorations of BiOI(001) initiated by a number of wet chemical processing steps. This led us to investigate the surface chemical and electronic states throughout the sequential chemical treatments as quantified by angle-resolved X-ray photoelectron spectroscopy (ARXPS) and ultraviolet photoelectron spectroscopy (UPS). We ultimately proposed a wet chemical etch for achieving chemically and electronically pristine BiOI(001) interfaces that circumvents the mechanical constraints of traditional physical cleaning methods for layered materials such as tape-cleaving. This holds implications for minimizing performance-limiting interfacial defects for device-relevant nanostructured BiOI.

Elsewhere, our colleagues at Drexel University became increasingly interested in MXene materials for their excellent electrical conductivities reaching 20,000 S cm^{-1} and favorable mechanical properties for energy, shielding, and sensing applications. We initiated collaborations with them to leverage our surface chemical treatments and physical characterizations aligned with their growing interests for this emerging 2D material. A number of MXene phases suffer from oxidative stability issues which limits widespread application. Moreover, for energy and shielding applications, robust control over the electronic structure of the material is highly desired. Chapter 5 details our surface derivatization efforts for $Ti_3C_2T_x$ MXene which achieve tunable work-function values based on covalent derivatization with organosilanes. We ultimately demonstrated relative interfacial dipoles for derivatized material that are tunable based on the chemical functionality of the derivatizing molecules. Based on the utility of interfacial dipoles for silicon-based sensors and photovoltaics, this holds promising implications for practical MXene devices.

Concurrently with exploring alternative etchants for generating MXene that preclude the use of hydrofluoric acid, our collaborators discovered a new synthesis route for an underexplored polymorph of TiO_2. They demonstrated a near-ambient, scalable, one-pot synthesis that yields one-dimensional, titania lepidocrocite (1DL) nanofilaments from earth-abundant compounds such as TiC, TiB_2, TiN, etc. Despite promising initial results in photocatalysis, substantial questions remain regarding the surface chemistry and carrier dynamics for this emerging TiO_2 material. We furthered our collaborations to investigate the surface chemical and optoelectronic states for the 1DL material to best inform future studies that rely on this insight. Chapter 6 details these

explorations and ultimately demonstrate a highly-quantum confined material with long-lived visible photoexcitations which holds strong implications for practical applications in photocatalysis and optoelectronics.

In the case of BiOI, preliminary photoluminescence spectroscopy studies indicate photooxidative instability which must be addressed. Additionally, the present chemical etching studies demonstrate chemically reactive step-edges, but questions remain regarding the optoelectronic and photocatalytic implications of the orthogonal reactivities across surface morphologies for BiOI(001). Moreover, while the fundamental surface chemistries for other titania polymorphs including the anatase and rutile phases are well characterized, the lepidocrocite phase remains underexplored. Additionally, present surface derivatization approaches for Ti-based MXenes are largely directed toward improving atmospheric stability or dispersibility in organic solvents and few studies correlate the interfacial chemical transformations with the subsequent changes in optoelectronic properties. Chapter 7 addresses present challenges and knowledge gaps surrounding these emerging low-dimensional materials in the context of future studies which are critical for scalable, highly-efficient practical applications.

Appendices A, B, and C respectively present supplemental information sections for Chapters 4, 5, and 6 of this thesis. Appendix D details modifications to the XPS including wiring that often comes undone in the birds nest of wires behind the card rack in §D.3. Appendix E includes detailed outlines of our air-free MXene derivatization procedures, some additional preliminary XPS and UPS studies in Appendices F and G, as well as custom Igor scripts in Appendix H that facilitate batch processing.

This thesis explores surface chemical transformations for a number of emerging low-dimensional materials including Bi-based oxyhalides and Ti-based carbides and oxides. Studies surrounding BiOI probed changes in surface chemical and electronic states as a function of wet chemical processing. In the case of 1DL TiO_2 and $Ti_3C_2T_x$ MXene, we explored the optical and electronic implications of interfacial dipoles from intercalated cations and covalent molecular overlayers. Our derivatization strategies and physical characterization efforts should inform present studies for other emerging materials that rely on interfacial tunability for highly efficient, scalable practical applications.

CHAPTER 2

SURFACE SCIENCE IN TRADITIONAL MATERIALS, EMERGING MATERIALS, AND BEYOND

2.1 Introduction

This thesis explores a range of surface chemistry techniques for various low-dimensional materials in the context of atmospheric stability, connecting materials, and imparting selectivity and tunability. When addressing present, fundamental knowledge gaps surrounding the surface chemistries of new and emerging materials, it is critical to look toward literature-precedented approaches for conventional, well-studied materials. Studies in subsequent chapters in this thesis exploit the decades of established surface chemistry strategies for traditional materials toward improving atmospheric stability, installing selective chemical handles for subsequent adsorption or covalent attachment, and imparting chemical and electronic tunability for newer, under-explored materials. As such, the present chapter reviews surface derivatization strategies and characterization techniques not only for conventional materials including silicon and graphene, but also for emerging, low-dimensional materials.

Some applications for the 2D materials discussed herein include solar energy conversion, electromagnetic interference (EMI) shielding, and catalysis which rely on interfaces with high electronic and chemical quality. Interfacial defects and atmospheric instability can have devastating impacts on device performance as well as interfere with redox reactions involved in catalytic systems of interest. In addition, robust control over interfacial chemical and electronic properties is critical for highly efficient photovoltaics, EMI shielding, and chemical sensing.

Section §2.2 reviews the broad range of motivations for surface derivatization strategies with applications across materials science, biomedical engineering, environmental science, electronics, and chemistry that have revolutionized everyday life in ways that are often overlooked.

Among the myriad of established surface chemistry techniques, work performed towards this thesis largely employed selective etching chemistry or covalent attachment of small, organic molecules to the surface of various low-dimensional materials. When changing the interfacial composition of a material, it is critical to identify and quantify the resulting chemical and electronic changes. As such, brief discussions of various spectroscopic and microscopy-based techniques for quantifying surface chemical states encompasses §2.3. Among these tools, our studies relied heavily on X-ray photoelectron spectroscopy (XPS), ARXPS (angle-resolved XPS), and ultraviolet photoelectron spectroscopy (UPS). A historical perspective of these techniques is detailed here in §2.3 while a more practical, theoretical discussion is contained in Chapter 3.

Since the rediscovery of graphene in 2004 by Novoselov and Geim,[1–2] 2D-layered materials have demonstrated remarkable utility across a range of applications for unique physical, chemical, and optoelectronic properties.[3–6] Among them, Van der Waals (VDW) materials, including graphite, are particularly compelling for the unique optical, electronic, and mechanical properties afforded by their layered structure. They are characterized by strong, intralayer covalent bonds and weak interlayer van der Waals forces, between which chemical or mechanical cleavage can yield pristine, single-layer 2D sheets. In many cases, the layered structure affords high in-plane electrical conductivity as well as excellent effective charge separation perpendicular to the layers, which posits them as strong candidate materials for applications in photocatalysis, energy conversion and storage, and chemical and biological sensing. Section §2.4 surveys a number of well-established surface derivatization techniques for conventional bulk materials such as silicon, as well as for traditional 2D layered materials such as graphene, group-16 dichalcogenides, and bismuth-based oxyhalides. In many cases, the changes in interfacial chemical states following chemical derivatization have strong implications for the electronic properties of the material. For materials like silicon and graphene which have been of exceptional interest for decades, the

intimate relationship between interfacial chemical states and optoelectronic properties have been explored extensively. This thesis work exploits this precedence for emerging low-dimensional materials, some being only few atomic layers thick, for which small changes in surface chemistry could influence the electronic properties of the bulk material. This could be particularly useful for energy and EMI shielding applications for which optoelectronic tunability is desired.

Following, an introduction to the discovery and initial reports surrounding some emerging low-dimensional materials is detailed throughout §2.5. MXenes, a class of 2D transition metal carbides or nitrides, have shown promising results for photocatalysis, electrochemical energy storage, chemical sensing, and more.[7–13] Nonetheless, many MXenes tend to suffer from oxidative instability, which limits scalability and widespread application.[14–15] Quaternary-derived nanomaterials, a recently discovered class of metal-oxide materials that possess a 1D lepidocrocite-like (1DL) TiO_2 nanofilament structure when Ti is the metal, possess remarkable oxidative stability and compelling optoelectronic properties afforded by their extremely-high-aspect-ratio structures and strong quantum confinement effects.[16–17] While these properties posit 1DL as strong candidate materials for battery applications and photocatalysis, questions remain regarding interfacial chemical and electronic states that must be explored to realize practical implementation. Section §2.6 explores the present challenges and fundamental knowledge gaps limiting the widespread application of these emerging low-dimensional materials. The investigations surrounding Ti-based MXenes and 1DL detailed in Chapters 5 and 6 respectively were carried out to address several of these knowledge gaps with a view, in part, toward applications in heterogeneous catalysis, the foundations for which were laid by Gerhard Ertl, Gabor Somorjai, and others. Finally, concluding remarks are summarized in §2.7.

2.2 Motivations for chemically derivatizing a surface

In the context of materials science and engineering, chemical derivatization can be broadly described as the process of attaching molecules to the surface of a material, thus altering its surface chemistry, to impart new functionality and capabilities. The molecules or particles can be either strongly attached via covalent linkages, or less robustly adsorbed through electrostatic or physical interactions to the surface of interest. In either case, chemical derivatization has been employed extensively in ways that have revolutionized everyday life, and with recent advancements to vacuum technology and high-resolution surface characterization techniques, practical applications only continue to rise. One motivation for derivatizing a surface includes controlling surface adhesion or surface repulsion of a species of interest, one prominent example being waterproofing. Hydrophobic coatings are utilized extensively including on paper cups or boxes (wax coatings), windshields for repelling rain

and fog (RainX, Aquapel), footwear and outerwear, furniture and carpet to prevent stains (Scotchgard^{TM}), among others. Other examples of derivatization for repulsion include Teflon-coating for non-stick cookware as well as antimicrobial and antifungal coatings in a range of applications including high-touch household surfaces and hardware, and tools and equipment in sterile environments, and HVAC systems. Alternatively, in some cases selective adhesion is desired. For example, chemical derivatization of glass dishes and microscope slides to promote cell adhesion or the immobilization of proteins and enzymes is useful in the fields of biology and biomedical engineering. Interfacial derivatization can also improve the atmospheric stability of a material, anti-corrosion coatings being a widely applicable case. In some instances, depending on the nature of the adsorbates, changes in surface chemistry can subsequently influence the electronic properties of a material, which holds significant implications for applications in catalysis, energy conversion and storage, and electromagnetic shielding, and will be discussed more thoroughly in §2.4.

2.2.1 Covalent derivatization

Chemical derivatization of surfaces can include molecular thin films that are attached though robust covalent linkages. Those that are formed by self-assembly, or self-assembled monolayers (SAMs), encompass one class of interfacial covalent adsorbates. Self-assembling molecules generally consist of a head group that chemically anchors the molecule to a surface, an alkyl chain, and a terminal end group. Conveniently, the terminal end can be selectively tailored to impart the desired chemical functionality for secondary chemical reactions or adsorptions, for molecular recognition for subsequent thin film deposition or growth, or for tuning electronic and optical properties. Among them, organosilanes (organometallic compounds containing silicon-carbon bonds) are ubiquitous for their facile self-assembly on sufficiently hydroxylated surfaces.[18] The head group generally consists of -trichloro, -trimethoxy, or -triethoxy functionality, thusly linking the molecule to a surface at –OH sites through covalent silicon-oxygen bonds. Organosilanes are widely employed for covalent attachment to metal oxide surfaces for a range of applications. In the case of silicon oxide surfaces for example, silane-treatment of glass beads, silica gel, and sand in lab settings can impart hydrophobicity to conventional stationary phase materials for column chromatography. More broadly, silane surface chemistry has been employed extensively to various materials across disciplines to promote immobilization of enzymes, proteins, or cells,[19–21] to impart selectivity and sensitivity for chemical and biological sensors,[22–23] to improve carrier transport and selectivity for energy applications,[24–25] to promote adhesion of hydrophobic coatings to metals,[26] and to aid in passivation against atmospheric degradation.[27–28]

Other commonly employed SAMs include organosulfur or phosphate species which covalently bind directly at interfacial metal sites, precluding the need for a hydroxylated surface. Organosulfur compounds including alkyl disulfides and alkylthiols exhibit strong binding affinities toward metal surfaces through covalent sulfur-metal bonds including silver, copper, platinum, mercury, and iron.[18] Nonetheless, thiol-based SAMs have been studied most extensively on Au(111) surfaces. Similarly to silanes, organosulfur-based covalent derivatization is commonly employed for cell adhesion and the immobilization of proteins and enzymes,[29–31] and for sensitive and selective gas sensing.[32–33] Additionally, thiol surface chemistry has assisted in catalyst design,[34] in templating for various photolithographic techniques,[35–37] and in imparting pH sensitivity for electrode surfaces.[38]

Alkylphosphates also readily form SAMs on metal surfaces through covalent metal-oxygen bonds[39–40] and have been investigated for covalently grafting molecular sensors onto surfaces for trace explosive detection,[41–42] for coatings on metal stents for biomedical applications,[43] for gate dielectric materials in transistor applications,[44] among others. Moreover, alkyl or aromatic species with amine functionality can be grafted onto surfaces through covalent amide bonds. For example, this chemistry has been used to graft amine-terminated chromophores (poly- and oligothiophenes) with to graphene-oxide for optoelectronic applications[45] as well as to improve dispersion in common organic solvents for applications that rely on solution-phase processing.[46]

2.2.2 Noncovalent derivatization

Non-covalent attachment where molecular overlayers coat surfaces through ionic or van der Waals interactions as opposed to covalent linkages encompasses another class of interfacial chemical derivatizations. A prevalent example includes the adsorption of metal atoms on surfaces, which to date has served an indispensable purpose for the electronics and sensing industries in the fabrication of contacts for transistors and integrated circuits (ICs). In practice, thin-film metal evaporation involves heating a metal in vacuum to its melting point, with the resulting vapors condensing and depositing on a substrate of interest. The technique dates back to the middle of the 19th century, with early applications dominated by the optical-coating market, including reflective or anti-reflective coatings on mirrors, or for decorative purposes.[47] With advancements in vacuum technology and the development of magnetron sputtering, metal atom evaporation has become a prolific tool across various industries and disciplines including electronics, chemical and biological sensing, architecture, transportation, and renewable energy. More specifically, the need for transistors and ICs has pervaded nearly every sector of electronics, and in most cases, their fabrication heavily relies on the physical adsorption of metals on wafer substrates to form electrical contacts among other things. Beyond metal adsorption, pyrene derivatives have been lami-

nated onto graphene to yield enhanced power conversion efficiencies, strong UV absorption for UV filtering applications, and enhanced electrical resistance sensitive to atmospheric changes in the context of flexible electronics.[48] Moreover, thin-film depositions of electron- and hole-transport layers or dielectric materials (Spiro-OMeTAD, PEDOT:PSS) via spin coating or thermal evaporation often rely on non-covalent interactions and are utilized extensively for energy and sensing applications.[49–51]

2.3 Tools for quantifying surfaces and chemical derivatization

The fascination and interest in material interfaces has existed since antiquity, and in the field of material science, the 1800s in particular were characterized by several scientific breakthroughs surrounding the ways in which material interfaces interact with their surroundings. Nonetheless, the tools for studying the chemical and electronic properties of surfaces did not develop in a commercially scalable way until the mid 1900s. Prior to the turn of the 20th century, theoretical and experimental considerations of material interfaces were dominated by molecular approaches. Characterization techniques centered around describing and quantifying physical, chemical, and optoelectronic properties of materials as a bulk ensemble of molecules. The pioneering work of Lord Rayleigh (John William Strut) and Irving Langmuir among others effected a shift in the surface science community toward considerations of individual atoms at material interfaces as distinct from their bulk counterparts. The advent of ultra-high vacuum (UHV) technology, semiconductor electronics, and tunable synchrotron radiation in the mid-to-late 1900's enabled the realization of scalable, high-resolution, commercial instrumentation for characterizing a wide range of surfaces far beyond the solid-vacuum interfaces that dominated initial studies. This section addresses several of these techniques in brief, as well as details historical perspectives for those most relevant to this thesis work more thoroughly.

2.3.1 Lab-based techniques

Presently, myriad powerful lab-based characterization techniques exist for studying surfaces. Among them, several X-ray-based tools including X-ray photoelectron spectroscopy (XPS), X-ray absorption near-edge structure (XANES, also known as near-edge X-ray adsorption fine structure, NEXAFS), X-ray fluorescence (XRF), and X-ray diffraction (XRD) are particularly useful for probing surface chemical states. Moreover, several optical and vibrational techniques are widely employed to probe surface and molecular structure as well as bonding geometry including Fourier-transform infrared spectroscopy (FTIR), infrared reflection-absorption spectroscopy (IRAS), Raman spectroscopy and surface-enhanced Raman spectroscopy (SERS), and sum frequency generation (SFG). In terms of microscopy-based tools, scanning

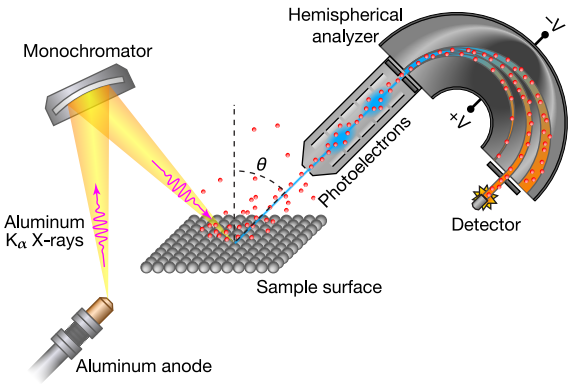

Figure 2.1. Cartoon illustration of traditional, monochromated XPS analysis with monochromated 1486 eV Al K_α X-ray excitation.

electron microscopy (SEM), tunneling electron microscopy (TEM), scanning tunneling microscopy (STM), field-emission microscopy (FEM), and field-ionization microscopy (FIM) offer powerful insight into surface structure and morphology. Additionally, for insight into electronic and valence structure, photoemission or ultraviolet photoelectron spectroscopy (PES or UPS), inverse photoemission spectroscopy (IPES), ion neutralization spectroscopy (INS), and electron-energy loss spectroscopy (EELS) are particularly useful. These aforementioned techniques have demonstrated remarkable utility across disciplines for probing surface chemical and electronic states, however many are not relevant to this thesis and, thus, only a handful will be discussed further.

Among lab-based characterization tools, the studies herein relied heavily upon X-ray photoelectron spectroscopy (XPS), a powerful UHV technique for probing surface chemical states, shown in Fig. 2.1. XPS gleans interfacial chemical insight by exploiting the photoelectric effect, a phenomenon that predates the realization of commercial XPS systems by over 60 years. German physicist Heinrich Hertz paved that way for this discovery in 1886 when he demonstrated that a charged object loses its charge more rapidly upon UV illumination during experiments that were designed to produce and quantify electromagnetic waves.[52–53] Over the proceeding two decades, this phenomenon was studied more extensively but it was not until Albert Einstein proposed quantum-mechanical explanations in 1905 that the potential of XPS for quantitative chemical analysis started to become clear.[53] In 1914, shortly after Einstein's theoretical work, New Zealand physicist Ernest Rutherford established photoelectron binding energy as the difference between the inci-

dent X-ray energy and the kinetic energy of the emitted photoelectron[5]3, as defined by eq 2.1:

$$\mathbf{BE} = h\nu - \mathbf{KE} - \Phi_{\mathrm{D}} \tag{2.1}$$

In eq 2.1 **BE** is the binding energy, $h\nu$ is the photon energy, **KE** is the kinetic energy, and and Φ_{D} (capital Phi) is the inherent spectrometer work function. This realization demonstrated that the kinetic energies of photoelectrons carry indispensable chemical information regarding the material from which they were emitted, but it still took more than 30 years for photoelectron spectroscopy to be realized as the prolific surface characterization tool that it is today. It wasn't until the 1950's that Swedish physicist Kai Seigbahn developed the method of Electron Spectroscopy for Chemical Analysis (ESCA) that produced the first high resolution XP spectrum which later won him the 1981 Nobel Prize in physics.[53] Over the next two decades of the analog age, commercial systems grew more widely available and XPS steadily became a ubiquitous surface characterization tool for chemists. Its popularity was rapidly accelerated in the mid 1980s with the rise of digital instrumentation, and since then the practical use of XPS has broadened its scope far beyond the field of chemistry and continues to rise in both popularity and utility. For discussions beyond historical perspectives, XPS theory of operation; post-acquisition data fitting; and quantitative interpretation of peak-area ratios as it pertains to the studies herein is detailed more thoroughly in §3.2.

While XPS is primarily a surface-sensitive characterization technique due to the short mean free path of electrons, several methods exist for probing bulk versus surface contributions. One such method for depth profiling in XPS was first demonstrated in the early 1970's[54–55] and employs ion beam etching to physically remove material from the sample surface down into the bulk. This destructive method commonly utilizes heavy argon ions, Ar^{+}, that are accelerated towards the sample to ionize and remove smaller atoms from the material's surface. Ion beam sputtering is most commonly utilized as a method for surface cleaning of metals and other solid materials, however careful calibration of the instrument to samples with known thicknesses enables correlation of sputter timescales with depth into the bulk material. Other methods for surface cleaning includes *in vacuo* crystal cleavage[56–59] during which an in situ abrasive apparatus inside the UHV chamber is externally manipulated toward the sample surface to cleave the topmost layers of crystalline material, revealing a pristine interface as in the cartoon in Fig. 2.2. These methods for depth profiling in XPS can be useful, as we have demonstrated for characterizing the band structure of *in vacuo*-cleaved, pristine Cs_2TiBr_6 interfaces,[59] but the destructive nature limits their applications. For materials that are low-dimensional and delicate in structure or are par-

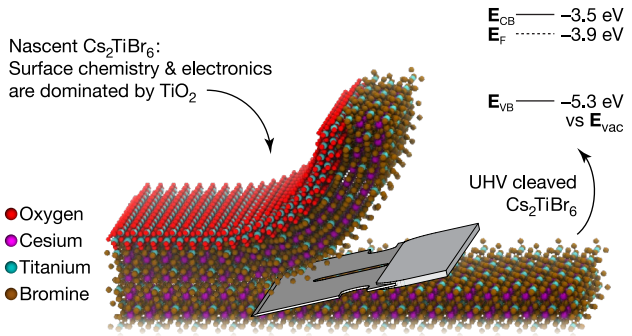

Figure 2.2. Cartoon illustration of *in vacuo* crystal cleavage and resulting band-edge alignment for antifluorite cesium titanium bromide, Cs_2TiBr_6. Adapted from ref. 59.

ticularly prone to beam damage,[60] as was the case for studies surrounding bismuth oxyiodide (BiOI), other less destructive methods are necessary.

One such non-destructive method includes angle-resolved XPS (ARXPS) that deconvolves surface and bulk contributions by exploiting the exponential decay of photoelectron current as a function of depth below the surface of the material. In brief, ARXPS relies on tilting of the sample stage to vary the photoelectron takeoff angle to selectively alter the relative sensitivities to photoelectrons originating from the surface and from the bulk material relative to the total photoelectron counts. Since bismuth oxyhalides are particularly prone to reduction under Ar ion bombardment, this technique was employed extensively for studies herein probing chemical terminations at BiOI interfaces as a function of surface chemical treatments. Practical discussion of ARXPS theory and overlayer models as it pertains to this thesis work is detailed in §3.3 as well as throughout Chapter 4.

While XPS analyzes photoelectron energies from core energy levels to probe surface composition, several other surface characterization methods utilize significantly lower incident photon energies that instead emit valence photoelectrons to gain electronic insight into the material. Among such techniques, ultraviolet photoelectron spectroscopy (UPS) was employed extensively throughout this work to quantify interfacial electronic structure of various solid low-dimensional materials as a function of surface chemical treatment, shown in Fig. 2.3. With the inception of practical photoelectron spectroscopy methods in the 1960s, UPS was pioneered by physicists Feodor I. Vilesov and David W. Turner for analyzing photoelectron energies of free molecules in the gas phase.[61] Vilesov's methods employed UV excitation from a hydrogen source, while Turner's studies utilized a differentially pumped He I discharge lamp ($h\nu$ = 21.218 eV), a UV source that is still commonly employed in current UHV systems. Shortly after, William E. Spicer at Stanford is credited with acquiring the first UP spectrum of copper as well as

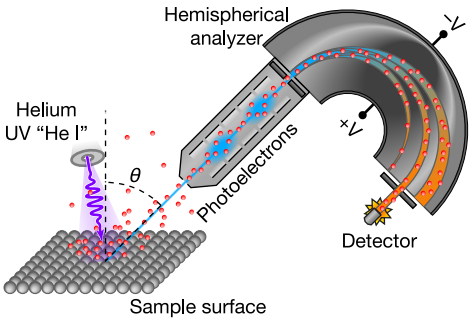

Figure 2.3. Cartoon illustration of traditional UPS analysis with 21.218 eV He I UV excitation.

correlating the experimentally determined valence band structure with a calculated density of states.[62] Spicer's contributions were a critical step toward the development of practical, scalable UPS techniques for quantifying the electronic and valence structure of solid, crystalline materials. Presently, UPS is widely employed for probing solid-state band structure of materials for energy conversion and storage,[59,63–65] catalysis,[66–67] optoelectronics,[68] and more.

In practice, lab-based multi-technique UHV systems are often equipped with two or more incident photon sources, commonly Al and Mg for soft X-rays and He I for UV excitation, allowing for sequential XPS and UPS measurements in a single analysis chamber on the same sample. This is particularly useful for materials prone to inhomogeneity or inconsistencies, but more importantly, it also enables correlation of UPS-determined electronic structure of a material to specific interfacial chemical features observed in XPS. Our UHV system follows this design, which was critical for the studies herein which rely on the quantification of the chemical and electronic changes following interfacial chemical derivatization. Additionally, the sample stages in current commercial systems are often equipped with heaters and thermocouples for in situ heating of samples in UHV. While this is most commonly employed to desorb surface contaminants for sample cleaning purposes, in some cases it also enables isothermal desorption experiments in the context of interfacial derivatization. In such studies, XP spectra may be acquired prior to and following several hours of sample heating at ~200–250 °C to quantify relative changes in photoelectron intensities. Quantitative analysis of peak-area ratios of, say, an atom in the substrate material to a heteroatom in a molecular overlayer, may discriminate between contributions to the photoelectron signal from covalent attachment versus physical adsorption. Desorption experiments of this nature can be useful for this reason as well as for the convenience of the in situ execution, however they are limited by the heating capacity of the sample stage and adjacent components and offer little

quantitative insight into bond strengths and stabilities beyond that narrow thermal range.

Temperature programmed desorption (TPD) is a much more robust technique for quantifying bond strengths and desorption kinetics of covalent monolayers on material interfaces. While the original theory of TPD was introduced by theoretical physicist Eugene Vigner, experimental methods were pioneered by Michael C. Polanyi[69] with presently accepted theoretical models due to Redhead.[70] TPD commonly employs a linear thermal ramp from room temperature in UHV to upwards of ~500 °C and simultaneous mass spectrometry analysis of the thermal desorbates. Linear heating at a constant rate correlates time- and temperature-domain data to enable quantitative analysis of desorption kinetics of specific mass/charge features as a function desorption temperature. Such experiments are prone to misinterpretation and generally require rigorous control experiments, but when executed properly, TPD serves as a powerful material characterization tool for quantifying thermal stability, bond strengths, and desorption kinetics. The studies in this thesis work surrounding chemical derivatization of low-dimensional materials with organosilanes utilized isothermal desorption at 200 °C and interpretation of relative photoelectron ratios prior to and following heating to probe covalent attachment, but due to time constraints did not employ any TPD analysis. Future studies surrounding these low-dimensional materials should employ TPD studies of the derivatized surfaces to quantify the relative bond strengths and desorption kinetics of the molecular overlayer. Such insight will greatly inform future studies that rely on this knowledge for secondary functionalization to impart selectivity or sensitivity, incorporation into flexible polymers, and more.

In terms of bulk characterization, X-ray diffraction (XRD) is one of the most widely utilized lab-based X-ray tools for probing crystal structure, symmetry, and lattice dynamics of solid, crystalline materials. XRD relies on the constructive interference of incident X-radiation with a regular array of atoms in the crystalline material. A diffracted beam results when that constructive interference satisfies Bragg's law, defined by eq 2.2.

$$n\lambda = 2d \sin\theta \tag{2.2}$$

In eq 2.2, n is any integer corresponding to the diffraction order, λ is the wavelength of the incident beam, d is the spacing between diffracting planes in the crystal lattice, and θ is the angle of incidence with respect to the surface normal angle. As such, the diffraction angle, 2θ, carries crystallographic information regarding the arrangement of atoms in the material. For powdery material with micro- or nano-scale crystallites, quantitative analysis of the 2θ angles yield insight into not only the bulk crystal structure, but also the

average particle size via Scherrer analysis[71] when the full-width-at-half-max of the characteristic peak exceeds that of the instrumental limits inherent to the X-ray source. Additionally, shifts in 2θ peak location can indicate lattice stretching as a function of thermal changes or ion intercalation for layered materials.[72–74] Single-crystal XRD relies on high-quality, larger crystals with inherently more sample constraints, but yields more comprehensive chemical insight compared to powder XRD (pXRD). The studies detailed in Chapter 4 relied heavily on pXRD for probing changes in crystalline chemical features at distinct surface morphologies for BiOI single-crystal interfaces, and it was also employed for bulk characterization of low-dimensional materials prior to and following chemical derivatization, as in Chapter 5.

Beyond spectroscopy, several electron microscopy techniques are exceedingly useful for probing surface morphology and structure for various solid materials. Among them, scanning electron microscopy (SEM) and transmission electron microscopy (TEM) were employed regularly throughout this thesis work. While both methods employ an incident electron beam, conventional SEM analyzes scattered electrons while TEM quantifies electrons transmitted through the sample. Detection of secondary electrons from an incident electron beam rastered across the surface of a sufficiently conductive sample produces an SEM image of the surface topography of the material. As such, SEM is a widely employed characterization tool for probing surface morphology and roughness. TEM images yield similar results but can also glean insight into the internal structure of the material. For studies surrounding BiOI as in Chapter 4, SEM demonstrated the presence hexagonal BiI_3 present at step-edges of HF-etched BiOI single-crystals to complement the observance of a characteristic BiI_3 in pXRD. For the thesis work involving emerging low-dimensional materials as in Chapter 6, TEM was utilized to probe morphology of 1DL, a new class of lepidocrocite-like highly-quantum-confined TiO_2 nanofilaments, as a function of synthesis parameters and deposition conditions.

2.3.2 Synchrotron techniques

The discovery of synchrotron radiation emitted from a particular type of circular particle accelerator revolutionized the capabilities of XPS techniques for studying surfaces. In practice, synchrotrons accelerate charged particles radially around a vacuum tube through sequential magnetic fields to produce highly collimated and intensely bright light. Theoretical considerations that an electric charge moving in a circular path should radiate energy dates back to the turn of the 20th century, but practical designs for circular electron accelerators did not come to fruition until 1946 by Edwin McMillan at Berkeley with a team at General Electric Research Laboratory.[75] McMillan et al. constructed a 70-MeV synchrotron accelerator and by the following spring, the team made the initial observation of synchrotron radiation which they

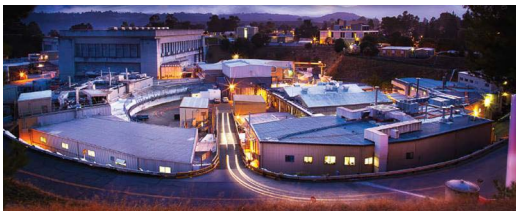

Figure 2.4. Stanford Synchrotron Radiation Light Source (SSRL) at the SLAC National Accelerator Laboratory in Menlo Park, California at dusk. Adapted from ref. 77.

described as a stable beam with an approximate one square mm cross section. Over the proceeding decades, the emergence of next-generation synchrotron facilities had remarkable implications for surface characterization technology, including and especially photoelectron spectroscopies. XPS historically employed conventional metallic-anode X-ray sources, such as aluminum and magnesium, which limits incident radiation energies to the fixed X-ray lines inherent to the metal anode material. Alternatively, synchrotron radiation is highly tunable ranging from infrared to hard X-rays, highly polarized, and is typically emitted in nanosecond pulses which enables time-resolved studies. As such, its discovery has propelled advancements in NEXAF (sometimes referred to as XANES, both defined earlier) techniques for insight into and valence structure and ARXPS methods for depth profiling. In practice, current synchrotron facilities as shown in Fig. 2.4 are about the size of a football field on average, the largest being seventeen miles in circumference,[76] and generally employ an ensemble of spectroscopic techniques at various points along the beamlines including but not limited to XPS, ARXPS, UPS, and NEXAFS to enable a comprehensive view of a material's interfacial chemical and electronic structure.

The implementation of XPS with synchrotron radiation not only drove the advancement of the aforementioned techniques, but also further evolved XPS analysis of chemical dynamics on surfaces both at ambient pressures and at fast timescales. Due to the large scattering cross section between emitted photoelectrons and neighboring gas molecules, traditional XPS necessitates a UHV environment. Nonetheless, the need for chemical and electronic investigations of in situ dynamics at material interfaces, such as the adsorption of gas molecules on metals, drove research into instrumentation that would enable XPS at higher, near-ambient pressures. Lab-based ambient-pressure XPS (APXPS) techniques that employ differential pumping stages between the high pressure sample chamber and the detector had been established since Seigbahn's studies in the 1970's. Even so, its applications were limited by the scarcity of available instrumentation and disadvantaged by contamination from oil-based diffusion pumps.[78] Since the advent of synchrotron radiation as well as the development of electrostatic condensing lenses, investigations

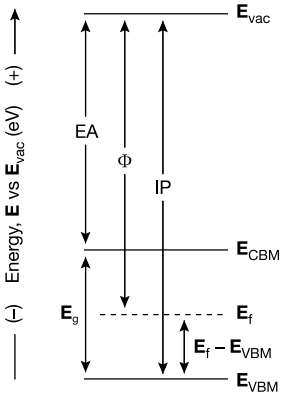

Figure 2.5. Generic band-energy diagram defining and localizing electron affinity, EA, work function, Φ, ionization potential, IP, band gap, $\mathbf{E}_g$, vacuum level energy, $\mathbf{E}_{vac}$, Fermi-level energy, $\mathbf{E}_f$, and valence band maximum energy, $\mathbf{E}_{VBM}$. Adapted from Carl, A. D. *Soft, Organic, Carrier-Selective Contacts at Inorganic Semiconductor Interfaces Enabled by Low-Defect Covalent Bonding*. Ph.D. Dissertation, Worcester Polytechnic Institute, Worcester, MA, **2020**.

of interfacial chemical dynamics afforded by APXPS techniques have risen drastically since the early 2000's.[78] To date, synchrotron sources have enabled in situ monitoring of: thin film and nanostructure syntheses,[79] the nature of adsorption and reactivity at metal catalyst surfaces,[80–82] chemical dynamics at electrochemically active interfaces,[83–85] among others. Conveniently, due to the limited availability of beamline time at synchrotron facilities, several lab-based systems have been also developed over the last decade to enable photoelectron spectroscopies at ambient or near-ambient pressures with the use of conventional UV or X-ray sources (Al, Mg, or He).[86–95]

2.4 Traditional materials

This section reviews literature precedented surface functionalization strategies for traditional materials including silicon, graphene, group six dichalcogenides, and oxyhalides in the context of informing surface chemistry studies for new and emerging low-dimensional materials. Among them, the surface derivatization approaches most relevant to this thesis work aim to improve atmospheric stability, to connect dissimilar materials, and to impart chemical and electronic tunability. In particular, the discussions surrounding surface chemistry for electronic passivation and optoelectronic control rely on fundamental understanding of the energetic band structure of crystalline solids including the concepts of Fermi level, work function, and band bending at material interfaces, including and especially dipole-induced band bending.

Figure 2.5 depicts a general band-energy diagram for a semiconductor material to illustrate fundamental definitions and positioning of various energy levels. Briefly, the band structure of a semiconductor-vacuum interface depends on its doping. For semiconductors, the Fermi-level energy, denoted herein as $\mathbf{E}_f$, is a hypothetical energy level that lies within the solid material's band gap that at thermodynamic equilibrium, would have a 50% probability of being occupied at a given time. For n-type semiconductors, the Fermi level is positioned closer to the lowest energy of the conduction band or the conduction band minumum, $\mathbf{E}_{CBM}$, relative to the middle of the band gap. For p-type materials, the Fermi level is relatively closer the valence band maximum energy, $\mathbf{E}_{VBM}$. As such, for semiconductors Fermi-level positioning is tunable as a function of dopant density. Conversely, for metals, the Fermi-level energy is equivalent to the material's work function, Φ (capital Phi), or the energy required to remove an electron from the surface of a condensed solid material into the external vacuum. In the case of a metallic or semiconducting material with no native surface charges or dipoles, the energy bands lie relatively flat in vacuum. Conversely, at the interface of two materials (metal-semiconductor, semiconductor-semiconductor, liquid-semiconductor) with distinct electronic structures, the relative carrier densities shift as the Fermi levels of the two materials equilibrate, leading to a 'bend' in the energy bands.

Band bending can also result from the presence of interfacial charge or surface dipoles. In the context of interfacial dipoles from covalently-tethered molecular organics, the magnitude and direction of dipole-induced band bending can be tuned by manipulating the chemical functionality of the derivatizing molecules to effect changes in electronic structure. For example, organic overlayers with largely electron-withdrawing (EW) functionality may impart a surface dipole that effects an increase in ϕ (lowercase phi) values with respect to vacuum energy, that magnitude of which is proportional to that of the dipole. Conversely, electron-donating (ED) functionality can yield interfacial dipoles opposite in directionality relative to those from EW groups, thus yielding ϕ shifts to lower energies relative to vacuum. Dipole-induced band bending has been well explored for a number of traditional semiconductor materials in the context of interfacial passivation and optoelectronic tunability. The proceeding subsections review such surface derivatization strategies, among others, in the context of exploiting them for emerging or under-explored materials.

2.4.1 Silicon

Research into silicon (Si), an intrinsic semiconductor with an indirect band gap of 1.12 eV, for electronics encompasses more than a century of precedence, and current state-of-the-art technology remains dominated by silicon-based electronic devices including transistors, integrated circuits, and diodes.

Presently, the utility of crystalline silicon as a robust semiconductor substrate includes applications in photovoltaics, chemical and biological sensing, catalysis, and Li-ion batteries, among others. Nonetheless, the H-terminated Si(111) surface is prone to oxidation and the subsequent formation of dangling bonds and mid-gap defects under ambient conditions which have deleterious implications for overall performance.[9]6 Energy storage and conversion applications for Si generally rely on interfaces with high chemical- and electronic-quality, and as such, various strategies for passivation of silicon interfaces have been investigated. In terms of chemical stability, the nascent Si(111) surface is terminated in Si–H bonds which readily oxidize under ambient conditions. Moreover, from an electronics standpoint, the Si surface is most susceptible relative to the bulk material to disturbances in lattice symmetry and electronic defect states that negatively impact carrier dynamics. As such, passivation efforts to minimize oxidation and concomitant recombination losses are dominated by surface chemistry approaches. Thick thermally-grown oxides or deposition of metal oxide thin films including Al_2O_3, HfO_2, Ga_2O_3, and Ta_2O_5, can achieve electronic passivation of the Si(111) surface, however challenges associated with harsh experimental conditions, expensive vacuum instrumentation, or their insulating nature necessitate alternative methods, particularly for applications that rely on high electrical conductivity and scalability.[96] Moreover, it is established that Si(111) surfaces in contact with acidic aqueous solutions[97–98] (*e.g.* 18 M H_2SO_4, 11 M $NH_4F_{(aq)}$, pH = 5 buffered $HF_{(aq)}$) or some electrolytic redox solutions yields exceedingly low surface recombination rates.[99–100] This has been attributed to interfacial band bending and the formation of an inversion layer at the semiconductor-liquid interface that drives carriers away from the surface and into the bulk.[99–100] Nonetheless, the experimental constraints involving semiconductor-liquid interfaces for this form of electronic passivation pose issues for scalability and practical applications that necessitate fully solid-state configurations. For such instances, passivation efforts employing surface chemical derivatization using straightforward, benchtop methods may be more suitable.

Among molecular approaches to Si passivation, those employing derivatization with covalent organic monolayers are most relevant to the studies herein. As discussed thoroughly elsewhere,[96] strategies for covalently tethering aliphatic or aromatic organics to H-terminated Si(111) surfaces can include silanization, hydrosilylation, halogenation-alyklation, electrochemical methods, among others. Conveniently, based on the lattice spacing between adjacent silicon atoms at Si(111) interfaces, methylation via two-step chlorination-alkylation yields nearly complete surface coverages.[101] Due to the total conversion of Si–H bonds to stable Si–C bonds, the resulting methylated surfaces demonstrate remarkable resistance to oxidation as compared to H–Si(111) surfaces under ambient conditions as evidenced by XPS analyses,[102–104] as well as comparably lower surface recombination

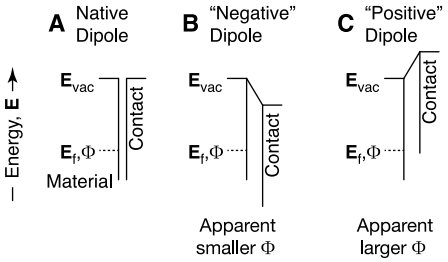

Figure 2.6. Energy diagram illustrating the energy alignment at a material and a surface contact at equilibrium for **A** a native dipole, **B** a "negative" dipole, and **C** a "positive" dipole.

velocities.[103,105–106] Packing densities and subsequent monolayer coverages decrease according to relative size and steric hindrance of the organic groups. Nonetheless, H–Si(111) surfaces covalently derivatized with various alkyl chains (ethyl, *iso*-propyl, *tert*-butyl, and octyl) as well as phenyl functionality all demonstrate significant resistance to chemical oxidation as well as longer charge-carrier lifetimes as compared to H-terminated surfaces despite lower relative coverages.[103] Moreover, similarly to the band bending that occurs at semiconductor-liquid junctions as discussed prior, covalent derivatization of Si surfaces can impart relative interfacial dipoles that can effect changes in photoelectrochemical behavior, photovoltaic properties, carrier dynamics, as well as electronic interactions between that material and other contacting phases.[107–109] Figure 2.6 demonstrates relative Fermi-level equilibration at the interface of a metallic material and a surface contact at equilibrium for a native dipole, a "negative" dipole, and a "positive" dipole. For Si, such molecular dipoles also play a role in electronic passivation as evidenced by low SRV values, however it is likely secondary to the oxidative stability afforded by Si(111) interfaces dominated by Si-C bonds. Additionally, surface derivatization with mixed monolayers, such as mixed methyl and allyl or amino functionality, presents an opportunity for secondary chemistry at that terminal site while retaining the passivating effects that near-complete methylation achieves.[110] This is particularly attractive for silicon applications that necessitate high electronic quality and atmospheric stability but also rely on specific chemical functionality, such as photovoltaics, catalysis, or chemical and biological sensing.

Beyond the passivation of H–Si(111) surfaces, chemical derivatization of silicon oxide (SiO_x) surfaces exploit a number of surface chemistries to achieve chemical and electronic tunability for a range of practical applications. This can include silicon oxide surfaces such as glass, silica, and sand, however the discussions throughout the proceeding paragraphs are focused mostly around bulk Si substrates terminating in a native or chemical SiO_x layer. Figure 2.7 summarizes conventional approaches for covalent derivatization of

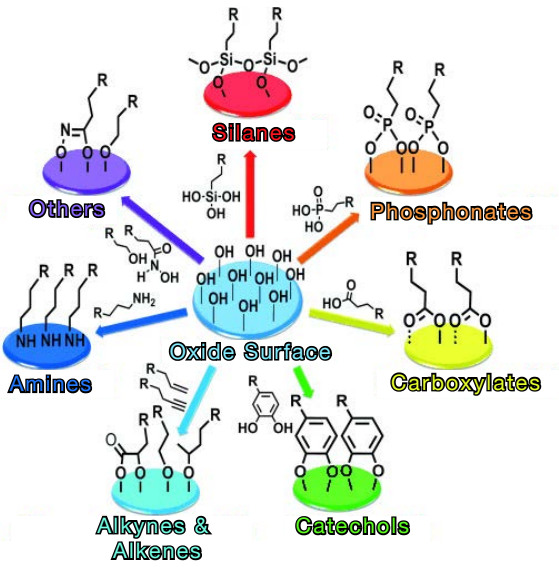

Figure 2.7. Covalent derivatization strategies amenable to oxide surfaces including SiO_x,TiO_2, graphene oxide, and others. Adapted from Pujari, S. P.; Scheres, L.; Marcelis, A. T. M.; Zuilhof, H., Covalent Surface Modification of Oxide Surfaces. *Angew. Chem. Int. Ed.* **2014**, *53*, 6322-6356.

oxide surfaces. Among attachment strategies for SiO_x interfaces, organosilanes are widely employed for their low-cost commercial availability and facile self-assembly on surfaces under near-ambient conditions and are most relevant to this thesis work. As discussed prior, organosilanes covalently tether to hydroxylated surfaces through the formation of O–Si–O bonds. In the context of SiO_x surfaces for chemical or biological sensing, silanization presents an opportunity for robust control over selectivity and sensitivity toward particular analytes based on the chemical functionality of the molecule. The terminal groups of a particular silane can be strategically selected or designed to adsorb, either reversibly or irreversibly depending on the application, specific gases, enzymes, and proteins that subsequently effect small but measurable changes in electrical properties for sensing applications. In one such case, a chemical field-effect transistor (chem-FET) employed an array of silicon nanowires derivatized with aminopropyltriethoxysilane (APTES) for sensing trace explosives. This particular instance exploited the affinity for the terminal $-NH_2$ to reversibly bind the common explosive trinitrotoluene (TNT) to enable highly sensitive detection at sub-fentomolar concentrations of TNT. Additionally, other silicon-based chem- or bio-FETs have employed functionalization with APTES using similar chemistries for the highly sensitive and selective detection of important biomarkers,[111–114] gases,[115–116] and

small molecular organics.[117–118] A number of these instances rely on secondary functionalization at the terminal amine site for added control over the required chemical functionality to achieve higher selectivity for a particular analyte. As will be discussed in proceeding sections, these particular applications of silanization on well-characterized Si surfaces strongly inform derivatization strategies for other emerging materials for sensing and energy applications that may demonstrate better cost-scalability factor or are more attractive for incorporation into polymers for applications in flexible, wearable electronics.

In addition to chemical tunability, covalent derivatization of SiO_x surfaces presents an opportunity for tunability of optoelectronic properties and carrier dynamics that is particularly useful for energy or catalysis applications. Secondary derivatizations at a terminal amine or allyl group on silanized Si surfaces can install larger aromatic organic molecules that are strongly absorbing and are amenable to functionalization that affords tunability of electronic structure. One such example which is particularly relevant to the future directions of this present work involves inexpensive and commercially available rylene derivatives, which are known to exhibit tunable shifts in electronic structure as a function of both chain length and substitution at the bay positions.[119–120] This is especially attractive for energy applications for which carrier selectivity through absolute energy level tuning is desired. As demonstrated previously,[96] perylene tetracarboxylic dianhydride (PTCDA) can be covalently tethered to aminosilanized SiO_x surfaces through an imide linkage. Our group explored this primarily in the context of silicon-based multi-junction photovoltaics for imparting carrier selectivity afforded by energy level tuning. Beyond parameterizing the initial PTCDA attachment, our group also demonstrated straightforward anhydride-to-imide conversions at the terminal ends of surface-bound PTCDA to install specific chemical handles for further attachment of tandem-relevant contacts or semiconductor layers.[96] The rationale for these studies is that flexible, organic linkers should obviate misalignment from lattice-mismatching of dissimilar semiconductor materials to enable enhanced conductivity and minimize interfacial electronic defects. This precedence posits surface- or edge-functionalization with perylene derivatives as a powerful opportunity for covalently connecting rigid, inorganic materials for applications that rely on high conductivities and minimal electronic defects. As will be discussed more thoroughly in subsequent chapters, future studies surrounding emerging low-dimensional materials could exploit this chemistry for covalently "sewing" 2D sheets or filaments together at their high-conductivity axes for enhanced carrier transport and electronic tunability for a range of applications.

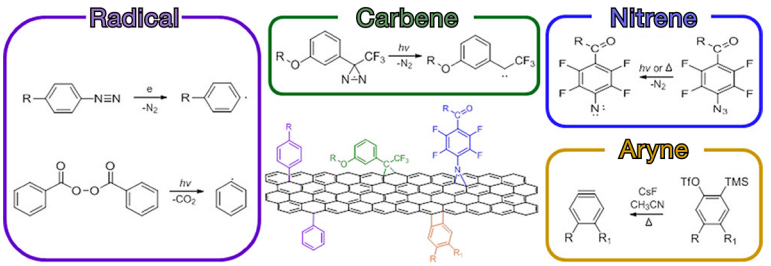

Figure 2.8. Covalent functionalization strategies amenable to graphene surfaces. Adapted from Park, J.; Yan, M., Covalent Functionalization of Graphene with Reactive Intermediates. *Acc. Chem. Res.* **2013**, *46*, 181-189.

2.4.2 Graphene

Since its re-discovery in 2004 by Novoselov and Geim,[1–2] graphene has become one of the most widely studied and applied materials for its compelling mechanical and electronic properties as well as its wide range of nano-scale structures. Pristine graphene is a single-layer 2D allotrope of the Van der Waals material graphite consisting of a π-conjugated carbon atoms arranged in a honeycomb crystal lattice.[121] Its crystal structure affords a range of unique properties that are uncommon for traditional nanostructured materials including ultrahigh carrier mobility; excellent thermal conductivity, mechanical strength, and flexibility; long electron mean free paths; and some remarkable quantum effects including the observation of quantum Hall effect even at room temperature.[121] In addition, due to the high surface area and optical transparency, graphene is widely employed as a transparent conductive electrode material for energy and electronics applications. While graphene was initially discovered by mechanical exfoliation from graphite, the current breadth of synthetic routes for producing well-defined graphene sheets and nanostructures most commonly include chemical exfoliation; chemical vapor deposition; electrochemical methods; and chemical, electrochemical, thermal, or photocatalytic reduction of graphene oxide.[48] While graphene is generally a zero-band-gap material, few-layer graphene structures are amenable to bang-gap opening when the interlayer symmetry is broken by an external, perpendicular electric field.[122] Chemical derivatization or oxidation of graphene surfaces has since been shown to achieve similar results, with the magnitude of the induced band gap being tunable from ~0.1–2.5 eV as a function of the oxidation conditions or the electronic structure of the grafted molecular organics. This is particularly useful for applications that rely on the quasi-semiconducting behavior of band-gap-opened graphene and the resulting changes in optoelectronic properties.

Compared to the wide array of functionalization chemistries available for H–Si or SiO_x –OH-containing surfaces, chemical derivatization approaches

for graphene are much more constrained. Chemical routes for covalent attachment that Fig. 2.8 graphically summarizes generally rely on either the cleavage of conjugated C=C bonds to attach free radicals or dienophiles, or the oxidation of graphene to graphene oxide (GO), which significantly broadens the scope of attachment strategies. The primary motivation for graphene functionalization is to improve its dispersion in common organic solvents, as many practical applications rely on solution phase chemical processing. As such, in many of the instances mentioned throughout this section, enhanced dispersibility in various organic solvents was achieved. Additionally, a vast number of studies demonstrate enhanced photocatalytic activity of graphene structures by way of chemical doping. Nonetheless, as similar results were achieved using guano,[123] the discussions surrounding chemical derivatization strategies will focus instead on other more impactful applications. Among them, a number of molecular organics have been covalently attached to graphene surfaces to effect changes in electronic structure or to impart desired chemical functionality for subsequent attachment or molecular recognition for a range of applications.[48,121–122]

A number of non-covalent surface attachment strategies that rely on ionic or van der Waals interactions with the π-system of graphene exist. Among them, functionalization with nanoparticles or evaporation of metals for electrical contacts among other things are commonly employed. Interfacial adsorption of nanostructures precious metals such as Pt, Au, Ag, Rh, and Pd are particularly useful for catalytic applications including sensors, supercapacitors, and energy storage and conversion. Moreover, nanostructured metal oxides can be deposited onto graphene surfaces for similar applications as well as for flexible electronics, gas sensing, and transparent conductive electrodes.48 Nonetheless, covalent derivatization strategies for graphene and graphene oxide surfaces are more relevant to this thesis work and will be discussed more thoroughly.

Covalent attachment to π-conjugated graphene maintains the 2D hexagonal symmetry of the lattice, and therefore can be preferrable for applications that rely on the robust physical and mechanical properties afforded by this structure. Without oxidation, covalent derivatization generally employs free radical chemistry with diazonium salts or benzoyl peroxides, or the grafting of dienophiles which generally react through 1,3 dipolar cycloaddition or nitrene addition.[48] Free radical addition of nitrophenyls onto graphene have been shown to induce a controllable band gap[48,124–125] or afford changes in conductivity that are tunable as a function of reaction time.[48,126] This is particularly useful for applications that rely on semiconductor properties of graphene including photovoltaics, nanoelectronics, among others. In terms of dienophiles, 1,3 dipolar cycloaddition with azomethine ylide is commonly employed to nanostructured graphene, most notably for grafting pyrrolidine rings to the surface. Because the ring is amenable to diverse functionalization, pyrrolidine attachment is especially useful for applications that rely

on specific chemical handles including drug delivery, fluorescence imaging, chemical or biological sensing, and polymer composites.[48] Beyond pyrrolidine, phenyl and alkyl azides can covalently attach through nitrene addition. In one such case, graphene sheets functionalized with alkylazides of varying chain lengths facilitated the attachment of gold nanoparticles to investigate reactive site distribution.[127] Additionally, a range of functional groups and polymer chains have been attached to graphene for the purpose of secondary modification including surface-initiated polymerization and metal-ion reduction.[48] While derivatization of conjugated graphene has been remarkably useful, the disruption of the π system yields significant changes in the electronic properties and local structure, including a decrease in carrier mobility by multiple orders of magnitude,[48] that may be disadvantageous for some applications.

Beyond π-conjugated graphene, derivatization of graphene oxide (GO) is amenable to a much broader range of surface chemistries afforded by the addition of oxygen-containing functional groups. Many of the derivatization strategies depicted in Fig. 2.7 can be employed for graphene oxide surfaces. While the explicit interfacial chemistry and homogeneity of graphene oxide remains a topic of debate, a broad consensus is that GO surfaces contain regions of oxygenated aliphatic regions dispersed throughout regions of π-conjugated graphene.[48] Generally, the surface contains epoxy and hydroxyl terminations while carboxylic groups decorate the edges. This presents an opportunity for orthogonal functionalization of terraces and edges which may be convenient for a number of applications. For example, one study demonstrated effective cross-linking of graphene sheets to form a paper-like membrane via amidation with polyallylamine at the edges of adjacent sheets.[128] The relative improvement to mechanical strength as compared to non-functionalized graphene may posit this and other polymer-crosslinked graphene composites as candidate conductive polymers for applications in flexible, wearable electronics and sensors. Moreover, graphene is commonly functionalized with a number of biocompatible polymers, including polyethylene glycol, as a means for secondary adsorption of other chemical species of interest. PEGylated nanographene oxide has been employed to further functionalize the surfaces with antibodies or peptides for selective cancer therapy and drug delivery[129–133] or with photosensitizers for intracellular imaging applications.[134–136]

Apart from polymers, covalent functionalization of graphene oxide for the purpose of sensitive and selective sensors encompasses a large portion of derivatization efforts.[137] One compelling study imbedded functionalized GO in cotton yarn to develop highly sensitive, wearable fiber-type gas sensors.[138] Derivatization included covalent grafting of heptafluorobutylamine (HFBA), 1-(2-methoxyphenyl)piperazine (MPP), or 4-(2-keto-1-benzimidazolinyl)piperidine (KBIP) that react via nucleophilic substitution at the epoxy groups. Conveniently, MPP and KBIP are amendable to diverse chemical functional-

ization at their respective terminal ends to enable highly selective sensing of a broad range of adsorbates. Additionally, GO nanoplatelets derivatized with the enzyme glucose oxidase reacted at the interfacial carboxylic acid groups to enable highly sensitive, biocompatible glucose sensors.[139] As high sensitivities in these sensing applications rely on high surface areas, graphene oxide is a highly suitable material due to the broad collection of synthetic routes for various graphene nanostructures.[140] Nonetheless, while graphene remains a useful conductive material for a number of practical applications, the lack of a nascent electronic band gap and relatively simple interfacial chemistry limits its applications. This drives research into other low-dimensional semiconductors with more diverse chemical compositions and subsequent opportunities for tunability in the context of energy and catalysis applications.

2.4.3 Layered 2D materials Beyond Graphene

The discovery of graphene and its derivatives is thought to have marked the inception of new and diverse classes of low-dimensional materials, including other layered 2D structures which are most relevant to this thesis work. Figure 2.9 summarizes a number of bioelectronics-related 2D materials and their applications. Among them, Van der Waals (VDW) materials are particularly compelling for the unique optical, electronic, and mechanical properties afforded by their layered structure. As discussed prior, the layered structure affords high in-plane electrical conductivity as well as excellent effective charge separation perpendicular to the layers, which posits them as candidate materials for applications in electronics, photocatalysis, and energy conversion and storage. For example, hexagonal boron nitride (*h*-BN) is a layered material isostructural to graphite with alternating honeycomb lattices of boron and nitrogen. Due to the effective separation of photogenerated charges, *h*-BN is often coupled with traditional semiconductor photocatalysts, such as TiO_2, to yield composite materials with comparatively enhanced photocatalyic and photovoltaic performance.[141] Moreover, since it is a wide-band-gap insulator (~5.9 eV), *h*-BN is most commonly employed as a dielectric layer for energy or sensing applications.

Beyond *h*-BN, transitional metal dichalcogenides (TMDs) are ubiquitous VDW materials for their compelling physical and optoelectronic properties, natural abundance, and relative atmospheric stability in many cases. The general structure of TMDs, the first of which was discovered in 1923 by Linus Pauling,[142] follows the formula MX_2 where M is a group 4–10 transition metal (typically Mo, Nb, W, Ni, V, or Re) and X is a chalcogen (typically Se, Te, or S).[4] The bulk crystal structure consists of a covalent, atomic M layer sandwiched between two weakly VDW-bonded X layers. Among the present library of around sixty TMDs, those that are Mo- or W-based, including and especially molybdenum disulfide (MoS_2), are the most widely studied and employed as they are semiconducting with sizeable band gaps

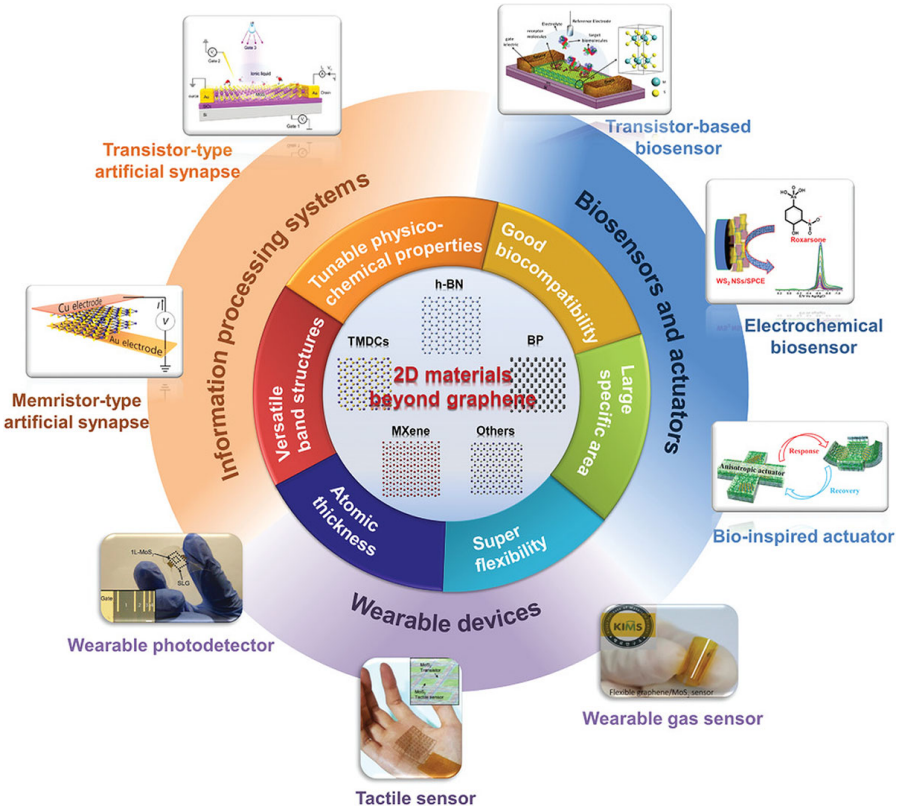

Figure 2.9. Bioelectronics-related 2D materials beyond graphene, their unique properties, and practical applications. Reproduced from Wang, B.; Sun, Y.; Ding, H.; Zhao, X.; Zhang, L.; Bai, J.; Liu, K., Bioelectronics-Related 2D Materials Beyond Graphene: Fundamentals, Properties, and Applications. *Adv. Funct. Mater.* **2020**, *30*, 2003732.

between 1–2 eV and are generally stable under atmospheric conditions.[143] Since it maintains its mechanical strength under a wide range of temperatures and pressures, early uses employed MoS_2 as an efficient dry lubricant or additive in greases, polymers, paints, and other coatings.[144] Presently, two-dimensional bulk and nanostructures of MoS_2 have demonstrated utility in various energy storage and conversion applications. For example, the effective charge separation and possibility of ion intercalation afforded by the 2D-layered structure make MoS_2 a common anode material for Li- or Na-ion batteries or for supercapacitor applications.[145] Nonetheless, for many such applications, optoelectronic and chemical tunability is largely desired.

As is the case for silicon, graphene, and other traditional materials, functionalized TMDs afford robust control over energy band structure and selective chemical handles to enable enhanced selectivity and specificity for

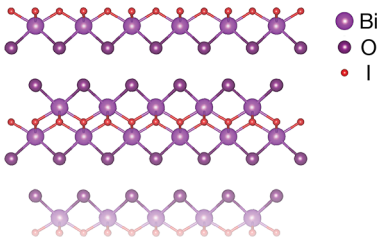

Figure 2.10. Crystal structure of BiOI(001) showing a bismuth-oxide termination considered further in Chapter 4.

energy and sensing applications. In the case of MoS_2, as sulfur vacancies are commonly present at lattice edges or corners,[146] covalent derivatization approaches often employ molecules with thiol functionality to occupy those vacancy sites. The earliest known reports for covalent functionalization of MoS_2 demonstrate the corner-site-selective attachment of dibenzothiophene (DBT) to MoS_2 nanoclusters in the context of desulfurization of fossil fuels. Since then, MoS_2 structures have been derivatized with thionin for the highly sensitive detection of DNA,[147] with thiol-terminated PEG ligands to modulate the catalytic activity of β-galactosidase,[148] with lipoic acid/PEG composites to enable chemotherapy treatment for breast cancers, among others. Additionally, covalent attachment of thiols with terminal carboxyl, hydroxyl, or amino functionality provide chemical handles for further derivatization which is particularly useful for sensing applications to improve selectivity and sensitivity as well as for energy applications that rely on connecting dissimilar materials. Such approaches are most relevant to this thesis as a number of emerging materials discussed in subsequent sections may exploit them for similar applications.

Apart from TMDs, bismuth-based layered structures encompass another particularly promising class of traditional VDW materials as bismuth itself is non-toxic and layered bismuth-based materials can be produced via several low-cost methods.[149–157] Among them, bismuth oxyhalides, BiOX (X = Cl, Br, or I), are a family of V–VI–VII layered semiconductors that have been known since antiquity, as evidenced by the longstanding, multi-millennia use of BiOCl as a popular cosmetic ingredient.[158] Nonetheless, one may consider bismuth oxyhalides an emerging class of 2D materials as they have only recently been investigated for energy conversion applications including photovoltaics and photocatalysis. The VDW structure of these materials consist of a covalent bismuth oxide layer with $[Bi–2\,O–Bi]^{2+}$ stoichiometry that alternates with double slabs of weakly VDW-bonded halide layers, each with X^- stoichiometry, Fig. 2.10. Among studies that have investigated these oxyhalides for energy storage and conversion,[159] photocatalysis,[155–157,160–162] or water-splitting,[163–167] BiOI has consistently exhibited enhanced photocat-

alytic activity as compared to BiOCl or BiOBr.[161,168] In addition to its ~1.8 eV indirect band gap,[157,160] literature reports often attribute favorable electronic properties to the layered two-dimensional structure with static charges and repeating electric fields in the [001] direction. For example, researchers attribute high photocatalytic activity of oxyhalides under UV and visible light to efficient charge separation of photogenerated electron-hole pairs afforded by the inherent static electric field.[166] However, other electronic properties demonstrate varying behavior. For instance, most hydrothermal or solvothermal routes yield p-type BiOI,[152] however spray pyrolysis[169] and microwave hydrothermal[154] methods have produced n-type behavior. In addition, the exact chemical species, contaminants, and interfacial states at BiOI interfaces remain unknown. Fundamental insight into the interplay between synthesis parameters, interfacial chemical states, and the resulting optoelectronic properties is critical for highly efficient, practical applications in catalysis and energy conversion and storage. Moreover, the wide variety of synthetic methods yield varying polycrystalline and nanostructured BiOI in addition to high-temperature vapor-transport that yields large, single-crystalline material. As is the case for many layered VDW materials, mechanical exfoliation of large single crystals straightforwardly yields chemically pristine surfaces of this 2D-layered material, but such macroscopic physical methods are unavailable to "clean" device-relevant nanostructures, such as vertically-oriented nanofilms. The work detailed in Chapter 4 aims to understand how chemical processing can bridge the gap between nascent BiOI and chemically pristine surfaces, as well as quantify the resulting chemical and electronic properties. Since high-resolution XPS reveals oxide-rich surface terminations and XRD reveals the presence of crystalline BiI3 features, we looked toward established chemical etchants for metal oxides as well as organic solvents known to well-dissolve the interfacial contaminant BiI_3.

2.5 Emerging Materials

2.5.1 MXene Discovery from MAX Phases and Applications

The re-discovery of $M_{n+1}AX_n$, or MAX, phase materials (where M is an early transition metal, A is a group 13 or 14 element, X is carbon or nitrogen (n = 1, 2, or 3) in 1995 by Barsoum and El-Raghy[170–171] had tremendous technological impact for their unique electronic and mechanical properties. The ternary MAX phases are hexagonal in crystal structure with edge-sharing 'M6X' octahedra alternating with atomic A-element layers. Further, they can crystallize into one of three distinct phases that are distinguished only by the number of M layers separating the A layers.[172] While initial reports of the MAX phase materials date back to the 1960's,[173–174] it wasn't until two decades later that their unseeming combination of metallic and ceramic properties were uncovered. Barsoum and El-Raghy revealed that like ceramics, the MAX phase

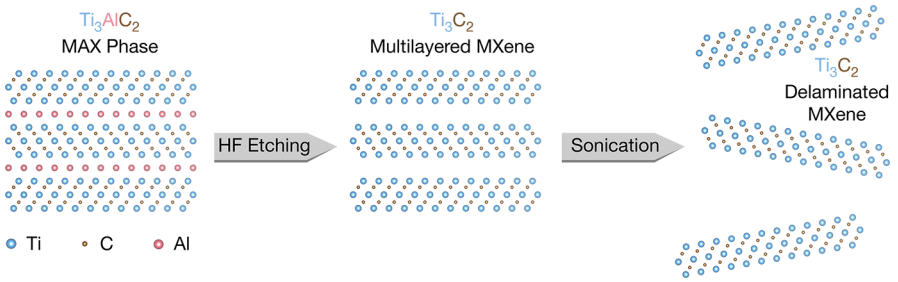

Figure 2.11. Cartoon illustration depicting the synthesis of multilayered Ti_3C_2 MXene from MAX-phase Ti_3AlC_2 by etching treatment with HF. Sonication can further delaminate the multilayered Ti_3C_2 to yield individual 2D sheets.

material Ti_3SiC_2 is stiff and relatively light with high thermal stability and oxidation resistance. Nonetheless, it was surprisingly machinable, thermally and electrically conductive, resistant to chemical shock, and plastic at elevated temperatures. This was an impactful discovery in that materials that are well-suited for high temperature applications, like ceramics, are generally hard, brittle, and not well machinable which poses limitations in practicality and scalability. Moreover, the fabrication of conventional nanolayered materials tends to be costly and not suitable for high-temperature applications. As such, these newly-uncovered MAX phase carbides and nitrides fulfilled a critical need for materials with high thermal and oxidative stability that are also highly machinable, electrically conductive, damage tolerant, and can be synthesized from chemically diverse and abundant materials. Presently, MAX phases have demonstrated utility in transportation and petroleum industry applications as candidate materials for jet engines, gas turbines, heating elements, furnaces, nozzles, and hypersonic vehicles.[175]

Like many other layered materials, some MAX phase crystals are amendable to chemical exfoliation to yield 2D sheets and nanostructures. In 2011, Barsoum and colleagues further demonstrated that exposure of MAX phase Ti_3AlC_2 to concentrated hydrofluoric acid (HF) selectively etched the Al atomic layers to yield laminated sheets of Ti_3C_2 that could be subsequently separated with sonication in water, Fig. 2.11.[176–177] The resulting 2D material follows the general formula $M_{n+1}X_nT_x$ where T_x denotes surface functional groups including –O, –OH, and –F. This marked the discovery of MXenes, a new class of 2D carbides and nitrides, aptly named for their structural similarities to graphene and other conventional 2D materials. The low-dimensional nature of MXenes yields comparably higher surface areas and aspect ratios, making them exceptionally more electronically conductive than their MAX phase counterparts. This fact, in combination with the favorable mechanical properties, have afforded practical success for MXenes in a number of applications, most notably including chemical and biological sensing,[178–183]

energy storage and conversion, and electromagnetic shielding.[9–10] The MAX phases most amenable to chemical exfoliation generally contain an Al "A" layer and among them, Ti_3C_2 is by far the most widely studied and employed MXene to date. For this reason, and because the work involving MXene surface chemistry detailed in subsequent chapters of this thesis solely considered Ti_3C_2, discussions regarding surface derivatization strategies will be mostly limited to Ti-based MXenes.

Nascent MXenes following chemical etching and rinsing procedures generally demonstrate a combination of interfacial O, OH, and F species, and thus are denoted $M_{n+1}X_nT_x$, where T represents surface-terminating functional groups. As such, MXenes are amenable to covalent derivatization that exploits not only interfacial or edge-localized metal atoms, but also the diverse chemical toolbox for attachment to oxygen-containing functional groups. Additionally, a simple treatment with strong base, NaOH, straightforwardly minimizes F terminations and maximizes O terminations.[184] This yields MXene interfaces with substantially more reactive O sites which can subsequently enable higher molecular coverages.

Despite their favorable properties, many MXenes tend to suffer from oxidative degradation to their metal-oxide counterparts, which deleteriously impacts optoelectronic structure. As such, a large portion of present research efforts into MXenes are directed toward improving atmospheric stability. Passivation efforts have included thermal annealing to remove oxidation-prone surface functional groups,[185–188] deposition of passivating, ultrathin TiO_2 layers,[189] or treatment with molten inorganic salts.[190] Nonetheless, covalent derivatization with molecular organics may ultimately be a more favorable route for minimizing oxidation due to the diverse chemical and electronic tunability afforded by strategically designing the candidate passivating molecules.

Covalent functionalization efforts for MXene surfaces in the context of passivation have most notably included edge-capping with polyanionic salts. In this study, inorganic sodium salts of polyphosphates, polyborates, and polysilicates were shown to selectively tether to the edges of $Ti_3C_2T_x$ and V_2CT_x sheets and the resulting derivatized MXenes showed improved oxidative stability in water.[15] For these adsorbates, the carbonyl end of the salt coordinates at the presumably Ti-rich edges of Ti_3C_2 MXene sheets. Beyond edge-capping with polyanionic salts, most other covalent attachment strategies for MXene surfaces were directed toward improving dispersibility in common organic solvents, modifying electronic properties in the context of energy conversion and storage, or to improve sensitivity and selectivity for sensing applications. In separate studies, Gogotski and Zhang covalently attached different amino-terminated organosilanes to $Ti_3C_2T_x$ and to yield net positively charged surfaces at neutral pH.[191–192] Due to the presence of O- and and F-based terminations, MXenes generally demonstrate a net neg-

ative charge at their in-plane surface and net positive charge at the edges.[193] The ability to selectively alter the magnitude and signage of the overall surface charge may have implications for applications that rely on selective adsorption of charged species, such as chemical and biological sensing. Other studies have employed covalent attachment with long-chain organosilanes to produce hydrophobic MXene surfaces in the context of solar desalination,194 self-cleaning coatings,195 and dispersibility in non-polar solvents.[196] In the context or biological sensing applications, another study employed silanization of $Ti_3C_2T_x$ surfaces with 3-(aminopropyl)trimethoxysilane (APTMS) and subsequent functionalization with a bio-receptor (anti-CEA) to enable ultrasensitive detection of the important cancer biomarker carcinoembryonic antigen (CEA).[197] A separate study directed toward chemical sensing employed functionalization of $Ti_3C_2T_x$ surfaces with fluoroalkylsilane to enable sensitive and selective sensing of various volatile organic compounds.[178] The fluoroalkylsilane-functionalized MXene also demonstrated improved atmospheric stability.

Beyond organosilanes which primarily tether at the in-plane surfaces, two recent studies have demonstrated covalent attachment of catechol derivatives to MXenes. It is well established that *ortho* diols are excellent ligands for metal chelation.[198] As such, catechol derivatives with this functionality should selectively ligate at surface-available metal sites on MXenes. One study covalently attached dopamine and pyrocatechol to $Ti_3C_2T_x$ surfaces to enable subsequent functionalization with fluorescein in the context of biological imaging.[199] Another study employed covalent attachment of catechol derivatives with long fluoroalkyl chains to various Ti-, Mo-, N-, and V-based MXenes to afford improved oxidative stability and dispersion in common organic solvents including methanol, ethanol, isopropyl alcohol, acetone, and acetonitrile.[200] This is particularly useful across a number of application that rely on solution phase processing. Nonetheless, questions remain regarding the localization of catechol attachment to Ti-based MXenes. The former study employed a combination of density functional theory (DFT) calculations and Raman spectroscopy to demonstrate the presence of metal-catechol bonds between the Ti in the MXene lattice and the O atoms in the catechols and cartoon illustrations depict the attachment of the catechols to the in-plane surface of the $Ti_3C_2T_x$ sheets.[199] This stands in contrast to reports that explored the distinct chemical states at the terraces and the edges to demonstrate in-plane surfaces dominated by surface functional groups and edges dominated by Ti atoms.[15,201] As such, catechol attachment at the $Ti_3C_2T_x$ sheet edges may be more likely. These discrepancies necessitate further studies probing the orthogonal reactivities at MXene terraces versus edges to better understand the binding dynamic of catechol-based derivatization efforts.

As discussed prior in the context of other traditional materials, covalent attachment of molecular species with terminal amine functionality presents an opportunity for further functionalization to enable diverse chemical handles

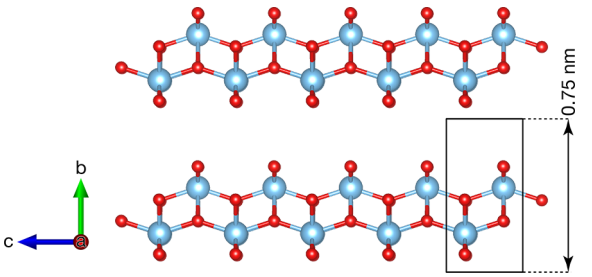

Figure 2.12. Schematic of titania-based 1D lepidocrocite, 1DL. Adapted from ref. 16.

for a number of applications. Such derivatization routes have been explored extensively for other materials, but more sparingly for MXenes and other newly discovered low-dimensional materials. More importantly, little had been done to directly probe and quantify the changes in optical and electronic structure that result from covalent attachment of organic species. This fundamental insight is critical for applications in sensing, electromagnetic interference shielding, and energy applications that rely on low-defect surfaces and electronic or chemical tunability. The studies detailed in Chapter 5 aim to characterize and quantify the interplay between the interfacial chemical and optoelectronic properties of $Ti_3C_2T_x$ as a function of derivatization with various organosilanes. We aimed to establish robust control over the electronic structure and optical properties via surface dipoles based on the inclusion of electron-donating or electron-withdrawing functionality.

2.5.2 Hydroxide-Derived Nanomaterials

The scalability issues associated with the safety hazards and acute toxicity of hydrofluoric acid often drives research into alternate chemical routes for achieving comparable etching effects. Since the synthesis of MXenes from their MAX counterparts historically involves the use of HF, research groups have explored alternate combinations of acid etches and rinsing with inorganic fluoride salts to achieve the A-layer etching. Barsoum and colleagues have since demonstrated that a slow addition of Ti_2AlC_2 to a solution of lithium fluoride (LiF) dissolved in 6 M $HCl_{(aq)}$ is sufficient to etch the Al layers to yield $Ti_3C_2T_x$ MXene.[202]

Other HF-free MXene synthesis routes have employed a base wash step with quaternary ammonium hydroxides. Interestingly, though, it was realized that rather than yielding multilayered MXenes, the combination of Ti-based carbides, borides, or silicides with such bases, most commonly tetramethylammonium hydroxide (TMAOH), yielded a different material entirely. We reported the bottom-up synthesis of 1D TiO_2-based nanofilaments (NFs) from the reaction of TiC, TiB_2, TiN, Ti_3AC_2 (A = Al, Si, Ga, Sn, etc.) and Ti_2SbP

with TMAOH at near-ambient conditions.[17] While initial DFT calculations suggested a structure involving a 1D analog of anatase,[17] more recent TEM and Raman spectroscopy with updated calculations reveals lepidocrocite-like 1D titania NFs, approximately 5×7 Å^2 in cross-section.[16] Reports of lepidocrocite-like titania include its formation on templating surfaces such as Cu(001),[203] as well as free-standing films,[204] but this form is comparatively understudied relative to anatase and rutile forms of TiO_2. Interestingly, related investigations revealed that the sub-nanometer 1DL filaments can self-assemble into a plethora of nanomaterials, from NFs, to bundles of NFs, to micrometer long filaments, to two-dimensional, 2D, flakes that are readily filtered into self-standing films.[17] Recent Raman and high-resolution transmission electron microscope, TEM, studies of 1DL films revealed the structure to be comprised of one dimensional nanofilaments that are capable of self-alignment into pseudo 2D sheets.[16] These initial reports marked the discovery of a new class of 1D TiO_2-based material we refer to as hydroxide-derived nanomaterials.

In terms of optoelectronic properties of hydroxide-derived nanomaterials, light absorption results from the initial report suggest a highly quantum-confined material.[17] While there is a wide body of literature that reports and discusses 1D anatase based on extremely-high-aspect-ratio structures, as far as we are aware, this material is unique in showing substantial quantum confinement as evidenced by the wide 4.1 eV band-gap energy. Moreover, likely due in part to the optoelectronic properties afforded by these confinement effects, films of 1DL material demonstrate good performance as electrodes in lithium-ion and lithium-sulfur systems, as well as excellent oxidative stability.[17] They are also quite good at photocatalytically producing hydrogen, H_2. The latter results are particularly topical as nanostructured[205–206] and doped[207–210] titanium oxides are some of the most extensively investigated materials for photocatalytic and photoelectrochemical applications.

Nonetheless, despite promising initial results for this 1D lepidocrocite-like titania nanomaterial, questions remain regarding the specific chemical structure, surface states, and the interplay between those chemical features and the resulting electronic properties. This fundamental insight is critical to realize scalable, practical applications for this emerging material. The studies detailed in Chapter 6 of this thesis work quantified the chemical and electronic states at the surface of the IDL titania nanofilaments as well as investigated the resulting optical behavior and carrier dynamics.

2.6 Present Challenges and Materials Outlook

This thesis primarily addresses two classes of emerging, low-dimensional materials: bismuth-based oxyhalides and titanium-based carbides and nitrides. Bismuth oxyhalides are an attractive 2D VDW material for applications in

photovoltaics, photocatalysis, and water splitting. Among them, its ~1.8 eV indirect band gap makes BiOI energetically well-matched for silicon-based tandem junction PV. While initial reports surrounding BiOI for energy applications are promising, challenges remain in terms of producing BiOI nanomaterials and composites that are of high chemical- and electronic-quality. While mechanical exfoliation methods such as tape-cleaving are quite good at producing high-quality surfaces, practical nanostructured BiOI is not susceptible to such cleaning methods. As detailed in Chapter 4, we have explored a chemical cleaning procedure for producing single crystals of BiOI with interfacial qualities that are well-aligned to mechanically exfoliated, pristine BiOI. This work is impactful for its ability to overcome the mechanical constraints of traditional exfoliation methods to enable highly-efficient, scalable photovoltaics and photocatalysis.

Additionally, many 2D materials tend to demonstrate various distinct interfacial morphologies and defects including step edges and dislocations hold conflicting implications for overall performance.[211–219] For BiOI, it remains unclear the relative chemical and electronic structures present at terraces versus step edges and the interplay between these surface morphologies and overall device efficiencies. As detailed in Chapter 4, we explore the orthogonal reactivities of step-rich vs terrace-rich domains for BiOI(001) single crystals and quantify the chemical terminations at these surface sites as a function of chemical etching and rinsing protocols. Beyond our studies, more work is needed to ascertain the implications of these domains for photocatalytic and photoelectrochemical performance.

Beyond BiOI, MXenes are highly favorable for sensing, shielding, and energy storage applications for their exceedingly high electrical conductivities reaching 24,000 S cm^{-1}.[8–11,13,179–183,197,220] Surface chemistry approaches have demonstrated the utility of organic monolayers for improving dispersibility in non-polar solvents,[196,200] for altering surface charge,[192] for improving atmospheric stability,[15,191] and for enhancing selectivity and sensitivity toward various analytes for sensing applications.[178,197] Nonetheless, the optoelectronic implications of covalently-tethered organic monolayers remains largely underexplored.[221–223] This thesis work explores covalent attachment of various organosilanes to $Ti_3C_2T_x$ surfaces and quantifies the resulting chemical and optoelectronic changes. Since ample reports surrounding silicon surface science has demonstrated the utility of molecular interfacial dipoles for controlling electronic and optical behavior, we were motivated to explore similar approaches for this promising 2D material. As detailed in Chapter 5, THz and TA spectroscopy probed changes in lifetimes and carrier dynamics and UPS demonstrated changes in work function as a function of molecular dipoles. This work is impactful for establishing a chemical roadmap for installing specific organic functionality without deleteriously affecting morphology and structure of the $Ti_3C_2T_x$ material. Similar molecular approaches with a view toward passivation remains largely underexplored.

Our studies should inform functionalization strategies with covalent monolayers for optoelectronic tunability, cross-linking adjacent sheets to improve conductivity and carrier dynamics, as well as improve atmospheric stability. Nonetheless, more fundamental studies are required to realize these strategies in a scalable way.

Contrary to BiOI and MXenes, recently-discovered Ti-based 1DL QDNs[16–17] demonstrate remarkable oxidative stability. Preliminary studies demonstrate that films of the Ti-based 1DL material demonstrate good performance as electrodes in lithium-ion and lithium-sulfur systems, as well as excellent oxidative stability.[17] They are also quite good at photocatalytically producing hydrogen, H_2. As detailed in Chapter 6, our optical studies demonstrate a highly-quantum-confined material as evidenced by the wide band-gap energy of 4.0 eV which holds implications for unique optoelectronic properties that are often advantageous for energy storage and catalysis applications. Nonetheless, widespread application of the 1DL material necessitate robust quantification of the exact chemical and electronic states present at the surface of this emerging class of material. Among the studies investigating lepidocrocite titania, few provide insight into the relative band gaps.[203–204*a*] Presently, our evidence for quantum confinement is limited to the understanding of band-gap energy shifts based on nanostructured titania of other polymorphs.[292] We envision future studies quantifying the band-energy alignments for bulk leipdocrocite titania compared to 1-dimensional nanostructured lepi-titania to strongly inform our current interpretations of quantum confinement effects. In addition, while we have probed the electronic structure of this material to yield the first report of energetic band structure for 1DLs, questions remain regarding some of the relative band positions. Future studies characterizing the band-energy alignment electrochemically may grant some clarity in our UP-determined band structure.

Additionally, our studies characterizing the electronic structure and transient dynamics of the 1DL titania as detailed in Chapter 6 demonstrate have demonstrated long-lived sub-gap photoexcitations that we postulate arise from defect states within the band gap. From a combination of UV-Vis and XANES studies, initial reports for 1DL titania demonstrate the existence of Ti^{3+} defect states which may explain the "black" coloration of the synthesized material.[17] Further, XP spectra for the 1DL material demonstrate a trace feature in the Ti 2p region consistent with the binding-energy positioning for Ti^{3+} which further support these interpretations. Systematic defect engineering and subsequent changes in optoelectronic properties and carrier dynamics for other titania polymorphs is well studied.[204*b*] Nonetheless, the origin, dynamics, and localization of these defect states for our 1DL titania remain largely unexplored in the present studies and it is critical for future work to probe this further. Moreover, while our collaborators demonstrated that at lower synthesis temperatures (<50 °C), the one-dimensional nanofilaments are capable of self-alignment into pseudo 2D sheets,[16] the interplay

between the driving forces for this aggregation and the subsequent optoelectronic implications of these distinct morphologies remains under-explored. Our initial reports, while unambiguously promising, inform the multitude of avenues for future studies surrounding this promising, newly-discovered 1D titania material.

2.7 Conclusions

A large portion of materials engineering for the purpose of improving quality of life and tackling global issues is driven by surface chemistry approaches. Such strategies aim to solve not only seemingly inconsequential concerns like protection from the elements and non-stick cookware but also more critically pervasive challenges associated with atmospheric pollution, climate change, chemical warfare threats, cost-scalability factors of industrial processes, among many others. Surface chemical approaches for the purpose of addressing such needs relies on fundamental understanding of the chemical and electronic states present at material interfaces. For many widely applied materials such as silicon for electronics and metals and metal-alloys for building and industrial applications, this knowledge has been extensively probed. It is beneficial to look toward these surface functionalization approaches for well-defined chemical systems to inform studies surrounding emerging materials that may demonstrate better efficiencies per cost or compatibility with environmental concerns. Nonetheless, much more fundamental research surrounding these material interfaces is needed to realize practical and globally impactful applications. This thesis work aims to borrow from chemical derivatization techniques widely explored for traditional materials like silicon and graphene for newer chemical systems for applications in solar energy and photocatalysis, sensing, electromagnetic shielding, protective barrier materials, and others. While the studies herein primarily surround two classes of low-dimensional materials, bismuth-based oxyhalides and titanium-based carbides and nitrides, our derivatization strategies should inform present approaches for covalently connecting other dissimilar materials to enhance carrier transport and conductivities, improve atmospheric stability, design highly sensitive and selective sensors, and more.

CHAPTER 3

SPECTROSCOPIC SURFACE CHARACTERIZATION TECHNIQUES

Portions adapted from:

1. Alexander D. Carl. *Soft, Organic, Carrier-Selective Contacts at Inorganic Semiconductor Interfaces Enabled by Low-Defect Covalent Bonding*. Ph.D. Dissertation, Worcester Polytechnic Institute, Worcester, MA, **2020**. digital.wpi.edu/show/hq37vr534

2. Alexander D. Carl, Roghi E. Kalan, John David Obayemi, Martiale Gaetan Zebaze Kana, Winston Oluwole Soboyejo, and Ronald L. Grimm. Synthesis and Characterization of Alkylamine-Functionalized Si(111) for Perovskite Adhesion With Minimal Interfacial Oxidation or Electronic Defects. *ACS Appl. Mater. Interfaces* **2017**, *9*, 34377–34388. 10.1021/acsami.7b07117

3. Julia L. Martin, Roy Stoflet, Alexander D. Carl, Katarina M. Himmelberger, Sergio Granados-Focil, and Ronald L. Grimm. Quantification of Surface Reactivity and Step-Selective Etching Chemistry on Single-Crystal BiOI(001). *Langmuir* **2020**, *36*(32), 9343–9355. 10.1021/acs.langmuir.0c00980

3.1 Abstract

X-ray and ultraviolet photoelectron spectroscopy was employed extensively throughout this thesis work to characterize the chemical and electronic states present at low-dimensional material interfaces. Sections §3.2 and §3.2 detail the theory and practical applications of XPS and UPS respectively in brief: a more comprehensive description of XPS and UPS theory as it relates to our PHI 5600 multi-technique system is detailed elsewhere.[96] A historical perspective of these techniques is detailed earlier in §2.3. For investigations surrounding surface chemical terminations for BiOI(001) interfaces, we utilized angle-resolved XPS to probe surface versus contributions to photoelectron intensities. Quantification of BiOI surface states employed substrate-overlayer models which are detailed in Appendix A.

3.2 X-Ray Photoelectron Spectroscopy (XPS)

X-ray photoelectron spectroscopy (XPS) was employed throughout these studies as a highly surface-sensitive characterization method for identifying interfacial chemical species and states for various low-dimensional materials. For studies surrounding BiOI as detailed in Chapter 4, XPS probed changes in surface chemical states for single-crystal BiOI(001) as a function of chemical treatments. For investigations of Ti-based MXenes and QDNs, as in Chapters 5 and 6 respectively, XPS determined surface coverages of covalently-tethered organic monolayers and further quantified relative atmospheric oxidation in the case of MXenes.

Traditional XPS studies irradiate the first 1–10 μm of a sample surface with soft X-rays, generally between 1 and 5 keV, which are absorbed by many-electron orbitals to emit photoelectrons via the photoelectric effect.[52–53] When the energy of an incident photon exceeds the binding energy of an electron, it is emitted from the atom within the sample. Equation 3.1 gives the kinetic energy of an emitted photoelectron.

$$\mathbf{KE} = h\nu - \mathbf{BE} - \Phi_{\mathrm{D}} \tag{3.1}$$

In eq 3.1, **KE** is the kinetic energy, $h\nu$ is the photon energy, **BE** is the binding energy, and and Φ_{D} (capital Phi) is the inherent spectrometer work function. Photoelectrons that escape from the sample surface pass through a series of electrostatic condensing lenses, a spherical capacitor analyzer (SCA), and then through an electron multiplier to amplify the signal. Finally, the emitted photoelectrons are counted by a position-sensitive sixteen-channel detector that measures kinetic energies. Photoelectrons generated in XPS experiments are typically presented by their binding energy, thus eq 3.1 may be rewritten as eq 3.2.

$$\mathbf{BE} = h\nu - \mathbf{KE} - \Phi_{\mathrm{D}} \tag{3.2}$$

The measured binding energy of a core-level photoelectron carries chemical insight into a sample surface because each element has a unique nuclear charge and electronic structure. In addition, electronegativity changes effected by the atoms surrounding an element of interest often shift that electron's binding energy. When that binding-energy shift is within the detection limits of the instrument, XPS can further discriminate between oxidation states and chemical species of a single element of interest. These BE positions have been characterized extensively and are well tabulated.[224] Moreover, unlike photons, photogenerated electrons can only travel a short distance through a material, about 1–4 nm, before experiencing an inelastic scattering event.[225–228] As such, XPS is a highly surface-sensitive experiment compared to traditional bulk techniques.

For this thesis work, a PHI 5600 multi-technique XPS system with a third-party data acquisition system (RBD Instruments, Bend Oregon) acquired all photoelectron spectra as detailed previously.[96,229] UHV chamber base pressures were $< 1 \times 10^{-9}$ Torr for all analyses. The optics configuration of the system is presented in Fig. 3.1 and discussed in more detail elsewhere.[96] In brief, the PHI 5600 system is equipped with two separate X-ray sources: a monochromated Al source and a non-monochromated "twin" source with Al and Mg anodes. For all XP spectra acquired throughout this thesis work with the exception of angle-resolved studies, the monochromated Al source was used. The incident X-rays from the monochromated source were positioned at 45° with respect to the surface normal angle, δ. In all cases, survey spectra utilized a pass energy of 117 eV, a 0.5 eV step size, and a 50 ms dwell time while high-resolution "multiplex" spectra utilized a pass energy of 23.5 eV, a 0.025 eV step size, and a 50 ms dwell time. Additionally, the fermi edge of the spectrometer was periodically calibrated with sputter-cleaned gold and copper to align the Au $4f_{7/2}$ and Cu $2p_{3/2}$ features to exactly 84.00 and 932.67 eV respectively.

Post-acquisition data fitting utilized an in-house-developed LabVIEW-based program. Spectral background shapes that describe the contribution from inelastically scattered electrons include a linear background, Shirley-shaped background, or the integration of a Tougaard shape based on $B = 2900$ eV^2 and $C = 1643$ eV^2 within a universal function that is scaled to the height of the photoelectron data.[2]30 – 231 A pseudo-Voigt-style function, GL(x), describes each peak shape where x scales nonlinearly from 0 as a pure Gaussian form to 100 as a pure Lorentzian shape. Optimization routines utilize the built-in LabVIEW implementation of the Levenberg–Marquardt algorithm for multi-parameter fitting. The studies in Chapters 4, 5, and 6 of this thesis work were centered around three different materials: BiOI, $Ti_3C_2T_x$ MXene, and Ti-based

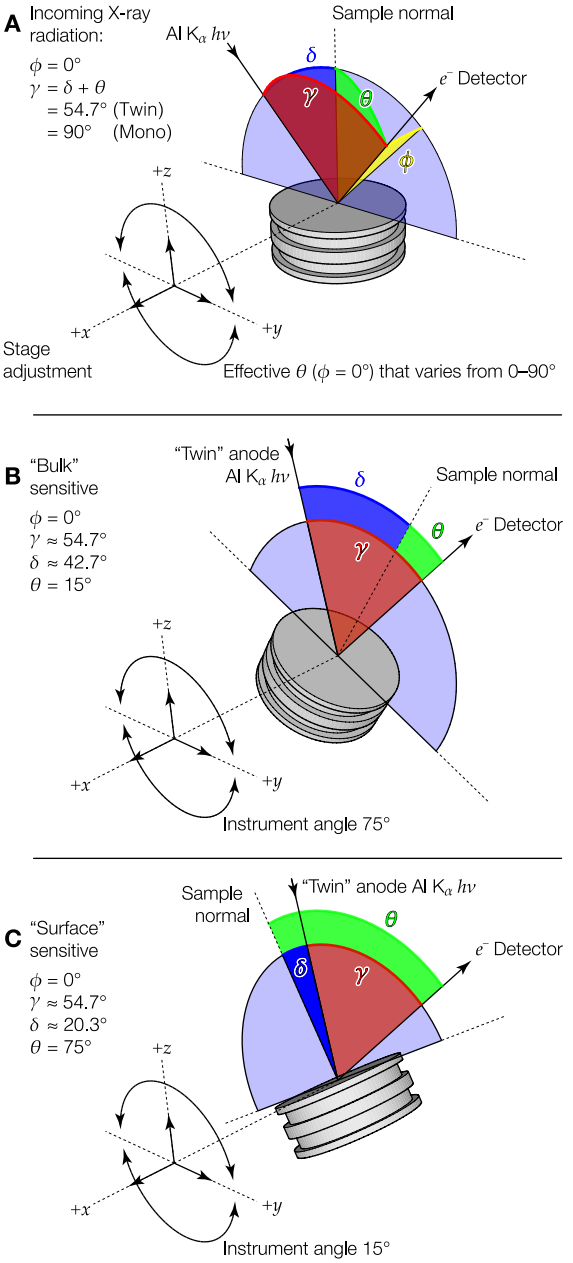

Figure 3.1. Configuration of the Phi 5600 XPS system and labeling of angles pertinent to quantification. Frame **A** presents the typical orientation of the sample stage with respect toward incoming X-rays and the detector. Frames **B** and **C** present the sample stage in the two extreme tilted positions, $\theta = 15°$ and $75°$ respectively.

1DL respectively. Because these materials contain distinct chemical states and environments, the fitting parameters for the photoelectron regions of interest in each particular case necessitated distinct spectral background shapes and fitting constraints. As such, detailed accounts of the fitting constraints of the photoelectron regions are contained within the supplementary information sections associated with the respective chapters (§A.4.1, §B.1, and §6.3.3 for BiOI, $Ti_3C_2T_x$, and 1DL TiO_2 respectively).

3.3 Ultraviolet Photoelectron Spectroscopy (UPS)

Ultraviolet photoelectron spectroscopy (UPS) experiments were accomplished using the same UHV photoelectron system described in the XPS section, §3.2. UPS is primarily employed to probe valence electrons at the surface of samples and utilized to determine the surface work function, Φ_S, Fermi level, E_f, and the valence-band maximum, E_{VBM}, of metals and semiconductors. UPS employs ultraviolet radiation which is absorbed by valence-state electrons at the surface. Provided enough energy, these electrons are emitted with a kinetic energy equal to $h\nu$ (21.218 eV) minus the binding energy, following as eq 3.1. Compared to soft X-rays, the energy of ultraviolet light is significantly lower, thus, the kinetic energy of ejected electrons is substantially lower than core-level photoelectrons. For this reason, the attenuation lengths of electrons emitted during UPS experiments are almost an order of magnitude shorter than for XPS. The analysis depth for a typical UPS experiment is ~2–3 nm. Consequently, organic contamination on surfaces will strongly attenuate low-energy electrons and surfaces require in-situ cleaning or thorough sample rinsing before analysis. A UP spectrum for sputter-cleaned Au is presented in Fig. 3.2.

At the high kinetic energy side of the UP spectrum, peaks here represent photoelectrons emitted from directly from valence electrons. The sharp edge at the high kinetic energy side is given by electrons coming directly from the Fermi energy level, $\mathbf{E}_f$. In the case of semiconductors, this edge represents ($\mathbf{E}_f$–$\mathbf{E}_{VBM}$) or the distance from the sample's Fermi level to the valence-band maximum energy. Located at the low-kinetic-energy end of the spectrum is the onset of photoemission or the secondary-electron cutoff energy. These are valence-band electrons which have experienced some inelastic scattering event on the way to the surface yielding an increasing background in addition to the primary photoelectrons. The electrons right at the leading edge of the secondary-electron cutoff have just enough energy overcome the local vacuum level. When in electrical contact, the Fermi levels of the spectrometer and sample equilibrate. Using a metal sample, such as sputter-cleaned Au, the Fermi energy level, E_f, of the spectrometer is calibrated to 0 eV, in terms of binding energy. With the instrument properly calibrated, we can determine the surface's work function, Φ_S, or the distance of the sample's Fermi level to the vacuum level, $\mathbf{E}_{vac}$, with eq 3.3.

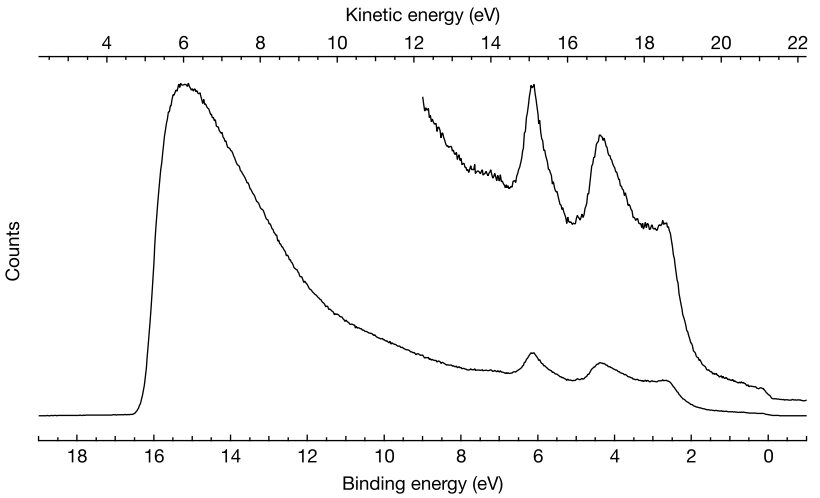

Figure 3.2. Ultraviolet photoelectron spectrum of sputter-cleaned gold foil. The high kinetic energy inset has been magnified by 5×. Adapted from Carl, A. D. *Soft, Organic, Carrier-Selective Contacts at Inorganic Semiconductor Interfaces Enabled by Low-Defect Covalent Bonding*. Ph.D. Dissertation, Worcester Polytechnic Institute, Worcester, MA, **2020**.

$$\Phi_S = \mathbf{E}_{\text{He I}} - \mathbf{E}_{\text{SEC}} \tag{3.3}$$

In 3.3, *hv* is 21.218 eV, the energy of the He I line, and $\mathbf{E}_{\text{SEC}}$ is the secondary-electron-cutoff energy, after fitting to the leading edge to the *x*-axis. ($\mathbf{E}_f$–$\mathbf{E}_{\text{VBM}}$) is fit by a linear-regression of high-kinetic-energy edge of the trace to the *x*-axis. $\mathbf{E}_{\text{VBM}}$, which is the opposite sign of ionization potential, IP, the distance from $\mathbf{E}_{\text{vac}}$ to $\mathbf{E}_{\text{VBM}}$, is then calculated with eq 3.4.

$$\mathbf{E}_{\text{VBM}} = \mathbf{E}_f - (\mathbf{E}_f - \mathbf{E}_{\text{VBM}}) \tag{3.4}$$

In eq 3.4, the value within the parentheses was determined from fitting the high-kinetic-energy edge and $\mathbf{E}_f$ is derived from the Φ_S after switching the sign. In the absence of inverse photoelectron spectroscopy (IPES), the location of the conduction band $\mathbf{E}_{\text{CBM}}$, or the negative of electron affinity, EA, the distance from $\mathbf{E}_{\text{vac}}$ to $\mathbf{E}_{\text{CBM}}$, per eq 3.5.

$$\mathbf{E}_{\text{CBM}} = \mathbf{E}_{\text{VBM}} + \mathbf{E}_g \tag{3.5}$$

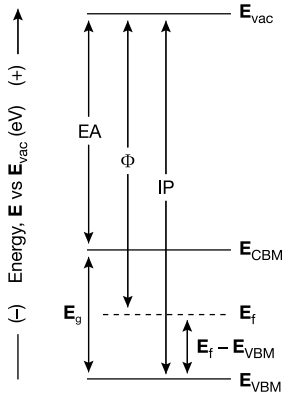

Figure 3.3. Generic band-energy diagram defining and localizing electron affinity, EA, work function, Φ, ionization potential, IP, band gap, $\mathbf{E}_g$, vacuum level energy, $\mathbf{E}_{vac}$, Fermi-level energy, $\mathbf{E}_f$, and valence band maximum energy, $\mathbf{E}_{VBM}$. Adapted from Carl, A. D. *Soft, Organic, Carrier-Selective Contacts at Inorganic Semiconductor Interfaces Enabled by Low-Defect Covalent Bonding*. Ph.D. Dissertation, Worcester Polytechnic Institute, Worcester, MA, **2020**.

In 3.5, $\mathbf{E}_g$ is the band gap of the sample. Figure 3.3 presents a general band-energy diagram that relates some of the previous equations and values.

In terms of UPS experimental settings and procedures, He I (21.218 eV) radiation was provided by a helium-gas discharge UVS 40A2 (PREVAC, Poland) UV source and UV40A power supply. A leak-valve allowed ~15 mTorr of ultrahigh purity (UHP) He gas into the UV source and the power was maintained at 80 mA to ensure a high ratio of He I to He II radiation. Differential pumping of the UV source helped keep a majority of helium gas from the analysis chamber. During UPS measurements, the base-pressure of the chamber was maintained $< 3 \times 10^{-8}$ Torr.

Samples were positioned at 0°, with respect to the surface normal, toward the analyzer during UPS measurements as portrayed in Fig. 3.4. This geometry ensures that with the electric field oriented toward the analyzer, the majority of low-energy photoelectrons are accelerated into the analyzer. The low-energy, secondary electrons used to determine the surface work function require additional kinetic energy to overcome the spectrometer work function. Applying a potential bias to the sample linearly increased the energy of all electrons within the sample. For all experiments, a sample bias of –35 V was employed, based on calibration with sputter-cleaned gold UP spectra over a range of biases as detailed elsewhere.[9]6 In some cases where counts exceeded 1 million CPS, the multiplier voltage was stepped down. High-resolution UP spectra utilized a pass energy of 5.85 eV, a 0.025 eV step size, and a 50 ms dwell time.

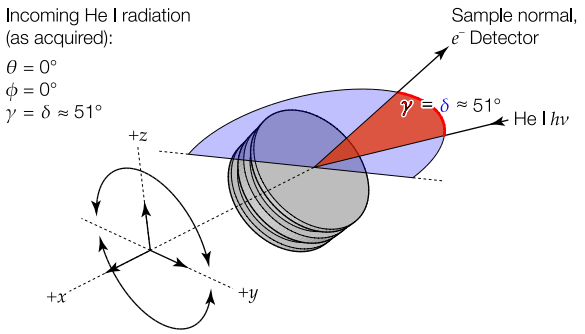

Figure 3.4. Configuration of the typical orientation of the sample stage with respect toward incoming UV illumination and the detector during UPS analyses. Adapted from Carl, A. D. *Soft, Organic, Carrier-Selective Contacts at Inorganic Semiconductor Interfaces Enabled by Low-Defect Covalent Bonding*. Ph.D. Dissertation, Worcester Polytechnic Institute, Worcester, MA, **2020**.

Determination of $\mathbf{E}_{\mathrm{SEC}}$ and $\mathbf{E}_{\mathrm{VBM}}$ were accomplished with an in-house developed script in IGOR Pro (Wavemetrics Inc., Lake Oswego, Oregon). UP spectra were first calibrated to a 0 eV binding energy after accounting for –35 V bias and the counts after the Fermi edge were adjusted to 0 CPS. To determine the energies of the $\mathbf{E}_{\mathrm{SEC}}$ and $\mathbf{E}_{\mathrm{VBM}}$, a linear regression to the x-axis was employed.

3.3.1 Angle-Resolved XPS

Angle-resolved XPS (ARXPS) is a powerful, non-destructive technique for probing surface versus bulk contributions to the total photoelectron signal in XPS. Other commonly employed methods for depth-profiling in XPS are detailed in brief in §2.3.1. Among them, Ar^+ sputtering is by far the most common. Nonetheless, this method is destructive for samples that are particularly prone to degradation under such conditions, as is the case for BiOI which forms reduced Bi metal under Ar^+ bombardment, and thus our studies surrounding this material in Chapter 4 alternatively employed ARXPS.

Angle-resolved XPS studies deconvolve surface and bulk contributions by exploiting the exponential decay of photoelectron current as a function of depth below the surface of the material as described by eq 3.6.

$$\frac{\partial I_A}{\partial z} \propto \rho_{A(z)} \exp \frac{-z}{\lambda_{\mathrm{A,self}} \cos\theta} \tag{3.6}$$

In eq 3.6, "A" describes the partial contribution of photoelectron intensity, I, from an infinitesimally thick layer at depth z below the surface. Equation 3.6

relies on terms including the number density per unit volume of species A as a function of depth ρA(z), the photoelectron takeoff angle θ vs the sample normal angle, and the photoelectron attenuation length λ. In brief, ARXPS relies on tilting of the sample stage to vary the photoelectron takeoff angle θ relative to the surface-normal angle to selectively alter the relative sensitivities of surface and bulk contributions to the total photoelectron counts.

Figure 3.1 depicts the optical configuration of the PHI 5600. The system is equipped with a four-axis stage which enables tilting of the sample along the axis containing the incoming photon beam and the collection vector for the photogenerated electrons. Frame A presents the configuration of the sample stage in its "flat" position for a typical XPS experiment with monochromated Al K_α X-rays where the photoelectron takeoff angle θ = 45° relative to the surface normal angle, δ. Alternatively, in a typical ARXPS experiment, XP spectra are collected for several photoelectron take-off angles between 15 and 75°. As demonstrated in Fig. 3.1 Frame B, when the sample stage is tilted toward the detector, which corresponds to smaller θ angles, the total photoelectron intensity is comparably more sensitive to contributions from photoelectrons originating from the bulk of the material. Conversely, as demonstrated in Frame C, for higher θ angles as the sample stage is tilted away from the detector, the total photoelectron intensity is comparably more sensitive to chemical speciation at the surface of the sample. As such, ratios of photoelectron counts arising from one chemical species to counts from another will demonstrate a strong take-off-angle dependence based on which atomic species is closer to the surface. This was particularly useful for studies surrounding 2D BiOI single crystals to probe surface terminations as a function of chemical treatments. In terms of ARXPS experimental settings and procedures, analysis was accomplished using the same photoelectron system described in the XPS section, §3.2. ARXPS relied on non-monochromated Al X-rays from the "twin" source which was positioned at 9.7° with respect to the surface-normal angle, δ. Spectra for survey scans and high-resolution multiplex regions were collected at θ = 15°, 30°, 45°, 60°, and 75° with respect to δ and utilized the software parameters detailed prior in §3.2.

3.4 Substrate Overlayer Model for BiOI Work in Chapter 4

Discussion of our theoretical substrate overlayer models for two idealized surface terminations for BiOI(001) is detailed in §A.4.3, while §A.4.4 details model results.

CHAPTER 4

QUANTIFICATION OF SURFACE REACTIVITY AND STEP-SELECTIVE ETCHING CHEMISTRY ON SINGLE-CRYSTAL BIOI(001)

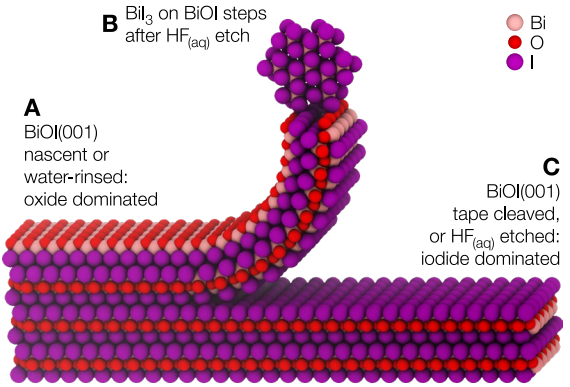

Portions adapted from:

Julia L. Martin, Roy Stoflet, Alexander D. Carl, Katarina M. Himmelberger, Sergio Granados-Focil, and Ronald L. Grimm. Quantification of Surface Reactivity and Step-Selective Etching Chemistry on Single-Crystal BiOI(001). *Langmuir*, **2020**, *36*(32), 9343–9355. 10.1021/acs.langmuir.0c00980

Special thanks to Professor Sergio Granados-Focil of Clark University for SEM studies.

4.1 Abstract

To bridge the gap between the cleanliness of a freshly cleaved surface of 2D BiOI and that available from a purely chemical etching means, we subjected single-crystal BiOI to a series of surface treatments and quantified the resulting chemical states and electronic properties. Vapor transport syntheses included both physical vapor transport from single-source BiOI, as well as chemical vapor transport from Bi_2O_3 + BiI_3 and from Bi + I_2 + Bi_2O_3. Surface treatments included tape cleaving, rinsing in water, sonication in acetone, an aqueous HF etch, and a sequential HF etch with subsequent sonication in acetone. X-ray diffraction, XRD, and X-ray photoelectron spectroscopy, XPS, probed the resulting bulk crystalline species and interfacial chemical states, respectively. In comparison with overlayer models of idealized oxide-terminated or iodide-terminated BiOI, angle-resolved XPS elucidated surface terminations as a function of each treatment. Ultraviolet photoelectron spectroscopy, UPS, established work-function and Fermi-level energies for each treatment. Data reveal that HF etching yields interfacial BiI_3 at BiOI steps that is subsequently removed with acetone sonication. UPS establishes n-type behavior for the vapor-transport-synthesized BiOI, and surface work function and Fermi level shifts for each chemical treatment under study. We discuss the implications for processing BiOI nanofilms for energy-conversion applications.

4.2 Introduction

Efficient, inexpensive, and scalable solar energy conversion is critical for overcoming challenges associated with greenhouse gas emission and climate change. Among routes to maximizing photovoltaic (PV) efficiency per module cost, tandem-junction photovoltaics are particularly compelling. Presently III-V materials dominate the tandem junction PV market for their strong light absorption, excellent carrier dynamics, and good lattice matching at contacting layers which minimize interfacial defects and strain. Present III-V tandem efficiencies exceed 35%,[232–235] however the fabrication costs and safety considerations in III-V device production drives research into non-traditional materials and structures.[236]

Among emerging materials for tandem PV applications with silicon as a bottom absorber, lead- and tin-based perovskites are particularly attractive for their excellent optical properties, steep absorption edge, facile synthesis procedures, and wide, tunable bandgaps.[237–238] However, atmospheric stability issues exist for many solar-relevant perovskites, which often contain toxic heavy metal species. The challenges presented with these perovskite-based devices motivates research into non-toxic, stable alternatives.

Among non-toxic solar absorbers, bismuth-based materials are particularly promising.[159] Bismuth itself is non-toxic, and layered bismuth-based materials are produced via several low-cost methods.[149–157] Among all bismuth-based layered materials, bismuth oxyhalides, BiOX (X = Cl, Br, of I) are an emerging class of group V–VI–VII layered semiconductors that exhibit unique optical, electronic, and mechanical properties. While BiOCl has been used since antiquity and remains a popular cosmetic additive that supports its low toxicity,158 this class of material has only recently been investigated for energy conversion applications. The unit cell structure consists of two adjacent and weakly Van-der-Waals-bonded atomic layers of halogen atoms each with X– stoichiometry.[239] The halide layers sandwich a bismuth oxide layer that has strong ionic covalent bonds with $[Bi–2O–Bi]^{2+}$ stoichiometry.[239] Among studies that have investigated these oxyhalides for energy storage and conversion,[159] photocatalysis,[155–157,160–162] or water-splitting,[163–167] BiOI has consistently exhibited enhanced photocatalytic activity as compared to BiOCl or BiOBr.[161,168] In addition to its ∼1.8 eV indirect band gap,[157,160] literature reports often attribute favorable electronic properties to the layered two-dimensional structure with static charges and repeating electric fields in the [001] direction. For example, researchers attribute high photocatalytic activity of oxyhalides under UV and visible light to efficient charge separation of photogenerated electron-hole pairs afforded by the inherent static electric field.[166] However, other electronic properties demonstrate varying behavior. For instance, most synthetic routes hydrothermal or solvothermal methods yield p-type BiOI,[152] however spray pyrolysis[169] and microwave hydrothermal154 methods have produced n-type behavior. In addition, the exact chemical species, contaminants, and interfacial states at BiOI interfaces remain unknown. The wide variety of synthetic methods yield varying polycrystalline and nanostructured BiOI in addition to high-temperature vapor-transport that yields large, single-crystalline material. Exfoliation of large single crystals straightforwardly yields chemically pristine surfaces of this 2D-layered material, but such macroscopic physical methods are unavailable to "clean" device-relevant nanostructures. Understanding how chemical processing can bridge the gap between nascent BiOI and chemically pristine surfaces, and quantifying the resulting chemical and electronic properties motivates the present investigation.

Herein, we synthesize single-crystal BiOI via high-temperature, in vacuo vapor transport, and characterize the interplay between both rinsing and etching chemistry with the subsequent interfacial chemical and electronic structure. Vapor transport syntheses utilize single-source BiOI; as well as stoichiometric Bi_2O_3 and BiI_3; and a combination of Bi_2O_3, Bi, and I_2. Rinses include water as well as an acetone sonication that we chose for their ability to sparingly dissolve Bi_2O_3,[240] and well dissolve BiI_3,[241–242] respectively. We additionally probe the chemical and electronic implications of an aqueous HF etch that is commonly employed for dissolution of oxides,[243] including

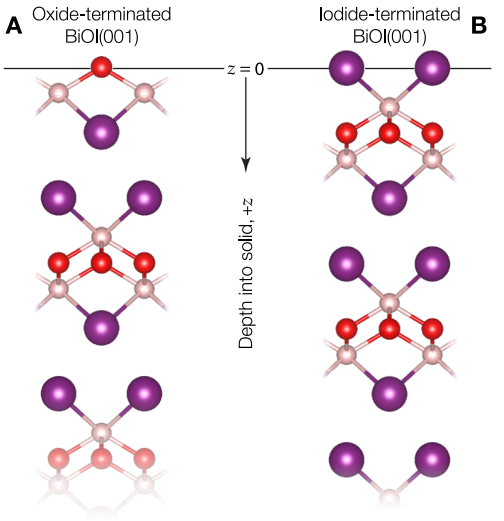

Figure 4.1. Idealized models of BiOI(001) surface termination include **A** oxide termination in which the repeating crystal "stops" at an oxygen layer that contains only half the layer density of oxygen atoms to preserve charge neutrality and **B** iodide termination from a hypothetical cleaving between the two weakly van-der-Waals-bonded iodide layers

silicon oxide[244–246] and the related antimony oxide.[247–248] X-ray photoelectron spectroscopy (XPS) quantified the surface species, and stoichiometry as a function of the surface chemical treatments.[249] XRD revealed trace chemical species that exist following synthesis or as a result of the chemical surface processing. Ultraviolet photoelectron spectroscopy (UPS) established the band energetics for each chemical treatment that enabled correlations between interfacial chemical species established by XPS and XRD with the resulting electronics. Lastly, angle-resolved XPS[228,250] explored the interfacial chemical speciation against two specific model BiOI(001) surface as presented in Fig. 4.1. Idealized model surfaces in Fig. 4.1 include an oxide-terminated surface in which BiOI(001) ends in an oxygen-terminated layer in frame A and iodide-terminated BiOI(001) in frame B. The oxide-terminated surface in Fig. 4.1A would contain only half the number of oxygen atoms to maintain surface charge neutrality.[251] In contrast, calculations implicate iodide-terminated BiOI(001) as in Fig. 4.1B as the dominant low-energy surface that would correspond to hypothetically cleaving the crystal between the two weakly Van-der-Waals-bonded iodide layers.[252] Such angle-resolved XPS studies are particularly important for BiOI as possible contaminants of BiI_3 and Bi_2O_3 together add up to three stoichiometric units of BiOI, and all three materials share identical Bi^{3+}, O^{2-}, and I^- oxidation states that complicate a straightforward deconvolution of photoelectron features. With these studies we aim to

elucidate the interplay between surface chemistry and electronic properties of this emerging solar-relevant material.

4.3 Experimental

The supplementary information section for this chapter is contained in Appendix A and details in full the materials and chemicals, experimental methods, and analyses employed. Here we present each in brief.

4.3.1 Synthesis of Single-Crystal and Large-Grain BiOI

Single crystal BiOI was synthesized via vapor transport[253] in evacuated, sealed quartz ampoules from either single-source BiOI, BiOI with additional I_2 for transport, Bi + I_2 + Bi_2O_3, or BiI_3 + Bi_2O_3. Growth conditions included a 725–775 °C source zone, 525–575 °C deposition zone, and a growth time of 64 h. No significant variation was observed in the physical characteristics of the resulting BiOI with these variations in growth temperature, time, or precursor combination.

4.3.2 Etching and Surface Reactivity

Samples were individually subjected to etchants, solvent cleaning, or both in ambient air. Treatments included sonication in water; sonication in acetone; immersion for 10 s in 6 M $HF_{(aq)}$ and a subsequent water rinse; or sequential steps of immersion for 10 s in 6 M $HF_{(aq)}$, a water rinse, and sonication in acetone. All HF-etching procedures consisted of single-side exposures with a disposable plastic pipette,[254] while rinses with water or organic solvents immersed the entire sample.

4.3.3 X-Ray Photoelectron Spectroscopy (XPS)

A PHI 5600 multitechnique system acquired all X-ray and ultraviolet photoelectron spectra as described previously.[25,229,249] Aperture and lens voltage parameters defined an 800-μm-diameter sampling area to isolate X-ray photoelectrons from edge-rich or terrace-rich sample domains, and 150 μm diameter areas when collecting ultraviolet photoelectrons. Surface states and stoichiometry studies utilized monochromatic Al K_α radiation incident at 90° relative to detection. Peak quantification utilized an in-house-developed program[229] based on published spectral shapes[255] and corrected for instrument specific sensitivity factors,[224] and background energy loss functions.[256–258] Angle-resolved XPS utilized a non-monochromatic Al K_α X-radiation source that is positioned at 54.7° relative to the detector with photoelectrons collected at takeoff angles between 15 and 75° relative to the surface normal angle.

4.3.4 Ultraviolet Photoelectron Spectroscopy (UPS)

A gas discharge lamp (PREVAC, Rogów, Poland) generated the He I spectroscopic line, $\mathbf{E}_{\mathrm{He\,I}} = h\nu = 21.218$ eV for UPS. Analyses of a freshly evaporated and a freshly argon-sputter-cleaned gold sample verified instrumental calibration with a Fermi-level energy, $\mathbf{E}_{\mathrm{f,Au}} = 0.00 \pm 0.03$ eV. We report Fermi energies are reported relative to each sample's valance-band-maximum energy, or $\mathbf{E}_{\mathrm{f}} - \mathbf{E}_{\mathrm{VBM}}$. The difference between $\mathbf{E}_{\mathrm{He\,I}}$ and an x-axis linear extrapolation of the secondary-electron-cutoff energy, $\mathbf{E}_{\mathrm{SEC}}$, defines a sample work function, $\Phi = \mathbf{E}_{\mathrm{He\,I}} - \mathbf{E}_{\mathrm{SEC}}$.

4.3.5 X-Ray Diffraction (XRD)

A Bruker-AXS D8 focus powder X-ray diffractometer with Cu K_α radiation collected X-ray diffraction (XRD) traces in the range of 5–45° (2θ). Samples were freely situated or tape-adhered to a stage for analysis under an air ambient directly following chemical processing.

4.3.6 Scanning Electron Microscopy (SEM)

Both a Vega 3 (Tescan Orsay Holding, A.S., Brno-Kohoutovice, Czechia) and a Phenom Pro (Phenom-World BV, Eindhoven, Netherlands) collected SEM images.

4.4 Results

4.4.1 Nascent and Tape-Cleaved Crystal Structure and Surface Chemical States

Crystal growth methods included physical vapor transport (PVT, or sublimation) of the single-source material, and chemical vapor transport (CVT) from the single-source material with additional molecular iodine as a transport agent. While we synthesized 0.1–1 cm^2 single-crystal and large-grain BiOI flakes from stoichiometric combinations of Bi metal, BiI_3, Bi_2O_3, and molecular I_2, all results presented herein utilized a single-source BiOI reagent powder. We report data only from single-source syntheses for consistency, and we did not observe statistical differences in any quantifiable metric between crystals that were grown from different synthesis methods.

Frame A in Fig. 4.2 presents an optical image of a typical nascent BiOI flake grown via PVT. We apply the term 'nascent' to as-grown crystals with minimal physical handling and no etching, rinsing, or cleaving protocols. The temperature program for the synthesis that yielded the sample in Fig. 4.2 employed a deposition zone soak temperature of 525 °C and a source zone soak temperature of 775 °C yielding a zone temperature difference, ΔT, of

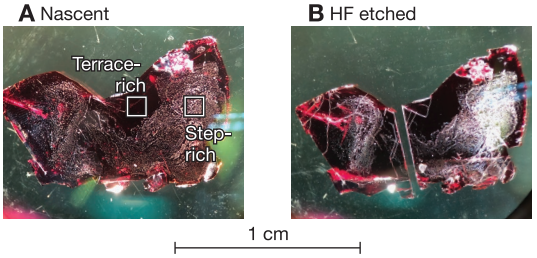

Figure 4.2. Optical image of **A** a nascent, CVT-grown BiOI flake, and **B** the same flake following a 10 s exposure to 6 M $HF_{(aq)}$. The boxes in frame A slightly overestimate the sampling areas for X-ray photoelectron collection, which validates photoelectron collection from terrace-rich and step-rich domains.

250 °C. We have synthesized PVT- and CVT-grown crystals with ΔT values ranging from 25-250 °C. We informally delineate large ΔT values as those exceeding 100 °C, and small ΔT values as being less than 100 °C.

As indicated in frame A of Fig. 4.2, typical crystals grown via large ΔT CVT contain two distinct morphologies on sample surfaces. We delineate these morphologies to include 'terrace-rich' domains that are dominated by macroscopic regions with large terraces and minimal step edges, as well as 'step-rich' domains that are dominated by step-edges and dislocations with minimal terrace areas. The white boxes in Fig. 4.2A highlight 1.2 mm^2 regions that overestimate XPS sampling areas. Importantly, in all cases the distinct terrace-rich and step-rich domains have comparable or larger areas than our XPS sampling areas, which enables discriminant analyses of these two surface morphologies.

Generally for both PVT and CVT, large ΔT syntheses yielded crystals with significant distributions of both terrace-rich and step-rich domains across the sample surfaces. Conversely, crystals grown via small ΔT PVT or CVT were dominated by terrace-rich domains and rarely contained distinct step-rich domains. Furthermore, typical small-ΔT syntheses yielded small, thin flakes ~0.1–0.4 cm^2 in size while large-ΔT syntheses yielded larger flakes ~0.1–1 cm^2 in size. Moreover, the inclusion of molecular I_2 as a transport agent did not notably affect the size of the grains or step-edge density as compared to the effects of ΔT or growth time.

X-ray diffraction (XRD) characterized nascent BiOI samples as well as water-rinsed, and tape-cleaved samples with a sample size of at least five each. All XRD traces herein plot intensity on a logarithmic scale to highlight trace features. Figure 4.3A presents a representative XRD trace for a nascent, PVT-grown sample that primarily demonstrates features consistent with tetragonal phase of BiOI (powder diffraction file 00-010-0445), as well as substrate features denoted as ◊, and minimal Bi_2O_3. The trace for PVT-grown BiOI in

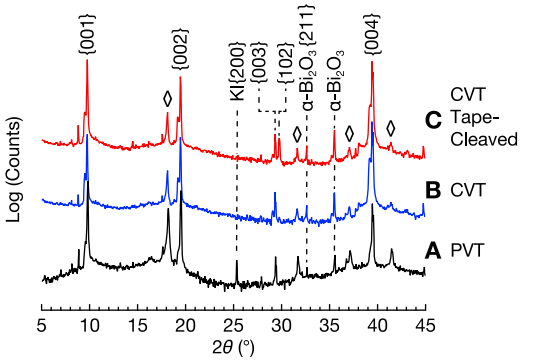

Figure 4.3. X-ray diffraction (XRD) BiOI traces for **A** nascent PVT-grown and **B** nascent CVT-grown samples both demonstrate BiOI, substrate features denoted as ◊, and trace Bi_2O_3. Uniquely, the nascent PVT-grown sample trace in frame A contains a feature at 25.3° demonstrative of KI(200). Following a tape-cleaving under an air ambient, a **C** CVT-grown sample trace resembles that of a nascent CVT-grown as in frame B but contains an additional BiOI ascribable feature.

Fig. 4.3A uniquely contains a feature at 25.3° that we ascribe to crystalline potassium iodide, specifically KI(200). Trace B in Fig. 4.3 presents a representative XRD trace for a CVT-grown nascent crystal that is dominated by BiOI features, with substrate features denoted as ◊, and minimal Bi_2O_3. Although not present in the CVT-grown sample in trace B, in a limited number of cases we observed features at 25.3° in nascent CVT-grown samples that are demonstrative of crystalline potassium iodide. Additionally, in a limited number of instances we observed features demonstrative of crystalline BiI_3 in XRD traces of nascent CVT-grown samples. Conversely, we observed no BiI_3-ascribable features in XRD traces of PVT-grown samples within the limits of detection. Trace C in Fig. 4.3 presents a typical XRD trace for a CVT-grown sample following a tape-cleaving under an air ambient. Trace C in Fig. 4.3 resembles that of the nascent CVT-grown sample in Trace B with additional BiOI features. Importantly, traces for tape-cleaved samples do not contain BiI_3 or KI ascribable features within detection limits. Additionally, we observed no consistent differences between XRD traces of PVT- and CVT-grown samples following a tape cleave within the limits of detection. Figure A.8 in the supporting information Appendix A plots the diffraction trace in frame C as aligned with the literature trace in powder diffraction file 00-010-0445.

X-ray photoelectron spectroscopy (XPS) quantified the surface chemistry of BiOI surfaces. Unless indicated in the angle-resolved XPS results, all data was collected at a photoelectron takeoff angle of 45° vs the sample normal angle. Figure 4.4 presents representative I $3d_{5/2}$, O 1s, C 1s, and Bi 4f XP spectra for an (A) terrace-rich domain, and a (B) step-rich domain of a nascent, CVT-grown flake. The I $3d_{5/2}$ region for Fig. 4.4A and for 4.3B is well fit by a singular

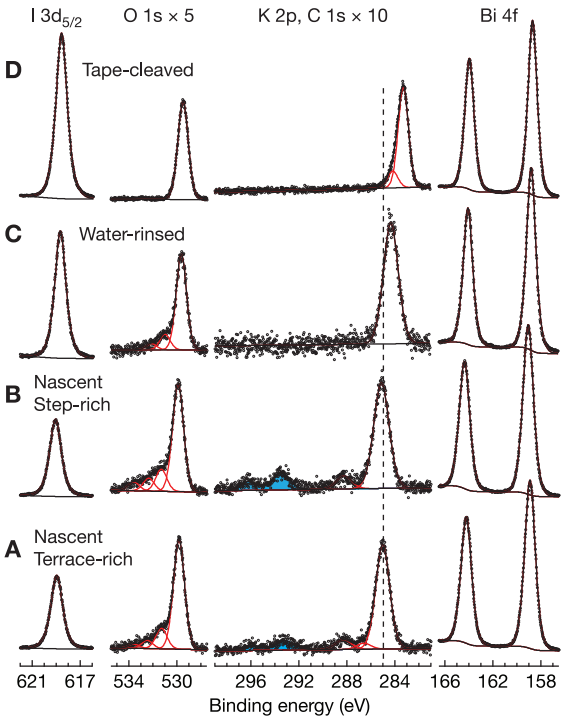

Figure 4.4. Representative I $3d_{5/2}$, O 1s, C 1s, and Bi 4f XP spectra for an **A** terrace-rich domain, and a **B** step-rich domain of nascent BiOI grown by CVT. Frame **C** presents spectra for a BiOI sample following a 30 s sonication in water and frame **D** presents spectra for a BiOI sample following tape cleaving under an air ambient. Each frame is normalized to the height of the Bi $4f_{7/2}$ feature with other regions magnified as indicated. Accounting for instrument sensitivity, Bi:I and Bi:O ratios better match the 1:1 stoichiometry for tape-cleaved compared to nascent and water-rinsed. All data was collected at a 45° takeoff angle vs the surface normal.

feature that is centered at a binding energy of ~618.9 eV. Across all samples studied, the position of the I $3d_{5/2}$ feature had a standard deviation in its binding energy position of 0.1 eV. Mean, μ, and standard deviation, σ, values are represented as $\mu \pm \sigma$. One doublet describes the Bi 4f regions in Fig. 4.4A and B with the Bi $4f_{7/2}$ centered at 158.9 ± 0.1 eV. The O 1s regions of Fig. 4.4A and B contain multiple features including a dominant one that is centered at 529.8 ± 0.1 eV that we ascribe to BiOI lattice oxygen. The smaller features are likely due to adventitiously adsorbed contaminants as their presence tracks with oxidized features in the C 1s region between 286–288 eV, however, we cannot rule out the possibility of Bi–O–H moieties at the sample surface or at step edge terminations. Ascertaining the nature of these oxygen features between 530–534 eV merits further study. The fitted binding energies of the I

3d, O 1s, and Bi 4f features in the terrace-rich samples are well aligned to the binding energy positions for the respective features on step-rich domains of nascent BiOI samples. Lastly, we attribute all features in the C 1s region for nascent BiOI samples to adventitiously adsorbed contaminants. For nascent terrace-rich domains in Fig. 4.4A and step-rich domains in Fig. 4.4B, the C 1s region demonstrates a primary adventitious feature at 285.0 eV that is well aligned with the dashed line through each C 1s region in Fig. 4.4. For all of the nascent BiOI samples studied, the primary carbon adventitious feature appeared at 284.8 ± 0.3 eV as well as additional features at 286–289 eV that we ascribe to oxidized adventitious contaminants. Extending the C 1s region for nascent terrace-rich domains in Fig. 4.4A and step-rich domains in Fig. 4.4B reveals a K 2p doublet that is indicated by blue shading with a K $2p_{3/2}$ peak centered at 293.3 ± 0.1 eV. Potassium appears in spectra of samples synthesized both in KOH and in NaOH base baths, and appears in XP spectra of the BiOI source material that localizes the trace contamination. Further, the location of adventitious carbon features at 284.8 eV demonstrates that nascent BiOI samples are sufficiently conductive to obviate a need for charge neutralization.

Figure 4.4 further presents representative photoelectron data for a (C) CVT-grown flake following a 10 s sonication in water and a (D) CVT-grown flake following tape cleaving under an air ambient. The water-rinsed samples exhibit discernible terrace- and step-rich domains in optical images that remain from the nascent samples, but no significant differences in the XP spectra exist between these two morphologies within the limits of detection. Given the spectral similarities between water-rinsed terrace- and step-rich domains, all results for water-rinsed samples presented herein are based on analyses of terrace-rich domains. Conversely, tape-cleaved samples do not exhibit any visually discernible terrace- or step-rich morphologies following exfoliation. For both the water-rinsed sample in Fig. 4.4C and the tape-cleaved sample in frame D, the I 3d, O 1s, and Bi 4f regions all demonstrate peak features that are well aligned with the respective features in the nascent samples in frames A and B. One particularly notable deviation is that the O 1s region for the tape-cleaved sample in Fig. 4.4D demonstrates significantly attenuated features ascribable to adventitiously adsorbed oxygen species as compared to the other samples. Unlike the other regions, the combined C 1s + K 2p region contains several important differences when compared to the nascent samples. Both the water-rinsed sample data in Fig. 4.4C and the tape-cleaved sample data in Fig. 4.4D demonstrate no K 2p features within detection limits. Further, the primary C 1s feature attributable to adventitious carbon is shifted away from the dashed line towards lower binding energy in both Fig. 4.4C and D by 0.4 eV and 1.8 eV, respectively. While the carbon features appear shifted for the water-rinsed the tape-cleaved samples, none of the iodine, oxygen, or bismuth regions shift in binding energy position by more than 0.1 eV when compared to the nascent data in Fig. 4.4A and B. Specifically, the

Table 4.1. XPS-determined and sensitivity-factor-corrected peak area ratios for Bi, O, I as well as UPS-quantified work function and Fermi level energies as a function of physical or chemical processing of BiOI surfaces.[a]

	XPS-determined ratios			Work function	Fermi energy
	Bi	O	I	$E_{He\,I} - E_{SEC}$ (eV)	$E_f - E_{VBM}$ (eV)
Nascent	1.6 ± 0.3	1.1 ± 0.1	1	3.95 ± 0.30	1.62 ± 0.21
Water-rinsed	1.3 ± 0.3	1.0 ± 0.2	1	4.20 ± 0.10	1.61 ± 0.23
Tape-cleaved	1.2 ± 0.1	0.8 ± 0.1	1	5.35 ± 0.15	1.58 ± 0.17
Acetone only	1.3 ± 0.2	1.1 ± 0.1	1	4.00 ± 0.10	1.77 ± 0.10
HF only	1.2 ± 0.2	0.8 ± 0.1	1	4.55 ± 0.10	1.60 ± 0.34
HF + acetone	1.1 ± 0.2	0.8 ± 0.1	1	4.40 ± 0.20	1.81 ± 0.10

[a] XPS statistics derive from a minimum sample size of four, while UPS statistics utilize a minimum sample size of five with "±" values representing the standard deviation for each respective value.

primary C 1s adventitious features occur at 284.6 ± 0.2 eV for water-rinsed samples as in Fig. 4.4C, and at 283.2 ± 0.1 eV for tape-cleaved samples as in Fig. 4.4D. In general, the adventitious carbon features typically demonstrate shifts of ~0.5 eV for water-rinsed and of 1–1.5 eV for tape-cleaved samples as compared to nascent samples with little to no concomitant shift in bismuth or iodine spectra. The similarity in peak area for the adventitious C 1s feature across all samples in Fig. 4.4 implies that each sample has a similar level of surface contamination during XPS analyses. If the nascent sample is sufficiently conductive to not necessitate charge neutralization, the water rinsing and tape cleaving have not affected the conductivity of the samples so as to necessitate charge compensation. This is supported by the consistency in binding energy positions for the I 3d, Bi 4f, and O 1s substrate features across all samples in Fig. 4.4. We ascribe the shifts in the adventitious C 1s features to the presence of interfacial dipoles relative to the nascent sample that researchers have demonstrated elsewhere.[259–260]

In contrast to the binding-energy position invariance of the iodine, oxygen, and bismuth XPS features, relative peak areas showed considerable variation with surface processing. Table 4.1 presents bismuth:oxygen:iodide XPS peak-area ratios for nascent, water-rinsed, and tape-cleaved BiOI samples. For oxygen we only consider the low-binding-energy feature contribution to the O 1s region, and we report ratios as a sensitivity-factor-corrected value for our photoelectron spectrometer.[224] The nascent samples demonstrate a bismuth-rich interfacial stoichiometry as compared to both the water-rinsed and the tape-cleaved samples. The XPS-determined average bismuth:oxygen:iodide ratios for both water-rinsed and for tape-cleaved samples are well matched but not identical to the 1:1:1 stoichiometry of BiOI.

4.4.2 Surface Physical and Chemical States Following Chemical Etches and Rinsing

Beyond water rinsing, we explored the effect of HF etching and organic rinses on the chemical makeup and surface chemistry of BiOI. Frame B in Fig. 4.2 represents the same CVT-grown flake in frame A following a 10 s exposure to 6 M $HF_{(aq)}$ and a subsequent water rinse. For the terrace-rich domains, the $HF_{(aq)}$ exposure yielded optically sharper images with significantly less scattering as observed in terrace-rich domains of the nascent sample. In contrast to the terrace-rich domain changes, step-rich domains demonstrate significantly more optical scattering following $HF_{(aq)}$ exposure as compared to step-rich domains in nascent samples. Across the samples studied, the $HF_{(aq)}$ treatment diminishes granular features on terrace-rich domains present on nascent samples and increases such features in step-rich domains.

XRD characterized BiOI samples following sonication in acetone, following exposure to 6 M $HF_{(aq)}$, or following sequential $HF_{(aq)}$ exposure and sonication in acetone, with at least five samples of each. The comparatively large X-ray exposure and sampling areas in XRD do not grant discriminant analyses of terrace-rich and step-rich domains across a sample surface that may contain significant domains of both. For analyses of step edges, XRD quantified samples that were dominated by step-rich domains with minimal terraces across their entire (001) face, to which we assign the term "step-dominated." Similarly, for analyses of terraces, we studied samples that are dominated by terrace-rich domains with minimal step edges across their (001) face, to which we assign the term "terrace-dominated". Fig. 4.5A presents a representative XRD trace for a CVT-grown nascent BiOI sample with substrate features denoted as ◊, and minimal Bi_2O_3. Following a 10 s etch in 6 M $HF_{(aq)}$ and a subsequent water rinse, the terrace-dominated sample in trace B resembles that of a nascent crystal, while the step-dominated sample in trace C contains unique features at 12.9° and 25.8° that we ascribe to scattering off of the (003) and (006) faces of crystalline BiI3. In a limited number of cases, we observed small but demonstrable BiI3 features in XRD traces for CVT-grown nascent BiOI samples. Importantly, for step-dominated samples following $HF_{(aq)}$ exposure that demonstrate BiI3 ascribable features, as in Fig. 4.5C, traces of the same flake preceding $HF_{(aq)}$ exposure demonstrate no features ascribable to BiI_3 within the limits of detection. Following sequential $HF_{(aq)}$ exposure and sonication in acetone, trace D for a step-dominated sample trace resembles that of a nascent sample with no BiI_3-ascribable features within detection limits. In all cases, sonication in acetone following an $HF_{(aq)}$ exposure significantly diminishes or eliminates BiI_3 ascribable features present on samples that were previously exposed to $HF_{(aq)}$. Interestingly, samples exposed to $HF_{(aq)}$ continue to demonstrate trace features attributable to the alpha phase of Bi_2O_3 that may originate from the back surface that was not exposed to the $HF_{(aq)}$ treatment.

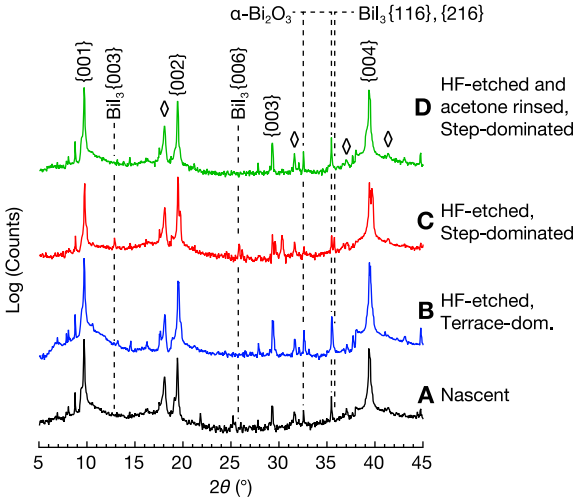

Figure 4.5. A representative X-ray diffraction (XRD) trace for **A** nascent BiOI demonstrates BiOI, substrate features denoted as ◊, and trace Bi_2O_3. Following HF exposure, a **B** terrace-dominated sample trace resembles that of a nascent sample while a **C** step-dominated sample trace reveals additional features ascribable to BiI_3. Following a sequential HF exposure and sonication in acetone, a (D) step-dominated sample trace resembles that of a nascent sample with no BiI_3 ascribable features within detection limits.

Scanning electron microscopy further revealed the physical changes in BiOI surfaces due to exposure to $HF_{(aq)}$. Frame A in Fig. 4.6 displays a BiOI sample both before and after a 10 s exposure to 6 M $HF_{(aq)}$ and a subsequent water rinse, while frame B presents representative SEM images following the $HF_{(aq)}$ exposure. Figure 4.6B includes a characteristic etch pit that was not observed in SEM images prior to the $HF_{(aq)}$ exposure, a characteristic crystal edge, and a 5× magnification of that crystal edge. Comparison of the before-and-after images in Fig. 4.5A presents a significantly cleaner surface, albiet one with a significant accumulation of platelets around a crystal edge as a result of the $HF_{(aq)}$ exposure. Examination of the platelets on surfaces following the $HF_{(aq)}$ exposure in Fig. 4.6B reveals a high density of platelets that are generally hexagonal in shape. We particularly note that the platelets display a strong size segregation and ordering into layers but with little alignment within a particular layer. Platelet size distributions are multimodal with 1–3-μm-diameter platelets observed in contact with the BiOI edges, and sub-100-nm-diameter platelets in layers beyond. Of greatest importance is that these platelets are not observed in SEM images of nascent BiOI or on BiOI following a sequential treatment of 10 s $HF_{(aq)}$, a water rinse, and sonication in acetone. The hexagonal platelets shape, their appearance an $HF_{(aq)}$ etch, and their disappearance following sequential $HF_{(aq)}$ and acetone treatments

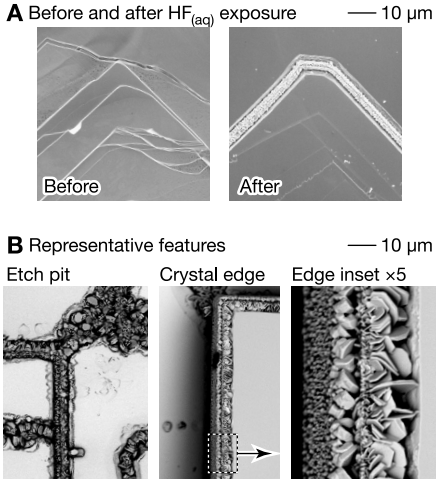

Figure 4.6. **A** Before and after images of a BiOI sample following a 10 s exposure to 6 M $HF_{(aq)}$ and a water rinse reveals a surface with fewer visible edges, but one edge that is dominated by hexagonal platelets. Representative images of platelet features **B** for etch pits and crystal edges demonstrate a significant aggregation of hexagonal platelets. The inset of the crystal edge in frame B reveals layers of platelets with large, 1–3-μm-diameter platelets against the BiOI edge and layers of smaller platelets beyond. The 10 μm scale bar applies to frames A and B and corresponds to 2 μm for the 5× magnification in the edge inset.

correlates strongly with the observation of BiI_3 features in the XRD trace in Fig. 4.5C.

XPS quantified the interfacial chemical speciation following sonication in acetone, following exposure to 6 M $HF_{(aq)}$, or following a sequential $HF_{(aq)}$ exposure and sonication in acetone. Figure 4.7 presents representative F 1s, I $3d_{5/2}$, O 1s, K 2p + C 1s, and Bi 4f regions for (A) terrace-rich and (B) step-rich samples following sonication in acetone. Frames C and D in Fig. 4.7 respectively present XP spectra for terrace-rich and step-rich regions for samples following a 10 s exposure to 6 M $HF_{(aq)}$ and subsequent water rinsing. Lastly, frames E and F in Fig. 4.7 respectively present XP spectra for terrace-rich and step-rich regions for samples following a sequential 10 s exposure to 6 M $HF_{(aq)}$, water rinsing, and sonication in acetone. For all samples, the F 1s region captures the high-binding energy shoulder of the Bi $4p_{3/2}$ that is centered at ~681 eV.

Relative to the photoelectron data for nascent samples in Fig. 4.7A and B, the XP spectra following sonication in acetone in Fig. 4.7A and B demonstrate only modest differences. For terrace-rich and step-rich regions of acetone-sonicated samples as in Fig. 4.7A and B, the peak position of the iodide, lattice oxygen, and bismuth features shifted by 0.3 eV towards lower binding

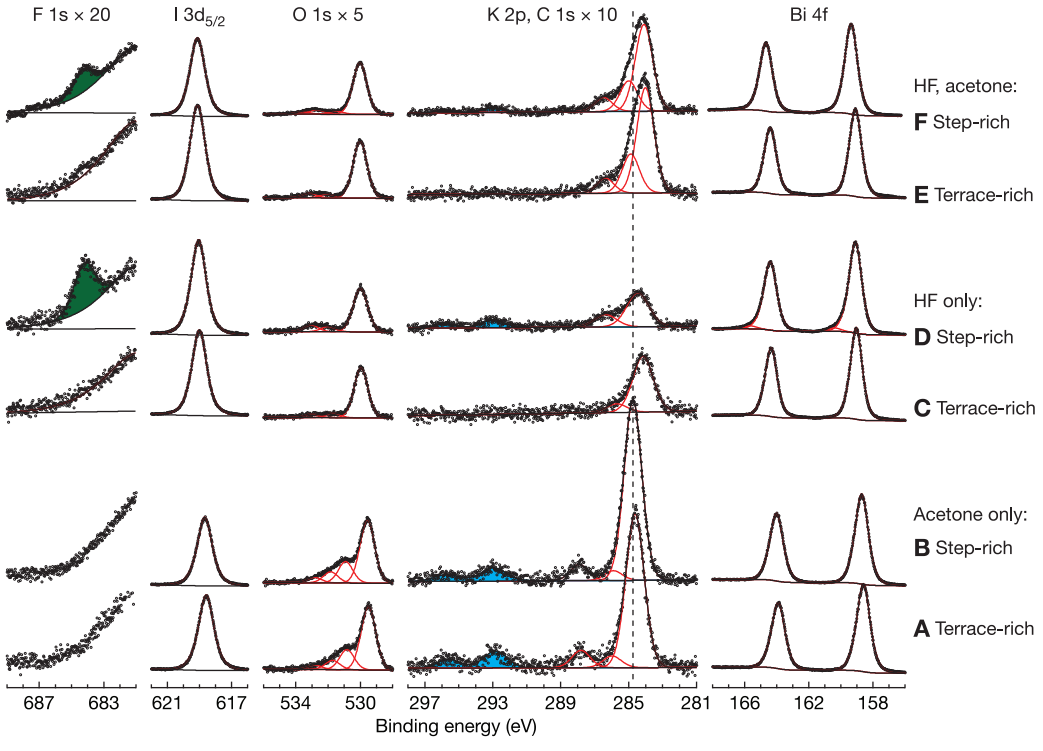

Figure 4.7. Representative XP spectra for **A** terrace-rich and **B** step-rich regions of acetone-sonicated BiOI; for **C** terrace-rich and **D** step-rich domains of $HF_{(aq)}$-etched samples; and for **E** terrace-rich and **F** step-rich domains for a sequential HF etch, water rinse, and acetone sonication. Each frame A–F is normalized to its respective Bi $4f_{7/2}$ height. HF etching attenuates or eliminates K 2p features (blue) in frames C–F vs A and B. Both (C) terrace-rich and (D) step-rich domains of only-HF-etched samples show higher I 3d ratios relative to acetone-only in frames A–B or to HF and acetone cleaning in frames E and F. Step-rich domains show strong F 1s features following an HF etch as in frame D that are attenuated but not completely eliminated with a subsequent acetone treatment as in frame F (green).

energy relative to their features on nascent BiOI samples as in Fig. 4.4A and B. As with the nascent samples, the acetone-sonicated samples as in Fig. 4.7A and B demonstrate observable K 2p signals as denoted with blue shading. Interestingly, the C 1s ascribable to adventitious features for the acetone-sonicated samples occurred at 284.6 eV, which also demonstrates a 0.3–0.4 eV shift to lower binding energy relative to comparable features from nascent samples.

A 10 s exposure to 6 M $HF_{(aq)}$ and subsequent water rinsing yields significant changes in the photoelectron spectra as revealed in Fig. 4.7C and D relative to nascent, water-, or acetone-rinsed samples. To account for possible sample-to-sample differences in HF etching and water rinsing protocols, frames C and D traces present terrace-rich and step-rich XP spectra from the same HF-etched flake. The I 3d, O 1s, and Bi 4f features are respectively well aligned for terrace-rich versus step-rich domains on BiOI samples following exposure to $HF_{(aq)}$. Further, the I 3d, lattice O 1s, and Bi 4f peak positions for the HF-etched then water-rinsed samples demonstrate the same relative positions as those of nascent BiOI surfaces. Terrace-rich samples as in Fig. 4.7C show no ascribable fluorine feature above the Bi $4p_{1/2}$ shoulder following $HF_{(aq)}$ exposure. In contrast to terrace-rich samples, step-rich BiOI samples exposed to $HF_{(aq)}$ demonstrate a significant, fluorine-ascribable feature at 684.2 ± 0.1 eV that is highlighted in green in Fig. 4.7D. In contrast to both nascent and to acetone-sonicated samples, exposure to $HF_{(aq)}$ yields significantly attenuated adventitious oxygen, carbon, and potassium species in Fig. 4.7C and D vs Fig. 4.7A and B as well as Fig. 4.4. For terrace-rich and step-rich domains of samples following $HF_{(aq)}$ exposure as in Fig. 4.7C and D, C 1s regions demonstrate a primary adventitious feature at 284.2 ± 0.3 eV.

Frames E and F in Fig. 4.7 respectively present XP spectra for terrace-rich and step-rich BiOI following a sequential 10 s exposure to 6 M $HF_{(aq)}$, a water rinse, and sonication in acetone. The I 3d, lattice O 1s, and Bi 4f features as in Fig. 4.7E and F are all shifted by eV 0.1–0.2 eV towards higher binding energy relative to their respective nascent analogs as in Fig. 4.4A and B. Notably, XP spectra for step-rich domains of a sample following sequential $HF_{(aq)}$ exposure and sonication in acetone as in Fig. 4.7F contains an F 1s feature indicated by green shading centered at 684.3 ± 0.1 eV that is not observed in Fig. 4.7E terrace-rich domains of the same flake. Importantly, for step-rich samples following an HF etch and a subsequent acetone sonication, F 1s features as in Fig. 4.7F are attenuated relative to comparable F 1s features following an $HF_{(aq)}$ etch and water rinse as in Fig. 4.7D. For terrace-rich and step-rich domains of samples following sequential $HF_{(aq)}$ exposure and acetone sonication as in Fig. 4.7E and F, the C 1s region demonstrates a primary adventitious feature at 284.0 ± 0.3 eV with only trace potassium-ascribable features.

As above, $HF_{(aq)}$ etching and acetone sonication affected the bismuth, oxygen, and iodide photoelectron peak area ratios for BiOI samples. Table 4.1 further presents sensitivity-factor-corrected XPS peak-area ratios for acetone-sonicated, for $HF_{(aq)}$-etched, and for sequentially $HF_{(aq)}$-etched and acetone-sonicated BiOI samples. As compared to the ratios for nascent, water-rinsed, or tape-cleaved BiOI, each of the processing conditions involving alternative combinations of $HF_{(aq)}$ and acetone treatment yield interfacial stoichiometries that are better matched to the 1:1:1 stoichiometry in BiOI.

4.4.3 Angle-Resolved XPS

Figure 4.8 presents experimental angle-resolved XPS data for several BiOI surfaces as well as results from numerical models of simulated XPS data corresponding to BiOI(001) with different surface terminations. As shown in the cartoon inset, the x-axis corresponds to the takeoff angle, θ, relative to the surface normal angle, and the angle between the incoming radiation, $h\nu$, and the takeoff angle remains fixed at 53.7° for non-monochromated X-radiation. We represent the experimental data as the ratio of Bi $4f_{7/2}$ intensity to the I $3d_{5/2}$ intensity, or $I_{\text{Bi } 4f_{7/2}} \div I_{\text{I } 3d_{5/2}}$, and further normalize experimental Bi-to-I ratios for each surface by their ratio at $\theta = 45°$. Thus the y-axis of Fig. 4.8 plots $\left(I_{\text{Bi } 4f_{7/2}} \div I_{\text{I } 3d_{5/2}}\right) \div \left(I^{\theta=45°}_{\text{Bi } 4f_{7/2}} \div I^{\theta=45°}_{\text{I } 3d_{5/2}}\right)$. We represent the data as a ratio of ratios for the ease of comparing and contrasting the results between sets of experimental data and between experimental and numerical model findings. We separate out the experimental data for visual clarity. The top plot includes $\left(I_{\text{Bi } 4f_{7/2}} \div I_{\text{I } 3d_{5/2}}\right) \div \left(I^{\theta=45°}_{\text{Bi } 4f_{7/2}} \div I^{\theta=45°}_{\text{I } 3d_{5/2}}\right)$ for a nascent BiOI sample and for a water-rinsed sample filled, and open blue squares, respectively. The bottom plot employs filled red circles to represent $\left(I_{\text{Bi } 4f_{7/2}} \div I_{\text{I } 3d_{5/2}}\right) \div \left(I^{\theta=45°}_{\text{Bi } 4f_{7/2}} \div I^{\theta=45°}_{\text{I } 3d_{5/2}}\right)$ for a BiOI sample subjected to a 10 s 6 M $HF_{(aq)}$ etch, and open red circles for results from a tape-cleaved BiOI sample.

Both the top and bottom plots in Fig. 4.8 include the results of a numerical model that is described in full in the supporting information section in Appendix A. The blue trace represents numerical results from an idealized BiOI(001) surface that terminates in a 1:1 stoichiometric BiO layer, while the red trace represents BiOI(001) surface that terminates in an atomic layer of iodide. To summarize the numerical results for an idealized oxide-terminated BiOI(001) surface, $\left(I_{\text{Bi } 4f_{7/2}} \div I_{\text{I } 3d_{5/2}}\right) \div \left(I^{\theta=45°}_{\text{Bi } 4f_{7/2}} \div I^{\theta=45°}_{\text{I } 3d_{5/2}}\right)$ is < 1 for more bulk sensitive angles $\theta < 45°$, and that ratio is >1 for more the surface sensitive photoelectron takeoff angles $> 45°$. In contrast to the oxide-terminated results, an idealized iodide-terminated BiOI(001) surface demonstrates $\left(I_{\text{Bi } 4f_{7/2}} \div I_{\text{I } 3d_{5/2}}\right) \div \left(I^{\theta=45°}_{\text{Bi } 4f_{7/2}} \div I^{\theta=45°}_{\text{I } 3d_{5/2}}\right)$ values >1 for bulk sensitive $\theta < 45°$, and <1 for more surface sensitive $\theta > 45°$.

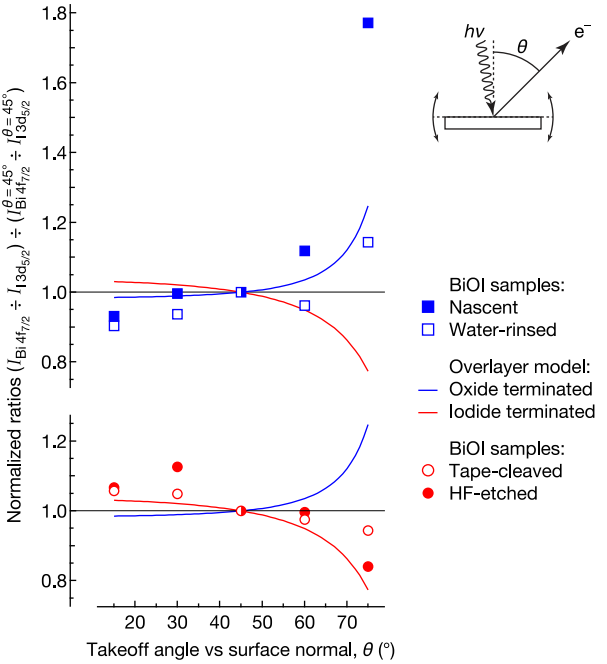

Figure 4.8. Angle-resolved XPS yields Bi $4f_{7/2}$-to-I $3d_{5/2}$ intensity ratios as a function of photoelectron takeoff angle, θ, which are normalized to the Bi $4f_{7/2}$-to-I $3d_{5/2}$ intensity ratio at $\theta = 45°$. For clarity, the top plot includes experimental data for nascent and for water rinsed samples respectively with filled and open blue squares, while the bottom plot separately plots the experimental data for tape-cleaved and HF-etched samples in open and filled red squares, respectively. Both plots replicate the numerical results from an XPS overlayer model in which BiOI(001) is terminated by a bismuth oxide layer (blue) or is terminated by an iodide layer (red).

Whilst the experimental data demonstrate scatter, straightforward agreements exist between the experimental data and the numerical model results. Angle-resolved XPS ratios both of nascent and of water rinsed samples demonstrate a trend that aligns best with the idealized oxide-terminated BiOI(001) model. Further, the angle-resolved XPS results for $HF_{(aq)}$-etched and for tape-cleaved samples follow trends that best align with the idealized iodide-terminated BiOI(001) model.

4.4.4 Electronic Properties

Ultraviolet photoelectron spectroscopy (UPS) probed the band electronics for nascent, rinsed, etched, and tape-cleaved BiOI samples. UPS quantified electronic structures for at least five samples for each nascent, tape-cleaved, or surface treated BiOI. The overall consistency in adventitious carbon features

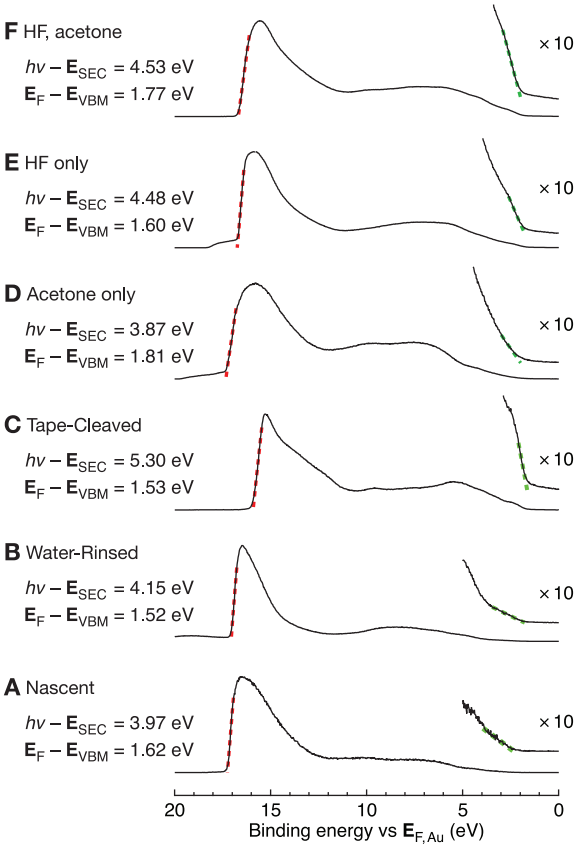

Figure 4.9. Ultraviolet photoelectron (UP) spectra for an **A** nascent BiOI, and for samples following treatments including **B** sonication in water, **C** tape-cleaving under air ambient, **D** sonication in acetone, **E** etching in HF, and **F** sequential HF etch and acetone sonication. Relative to nascent samples, samples in frame C–F reveal more valence band electronic structure.

in the XP spectra as revealed in Figs. 4.4 and 4.7 supports the interpretation of UPS results as being due to changes in surface chemistry rather than from residues of etching and cleaning. Table 4.1 summarizes the full statistics while Fig. 4.9 displays representative photoelectron spectra as well as calculated work function and Fermi energy values for BiOI samples for each of the cleaning, etching, and cleaving conditions presented above. Spectra include those of an A nascent sample, B water rinsed, C tape cleaved, D acetone sonicated, E etched for 10 s in 6 M $HF_{(aq)}$ etch followed by a water rinse, and F a sequence of $HF_{(aq)}$ etch followed by water rinsing and sonication in acetone. The green dashed lines in Fig. 4.9 represent linear regressions of each low-binding-energy edge of each valance-band feature whose *x*-axis in-

tercepts quantify valence-band maxima, $\mathbf{E}_{\mathrm{VBM}}$. With the 0 eV binding energy corresponding to the Fermi edge of sputter-cleaned polycrystalline gold (see Appendix A), the fitted $\mathbf{E}_{\mathrm{VBM}}$ reveals the position of each sample Fermi level with respect to its valence band maximum, or $\mathbf{E}_{\mathrm{f}} - \mathbf{E}_{\mathrm{VBM}}$. The red dashed lines in Fig. 4.9 represent a linear regression of the low-kinetic-energy (high-binding-energy) edge of the secondary-electron feature in each spectrum. The *x*-axis intercepts of each red-dashed regression reveal secondary-electron photoemission cutoff energies, $\mathbf{E}_{\mathrm{SEC}}$, that determine sample work functions, $\Phi = \mathbf{E}_{\mathrm{He\,I}} - \mathbf{E}_{\mathrm{SEC}}$, where $\mathbf{E}_{\mathrm{He\,I}} = h\nu = 21.218$ eV.

Work function values for the BiOI samples under study correlate strongly with surface treatment. Nascent samples demonstrated an average $\Phi = 3.95 \pm 0.28$ eV with a value for Fig. 4.9A of 3.97 eV. Water rinsed BiOI as in Fig. 4.9B yielded slightly larger work function values compared to nascent samples, while acetone sonication of BiOI samples yielded comparable work function values as in Fig. 4.9D to nascent samples themselves. In contrast to water and acetone, tape cleaving yielded an average work function of $\Phi = 5.35 \pm 0.14$ and 5.30 eV as in Fig. 4.9C that is significantly larger than that of the nascent samples. Both the $HF_{(aq)}$ etched and water rinsed as in Fig. 4.9E and the $HF_{(aq)}$ etched + water rinsed + acetone sonicated samples as in Fig. 4.9F yielded mutually comparable averages of $\Phi = 4.40$ and 4.55 eV respectively, that are ~0.5 eV larger than nascent BiOI work function values.

All BiOI samples studied demonstrated n-type behavior with average $\mathbf{E}_{\mathrm{f}} - \mathbf{E}_{\mathrm{VBM}}$ values ranging from 1.62 eV that would be indicative of moderate doping to 1.81 eV that would indicate high doping. The apparent n-type behavior of the single crystal, vapor-transport-synthesized material produced in the present work agrees with some reports of n-type material,[154,169] but stands in contrast to the majority of deposition methods that demonstrate p-type behavior from BiOI.[152]

Unsurprisingly, the UP spectra for tape-cleaved samples as in Fig. 4.9C reveals a high extent of valence-band structure. Features at binding energy values of 2.48, 5.40, 7.6, and 9.58 eV along with a shoulder feature at 3.42 eV vs $\mathbf{E}_{\mathrm{f,Au}}$ demonstrate qualitative agreement with a valence-band density-of-states calculation for BiOI.[157,168,261]

4.5 Discussion

4.5.1 Properties of Nascent and Tape-Cleaved BiOI

Investigations of bismuth oxyiodide or BiOI-based composite materials generally probe photocatalysis, water-splitting, and photovoltaics. Insight into the chemical states present on interfaces as well as relative band positions, carrier lifetimes, dopant densities, etc. is critical for efficient, scalable, and inexpensive solar energy conversion and catalysis applications.

X-ray photoelectron spectroscopic results yield significant insight into the interfacial chemical states on BiOI and how those species change with rinsing and etching processes. Considering the low signals for adventitious C 1s and O 1s features of tape-cleaved samples as in Fig. 4.4D, we attribute the Bi:O:I ratio of 1.2:0.8:1 presented in Table 4.1 for tape-cleaved samples to best represent the ratios that would exist for a "pure" BiOI surface. Importantly, the quantified Bi:O:I ratio of 1.2:0.8:1 is not identical to 1:1:1. However our experimentally determined ratios utilize published sensitivity factor values for the model instrument under study, and instrument-specific variations exist that will yield systematic deviations from published values.[262–263] Given the systematic nature of possible deviations and the overall cleanliness of the tape-cleaved BiOI samples, we interpret the experimentally quantified Bi:O:I ratio of 1.2:0.8:1 to be the ideal ratio for our instrument. Establishing an idealized set of values for Bi:O:I ratios quantified herein, we further interpret the quantified Bi:O:I ratio of 1.6:1.1:1 for nascent sample surfaces to be rich in bismuth oxide or deficient in iodide.

The angle resolved XPS results support the atomic ratios above and further elucidate the surface terminations on BiOI. The angle-resolved XPS ratios for nascent samples in the blue squares in Fig. 4.8 even exceeds the oxide-terminated BiOI(001) model results in the blue curve, which further supports the existence of surface bismuth oxide. Observation of a trace Bi2O3-ascribable feature by XRD as in Fig. 4.3 is supportive of surface oxide but indirect as XRD is not surface sensitive. We would stop short of specifically referring to the surface oxide as Bi2O3, but rather say that nascent BiOI has an oxide-rich or iodide-deficient surface. In contrast to the nascent surfaces, angle-resolved XPS of tape-cleaved BiOI as in the open, red circles in Fig. 4.8 demonstrates better qualitative alignment with the iodide-terminated overlayer model as in Fig. 4.1B. The observation of iodide-rich surfaces following tape cleaving is in strong agreement with rigorous computational studies[251] and intuition that breaking the weak van der Waals binding between adjacent, (001)-parallel iodide layers yields a low energy surface.

4.5.2 Influences of Rinsing and Etching Treatments on Interfacial Chemical States

Rinsing and etching strongly effects the interfacial chemical species on BiOI surfaces relative to nascent samples. Surface cleaning by water sonication, acetone sonication, HF etching, and a combination of sequential HF etching, water rinsing, and acetone sonication yield XPS-determined Bi:O:I ratios that are statistically comparable to that of tape-cleaved samples. First, water rinsing yields interfacial Bi:O:I ratios with lower bismuth oxide quantities and ratios that more closely approximate ratios from tape-cleaved BiOI as revealed in Table 4.1. Interestingly, angle-resolved XPS ratios for water-rinsed BiOI shown in the open blue squares in Fig. 4.8 best follows the pattern of the

blue trace for idealized oxide-terminated BiOI as in Fig. 4.1A. Taken together, a model that fits the experimental data for nascent and water rinsed samples is that vapor-transport synthesis yields oxide-terminated BiOI as in Fig. 4.1A. The oxide-terminated BiOI may be contaminated with a small quantity of bismuth oxide that is effectively removed by a water rinse.

Aqueous-phase HF etching significantly alters the surface chemistry of BiOI. The optical images in Fig. 4.2 demonstrate increased visual clarity in terrace-rich sample domains and significantly increased scattering in step-rich domains relative to nascent samples following an $HF_{(aq)}$ etch. Along with increased optical scattering at step-dense domains in Fig. 4.2B, an appearance of BiI_3 features in XRD traces as in Fig. 4.5C, and the hexagonal platelets decorating step edges in Fig. 4.6 cumulatively support an interfacial reaction at BiOI step edges that yields BiI_3.

A model that fits that data for a reaction between HF and BiOI(001) may involve an effectively HF-driven disproportionation and reaction at chemically active facets on BiOI. As BiI_3 + Bi_2O_3 comprise three stoichiometric units of BiOI, a reaction between HF and BiOI may work in reverse to yield an HF-inert species in BiI_3 and a HF-reacting species in Bi_2O_3. Bi_2O_3 reacts with HF in an established reaction to form BiOF,[264] but it remains unknown from the present study whether Bi_2O_3 exists as a stable intermediate in the reaction of BiOI with $HF_{(aq)}$. The observation of F 1s features in XP spectra of step-dense domains of BiOI(001) as in Fig. 4.7C may be an indication of deposited BiOF. Interestingly, crystalline BiOF yields XRD features at 2θ = 14.2° and at 27.8°. While trace peaks exist at those positions in the diffraction traces of HF-etched samples as in Fig. 4.5B–D, minor features exist in the XRD traces of non-HF-etched samples in Fig. 4.3 and Fig. 4.5A. Thus, the present results do not unambiguously confirm the observation of crystalline BiOF. However, if the product of HF with a bismuth oxide yields BiOF, a net reaction with BiOI may follow reaction 4.1.

$$3\,\mathrm{BiOI} + 2\,\mathrm{HF_{(aq)}} \longrightarrow \mathrm{BiI_3} + 2\,\mathrm{BiOF} + \mathrm{H_2O_{(aq)}} \tag{4.1}$$

For an initially oxide-dominated nascent BiOI(001) surface, we posit that HF adds across and breaks Bi–O bonds to form a Bi–F bond and an O–H bond similarly to the etching mechanism of other oxides.[265–266] From the first adsorption, the mechanism on BiOI likely departs from that of other oxides such as SiO_2 and Al_2O_3 where the respective products SiF_6H_2 and AlF_6H_3 are each water soluble.[267] In the present case, dissolution of some interfacial bismuth would leave undercoordinated I^- species that likely attack other bismuth cations rather than F^- in a reaction that ultimately yields solid-phase BiI_3. This reaction is particularly interesting as BiOI and BiI_3 have completely incommensurate crystal structures that leads to the growing platelet structure

seen in Fig. 4.6. Insight into the mechanism of this reaction remains the subject of ongoing study. Separately from the products of a reaction with $HF_{(aq)}$, angle resolved XPS data as in the filled red circles in Fig. 4.8 best fit an overlayer model in which a layer of iodide forms the topmost atomic layer of an idealized BiOI(001) surface. As above, we stop short of calling the HF-etched terraces iodide terminated, but would rather say that HF etching removes a surface oxide to reveal iodide-dominated (001) terraces on BiOI surfaces.

We were particularly interested in utilizing an organic rinse for its ability to dissolve BiI_3 that we expected may be a source contaminant from certain vapor transport growth recipes. However, an acetone sonication takes on new utility in the removal of BiI_3 that is produced in a reaction between BiOI and HF. The disappearance of BiI_3-ascribable features in the XRD traces such as in Fig. 4.5D upon acetone treatment, and the observation of no platelets in SEM images following sequential $HF_{(aq)}$-etching and acetone sonication suggests an effective removal of BiI3 that is produced from the $HF_{(aq)}$-etch itself. Importantly for the acetone sonication, fluorine features on step-dense domains of BiOI samples all demonstrate significantly smaller F 1s regions as a consequence of acetone sonication following an $HF_{(aq)}$ etch. Taken together, the sequence of an $HF_{(aq)}$ etch with a water rinse that is directly followed by an acetone cleaning yields high-quality BiOI surfaces.

4.5.3 Correlation of Surface Chemical States with UPS- Determined Electronic Structure

The XRD and XPS results guide expectations of chemical cleanliness for processed BiOI samples, and ultraviolet photoelectron spectra establishes work-function and Fermi-level energies for cleaning process. UPS-determined Fermi-level energies vs valance-band maxima, $\mathbf{E}_f - \mathbf{E}_{VBM}$, were 1.4 – 1.9 eV that corresponds to n-type doping for all samples measured irrespective of surface preparation. In contrast to the small variance in $\mathbf{E}_f - \mathbf{E}_{VBM}$ values, measured work-function values, Φ, varied across almost 2 eV as a function of surface preparation. The disparity between small variations in Fermi energies and large variations in Φ is well established by band-bending diagrams of semiconductors.[259] Based on the Fermi-level equilibration between a sample and the measuring instrument, surface charges, interfacial dipoles, and contamination all influence the measurements of Φ whereas measurements of $\mathbf{E}_f - \mathbf{E}_{VBM}$ do not shift with changes in these interfacial properties. That is to say, photoelectrons emitted from states near the valence-band edge experience an interfacial dipole that is directly cancelled out by the act of measurement. In contrast to valance-edge emission, low-kinetic-energy electrons in the secondary-cutoff region experience an energetic shift due to interfacial dipoles or changes that is not cancelled out by the act of measurement.[259] Separately from the UPS data, we ascribe such interfacial dipole effects to the

movement of adventitious C 1s features as revealed by the shifts about the dashed guide lines in photoelectron spectra in Figs. 4.4 and 4.7.

Comparisons of work function values as a function of surface preparation reveals that acetone treatment does not statistically affect Φ vs nascent samples, whereas water effects only a modest shift in Φ values vs those of nascent samples. In contrast to water and acetone, a $HF_{(aq)}$ etch and a sequential $HF_{(aq)}$ etch with acetone sonication each effect a significant shift in Φ vs nascent samples. The large work function value due to tape-cleaving is likely an artifact of the physical cleaving process leaving highly reactive dangling bonds with a surface charge that yields erroneous Φ values. Indeed, if we consider the sequential $HF_{(aq)}$ etch with acetone sonication process to yield the cleanest possible surface, we take Φ = 4.40 ± 0.20 eV as the "ideal" work function revealed by this study. In conjunction with Φ for a sequential $HF_{(aq)}$ etch with acetone sonication, the UPS-determined $\mathbf{E}^{f} - \mathbf{E}^{VBM}$ difference of 1.81 eV reveals a valance-band-maximum energy at ~6.2 eV more negative than the vacuum energy, $\mathbf{E}^{vac}$. From a bulk band gap of ~1.8 eV,[268] the position of the valence-band maximum would put the conduction-band-minimum energy at ~4.4 eV more negative than the vacuum energy, $\mathbf{E}^{vac}$. Band-edge energy assignments broadly agree with computational,[167,269–270] and spectroscopic results.[159]

4.5.4 Implications for Step-Dense, Nanocrystalline BiOI Films and Solar Energy Conversion

Chemically and electronically pristine interfaces are critical for efficient, cost-effective PV. Mechanical exfoliation of layered 2-D materials is well-precedented, however, reports of BiOI for applications in PV and photocatalysis have included thin film- and nanoscale-BiOI-based chemical systems. Delicate microstructures such as thin films or vertically-oriented nanoflakes are generally not susceptible to traditional exfoliation methods such as tape-cleaving or sonication. As such, we were motivated to establish chemical etching procedures that can achieve comparably pristine surfaces while circumventing these mechanical demands, as well as explore and quantify the chemical and electronic transformations that result.

The combination of $HF_{(aq)}$ etching and an acetone treatment effectively cleans BiOI surfaces, and could improve solar-energy conversion and catalytic processes. In the present study, 6 M $HF_{(aq)}$ etched the BiOI surfaces at reasonable rates for handling and processing steps. In preliminary and ongoing studies in our laboratory, exposure of 6 M $HF_{(aq)}$ to nanofilms of BiOI nearly instantaneously destroys such films in favor of disordered BiI_3 films. It is reasonable to assume that if HF attacks energetic edges, then high-edge-density and faceted nanofilm BiOI would present a highly reactive surface for HF reaction. Establishing the behavior of dilute $HF_{(aq)}$ exposures to photovoltaic-

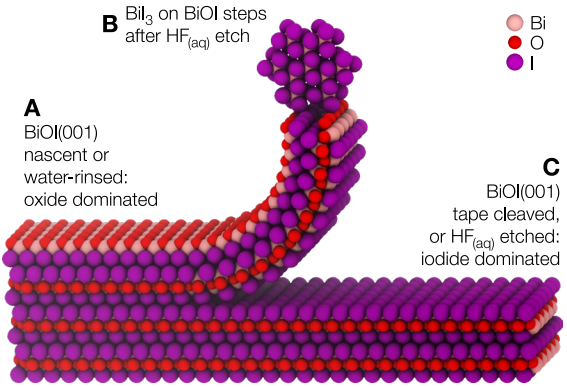

Figure 4.10. Angle-resolved XPS demonstrated that an interfacial oxide dominates nascent and water-rinsed BiOI surfaces. An aqueous-phase HF etch attacks step edges to yield hexagonal BiI3 platelets, while both HF etching and tape cleaving reveal iodide dominated surfaces.

and photocatalytic-relevant nanofilms of BiOI remains the subject of ongoing study.

4.6 Conclusion

We synthesized single-crystal BiOI via both chemical and physical vapor transport from several combinations of precursors that yield stoichiometric BiOI. The resulting crystals showed no significant variation based on precursor combination or in the presence or absence of an additional I_2 carrier for chemical vs physical vapor transport. The resulting large crystals demonstrated step-dense and terrace-dense domains that demonstrated unique reactivity to a series of chemical cleaning processes.

Figure 4.10 summarizes the principal conclusions for the present study. Nascent and water-sonicated BiOI surfaces are oxide dominated as shown in Fig. 4.10A as revealed by angle-resolved XPS. XRD demonstrated that $HF_{(aq)}$ etching produces interfacial BiI3 at BiOI step edges as in Fig. 4.10B that the acetone subsequently dissolved away to yield high-quality surfaces. Angle-resolved XPS further demonstrated that tape-cleaved and $HF_{(aq)}$-etched BiOI samples demonstrate an iodide-dominated surface as shown in Fig. 4.10C. XP spectra for tape-cleaved BiOI revealed a very low concentration of interfacial contaminants, and we subsequently assigned such spectra as the baseline for chemically cleaned surfaces. Between water sonication, acetone sonication, an $HF_{(aq)}$ etch, and a stepwise $HF_{(aq)}$ etch with an acetone sonication, the stepwise HF+acetone treatment yielded XP spectra that best aligned with the tape-cleaved results. UPS-demonstrated work-function and Fermi-

level values for a stepwise $HF_{(aq)}$ etch with an acetone sonication yielded valance- and conduction-band edges of approximately –4.4 eV and –6.2 eV vs the vacuum energy level, $\mathbf{E}^{vac}$. Further, all vapor-transport synthesized material demonstrated n-type behavior. We conclude that a stepwise $HF_{(aq)}$ etch with an acetone sonication may best clean BiOI surfaces for photovoltaic and photocatalytic applications with concentrations and protocols relevant to nanofilm BiOI material being the subject of ongoing study.

CHAPTER 5

CHEMICAL CONTROL OF $Ti_3C_2T_x$ MXene ELECTRONICS VIA COVALENTLY-TETHERED ORGANIC MONOLAYERS

5.1 Abstract

Two-dimensional MXenes have demonstrated promising success in catalysis, battery storage, electromagnetic interference (EMI) shielding, chemical and biological sensing, among others. Nonetheless, precise control over the chemical terminations and optoelectronic behavior is critical for scalable, widespread applications. Herein, we functionalized $Ti_3C_2T_x$ MXene surfaces with organosilanes to change local electron density based on the inclusion of electron-donating or electron-withdrawing groups. Ultraviolet photoelectron spectroscopy (UPS) quantified work-function values for resulting derivatized $Ti_3C_2T_x$ thin films. UPS reveals ~350–400 meV shifts in work-function values based on interfacial dipoles resulting from covalent organosilane attachment. These results inform current research efforts which aim to exploit chemical and optoelectronic tunability via mixed organic monolayers with orthogonal reactivities at $Ti_3C_2T_x$ edges and terraces. Candidate molecular organics to impart passivation against oxidation, optoelectronic tunability, and chemical handles for tethering to polymers and other surfaces include

silanes, catechols, and alkyl triphosphates as well as polyanionic salts. We discuss these results in the context of EMI shielding, catalysis, chemical sensing, and energy applications.

5.2 Introduction

Overcoming challenges associated with climate change and global energy necessitates inexpensive, scalable low-dimensional materials for a number of practical applications including energy storage and conversion, chemical and environmental sensors, water remediation, among others. Since the rediscovery of graphene in 2004 by Novoselov and Geim,[1–2] 2D layered materials have been remarkable useful across a range of applications for their unique mechanical, chemical, and optoelectronic properties.[3–6] Among them, Van der Waals (VDW) materials, which are characterized by strong, intralayer covalent bonds and weak interlayer van der Waals forces, are particularly compelling. In many cases, their layered structure affords high in-plane electrical conductivity as well as excellent effective charge separation perpendicular to the layers which posit them as strong candidate materials for applications in photocatalysis, energy conversion and storage, and chemical and biological sensing.

Among commonly employed VDW materials, transition metal dichalcogenides (TMDs) are ubiquitous for their favorable mechanical and optoelectronic properties, direct bandgap, natural abundance, atmospheric stability. Since single-layer MoS_2 enabled the discovery of the first practical transistor,[271] the present library of around 60 TMDs have demonstrated broad utility in chemical and biological sensors, batteries, solar cells, nanophotonics, wearable electronics, DNA sequencing, among others.[143,272] Nonetheless, charge carrier mobility for these materials is limited by lattice disruptions and defects states that deleteriously impact practical device performance and costly syntheses and fabrication pose scalability issues. This drives research into abundant, cost-effective alternative materials for energy and sensing applications with higher intrinsic conductivities.

Beyond TMDs, MXenes are an emerging class of 2D carbides and nitrides aptly named for their structural similarity to graphene and other conventional 2D materials. MXenes are synthesized by selective etching of the "A" layers, where A is a group 13 or 14 element, from MAX phase bulk crystals to yield 2D material with the general formula $M_{n+1}X_nT_x$ where where M is an early transition metal, X is carbon or nitrogen (n = 1, 2, or 3), and Tx denotes surface functional groups including –O, –OH, and –F.[8,176–177] At their time of discovery decades prior, MAX phases fulfilled a critical need in the field for materials with excellent thermal and oxidative stability that are also highly machinable, electrically conductive, damage tolerant, and can be synthesized from chemically diverse and abundant materials. 2D MXenes retain a num-

ber of these favorable mechanical and structural properties. Importantly, the low-dimensional nature of MXenes yields comparably higher surface areas and aspect ratios, making them exceptionally more electronically conductive than their MAX phase counterparts, reaching ~20,000 S cm^{-1}. This unique combination of material properties have afforded practical success for MXenes in a number of applications including chemical and biological sensing,[178–183] energy storage and conversion,[13,273–275] and electromagnetic shielding.[9–10,276] Among the present library of over 40 MXene compositions, $Ti_3C_2T_x$ is by far the most widely studied and employed MXene to date.

Despite promising reports for nascent material, interfacial functionalization of MXenes holds strong implications for designing chemically and electronically tunable surfaces for highly efficient, practical MXene-based devices. Covalent derivatization of MXene surfaces is most commonly employed to improve atmospheric stability as well as to enhance dispersion in organic solvents which is critical for solution phase processing involved in practical device fabrication. One route for surface functionalization exploits metal-ligand binding at presumably metal-rich edges of 2D MXene sheets. Since it is known that MXene surface oxidation generally begins at edge terminations and proceeds inwards, it has been demonstrated that edge-capping of $Ti_3C_2T_x$ and V2CTx sheets with polyanionic salts is successful in minimizing interfacial oxidation to improve stability in aqueous systems.[15] Moreover, it is well established that ortho diols are excellent ligands for metal chelation.[198] As such, two recent studies have demonstrated covalent attachment of catechol derivatives to MXenes. One study covalently attached dopamine and pyrocatechol to $Ti_3C_2T_x$ surfaces to enable subsequent functionalization with fluorescein in the context of biological imaging.199 Another study employed covalent attachment of catechol derivatives with long fluoroalkyl chains to various Ti-, Mo-, N-, and V-based MXenes to afford improved oxidative stability and dispersion in common organic solvents including methanol, ethanol, isopropyl alcohol, acetone, and acetonitrile.[200] This is particularly useful across a number of application that rely on solution phase processing.

Beyond edge-capping, since nascent material generally demonstrates a rich combination of interfacial –OH, –OH, and –F species, many MXenes are amenable to covalent derivatization that exploits the diverse chemical toolbox for attachment to oxygen-containing functional groups. Additionally, it is established that a simple treatment with strong base, NaOH, straightforwardly minimizes F terminations and maximizes O terminations.[184] This is particularly advantageous for maximizing coverages for self-assembling monolayers (SAMs) like organosilanes which covalently bind at interfacial hydroxyl sites. In separate studies, Gogotski and Zhang covalently attached different amino-terminated organosilanes to $Ti_3C_2T_x$ and to yield net positively charged surfaces at neutral pH.[191–192] Due to the presence of O- and and F-based terminations, MXenes generally demonstrate a net negative charge at their in-plane surface and net positive charge at the edges.[193] The ability to selectively alter

the magnitude and signage of the overall surface charge may have implications for applications that rely on selective adsorption of charged species, such as chemical and biological sensing. Other studies have employed covalent attachment with long-chain organosilanes to produce hydrophobic MXene surfaces in the context of solar desalination,[194] self-cleaning coatings,[195] and dispersibility in non-polar solvents.[196] In the context chemical tunability for biological sensing applications, another study employed silanization of $Ti_3C_2T_x$ surfaces with 3-(aminopropyl)trimethoxysilane (APTMS) and subsequent functionalization with a bio-receptor (anti-CEA) to enable ultrasensitive detection of the important cancer biomarker carcinoembryonic antigen (CEA).[197] A separate study directed toward chemical sensing employed functionalization of $Ti_3C_2T_x$ surfaces with fluoroalkylsilane to enable sensitive and selective sensing of various volatile organic compounds.[178] Conveniently, the fluoroalkylsilane-functionalized MXene also demonstrated improved atmospheric stability.

Initial reports for surface-functionalized MXenes are promising for their implications toward improving atmospheric stability, enhancing dispersibility in organic solvents, and achieving higher selectivity and sensitivity toward particular analytes. Nonetheless, to our knowledge little work has been done to correlate interfacial chemical states for functionalized MXenes to the resulting changes in electronic and optical properties. For applications in energy, sensing, and EMI shielding, robust control over the electronic and optical properties of MXenes is highly desirable. It is known for traditional materials like silicon that surface functionalization can change local electron density based on the inclusion of electron-donating or electron-withdrawing groups[277–279] and thus can influence photoelectrochemical and photovoltaic properties, carrier dynamics, and electronic interactions between the material itself and contacting phases.[48,107–109,117–118,120,280–283] Moreover, these concomitant changes be tuned by altering the chemical functionalities of the molecular overlayer. Our work exploits these established surface chemistry approaches for emerging materials including $Ti_3C_2T_x$ MXene.

Herein, we functionalized $Ti_3C_2T_x$ MXene surfaces with 3-aminopropyltrimethoxysilane (APTMS) and trimethoxy(3,3,3-trifluoropropyl)silane using air-free techniques. X-ray photoelectron spectroscopy (XPS) confirmed covalent attachment as well as quantified sensitivity-factor-corrected peak-area ratios for elemental species in the MXene versus species in the overlayer. Ultraviolet photoelectron spectroscopy (UPS) quantified work function values for $Ti_3C_2T_x$ as a function of covalent derivatization. We discuss these results in the context of molecular-dipole-induced electronic tunability of $Ti_3C_2T_x$-based materials and composites for applications in energy storage, chemical and biological sensing, electromagnetic shielding, among others.

5.3 Experimental

5.3.1 Materials and Chemicals

All reagents were used as received unless otherwise stated. A Millipore Milli-Q system provided 18 MΩ cm resistivity water for all water requirements. Silicon substrates for photoelectron spectroscopy experiments were single-sided polished, 525 ± 15 *mu*m thick, ≤0.006 Ω cm resistivity, degenerately arsenic-doped n^+-Si(111) (Addison Engineering). Quartz slides for optical spectroscopy experiments (Ted Pella) were cleaned with an Alconox solution, rinsed in water, and dried under argon, Ar, (ultrahigh purity, Airgas). Both quartz slides and silicon wafers were cleaned in piranha solution, rinsed in water, and dried under argon directly before use. Caution: piranha solution is a strong acid and a strong oxidant that reacts highly exothermically with organic matter. Piranha solution consisted of a freshly prepared 3:1 mixture of concentrated sulfuric acid (98%, Fisher Chemical) and $H_2O_{2(aq)}$ (35 wt %, Alfa Aesar). Glass test tubes and dram vials were cleaned in piranha solution, rinsed in water, and dried in a 100 °C oven overnight prior to use. Surface derivatization experiments utilized $Ti_3C_2T_x$ supplied by Barsoum and colleagues that was synthesized via established procedures.[202] The $Ti_3C_2T_x$ material was received in multilayered form and stored in a N2-purged flush box to minimize deleterious oxidation. Silanization procedures utilized ethanol (100% anhydrous, ACS/USP grade, Pharmaco-Aaper), water (Millipore Milli-Q, 18 MΩ cm resistivity), acetic acid (AcOH, 99.7%, Alfa Aesar), and either trimethoxy(3,3,3-trifluoropropyl)silane (98%, TCI) or 3-aminopropyltrimethoxysilane (APTMS, 95%, Acros Organics). Ethanol was stored over sieves (3Å, 1–2 mm beads, Thermo Scientific) that had been previously activated by heating in a flame on a diffusion-pump-equipped Schlenk line with a base pressure below 1×10^{-3} Torr. All degassing procedures employed N_2 gas (ultrahigh purity, Airgas).

5.3.2 Preparation of delaminated $Ti_3C_2T_x$

Sonication and subsequent separations via centrifugation to yield delaminated $Ti_3C_2T_x$ preceded silanization experiments as in Fig. 5.1. Here, 100 mg portions of multilayered $Ti_3C_2T_x$ were transferred from the N_2-purged flush box and combined with 10 mL water under an air ambient. Bubbling at <1 sccm N_2 for 3 h followed by 1 h of sonication in an ice-cooled water bath sufficiently delaminated the $Ti_3C_2T_x$ material. Following sonication, the $Ti_3C_2T_x$ colloid in water was transferred to a 15 mL polypropylene centrifuge tube and filled with water up to the 10 mL graduation line to account for water loss from evaporation. Centrifugation at 3000*g* for 10 min initially separated delaminated $Ti_3C_2T_x$ material from the comparatively larger particulates. This initial round of centrifugation yielded a black pellet and a dark green-black supernatant. The supernatant liquid was decanted and

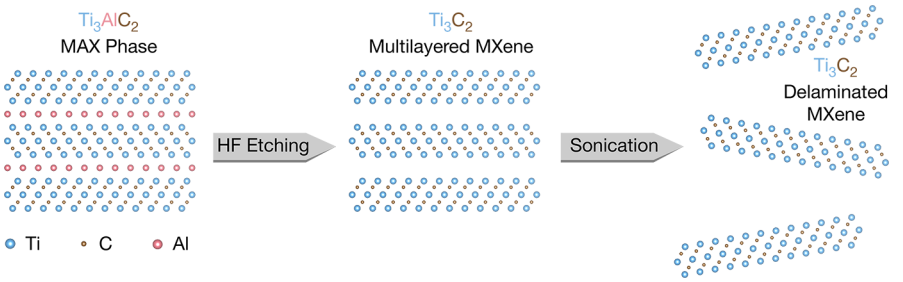

Figure 5.1. Cartoon illustration depicting the synthesis of multilayered $Ti_3C_2T_x$ MXene from MAX phase Ti_3AlC_2 by etching treatment with HF. Sonication can further delaminate the multilayered $Ti_3C_2T_x$ to yield individual 2D sheets

transferred to a separate, clean 50 mL centrifuge tube and filled to the 20 mL line with water and the pellet was discarded. To ultimately separate the solid material from the water, the colloid of delaminated $Ti_3C_2T_x$ was further purified by centrifugation at 5000g for 10 min which yielded a pellet containing a fractional percentage of the $Ti_3C_2T_x$ solid material and a supernatant which comprised a colloidal suspension of a fractional percentage of the $Ti_3C_2T_x$ material in water. Following decanting and discarding of the supernatant liquid, the $Ti_3C_2T_x$ material in the pellet was resuspended in 7 mL of fresh ethanol via physical agitation and sonication for 2 min with N_2 bubbling as described prior. The resulting $Ti_3C_2T_x$-containing suspension in ethanol was then subjected to functionalization as described in the proceeding sections.

5.3.3 Functionalization of $Ti_3C_2T_x$ MXene with organosilanes

Following delamination and solvent exchange from water to ethanol as described in §5.3.2, 1 mL of aqueous 0.1 M acetic acid was added to the 7 mL suspension of delaminated $Ti_3C_2T_x$ in ethanol. Bubbling at <1 sccm N_2 for 15 min preceded the addition of organosilane solutions. We utilized 5 mL of 0.2 M ethanolic solutions of the organosilanes to target ~2:1 molar ratios of the organosilane to the MXene, with all solution preparation occurring in a N_2-purged flush box. Ethanol for silane dilution had been stored over activated sieves prior to use. Upon removing the solution from the flush box, the ethanolic silane solution was added to the degassed $Ti_3C_2T_x$ solution by syringe at a rate of 1 mL per 15 min over the course of 75 min until the full 5 mL of silane solution was delivered. The silane-containing $Ti_3C_2T_x$ solution was sonicated for 4 h total from the first silane addition in an ice-cooled water bath with N_2 bubbling at <1 sccm.

Following the 4 h reaction, the $Ti_3C_2T_x$ solution was quantitatively transferred to a 15 mL centrifuge tube rinsing with small volumes of ethanol to reach a final volume of 15 mL. Centrifugation at 3000g for 2 min initially sepa-

rated the solid $Ti_3C_2T_x$ material from the ethanolic silane solution. Following decanting and discarding of the supernatant liquid, the $Ti_3C_2T_x$ material was resuspended in 6 mL of fresh ethanol via physical agitation and sonication. Three cycles of centrifugation as above, decanting, and re-suspension further purified the material left in the pellet after each stage of rinsing and centrifugation in ethanol. Through each stage of ethanolic centrifugation, the supernatant progressively transitioned from light gray to a clear solution. With the final decanting of the clear ethanolic supernatant, the $Ti_3C_2T_x$ centrifugation pellet was suspended in 10 mL ethanol and thoroughly sonicated with N_2 bubbling at <1 sccm. This suspension of functionalized $Ti_3C_2T_x$ in ethanol was stored inside a nitrogen-purged flush box until further use.

5.3.4 Film Preparation

XPS and UPS analysis for the $Ti_3C_2T_x$ material utilized films on n^+-Si(111) substrates. The films were deposited by a gravity-feed, compressed-gas-propelled commercial airbrush (Master Airbrush, G233). Spray depositions for nascent $Ti_3C_2T_x$ material utilized ¡0.5 mL of the aqueous $Ti_3C_2T_x$ colloid while depositions for functionalized $Ti_3C_2T_x$ material utilized <0.5 mL of the ethanolic $Ti_3C_2T_x$ suspension. Films were sufficiently thick such that the analysis depth for typical XPS and UPS experiments excluded photoelectron contributions from the silicon substrate. Routine cleaning of the airbrush body and components utilized dilute, aqueous glacial acetic acid (AcOH, 99.7%, Alfa Aesar). Components in frequent contact with $Ti_3C_2T_x$ material including the needles, fluid tips, and reservoir were sonicated in the aqueous, dilute acetic acid and rinsed with copious amounts of water in between subsequent depositions.

5.3.5 Photoelectron spectroscopy

See the supporting information section in Appendix B for instrumental details as well as quantification methods.

5.4 Results

5.4.1 Nascent and Functionalized $Ti_3C_2T_x$ Surface Chemical States

X-ray photoelectron spectroscopy (XPS) quantified the surface chemistry of both nascent and organosilane-functionalized $Ti_3C_2T_x$ that was freshly spray deposited on n^+-Si(111) prior to photoelectron spectroscopy. Figure 5.2 presents representative Si 2p, C 1s, N 1s, Ti 2p, O 1s, and F 1s XP spectra for (A) nascent, non-functionalized $Ti_3C_2T_x$, (B) $Ti_3C_2T_x$ functionalized with trimethoxy(3,3,3-trifluoropropyl)silane, and (C) $Ti_3C_2T_x$ functionalized with 3-aminopropyltrimethoxysilane. We fit and interpret XP spectra for

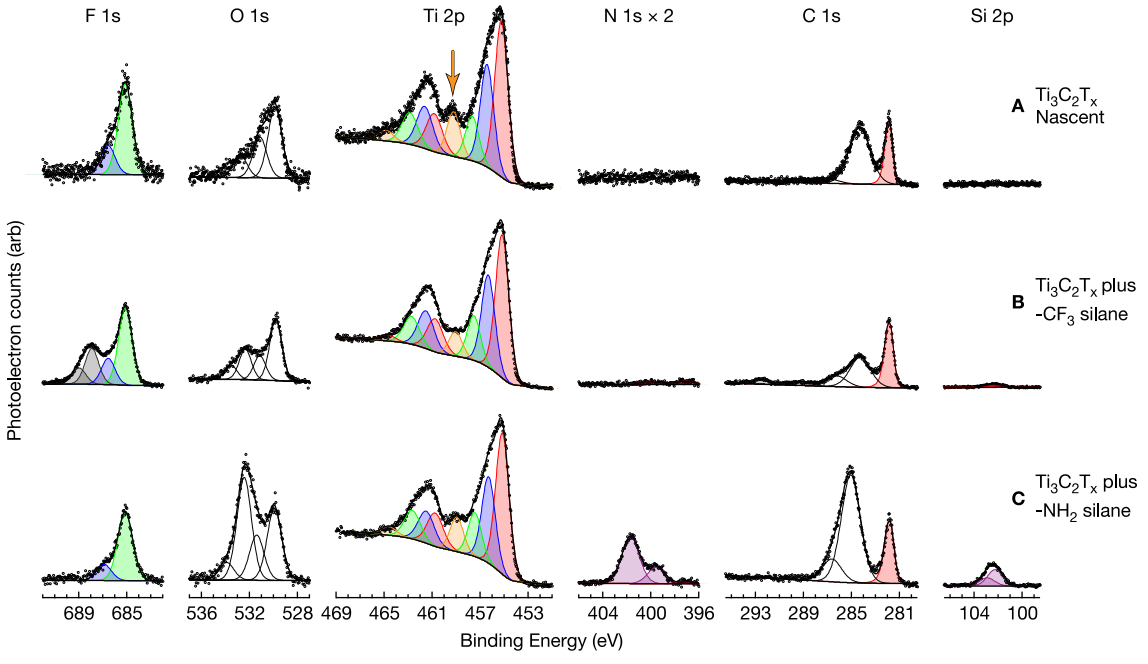

Figure 5.2. Representative XP spectra for **A** nascent, non-functionalized $Ti_3C_2T_x$, **B** $Ti_3C_2T_x$ functionalized with trimethoxy(3,3,3-trifluoropropyl)silane, and **C** $Ti_3C_2T_x$ functionalized with 3-aminopropyltrimethoxysilane. Importantly, the gray-shaded regions in the Si 2p, C 1s, and F 1s regions for B correspond to trimethoxy(3,3,3-trifluoropropyl)silane and are not observed for nascent $Ti_3C_2T_x$ in A. Similarly, the purple-shaded features in the Si 2p and N 1s regions for C are consistent with 3-aminopropyltrimethoxysilane and are not present for nascent $Ti_3C_2T_x$. The orange-shaded featured denoted with an arrow are consistent with Ti^{4+} in titanium oxides or oxyfluorides from deleterious oxidation of $Ti_3C_2T_x$.

$Ti_3C_2T_x$ herein similarly as discussed elsewhere[284–286] with some modifications. Across all samples, we ascribe the red-shaded C 1s and Ti 2p features to C–Ti–C and C–Ti–O\O\O local environments in which the atoms separated by a "\" denote three surface terminations to that particular titanium atom.[284] As such, we ascribe the red-shaded Ti 2p fitting feature to both middle-layer C–Ti–C atoms as well as interfacial C–Ti–O\O\O (i.e., Ti atoms in octahedra with 3 C atoms and 3 surface O atoms). Blue-shaded regions in the Ti 2p and F 1s regions likely correspond to C–Ti–O\O\F and C–Ti–O\F\F environments. We ascribe green-shaded peaks in the Ti 2p and F 1s regions to C–Ti–F\F\F, or Ti atoms in octahedra with 3 C atoms and 3 surface F atoms. The Ti 2p region further contains an additional higher-binding-energy doublet shaded orange and marked with an arrow in Fig. 5.2. We attribute this feature to Ti^{4+} in titanium oxides or oxyfluorides from deleterious oxidation of the material. Beyond the red-shaded carbidic carbon peak, the C 1s regions for all samples contain additional higher-binding-energy features that we attribute largely to adventitious contaminants in Fig. 5.2A and nonresolvable combinations of adventitious and organosilane components in Fig. 5.2B–C. The O 1s region for nascent $Ti_3C_2T_x$ as in Fig. 5.2A is described by three features centered at ~529.2, ~531.1, and ~532.8 eV. It not straightforward to deconvolve contributions to the O 1s region for this material without further experiments.223, 284-287 The O 1s region likely contains a mix of contributions from adventitious contaminants, C–Ti–O\O\O environments, C–Ti–(O,F) environments, as well as titanium oxides and oxyfluorides. For Fig. 5.2B–C, the three lower-binding-energy features in the O 1s region align well in position to those for nascent $Ti_3C_2T_x$ in Fig. 5.2A. The additional high-binding-energy feature centered at ~533.8 eV present for Fig. 5.2B–C may be due to additional adventitious contaminants from the chemical processing steps. Importantly, we ascribe the gray-shaded features in the Si 2p, C 1s, and F 1s regions for Fig. 5.2B to trimethoxy(3,3,3-trifluoropropyl)silane and they are not observed for nascent $Ti_3C_2T_x$ in Fig. 5.2A. Similarly, for Fig. 5.2C the purple-shaded features are consistent with Si 2p and N 1s features from 3-aminopropyltrimethoxysilane that are not present on nascent $Ti_3C_2T_x$ in Fig. 5.2A. Importantly, the binding-energy invariance of features ascribed to both $Ti_3C_2T_x$ and adventitious contaminants throughout the chemical processing steps obviated the need for charge neutralization.

5.4.2 Electronic Properties

Ultraviolet photoelectron spectroscopy (UPS) probed the work-function values for nascent and organosilane-functionalized $Ti_3C_2T_x$. Figure 5.3 presents ultraviolet photoelectron spectra with magnified insets of the Fermi region. We employed airbrush-deposited films for UP spectroscopy to yield a sufficiently thick film to obviate spectral contributions from the Si substrate. This enabled analyses of sensitivity-factor-corrected Si 2p:Ti 2p ratios for which the Si 2p photoelectron intensity originated solely from the organosilane over-

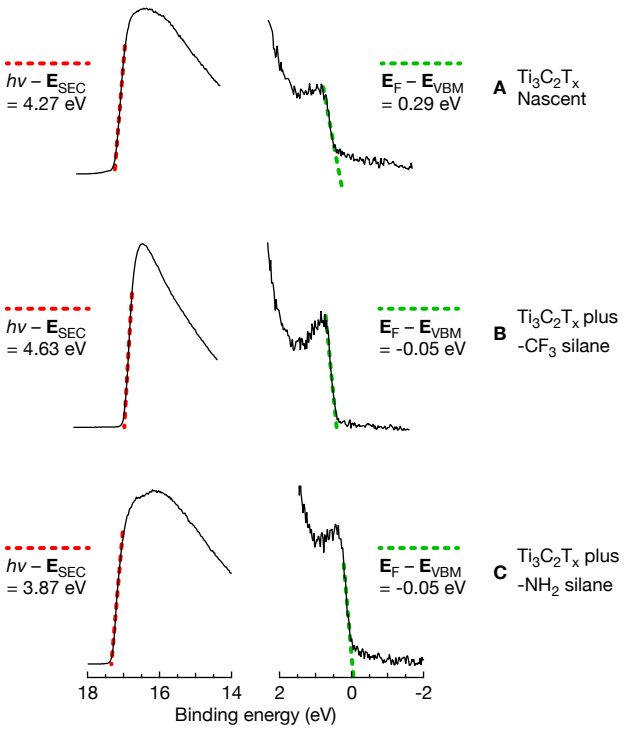

Figure 5.3. UP spectra for **A** nascent $Ti_3C_2T_x$, **B** $Ti_3C_2T_x$ functionalized with trimethoxy(3,3,3-trifluoropropyl)silane, and **C** $Ti_3C_2T_x$ functionalized with 3-aminopropyltrimethoxysilane. The low-binding-energy Fermi-edge regions for A, B, and C are magnified by 50, 200, and 50 respectively. Linear fits reveal the secondary-electron-cutoff energy $\mathbf{E}_{SEC}$ (red dashed line) and the *binding energy* of the valence-band maximum, $\mathbf{E}_{VBM}$, relative to its Fermi energy, $\mathbf{E}_f$.

layer. Frames A, B, and C in Fig. 5.3 represent UP spectra that respectively correspond to the XP spectra for samples presnted in frame A, B, and C in Fig. 5.2. UP spectra include those for A nascent, non-functionalized Ti3C2Tx, B $Ti_3C_2T_x$ functionalized with trimethoxy(3,3,3-trifluoropropyl)silane, and C $Ti_3C_2T_x$ functionalized with 3-aminopropyltrimethoxysilane. The green dashed lines in Fig. 5.3 represent linear regressions of the low-binding-energy edge for each valance-band feature whose x-intercepts quantify valence-band maxima, 5.2. With the 0 eV binding energy corresponding to the Fermi edge of sputter-cleaned polycrystalline gold (see Fig. B.1 in Appendix §B.1), the fitted $\mathbf{E}_{VBM}$ reveals the position of each sample Fermi level with respect to its valence-band maximum, or $\mathbf{E}_f - \mathbf{E}_{VBM}$. The red dashed lines in Fig. 5.3 represent a linear regression of the low-kinetic-energy (high-binding-energy) edge of the secondary-electron feature in each spectrum. The x-axis intercepts of each red-dashed regression reveal secondary-electron photoemission cutoff

energies, $\mathbf{E}^{SEC}$, that determine sample work functions, $\Phi = \mathbf{E}_{He\,I} - \mathbf{E}_{SEC}$, where $\mathbf{E}_{He\,I} = h\nu = 21.218$ eV.

Work function values for the $Ti_3C_2T_x$ samples under study correlate strongly with surface functionalization with organosilanes. Nascent, non-functionalized $Ti_3C_2T_x$ as in Fig. 5.3A demonstrates a work function value of $\Phi = 4.27$ eV. This stand in contrast to the work-function value of $\Phi = 4.63$ eV for $Ti_3C_2T_x$ functionalized with trimethoxy(3,3,3-trifluoropropyl)silane as in Fig. 5.3B which is ~350 meV larger than that for nascent $Ti_3C_2T_x$. Additionally, $Ti_3C_2T_x$ functionalized with 3-aminopropyltrimethoxysilane as in Fig. 5.3C demonstrates a work-function value of $\Phi = 3.87$ eV which is ~400 meV smaller than that for nascent $Ti_3C_2T_x$.

5.5 Discussion

For traditional semiconductors like silicon, surface derivatization imparts a surface dipole that results in changes to the local electron density of the material. The surface dipole magnitude and direction may be tuned based on the inclusion of electron-donating or electron-withdrawing functionality at the derivatizing molecule as compared to the nascent chemical and electronic structure.[277–279] The resulting interfacial dipoles influence photoelectrochemical and photovoltaic properties, carrier dynamics, and electronic interactions between the material itself and contacting phases.[48,107–109,117–118,120,280–283] For studies surrounding emerging, low-dimensional materials like MXenes for energy, shielding, and sensing applications, future research must critically incorporate such well-established surface chemistry approaches. Herein, we utilize differences in chemical structure for covalent molecular overlayers to effect changes in interfacial electronic structure on a material significantly less well studied than conventional semiconductors like silicon.

Investigations of Ti-based MXenes generally probe chemical and biological sensing,[178–183] energy storage and conversion,[13,273–275] and electromagnetic shielding.[9–10,276] Despite promising results for nascent $Ti_3C_2T_x$ with mixed –O/–OH and –F terminations, interfacial functionalization of MXenes holds strong implications for designing chemically and electronically tunable surfaces for highly efficient, practical MXene-based devices. Recent studies surrounding $Ti_3C_2T_x$ have primarily focused on covalent attachment of organosilanes and catechol derivatives toward improving atmospheric stability, enhancing dispersibility in organic solvents, and achieving higher selectivity and sensitivity toward particular analytes for sensing applications.[178,190–192,195–197,199–200] Nonetheless, to our knowledge, few studies have correlated interfacial chemical states for functionalized MXenes to the resulting changes in electronic and optical properties.[221–222] In this work, we derivatize $Ti_3C_2T_x$ with organosilanes and to impart interfacial dipoles and quantify the resulting changes in work-function values, Φ.

Figure 5.3 reveals UP spectra for A nascent, non-functionalized $Ti_3C_2T_x$, B $Ti_3C_2T_x$ functionalized with trimethoxy(3,3,3-trifluoropropyl)silane, and C $Ti_3C_2T_x$ functionalized with 3-aminopropyltrimethoxysilane. The UPS-determined work function for nascent $Ti_3C_2T_x$ yields Φ = 4.27 eV. Interestingly, $Ti_3C_2T_x$ material functionalized with trimethoxy(3,3,3-trifluoropropyl) silane as in Fig. 5.3B demonstrates Φ = 4.63 eV while material functionalized with 3-aminopropyltrimethoxysilane yields Φ = 3.87 eV. We attribute these discrepancies in work-function values to the interplay between the native surface dipole, δ, for $Ti_3C_2T_x$ with nascent –O and —F terminations and the induced molecular surface dipoles from the covalent organosilane overlayers. The work function for nascent $Ti_3C_2T_x$ is tunable based on changes in the interfacial surface chemistry. High-temperature vacuum annealing up to 750 °C for nascent $Ti_3C_2T_x$ demonstrates an increase to larger work-function values concurrently with the desorption of adventitious contaminants and a subsequent decrease to smaller work-function values as interfacial fluoride is desorbed.[223] Likewise, alkali treatment with KOH which minimizes –F terminations for Nb_2CT_x MXene yields comparably smaller work-function values.[222] As such, it is critical to consider the interplay between the nascent surface dipoles and those induced from covalent functionalization for $Ti_3C_2T_x$.

Based on the UP-determined work-function values, $Ti_3C_2T_x$ derivatized with the $–CF_3$ functionality demonstrates $\delta \approx +350$ eV while material derivatized with $–NH_2$ functionality yields $\delta \approx –400$ eV. Our interpretation considers relative changes based on the interplay between the native dipole for nascent $Ti_3C_2T_x$ and the molecular-induced dipole for organosilane-functionalized $Ti_3C_2T_x$ which we summarize in Fig. 5.4. For the trifluoro-functionalized material, the relative "positive" dipole and subsequent shift in work-function value as shown in Fig. 5.4C is consistent in directionality with studies surrounding Si derivatized with electron-withdrawing fluorosilanes[279] and are well-aligned with predicted dipole-induced changes in electronic structure predicted from molecular dynamics (MD) simulations.[278] In the case of amino silanes, the relative "negative" dipole and shift to smaller work-function values as shown in Fig. 5.4B is consistent with other reports surrounding amino-functionalized $Ti_3C_2T_x$,[221] as well as changes in electronic structure for amino-functionalized Si.[277] Taken together, we posit that the work function for $Ti_3C_2T_x$ is tunable with covalent derivatization based on the inclusion of electron-withdrawing and electron-donating functionality which holds strong implications for practical MXene applications.

5.6 Conclusion

Herein, we derivatized $Ti_3C_2T_x$ with organosilanes to impart relative interfacial dipoles based on the inclusion of electron-withdrawing or electron-donating functionality. Based on the UP-determined work-function val-

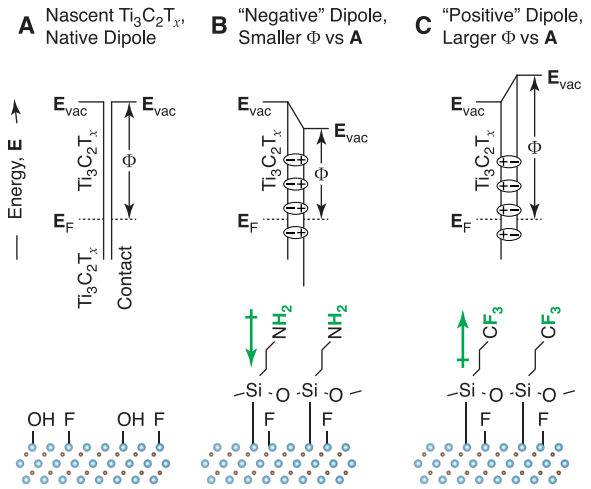

Figure 5.4. Band-energy diagram revealing relative Fermi-level equilibration at the interface of $Ti_3C_2T_x$ for various surface chemistries where **A** demonstrates the native dipole, δ, for $Ti_3C_2T_x$ with nascent –O/–OH and –F terminations. Frames **B** and **C** demonstrate relative Fermi-level changes from "negative" and "positive" dipoles versus the native dipole A for $Ti_3C_2T_x$ functionalized with 3-aminopropyltrimethoxysilane and trimethoxy(3,3,3-trifluoropropyl)silane respectively.

ues, $Ti_3C_2T_x$ derivatized with the $–CF_3$ functionality yields $\delta \approx +350$ eV while material derivatized with $–NH_2$ functionality yields $\delta \approx -400$ eV. We demonstrated relative changes in work-function values based on the interplay between the native dipole for nascent $Ti_3C_2T_x$ and the molecular-induced dipoles for organosilane-functionalized $Ti_3C_2T_x$. Further, based on the chemical features at the derivatizing molecule, the surface dipole magnitude and direction for $Ti_3C_2T_x$ may be tuned as compared to the nascent chemical and electronic structure.

In the context of Si-based field-effect transistors (FETs) for sensing applications, interfacial dipoles from covalent, directionally-aligned molecular organics enables controllable threshold voltage shifting, current modulation, and tunability of metal-gate work functions.[118,280–282] Moreover, surface dipoles can impart carrier selectivity at the interface of Si and other contacting phases which is favorable for energy applications including Si-based multijunction photovoltaics. Given these results for derivatized Si, it is promising to consider the implications of these interfacial dipoles for practical MXene-based devices with applications in energy storage, shielding, and chemical and biological sensing.

Given their tunable surface chemistries and exceedingly high electrical conductivities, MXenes have recently been investigated for electromagnetic in-

terference (EMI) shielding applications, often outperforming conventional metals and graphene, as well as for Li-based battery systems.[10] Often, favorable shielding behavior is attributed to the magnitude of the native positive dipole arising from electronegative –F, –O, and –OH terminations. Further, larger work-function values based on increasing contributions of –F terminations are highly favorable for EMI shielding.[276] Herein, we demonstrate comparably larger positive dipoles relative to that for nascent MXene based on covalent functionalization with fluorocarbon-based organosilanes. This may hold strong implications for EMI shielding ability for $Ti_3C_2T_x$ MXene and further investigations to better probe practical implications for molecular-induced dipoles are presently underway.

CHAPTER 6

ELECTRONIC STRUCTURE OF 1D LEPIDOCROCITE TiO_2 AS REVEALED BY OPTICAL ABSORPTION AND PHOTOELECTRON SPECTROSCOPY

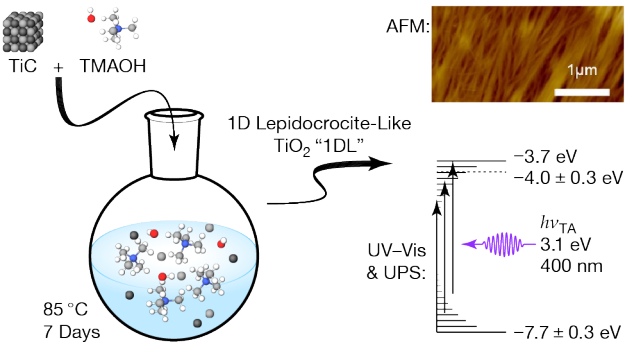

Portions adapted from:

Erika Colin-Ulloa,† Julia L. Martin,† Ryan J. Hanna, Michelle H. Frasch, Rebecca R. Ramthun, Hussein O. Badr, Michel W. Barsoum, Ronald L. Grimm,* and Lyubov V. Titova.* Electronic Structure of 1D Lepidocrocite TiO_2 as Revealed by Optical Absorption and Photoelectron Spectroscopy. *J. Phys. Chem. C* **2023**, *in press*. 10.1021/acs.jpcc.2c06719

† *Denotes equal contribution. ECU collected all ultrafast TA data, RJH and MHF synthesized all 1DL under study, while HOB and MWB originally discovered 1DL material.*

6.1 Abstract

We recently demonstrated scalable, one-pot syntheses of one-dimensional, titania lepidocrocite nanofilaments by reacting Ti-containing water-insoluble, earth-abundant compounds such as TiC, TiB_2, TiN, etc., with tetraalkylammonium hydroxide, TMAOH, for a few days at 85 °C under ambient pressure. The resulting one-dimensional lepidocrocite (1DL) titania-based nanofilaments, tend to self-align along the [100] growth direction to form nanofilaments that sometimes self-align into pseudo-two-dimensional (2D) sheets. With sub-square-nanometer cross sections, the resulting band gap energy, $\mathbf{E}_g$, at 4.0 eV is one of the highest ever reported for a titania material. Despite a large band gap, the nanofilaments exhibit significant absorbance throughout the visible spectrum ascribable to intra-gap defect states based on UV–Vis absorbance data and ultraviolet photoelectron spectroscopy (UPS). UP spectra demonstrate work functions of 4.0 ± 0.3 eV vs vacuum and Fermi energies of 3.8 ± 0.1 eV with respect to the valence-band edge. Transient absorption (TA) spectroscopy of the 1DL nanofilament thin films with sub-band-gap, visible-light illumination reveals photoexcitations with lifetimes in excess of nanoseconds. In combination with the established oxidative stability, long-lived visible photoexcitations bring forward possible applications of 1DL nanofilaments in photocatalysis and optoelectronics.

6.2 Introduction

Tackling global energy challenges requires inexpensive, nano- structured materials for a host of applications, including solar energy conversion via photocatalysis or generation of photocurrents in solar cells. Quite recently, we discovered a simple, one-pot, near-ambient, almost universal process to convert low-cost, ubiquitous nontoxic starting materials, such as TiC, TiN, TiB_2, and Mn_3O_4, into highly quantum-confined, oxidatively stable materials with excellent catalytic properties that are relevant to our global energy challenges.[17,288]

Early studies have elucidated important phenomena in the synthesis and properties of these new materials. When utilizing titanium-based precursors, the resulting materials demonstrate nanometer-to-microns-long filaments with sub-nm^2 cross sections. More recently, we reported on the general validity of this synthesis protocol not only with Ti-based powders but also with Mn-bearing precursors that yield crystalline two-dimensional (2D) MnO_2 birnessite sheets with lateral sizes of ≈200 nm.[288] However, we presently focus on materials with Ti-based precursors. While initial density functional theory (DFT) calculations suggested a structure involving a one-dimensional (1D) analogue of anatase,[17] more recent transmission electron microscopy (TEM) and Raman spectroscopy with updated calculations reveals a lepidocrocite-like one-dimensional titania 1DL nanofilaments with

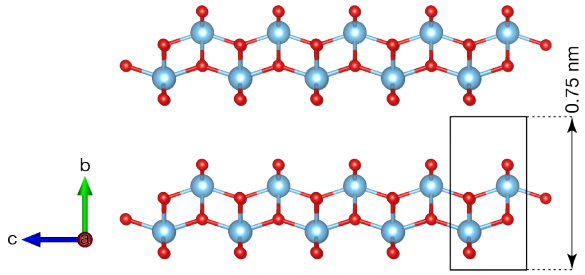

Figure 6.1. Schematic of nanomaterials composed of 1D lepidocrocite-like TiO_2, 1DL. Blue and red spheres represent Ti and O atoms, respectively. Adapted from ref 16.

sub-nanometer cross sections.[16] Reports of lepidocrocite-like titania include its formation on templating surfaces such as Cu(001),[4] as well as free-standing films,[204] but this form is comparatively under-explored relative to the anatase and rutile forms of TiO_2.

Precursors include TiC, TiB_2, TiN, Ti_3AC_2 (A = Al, Si, Ga, Sn, etc.), and Ti_2SbP that are immersed in an aqueous base at 85 °C for several days. The quaternary ammonium base may have propyl or butyl chains, but most commonly, we use tetramethylammonium hydroxide, TMAOH, that dissolves the precursor and, with time, results in the 1DL nanofilaments, the structure of which is shown in Fig. 6.1.[16,17] Interestingly, related investigations revealed that the sub-nanometer-wide products can self-assemble into a plethora of morphologies, from nanofilaments to bundles of nanofilaments, to micrometer-long filaments, and to two-dimensional flakes that are readily filtered into self-standing films.[17] Recent Raman and high-resolution transmission electron microscopy, TEM, studies of filtered films revealed the structure to be composed of 1DLs that are capable of self-alignment into pseudo-2D sheets.[16] The 1DL NFs grow along the [001] and stack along the [010]. X-ray photoelectron spectra, XPS, and near-edge absorption spectra are consistent with the inclusion of both Ti^{3+} and Ti^{4+} oxidation states.[17]

Light absorption results from the initial report suggest a highly quantum-confined material.[17] While researchers have previously produced 2D titania sheets with $\mathbf{E}_g \approx 3.6$ eV,[289–290] to our knowledge, the $\mathbf{E}_g = 4.0$ eV is the highest reported for titanium dioxide and remains consistent with quantum confinement effects as dimensions shrink.[291–292] The strong quantum confinement effect that yields the increased band gap indirectly supports the 1D nature of our filaments and implies that the absorption axis is coupled to the sub-nm^2 cross section rather than their micron-scale lengths. While there is a wide body of literature that reports and discusses 1D anatase based on extremely high-aspect-ratio structures, as far as we are aware, our material is unique in showing substantial quantum confinement. Considering the sub-nanometer cross section, the 1DL nanofilamens possesses extremely high theoretical

surface area of the order of ≈1000 m^2 g^{-1}. Films of 1DLs demonstrate good performance as electrodes in lithium-ion and lithium–sulfur systems, as well as excellent oxidative stability.[17] They are also quite good at photocatalytically producing hydrogen, H_2. The latter results are particularly topical as nanostructured,[205–206] and doped[207–210] titanium oxides are some of the most extensively investigated materials for photocatalytic and photoelectrochemical applications.

Despite promising initial results, questions remain regarding the specific chemical structure, surface states, and the interplay between those chemical features and the resulting electronic properties. Computational studies have postulated the properties of quantum-confined 1D titanium oxides;[293–296] however, few experimental reports exist on ultrathin titanium oxide with sub-nm thickness.[203–204,292] Further, the large $\mathbf{E}_g$ = 4.0 eV band gap for the 1DLs stands in contrast to the material's dark color,[17] which for $\mathbf{E}_g$ = 3.0 eV rutile and $\mathbf{E}_g$ = 3.2 eV anatase is frequently ascribed to be due to defects such as Ti^{3+} and oxygen vacancies.[297] Significant sub-band-gap optical absorption in 1DL films supports the presence of defect states. The paucity of knowledge about 1DL combined with its catalytic potential drives research to understand the optical and electronic structure of this material and motivates the present investigation.

Herein, we synthesized 1DL from TiC and 25 wt % aqueous tetramethylammonium hydroxide, TMAOH, at 85 °C for 7 days. Solution-suspended 1DL nanofilaments were spin-deposited or drop-cast onto quartz for optical experiments or degenerately doped silicon for photoelectron spectroscopy. Atomic force microscopy (AFM) and transmission electron microscopy (TEM) established the morphology of our nanostructures. A combination of ultraviolet photoelectron spectroscopy (UPS) and UV–Vis spectroscopy elucidated electronic structure. Finally, transient absorption (TA) spectroscopy characterized optical excitations. We find that sub-gap 3.1 eV (400 nm) laser pulses generate long-lived photoexcitations with lifetimes in excess of nanoseconds, ns. This observation, combined with their high oxidative stability and exceptionally high surface area, suggests possible applications in water remediation, photocatalysis, and sensing, among many others.

6.3 Experimental

6.3.1 Materials and Chemicals

Reagents for 1DL synthesis included TiC (99% pure, 2 μm gray powder, Strem, used as received) and tetramethylammonium hydroxide, TMAOH, (2.8 M or 25 wt. % in water, Thermo Scientific, used as received). Post-synthesis treatment included lithium chloride (LiCl, 99+%, ACS, Acros, as received) ethanol (anhydrous, histological grade, (Fisher, as received), and >18 MΩ

cm water (Millipore Milli-Q dispensing system). Chemicals for cleaning included concentrated sulfuric acid (H_2SO_4, ACS grade, Fisher, as received) and aqueous hydrogen peroxide (H_2O_2, 30%, Certified ACS, Thermo Scientific, as received). Quartz slides for optical spectroscopy experiments (Ted Pella) were cleaned with an Alconox solution, rinsed in water, and dried under argon, Ar, (ultrahigh purity, Airgas). Silicon substrates for photoelectron spectroscopy experiments were single-sided polished, 525 ± 15 μm thick, ≤0.006 Ω cm resistivity, degenerately arsenic-doped n^+-Si(111) (Addison Engineering). Both quartz slides and silicon wafers were cleaned in piranha solution, rinsed in water, and dried under argon directly before use. ***Caution***: piranha solution, a 3:1 mixture of concentrated H_2SO_4 and 30% $H_2O_{2(aq)}$, is a strongly oxidizing acid that reacts violently and exothermically with organic matter. Use appropriate safety measures for handling and disposal.

6.3.2 Synthesis of 1DL and Film Preparation

Synthesis of 1DL proceeded in capped 60 mL high-density polyethylene bottles (Nalgene). A 1/16″ hole was drilled in the bottle cap, prior to use, afforded venting during synthesis. Typical reagent quantities included 1.0 ± 0.03 g TiC and 10.3 ± 0.1 g $TMAOH_{(aq)}$. The precursor quantities specified yield a 1:2.2 ratio between Ti metal atoms and TMA cations. With vigorous stirring from a cross-type stir bar, reactions proceeded for seven days at 85 °C.

Following the synthesis, rinsing and purification steps yielded the 1DL films under study. Centrifugation at 3000*g* for 2 min initially separated the particulate products from the TMAOH solution. Following decanting and discarding of the supernatant liquid, the 1DL material was resuspended in 15 mL of fresh ethanol via physical agitation and sonication. Three cycles of centrifugation as above, decanting, and re-suspension further purified the material left in the pellet after each stage of rinsing and centrifugation in methanol. Through each stage of ethanolic centrifugation, the supernatant showed no signs of suspended material and progressively transitioned from light brown to a clear solution. With the final decanting of the clear ethanolic supernatant, the 1DL centrifugation pellet was suspended in 20 mL water and thoroughly sonicated. Following centrifugation at 3000*g* for 2 min, the aqueous supernatant demonstrated significant turbidity that was decanted and utilized for ongoing film preparation whilst the centrifugation pellet was discarded. This aqueous suspension of 1DL was alternatively stored as non-LiCl-rinsed material, or subsequently cleaned with LiCl to further remove any remaining tetramethylammonium cations.

For LiCl-rinsed 1DL films, we added 20 mL of 0.1 LiCl(aq) to the turbid, aqueous supernatant suspension, agitated to mix, and sonicated the mixture for 30 min. Following sonication of the LiCl-containing 1DL suspension, centrifugation at 3000*g* for 2 min revealed a pellet that was retained and a clear supernatant solution that was discarded. Redispersion of the pellet in

fresh water, sonication, and centrifugation at 3000*g* for 2 min yielded a turbid supernatant as above. This turbid supernatant was decanted and stored as a suspension of LiCl 1DL material while discarding the pellet.

Films for AFM analyses formed by spin coating a solution of 1 vol part 1DL suspension with 2 parts water onto quartz. Films for UV-Vis and transient absorption were deposited onto piranha-cleaned quartz from the 1DL supernatant suspension with no dilution. Films for photoelectron spectroscopy were drop cast onto piranha-cleaned Si with no dilution.

6.3.3 X-Ray Photoelectron Spectroscopy (XPS)

A PHI 5600 XPS system, with a third-party data acquisition system (RBD Instruments, Bend Oregon), acquired all photoelectron spectra as detailed previously.[298] The analysis chamber base pressures were $<1 \times 10^{-9}$ Torr. A hemispherical energy analyzer, positioned at 90° with respect to the incoming X-rays, collected the photoelectrons. Analyses utilized monochromated Al K_α X-radiation and employed a 45° angle between the sample normal angle and both the X-ray source and the analyzer. Instrumental calibration included positioning Cu $2p_{3/2}$ at 932.67 eV and Au $4f_{7/2}$ to 84.00 eV on freshly sputter-cleaned samples that yielded Fermi-level positioning $\mathbf{E}_{f,\,Au} \equiv 0.00 \pm 0.05$ eV.

The aforementioned thin films deposited on degenerately-doped n-type Si substrates were mounted on freshly-cleaned stainless steel pucks with Cu tabs and evacuated in the loading chamber for <1 h preceding direct transfer to the analysis chamber. Consistent binding-energy positions between samples and fitted Ti $2p_{3/2}$ features at ~459 eV obviated the need for charge neutralization in analyses of the 1DL films. In all experiments, survey spectra utilized a 117-eV pass energy, a 0.5-eV step size and a 50-ms-per-step dwell time. High-resolution XP spectra employed a 23.5-eV pass energy, 0.025-eV step size, and a 50-ms dwell time per step.

Post-acquisition fitting utilized an in-house-developed LabVIEW-based program. Data fitting employed baseline-corrected, pseudo-Voigt, GL(x)-style functions where x nonlinearly scales from a pure Gaussian ($x = 0$) to a pure Lorentzian ($x = 100$).[255] Baseline functions were either of a linear type, a Shirley type,[256] or a Tougaard style with $B = 2900$ eV^2 and $C = 1643$ eV^2 within a universal function that is scaled to the height of the photoelectron data.[257–258] Optimization routines utilize the built-in LabVIEW implementation of the Levenberg-Marquardt algorithm for multiparameter fitting. Fitting of the Li 1s, C 1s, and O 1s features utilized a Tougaard background and GL(30) functional peak shapes. The Li 1s region contained neighboring Ti~3s feature and trace I 4d and Br 3d features that may be contaminants in the TMAOH solution. Spin-orbit-split doublets were individually constrained to have mutually identical full-width-at-half-max (fwhm) values for I 4d and Br 3d in that region. Fitting of the C 1s or O 1s regions necessitated multiple

fit peaks. These peaks were constrained to have identical fwhm values with the exception of the low-binding-energy feature centered at ~281 eV present on some samples which was left unconstrained. A Tougaard background and GL(70) peak shapes describe the Ti 2p features. The widths of Ti 2p doublets were constrained such the width of each Ti $2p_{1/2}$ feature as 1.6× the width,[299] and 0.5× the area of its corresponding Ti $2p_{3/2}$ feature based on high-resolution spectra of TiC and TiO_2 samples collected in-house. Si 2p and N 1s features utilize a linear background and GL(30) peak shapes. (We collected Si 2p to verify that the 1DL deposition substrate was not contributing to any spectral features that would interfere with the collection or interpretation of the UP spectra.) Si 2p doublets were constrained to have identical fwhm with the $2p_{1/2}$ peaks containing 50% of the area of the $2p_{3/2}$ peaks. Fitting of the N 1s region necessitated multiple fit peaks and the fwhm values were left unconstrained.

6.3.4 Ultraviolet Photoelectron Spectroscopy (UPS)

For UP spectra collected in the PHI 5600 chamber, a gas discharge lamp (UVS 40A2, Prevac, Rogów, Poland) generated the He I spectroscopic line from research grade helium, He (Airgas). We utilize a –35 V substrate bias versus the grounded sample chamber to both maximize the desired spectral contributions of electrons from the sample and isolate unwanted secondary electrons from the analyzer. We chose the –35 V bias based on an invariance in spectral features and good linearity in analyzer response for UP spectra of a freshly Ar^+-sputtered gold foil between biases of –20 and –50 V vs the sample chamber ground. As above, UP spectra of a freshly Ar^+-sputtered gold foil verified instrumental calibration with the bias-corrected Fermi level of gold, $\mathbf{E}_{f,\,Au} \equiv 0.00 \pm 0.05$ eV. From plots of photoelectron counts vs. bias-corrected binding energy, the x-axis intercept of linear regressions quantifies a secondary-electron-cutoff energy, $\mathbf{E}_{SEC}$, and a valence-band-edge (maximum) energy, $\mathbf{E}^{VBM}$. Considering the binding energy calibration of the instrument, we report sample work function energy values, Φ, as the difference between $\mathbf{E}_{VBM} = h\nu = 21.218$ eV and the secondary electron cutoff energy, or $\Phi = \mathbf{E}_{He\,I} - \mathbf{E}_{SEC}$. We report Fermi-level energies vs. valence-band-maximum energies, or $\mathbf{E}_f - \mathbf{E}_{VBM}$. As ultrahigh vacuum bakeouts can yield a small perturbation in instrument calibration due to adsorbed contaminants changing the work function of instrument surfaces or the trajectory of photoelectrons between the sample and the hemispherical analyzer, both Au calibration and all 1DL data were acquired during the same "bakeout window."

6.3.5 UV-Vis Spectroscopy

A UV-Visible spectrometer (Evolution 300, Thermo Fisher Scientific, Waltham, MA) collected scattered light from drop-cast 1DL samples mounted in a Praying Mantis diffuse reflection accessory (Harrick Scientific Products, Pleas-

antville, NY) as well as transmitted light from 1DL samples mounted in a transmission-mode beam path. In both cases, films were deposited on 1″-diameter-Piranha-cleaned quartz rounds utilizing the deposition protocol described above. Clean quartz served as the background reference for each scan. Directly preceding drop-cast film deposition, the quartz rounds were cleaned in a Piranha acid solution, rinsed with Milli-Q water, and blown dry under an Ar stream. Scans were obtained in a range of 300 nm to 1000 nm, using a scan speed of 160 nm min^{-1} and a bandwidth of 1 in absorbance mode.

6.3.6 Atomic Force Microscopy (AFM)

AFM imaging was carried out in no-contact mode using a n AFM (NX20 Park Systems), with an Olympus cantilever OMCL-AC160TS. Images were recorded by Smart scan software (Park Systems) with a 5×5 μm^2 scan size and analyzed by XEI software (Park Systems).

6.3.7 Transmission Electron Microscopy (TEM)

TEM samples prepared by first diluting TiC-derived colloidal suspensions 1:300 in DI water, then a few drops were drop cast on a carbon-coated, lacey-carbon, copper TEM grid (Cu-400LD, Pacific Grid Tech, San Francisco, CA). Samples were left to dry in a vacuum chamber at ambient temperature overnight before characterization. Imaging acquired with a field-emission TEM (JEOL JEM 2100F) at an acceleration voltage of 200 kV using a Gatan USC1000 CCD camera.

6.3.8 Transient Absorption (TA) Spectroscopy

The TA measurements were carried out using a HARPIA-TA Ultrafast Transient Absorption Spectrometer (Light Conversion). In the measurement, 1030 nm, 290 fs pulses from a ytterbium laser (Carbide, Light Conversion) generated probe white light through a sapphire crystal. An optical parametric amplifier (Orpheus, Light Conversion) generated 400 nm (3.10 eV) pump pulses. Pump-induced differences in absorption were detected, in transmission mode, by an Andor spectrograph and a Si photodiode array as a function of pump-probe delay time.

6.3.9 X-Ray Diffraction (XRD)

A Bruker-AXS D8 Focus powder X-ray diffractometer with Cu K_α radiation collected X-ray diffraction (XRD) traces in the range of 5–45° (2θ) at a step size of 0.05° and a dwell time of 5 s per step. X-ray tube operating conditions were 40 kV and 40 mA. Samples were drop cast directly from the aqueous

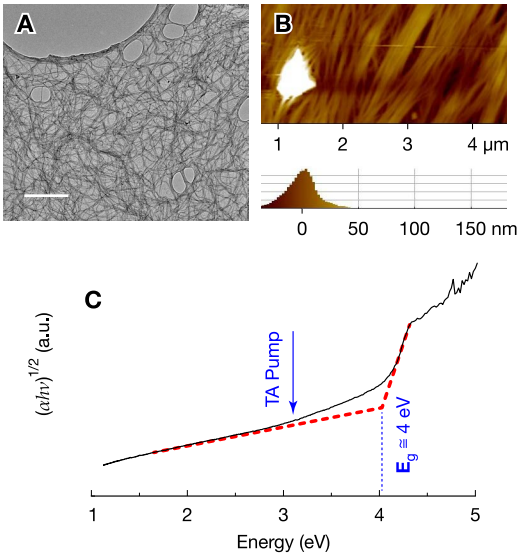

Figure 6.2. **A** TEM images from drop-cast 1DL porous films where the scale bar indicates 200 nm. **B** AFM image of spin-deposited film of 1DL with a histogram below that reflects the z-axis distribution of observed heights. **C** UV–Vis-spectroscopy-derived Tauc plots reveal an approximately 4 eV indirect band gap for drop-cast films. The arrow in frame C corresponds to the 3.1 eV energy of the optical pump pulses in transient absorption measurements.

supernatant suspension onto a poly(tetrafluoroethylene) sample holder in successive steps to build up sufficient material for diffraction analyses.

6.4 Results

In line with our previous work,[17] present TEM (Fig. 6.2A) and AFM (Fig. 6.2B) images demonstrate that the 1D character of our material synthesized at 85∼°C for seven days. Individual, separated, long films yield highly aligned films with spin deposition (not shown), when imaged away from the axis of rotation, while drop casting yields disordered nanofiber films as shown in the TEM image in Fig. 6.3A. XRD traces for 1DL films match previous reports,[17] and are not discussed further.

Figure 6.2C shows Tauc plot derived from UV-Vis spectra for a drop-cast film, for which Fig. C.1 in Appendix C includes the corresponding raw UV-Vis data. Compared to spin deposition, drop casting yielded thicker films and easier UV-Vis analyses with a higher signal-to-noise ratio. Tauc construction demonstrates an onset of an indirect transition at ∼4 eV, revealing the semiconducting nature of these structures. The 1DL films also exhibits an Urbach

tail of sub-gap optical transitions covering the entire visible range. Note that $\mathbf{E}_g$ is significantly blue-shifted compared to bulk anatase TiO_2 (3.2 eV) likely because of strong quantum confinement of electrons in the 1D nano- or micro-filaments that are approximately 5×7 Å^2 in cross-section. However, a long sub-gap tail extending from the UV down to the near-infrared range shows that the photoresponse due to optical excitation in the visible spectrum is possible in these emerging nanomaterials. The aforementioned independence of UV-Vis absorption properties with deposition methods implies that observed behaviors is intrinsic to the 1DL material rather than emergent behaviors in 1DL films.

Figure 6.3 presents representative XP spectra both (A) prior to, and (B) following the LiCl rinse step that are consistent with previously published 1DL data.[17] In Fig. 6.3, we ascribe the red shaded O 1s and Ti 2p features to the 1DL material itself. The Ti $2p_{3/2}$ feature occurs at 458.8–459.1 eV for all measured samples, which indicates that Ti^{4+} dominates as previously observed.[17] Green-shaded Ti $2p_{3/2}$ features at 455.2–455.3 eV and C 1s features at 281.8–282.0 eV are consistent with Ti^{2+} and reduced carbon that exist in the titanium carbide precursor. We conclude that a nominal amount of TiC precursor remains in some 1DL films, and we limit ourselves to quantifying films with <2% unreacted TiC as established by the Ti^{2+} to Ti^{4+} ratio of the Ti $2p_{3/2}$ features. Interestingly, accounting for one Ti^{4+} doublet and one Ti^{2+} doublet reveals another purple-shaded fittable doublet with Ti $2p_{3/2}$ at 457.0–457.8 eV, which is consistent with Ti^{3+} in the 1DL films. Observation of Ti^{3+} ascribable features is consistent with our previous results,[17] as well as preliminary electron-spin resonance experience that will be the subject of upcoming studies. A notable blue-shaded N 1s feature at 403.7 eV in concert with a blue-shaded C 1s feature at 287.1 eV imply significant quantities of tetramethylammonium hydroxide, TMAOH, cations present prior to aqueous LiCl rinsing. The blue-shaded features TMAOH cations largely disappear from XP spectra following an aqueous LiCl rinse while a demonstrable, green-shaded Li 1s feature appears at 55.9 eV. The carbon region further contains a gray-shaded feature at 284.6–285.4 eV that we ascribe to adventitious carbon contamination. In Fig. 6.3B, we further ascribe the gray-shaded feature at 286.3 eV to oxidized adventitious carbon species rather than ammonium carbon due to the absence of N 1s fittable features following the LiCl rinse.

Figure 6.4 presents an ultraviolet photoelectron spectrum with a 16× inset of the Fermi region. We employed drop-cast films for UP spectroscopy to yield a sufficiently thick film to obviate spectral contributions from the Si substrate. Figure 6.3B displays the corresponding XP spectra for this specific sample that well resembles our previously published results.[17] The x-axis intercept of the red dashed line at ~17 eV vs. the Fermi energy of Au, $\mathbf{E}_f \equiv 0$ eV reveals the secondary-electron-cutoff energy, $\mathbf{E}_{SEC}$, from which we derive work function values $\Phi \equiv h\nu - \mathbf{E}_{SEC}$. For the sample in Fig. 2, Φ = 4.03 eV,

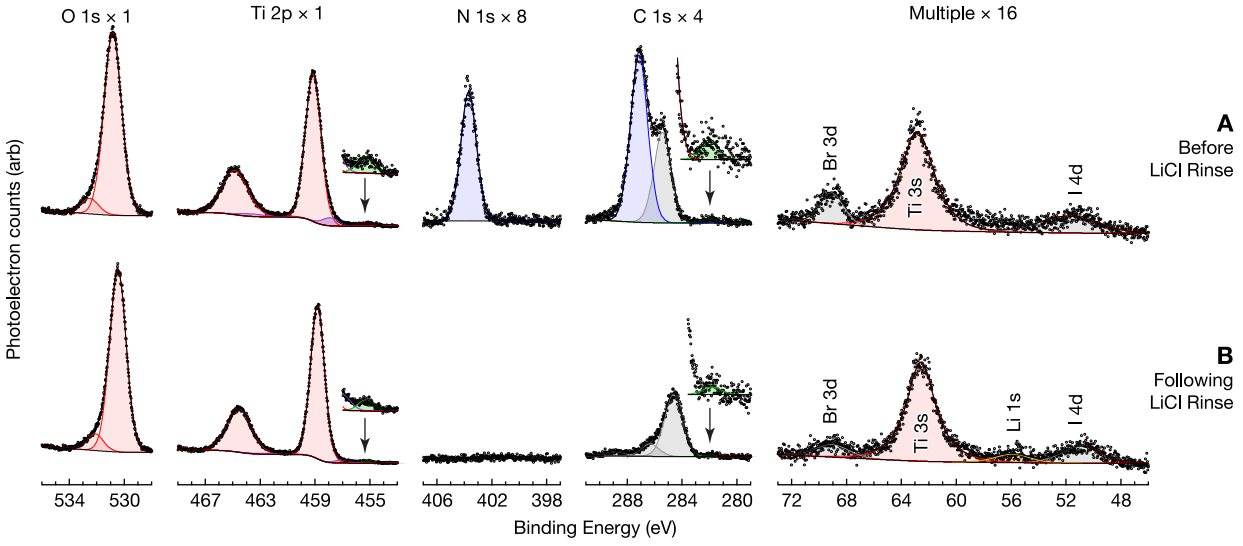

Figure 6.3. Representative XP spectra for drop-cast 1DL samples both (A) before, and (B) after LiCl rinsing. Red-shaded features are consistent with highly oxidized titanium oxides viz. Ti^{4+}, with trace purple-shaded features ascribable to Ti^{3+} at 457.0–457.8 eV. Green-shaded features and insets in the Ti 2p and C 1s region are consistent with the nominal TiC precursor. Insets represent a 5× zoom relative to their respective Ti 2p and C 1s regions. We ascribe blue-shaded features in panel (A) to residual TMA^+ cations that are exchanged with Li^+ cations during the LiCl rinse that yields the orange-shaded Li 1s feature in panel (B). Gray-shaded features are ascribable to adventitious carbon species as well as Br^- and I^- contamination in the TMAOH reagent.

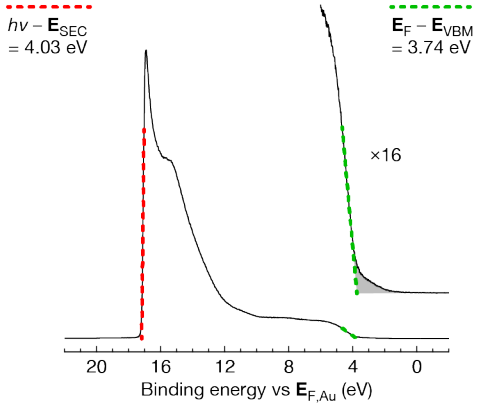

Figure 6.4. UP spectrum of a LiCl-rinsed 1DL thin film. Linear dashed fits reveal the secondary electron cutoff energy $\mathbf{E}_{SEC}$ (red dashed line) and the binding energy of the valence band maximum, $\mathbf{E}_{VBM}$, relative to its Fermi energy, $\mathbf{E}_f$. The inset spectrum on the right represents a magnified view to clarify the near-Fermi-edge density of states. Gray- shaded photoelectron counts at energies between $\mathbf{E}_{VBM}$ and $\mathbf{E}_f$ are ascribed to defect states within the band gap.

while for nine samples scanned the average was Φ = 4.0 eV with a standard deviation of 0.3 eV.

Consideration of band-edge positioning and previous UV-Vis data aids in the interpretation of Fermi regions for the UP spectra of the films studied. Revealed by the representative 16×-scaled Fermi region inset in Fig. 6.4, a green-dashed linear fit of the UP spectrum corresponds to the Fermi-level energy vs. the valence-band-maximum energy, $\mathbf{E}_f - \mathbf{E}_{VBM}$ = 3.74 eV. Interestingly, the green-dashed linear fit reveals a region of photoelectron signal that may be alternatively ascribed to photoemission from near-valence band-edge states or may be fit as the correct valence-band position itself. Considering the possibility of a different valence-band position, fitting a line above the gray-shaded photoelectron counts at binding energies between 4 eV and 1 eV would yield $\mathbf{E}_f - \mathbf{E}_{VBM}$ = 1.65 eV. Figure C.2 in the supporting information section in Appendix C, presents a fit of near-valence-edge photoemission such that $\mathbf{E}_f - \mathbf{E}_{VBM}$ = 1.65 eV that in concert with $\mathbf{E}_g$ = 4.0 eV from Fig. 6.2C and Φ = 4.0 eV imply a conduction band minimum $\mathbf{E}_{CBM}$ of –1.7 eV vs. the vacuum energy level, $\mathbf{E}^{vac}$. Such a high conduction-band maximum and small electron affinity should not be realistic for quantum-confined titanium oxides,[300] which implies that $\mathbf{E}_f - \mathbf{E}_{VBM}$ = 1.7 eV represents an erroneous fit to the Fermi-edge region of the UP spectrum. Thus, the green fitted line represents a more realistic $\mathbf{E}_f - \mathbf{E}_{VBM}$ = 3.74 with the lower-binding-energy states above the gray region resulting from near-valence-edge defects in the 1DL. For the nine samples studied, $\mathbf{E}_f - \mathbf{E}_{VBM}$ demonstrated a 3.8 eV average

with a 0.1 eV standard deviation. In concert with the UV-Vis absorption data, the UP spectra determine the band-edge positioning presented in §6.5 below to elucidate our observed transient absorption behavior of 1DL films.

In the absence of LiCl rinsing, UP spectra on films that are similar to that used for Fig. 6.3A demonstrate work function energies Φ = 2.6 eV with a standard deviation of 0.5 eV that we ascribe as erroneously low and an artifact of tetramethylammonium cations sitting above surface Ti–O^- states on 1DL nanofilaments yielding a large interfacial dipole normal to the surface. Conversely, LiCl rinsing may obviate interfacial dipoles as the small Li^+ may reside between adjacent Ti–O^- states that yield no significant dipole aligned with the surface normal angle. The exact nature of the cation-surface interaction remains the subject of ongoing study as surface dipoles demonstrate strong influences on charge transfer from valence band relevant to electrochemistry and catalysis,[301] but smaller effects on charge transfer from core levels.[259] However, we perform all subsequent transient absorption studies using LiCl-rinsed 1DL films.

Transient absorption (TA) following sub-gap optical excitation provides additional insight into the nature and lifetimes of resulting photoexcitations and energy levels for LiCl-rinsed 1DL films. Figure 6.5 shows transient-absorption kinetics and spectra following excitation with 400 nm (3.1 eV), 63.7 μJ cm^{-2} fluence, 90 fs pulses. Qualitatively similar results exist for lower energy, 485 nm (2.65 eV) excitation, but stronger pump absorption at 3.1 eV improved the signal/noise ratios. Importantly, sub-gap photoexcitation result in broadband, excited-state absorption that extends beyond our experimental window of ~1.4–2.5 eV. Photoexcited absorption is long-lived, as demonstrated by the excited absorption decay traces taken at 700 nm (1.76 eV) as well as 600 nm (2.06 eV). The behavior of excited-state absorption is essentially independent of the probe wavelength, suggesting that the broad photoinduced absorption arises from photoexcitation states that have the same origin. Decay traces can be fit to a double exponential decay with a short decay time of τ_1 = 58 ± 2 ps and a longer decay of τ_2 = 850 ± 10 ps. In addition, there is a much slower decay component that cannot be accurately determined given our experimental time window. Excited-states absorption signals decay only to >50% of the peak value by 3 ns, and persist for μs timescales as evidenced by a non-zero signal at negative times, or residual signal that does not fully recover between the time window of 10 μs between the two consecutive pump pulses.

6.5 Discussion

Both static and transient optical absorption spectroscopy reveal that our 1DL nanostructures absorb light across the visible range, owing to the presence of sub-gap states, as illustrated in Fig. 6.5. However, interpretation of tran-

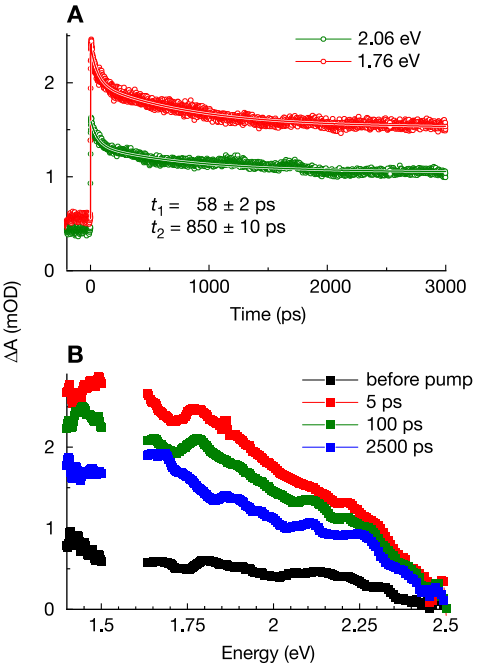

Figure 6.5. Transient absorption spectroscopy of thin 1DL films. Excited-state absorption taken at 700 nm (1.77 eV) and 600 nm (2.06 eV) in frame **A** are well described by the double-exponential-decay fits in solid lines. Transient absorption spectra in frame **B**, both prior to pump arrival (black) as well as following 5 ps (red), 100 ps (green), and 2.5 ns (blue) following excitation with 400 nm optical pulses. The nonzero differential absorption before pump arrival (black) indicates residual photoinduced absorption that persists longer than the time between two consecutive excitation pulses (10 μs).

sient absorption results presents challenges both due to the underexplored nature of 1DL material and the broad range of transient absorption results for titanium oxide in the literature. Elsewhere, TA experiments with a 350 nm (3.54 eV) pump at fluences up to 200 μJ cm^{-2} found a 3.0 ns transient-absorption decay time in single-crystal anatase, but a significantly longer 48 ns decay time in single-crystal rutile ascribed to optical absorption from photoexcited holes.[302] The presently quantified τ_2 lifetime of 850 ps in 1DL films demonstrates significantly closer agreement with the TA results for single crystal anatase. Conversely, experiments on nanocrystalline TiO_2 films demonstrated transient absorption behavior dominated by an intraband relaxation of hot holes with a lifetime longer than 100 ps following 266 nm photoexcitation.[303] Experiments on nanocrystalline TiO_2 with a 355 nm pump demonstrated transient absorption decay lifetimes of 500 ps for both a 1.54 eV probe for surface-trapped electrons and a 0.50 eV probe of bulk electrons.[304] For nanocrystalline TiO_2 films, high, 14 mJ cm^{-2} excitation fluences at 3.49 eV

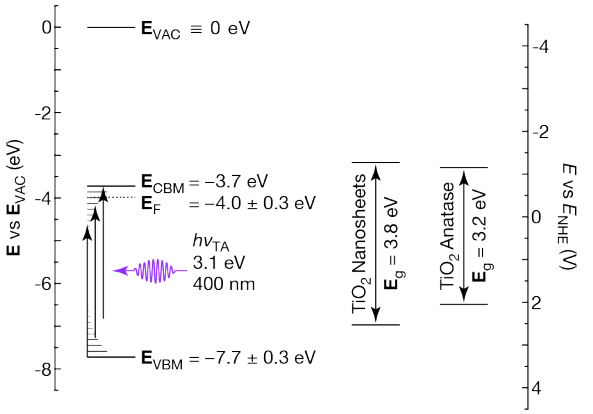

Figure 6.6. UV–Vis and UP spectra yield band-edge positions (left) for Ti-based 1DL nanofilaments vs the vacuum energy level, $\mathbf{E}^{vac}$. Observation of sub-gap excitation in transient absorption experiments implies the presence of intra-gap states that are consistent with near-valence edge defects observed in UP spectra and near-conduction-edge defects that are ascribable to the established Ti^{3+} for Ti-based 1DL nanofilaments. Comparison with literature reports of electrochemistry-derived band edges for nanosheet (middle) and anatase TiO_2 (right) from ref 37 support both the large quantum confinement in 1DLs and established offsets when comparing work functions derived from ultrahigh vacuum vs electrochemical methods per ref 39.

yielded transient absorption lifetimes of a few ns at probe energies between 0.95–1.55 eV,[305] while recent results establish an pump-fluence dependence on surface reorganization with profound impacts for the transient absorption dynamics.[306] The titanium-based 1DL filaments under study demonstrate crystallinity as revealed by the TEM in Figure 6.2A, but the structure of this material and correlations of spectroscopic results with its structure and defects remain the subject of ongoing efforts. Further, the recently updated structure[16] should enable computational insight the interplay between states, defects, band structures, and the resulting carrier dynamics for this lepidocrocite-like titanium oxide material.

Figure 6.6 presents a band energy diagram consistent with the UV-Vis, ultraviolet-photoelectron, and transient-absorption spectroscopies on the left as well as band edges for selected titanium oxide materials from the literature on the right. The UPS-determined work function yields $\mathbf{E}_f$ = –4.0 ± 0.3 eV vs. $\mathbf{E}_{vac}$ while the Fermi edge and Tauc-determined band-gap position the valence- and conduction-band edges at –7.7 ± 0.3 eV and –3.7 ± 0.3 eV, respectively. We consider the position of the Fermi energy relative to the band-edge positioning to indicate strong but not degenerate n-type doping with the Fermi level 0.2–0.3 eV or roughly 10 k_BT more negative than the conduction-band edge at the standard-state temperature. Absorption of 400 nm (3.1 eV) light implies

the existence of additional states in addition to the bands themselves. We therefore hypothesize that sub-gap states are associated with electronic defects that may result from surface states. Observation of photoelectron counts at binding energies in between the valence-band edge and the Fermi level implies the existence of defect states at least near the valence band. Such near-valence-band defect states are well precedented in the titania literature.[307] In addition to near-valence-band defect states, we cannot rule out the existence of near-conduction-band edge defect states such as arise from Ti^{3+} cations and/or oxygen vacancies as well.[308] Such Ti^{3+} defects and oxygen vacancies are notable for their implication in "black" TiO_2 in the literature,[297] and may explain the black coloration of our material. Thus, the observation of long-lived photoexcitations that yield the excited-states absorption (ESA) observed in Fig. 6.5, may be valence-defect, defect-defect, or defect-conduction transitions on the band diagram shown on the lefthand side of Fig. 6.6. Exploration of the nature of these transitions, and implications for the exceptional catalytic properties of 1DL TiO_2 remain the subject of ongoing study.

Comparison of the band edges with other TiO_2 materials further highlights the unique nature of 1DL films. The middle and righthand band edges respectively represent band-edge positions for nanosheet TiO_2 and bulk anatase as derived via electrochemical methods.[309] In Fig. 6.6, we relate electrochemical potentials, E, to energies, $\mathbf{E}$, via $-qE_{NHE} = \mathbf{E}_{NHE} = -4.44$ eV vs $\mathbf{E}_{vac}$ under standard conditions based on IUPAC recommendations.[310] Comparison with the 3.8 eV band gap for the nanosheet films,[309] 1DL films demonstrate a higher degree of quantum confinement resulting in their ~4.0 eV band gap. Notably, the band-edge positions for the literature TiO_2 reports in the middle and righthand side are offset as compared to the presently reported band edges for 1DL films on the lefthand side of Fig. 6.6. However, such offsets are consistent with discrepancies between work functions acquired via ultrahigh vacuum vs electrochemical methods.[66]

In summary, we report the properties of photoexcitations in a new class of lepidocrocite-like titania-based nanostructures and relate the nature of sub-gap excitation to band and defect structures. Important questions remain underlying the mechanism of synthesis, the presence of chemical defects, as well as the nature of light-emitting states. However, the scalability and ease of synthesis using common solvents such as TMAOH, and precursors such as TiC, TiB_2 etc., their extraordinary surface area, and exceptionally long-lived photoexcitations that can be excited with visible, sub-gap light, raise exciting prospects of application in solar energy conversion and visible optoelectronic devices among others.

CHAPTER 7

CONCLUSIONS AND FUTURE WORK

7.1 BiOI for Photovoltaics and Photocatalysis

The present work surrounding single-crystal BiOI for applications in solar energy and photocatalysis was primarily focused on quantifying the interfacial chemical and electronic states present at the (001) face as well as characterizing the interplay between these states as a function of various chemical treatments. XPS and XRD reveal the presence of interfacial contaminants for BiOI(001) large grains and single crystals that influence the work function of the material as quantified by UPS. In combination with a quantized numerical overlayer model, angle-resolved XPS further elucidated a (001) surface dominated by oxide terminations relative to the bulk material for nascent, as-grown material. Herein as detailed in Chapter 4, we demonstrated a that sequential treatment with $HF_{(aq)}$ and subsequent sonication in acetone removes interfacial metal-oxides and trace contaminants to yield an iodide-dominated surface with comparable chemical and electronic quality to "pristine" tape-cleaved BiOI interfaces. This is impactful for the ability to overcome the mechanical constraints of traditional exfoliation methods such

as tape cleaving. Nonetheless, robust parameterization is necessary to extend this chemical cleaning protocol to device-relevant nanostructured BiOI systems.

Preliminary experiments to extend this protocol for nanostructured BiOI employed chemical vapor synthesis of BiOI thin-films on FTO from BiI_3 reagent powder with continuous O_2 flow based on previously established procedures.[159] Exposure of the resulting BiOI thin films to dilute solutions of HF, ~0.01–1%, led to complete dissolution of the material within seconds of exposure yielding a pale yellow solution. Similarly, in our hands a large-grain BiOI flake sitting in 10% $HF_{(aq)}$ dissolves over the course of a few minutes to yield a yellow solution. More parameterization is needed in terms of suitable dilution factors for nanostructured BiOI. Moreover, the mechanism of HF etching for this particular material remains largely unexplored. A first step toward informing the best approach for thoroughly elucidating the kinetic and thermodynamic forces behind the mechanism may employ ICP-MS metals analysis on the post-HF-etch solution to quantify the chemical species formed from the dissolution of BiOI.

Beyond HF-etching, we also demonstrated that in vacuo CVT syntheses at high temperatures (ΔT >100 °C) yield single-crystal and large-grain BiOI with two distinct surface morphologies at the (001) face, terrace-rich and step-edge rich domains. As evidenced by XPS and XRD, HF-etching studies revealed that these morphologies exhibit orthogonal reactivities. XP spectra for step-rich domains demonstrate the presence of Bi–F species that are not observed for terrace-rich domains and XRD reveals crystalline BiI_3 for step-rich samples that are not observed for terrace-rich samples. For some 2D materials, the presence of step edges have demonstrated performance-limiting implications for the overall mechanical properties[218–219] or recombination dynamics.[215–217] Nonetheless, in other cases, step-edge densities have contributed favorably to photoelectrochemical behavior.[211–214] In the case of BiOI, the implications of these two distinct surface morphologies for practical applications in photovoltaics, photocatalysis, and solar water splitting remains unclear. Scanning photocurrent microscopy (SPCM) measurements enable mapping of the photocurrent densities across the (001) face. This may help elucidate the photocatalytic activities of step-rich versus-terrace rich domains to inform synthesis protocols for yielding the material most suitable for practical applications in energy storage and conversion and photocatalysis.

Beyond chemical reactivity, most literature reports favor BiOI for its low-toxicity and supposed robust atmospheric stability. Nonetheless, in our hands, initial optical studies surrounding vapor-transport-synthesized BiOI large grains and single crystals suggest photooxidative stability issues. Preliminary photoluminescence (PL) spectroscopy measurements as in Fig. 7.1 demonstrate quenching of the characteristic ~1.8 eV feature for BiOI as a function of total pulses delivered with successive scans under an air ambient.

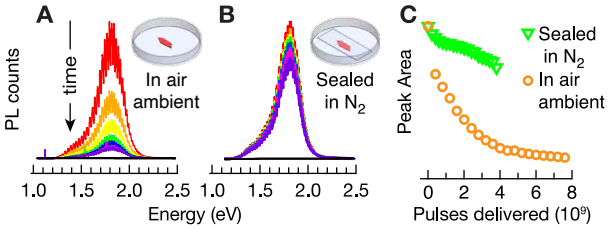

Figure 7.1. Successive photoluminescence spectra for a BiOI sample **A** in air ambient and **B** isolated in nitrogen. Frame **C** plots peak areas of the photoemission at 1.8 eV for A and B as a function of total pulses delivered.

Alternatively, for BiOI samples sealed in a nitrogen-sealed environment with O_2 concentrations <1 ppm, the optical emission of the ~1.8 eV feature with time-controlled successive scans is comparably much more stable.

For energy applications like photovoltaics, robust atmospheric stability is critical to achieve high efficiencies and long device lifetimes. As such, future studies surrounding BiOI for energy applications should address this issue and be aimed toward passivation against photooxidative degradation. Based on similar approaches for other commonly explored materials, we hypothesized that passivating ALD-deposited metal-oxide thin films may aid in suppressing surface oxidation. Our initial studies demonstrate that ALD-deposited TiO_2 were not sufficient to minimize quenching during PL measurements. It is likely that successful passivation necessitates a thermal anneal. In our hands, initial attempts at thermal annealing deleteriously degraded the chemical structure of BiOI. More parameterization is needed to achieve passivation with ALD-deposited metal oxides and other avenues for passivation that may be more successful have not yet been addressed. Moreover, the mechanism and timescales of atmospheric degradation remains largely underexplored. It is possible that quantification of the carrier dynamics as a function of incident exposure in the visible range may yield timescales of degradation that are reasonable for the lifetime constraints of practical devices. Quantitative investigation of the degradation mechanism for BiOI would better inform, or even negate, passivation strategies for this material.

7.2 Ti-Based MXenes for chemical and biological sensing, electromagnetic interference shielding, and as barrier materials

MXenes are an attractive 2D material most notably for their exceedingly high electrical conductivities reaching 20,000 S cm^{-1}.[8] This makes them attractive candidate materials for applications in chemical and biological sensing,[178–183] energy storage and conversion, and electromagnetic shielding.[9–10] Our present

funding source for MXene studies is a collaboration with a research group at the Natick Soldier Center under the Department of Defense, DOD. As such, our current explorations primarily consider the utility of MXenes for applications in selective sensing of chemical warfare agents and electromagnetic interference shielding as well as for barrier materials in personal protective gear. In such instances, robust control over the optical and electronic properties is highly favorable. As detailed in Chapter 5 of this thesis, we demonstrated that $Ti_3C_2T_x$ functionalized with various organosilanes exhibit distinct optical behavior and carrier dynamics as evidenced by THz and TA spectroscopy as well as work function shifts revealed by UPS compared to nascent $Ti_3C_2T_x$ with mixed –OH/F interfacial terminations. Given the surface –O and –OH terminations for nascent MXene that are amenable to functionalization, we demonstrate that silanization at interfacial hydroxyl sites can straightforwardly effect these electronic changes based on molecular-induced surface dipoles. Moreover, questions remain surrounding the correlation between work-function values and the related photoconductivity, which may both be largely influenced by surface dipoles for MXenes. Initial DFT calculations suggest localization of photoconductivity at the surfaces of 2D MXenes. Interfacial dipoles, whether they arise from native –O and –F terminations or from covalent overlayers, effect changes in local carrier densities from the material. We expect this holds implications both for relative work-function values as well as for localization of photoconductivity for the MXene sheets. It is possible interfacial dipoles may drive carrier away from the surface and closer to the middle of the MXene sheets, or it may be the case that carriers from the middle-layer titanium are driven toward the surface. The effects on carrier localization remain largely under-investigated in the present studies. A combination of DFT studies with UP-determined work-function values will better elucidate the relationship between the magnitude and directionality of interfacial dipoles and work-function values. Separately, we encourage DFT calculations on MXenes as a function of organic-derivatized surfaces and THz photoconductivity measurements to build relationships between surface dipoles and the resulting carrier dynamics. Because work function is a straightforward method to quantify surface dipole changes, we hope that work function changes become a strong predictor of carrier dynamics for organic-functionalized MXene systems. Moreover, while we demonstrated the utility of molecular dipoles from organic monolayers for imparting optoelectronic tunability, the implications for sensing applications in practical devices remains underexplored. Additionally, in the context of chemical sensing, more research is needed to quantify the interplay between interfacial molecular dipoles and the resulting impact on selectivity and sensitivity toward specific gaseous analytes.

Beyond electronic tunability, functionalization with molecular organics should also enable tunability of the terminal chemical functionality. Secondary derivatization at terminal allyl or amino sites can install selective chemical

handles for selective adsorption of analytes in the context of sensing applications. Additionally, based on our studies surrounding organic monolayers as connectors between dissimilar inorganic materials,[25,96,229] we further hypothesize that covalent derivatization with molecular organics should enable robust, chemical linkages between adjacent MXene sheets to improve conductivity and carrier transport for energy and sensing applications. Previous studies in our lab surrounding covalent functionalization of SiO_x surfaces for tandem-junction PV applications were motivated by this same rationale and demonstrate remarkable promise.[25,96] We employed highly-conjugated, tunable rylene derivatives with the long-term goal of enabling covalent attachment between dissimilar materials in multi-junction PV systems to improve carrier transport and selectivity. We envision future studies for MXenes to borrow this approach for installing chemically tailored handles for selective sensing applications as well as cross-linking adjacent MXene sheets for improved conductivity. As is the case for many 2D layered materials, nascent MXenes demonstrate exceedingly higher conductivities along their in-plane axis compared to carrier transport between stacked, adjacent 2D sheets. As such, edge-to-edge covalent, molecular linkages connecting MXene sheets at their high-conductivity axes may improve carrier dynamics for energy applications that rely on highly efficient carrier transport and charge separation. Moreover, cross-linking of MXene sheets in the context of incorporation into flexible polymer matrices may also improve their barrier capabilities against chemical warfare agents, which largely motivate our DOD-funded research efforts for this project. Beyond organosilanes, functionalization with catechol derivatives have recently been explored for applications involving polymer incorporation.[198] Moreover, based on reports surrounding other materials with oxidative stability issues, polymer-MXene composites may also demonstrate improved atmospheric stability and this should be explored concurrently with parameterizing and quantifying polymer incorporation for barrier material applications.

Beyond functionalization for chemical and electronic control, many MXenes tend to suffer from atmospheric stability issues that limit practical applications. A large portion of MXene literature is directed toward addressing these oxidative stability problems, but many rely on harsh conditions that may not be scalable. Based on the precedence of passivation of H–Si(111) interfaces with sterically bulky organic monolayers, it is possible that molecular approaches may be suitable in the case of MXenes. Practical applications would certainly rely on robust atmospheric stability. Nonetheless, our experimental efforts with a view toward energy and sensing applications thus far were largely directed toward imparting electronic and chemical tunability. Since ample reports surrounding silicon surface science has demonstrated the utility of molecular interfacial dipoles for controlling electronic and optical behavior, we are presently motivated to explore similar approaches for this promising 2D material. Our functionalization efforts so far have pri-

marily quantified the chemical and optoelectronic implications, but similar molecular approaches with a view toward passivation remains largely underexplored. Future studies employing covalent attachment of organics should concurrently probe the oxidative stability of the derivatized material as a function of overlayer coverage as well as characterize the interplay between the interfacial chemical changes and the subsequent optical behavior and carrier dynamics resulting from relative changes in oxidative stability.

7.3 Ti-based 1DL for Photocatalytic, Photoelectrochemical, or Battery Applications

Contrary to BiOI and MXenes, Ti-based 1DL QDNs demonstrate remarkable oxidative stability. Preliminary studies demonstrate that films of the Ti-based 1DL material demonstrate good performance as electrodes in lithium-ion and lithium-sulfur systems, as well as excellent oxidative stability.[17] They are also quite good at photocatalytically producing hydrogen, H_2. As detailed in Chapter 6, our optical studies demonstrate a quantum-confined material, as evidenced by the wide bang-gap energy of 4.0 eV, which holds implications for unique optoelectronic properties advantageous for energy storage and catalysis applications. Nonetheless, widespread application of the 1DL material necessitate robust quantification of the exact chemical and electronic states present at the surface of this emerging class of material. While it has been demonstrated that at lower synthesis temperatures (below 50 °C) or at low concentrations, the one-dimensional nanofilaments are capable of self-alignment into pseudo 2D sheets,[16] the driving force for this aggregation and the optoelectronic implications of these distinct morphologies remains underexplored. In addition, while we have probed the electronic structure of this material to yield the first report of energetic band structure for 1DLs as presented in Fig. 7.2B, questions remain regarding some of the relative band positions. As discussed in the supporting information section for Chapter 6 in Appendix C, UPS-based determination of band structure for this particular material presents some ambiguity specifically in linear fitting at the Fermi edge. Electrochemical approaches to probing the electronic structure of 1DLs may better inform interpretation of UPS-determined band edges and grant some clarity regarding the best linear fit at the high-kinetic-energy Fermi edge. Moreover, we envision success of 1DLs as barrier materials, and as such, studies surrounding MXenes for polymer incorporation should also consider similar molecular approaches for Ti-based 1DL as well.

In our studies, we attribute long-lived visible photoexcitations to intraband Ti^{3+} and oxygen vacancy states which is largely supported by UV-Vis and XANES studies in initial reports surrounding the 1DL titania that demonstrate Ti^{3+} defects.[17] We also observe trace features consistent with Ti^{3+} binding-energy positioning in XPS for 1DL titania which further support

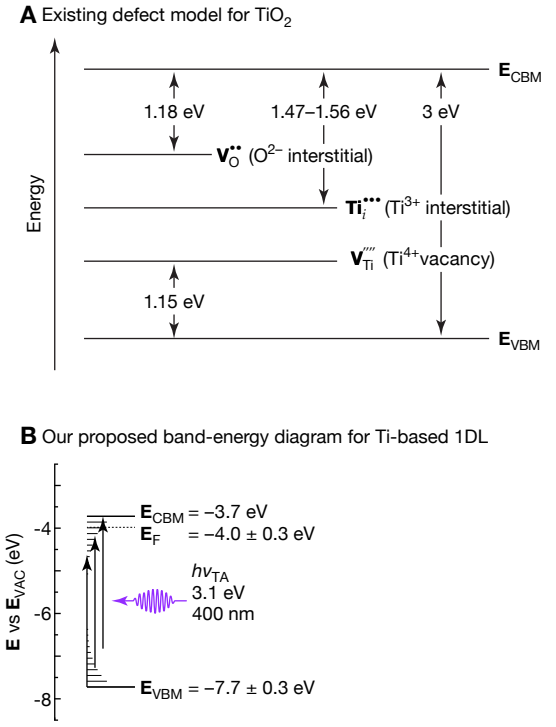

Figure 7.2. Band diagrams for A, the existing defect model for titania and B, our proposed band-energy alignment for our 1DL titania based on UV-Vis and UP spectroscopy. Titanium vacancies lie closer to the valence band, interstitial oxygen sites lie closer to the conduction band, while interstitial Ti^{3+} reside mid gap.

these considerations. As demonstrated in Fig. 7.2A, defect engineering for other polymorphs of TiO_2 is well investigated.[204b] Generally, titanium vacancies lie closer to the valence band, interstitial oxygen sites lie closer to the conduction band, while interstitial Ti^{3+} reside mid gap. Fig. 7.2B further presents our band-energy alignment for the 1DL material based on UV-Vis and UP spectroscopy. While we have demonstrated long-lived sub-gap photoexcitations likely originating from defect states within the band gap, the origin, dynamics, and localization of these defects remain largely unexplored. Nascent, undoped TiO_2 is often non-stoichiometric and oxygen vacancies dominate relative defect concentrations. Our results in combination with initial reports by Barsoum et al.[17] do support the existence of Ti^{3+} defects and it is reasonable to assume some concentration of oxygen vacancies based on reports for other nascent titania synthesized solvothermally, but more work is needed to strengthen these initial postulations. Further, it is well known that thermal annealing of titania under an air ambient can heal oxygen vacancies and oxidize Ti^{3+} and defects while hydrogenation in a high-pressure reducing

environment can selectively dope these defect concentrations.[204b,297]. Given that such manipulations often effect changes in optoelectronic properties and photoexcitation dynamics based on "black" titania literature, it is critical to further probe these considerations and explore the implications for photocatalysis. A set of experiments that would strongly support and inform our results would involve manipulation of defect concentrations for our 1DL titania via known defect engineering procedures and subsequent characterization with XPS, UPS, Raman, TA, and THz. We anticipate these systematic studies to broaden our insight into the interplay between defect states and optoelectronic properties of the 1DL titania as well as inform the implications for photocatalytic efficiencies in collaboration with the Barsoum group's photocatalytic H_2 production experiments. Additionally, lepidocrocite TiO_2 can readily convert to anatase under acidic conditions or high temperatures. It would also be interesting to probe the interplay between changes in Ti^{3+} and the lepidocrocite-anatase conversion as a function of temperature.

It is also critical to elucidate a fundamental understanding of the carrier dynamics and mobilities for the 1DL titania material. The first report surrounding this emerging 1D titania included DFT calculations based on a 1-dimensional anatase structure that should yield insight into local conductivity.[17] Nonetheless, updated calculations with the new insight of a lepidocrocite structured titania have not yet been explored. We envision that a combination of updated DFT calculations based on 1D lepi-titania with electrochemistry studies and four-point probe conductivity measurements should reveal bulk and sheet resistivities for films of the 1DL titania with well-defined thicknesses.

Additionally, preliminary functionalization efforts for Ti-based 1DL with organosilanes demonstrate exceedingly strong reactivities as evidence by high surface coverages in XPS over short reaction times (<3 h). More parameterization is needed to establish suitable attachment conditions for monolayer coverages. Beyond that, it is also critical to further explore the interplay between surface dipoles from intercalated cations as well as for organic-derivatized 1DL material. We have demonstrated based on UP-determined work-function values that interfacial TMA^+ yields a strongly negative surface dipole for the 1DL titania while interfacial Li^+ does not. While the nature of the cation intercalation has not been probed extensively in these studies thus far, Fig. 7.3 graphically demonstrates our interpretation of the interfacial interactions between the 1DL titania surfaces and adsorbed cations. We hypothesize that due the relative size, tetramethylammonium cations may not sufficiently intercalate toward the backbone of the titania and instead sit above the $-O^-$ sites. The resulting spatial localization of charges would likely yield a negative dipole at the 1DL surface and subsequently smaller Φ values which is consistent with our preliminary Φ values for TMA^+-containing material. Comparably smaller Li^+ cations may intercalate more closely toward the backbone of the 1DL titania and sit between adjacent $-O^-$ sites therefore

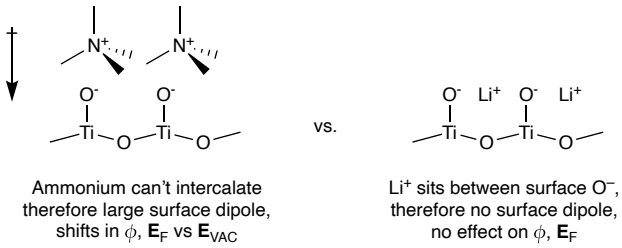

Figure 7.3. For an envisioned Ti−O^- surface for 1DL titania, we hypothesize that TMA^+ cations can't intercalate given their size, while smaller Li^+ cations can intercalate and reside between surface O^- sites.

yielding no net dipole and subsequently not effecting changes in Φ. We do not yet have robust experimental or computational evidence for these postulations, but we see this as a model that largely fits the data so far. We envision that DFT calculations with updated lepidocrocite structures modeling intercalated cations and covalent organic monolayers will better characterize the interplay between surface dipoles and resulting changes in Φ. Additionally, cation-exchange studies for 1DL titania surrounding a number of monovalent and divalent cations and their implications for photocatalytic efficiencies are already underway in the Barsoum lab. We envision contributing to these investigations with UPS studies to correlate those changes in photocatalysis dynamics with interfacial dipole behavior.

While we have investigated the band-energy alignment and transient state dynamics for LiCl-rinsed 1DL titania, it is critical to further probe resulting changes in the optoelectronic properties for the TMA^+-intercalated 1DL material. We would expect the strongly negative surface dipole for TMA^+-intercalated 1DL titania to effect changes in the carrier densities in the material, but it remains unclear whether the dipoles would drive carriers away from the surface toward middle-layer Ti, or instead drive carriers from the middle-layer Ti toward the surface. Further, surface dipoles may affect the localization of Ti^{3+} and oxygen vacancy states which may hold implications for optical properties and transient state dynamics. If our first idea at a model for TMA^+ versus Li^+ intercalation is correct, it would be reasonable to expect that larger cations that similarly face issues intercalating between adjacent $-O^-$ sites would yield some degree of a surface dipole that should influence the optoelectronic properties and carrier dynamics. For investigations surrounding other intercalations in collaboration with the Barsoum lab, it will be important to consider cation size relative to the spacing between adjacent $-O^-$ sites amidst considerations of these results. We envision further UV-Vis, UPS, and TA studies probing band structure and transient state dynamics for the TMA^+-intercalated 1DL titania to provide critical insight into the nature of the surface dipole and its subsequent effects on the optoelectronic properties

of the material. We would also envision probing relative resistivities for 1DL titania films of well-controlled thicknesses electrochemically and with four-point probe measurements as a function of cation-induced surface dipoles to further inform these interpretations.

CHAPTER 8

REFERENCES

1. May, J. W., Platinum surface LEED rings. *Surf. Sci.* **1969**, 17, 267–270.

2. Novoselov, K. S.; Geim, A. K.; Morozov, S. V.; Jiang, D.; Zhang, Y.; Dubonos, S. V.; Grigorieva, I. V.; Firsov, A. A., Electric Field Effect in Atomically Thin Carbon Films. *Science* **2004**, *306*, 666-669.

3. Zhang, X.; Hou, L.; Ciesielski, A.; Samorì, P., 2D Materials Beyond Graphene for High-Performance Energy Storage Applications. *Adv. Energy Mater.* **2016**, *6*, 1600671.

4. Gupta, A.; Sakthivel, T.; Seal, S., Recent development in 2D materials beyond graphene. *Progress in Materials Science* **2015**, *73*, 44–126.

5. Butler, S. Z.; Hollen, S. M.; Cao, L.; Cui, Y.; Gupta, J. A.; Gutiérrez, H. R.; Heinz, T. F.; Hong, S. S.; Huang, J.; Ismach, A. F.; Johnston-Halperin, E.; Kuno, M.; Plashnitsa, V. V.; Robinson, R. D.; Ruoff, R. S.; Salahuddin, S.; Shan, J.; Shi, L.; Spencer, M. G.; Terrones, M.; Windl, W.; Goldberger, J. E., Progress, Challenges, and Opportunities in Two-Dimensional Materials Beyond Graphene. *ACS Nano* **2013**, *7*, 2898–2926.

6. Bhimanapati, G. R.; Lin, Z.; Meunier, V.; Jung, Y.; Cha, J.; Das, S.; Xiao, D.; Son, Y.; Strano, M. S.; Cooper, V. R.; Liang, L.; Louie, S. G.; Ringe, E.; Zhou, W.; Kim, S. S.; Naik, R. R.; Sumpter, B. G.; Terrones, H.; Xia, F.; Wang, Y.; Zhu, J.; Akinwande, D.; Alem, N.; Schuller, J. A.; Schaak, R. E.; Terrones, M.; Robinson, J. A., Recent Advances in Two-Dimensional Materials beyond Graphene. *ACS Nano* **2015**, *9*, 11509–11539.

7. Naguib, M.; Mochalin, V. N.; Barsoum, M. W.; Gogotsi, Y., 25th Anniversary Article: MXenes: A New Family of Two-Dimensional Materials. *Adv. Mater.*. **2014**, *26*, 992–1005.

8. Naguib, M.; Barsoum, M. W.; Gogotsi, Y., Ten Years of Progress in the Synthesis and Development of MXenes. *Adv. Mater.*. **2021**, *33*, 2103393.

9. Iqbal, A.; Kwon, J.; Kim, M. K.; Koo, C. M., MXenes for electromagnetic interference shielding: Experimental and theoretical perspectives. *Materials Today Advances* **2021**, *9*, 100124.

10. Han, M.; Shuck, C. E.; Rakhmanov, R.; Parchment, D.; Anasori, B.; Koo, C. M.; Friedman, G.; Gogotsi, Y., Beyond $Ti_3C_2T_x$: MXenes for Electromagnetic Interference Shielding. *ACS Nano* **2020**, *14*, 5008–5016.

11. Zhu, J.; Ha, E.; Zhao, G.; Zhou, Y.; Huang, D.; Yue, G.; Hu, L.; Sun, N.; Wang, Y.; Lee, L. Y. S.; Xu, C.; Wong, K.-Y.; Astruc, D.; Zhao, P., Recent advance in MXenes: A promising 2D material for catalysis, sensor and chemical adsorption. *Coordination Chemistry Reviews* **2017**, *352*, 306–327.

12. Peng, J.; Chen, X.; Ong, W.-J.; Zhao, X.; Li, N., Surface and Heterointerface Engineering of 2D MXenes and Their Nanocomposites: Insights into Electro- and Photocatalysis. **Chem** *2019*, *5*, 18–50.

13. Anasori, B.; Lukatskaya, M. R.; Gogotsi, Y., 2D metal carbides and nitrides (MXenes) for energy storage. *Nature Reviews Materials* **2017**, *2*, 16098.

14. Cao, F.; Zhang, Y.; Wang, H.; Khan, K.; Tareen, A. K.; Qian, W.; Zhang, H.; Ågren, H., Recent Advances in Oxidation Stable Chemistry of 2D MXenes. *Adv. Mater.* **2022**, *34*, 2107554.

15. Natu, V.; Hart, J. L.; Sokol, M.; Chiang, H.; Taheri, M. L.; Barsoum, M. W., Edge Capping of 2D-MXene Sheets with Polyanionic Salts To Mitigate Oxidation in Aqueous Colloidal Suspensions. *Angew. Chem. Int. Ed.* **2019**, *58*, 12655–12660.

16. Badr, H. O.; Lagunas, F.; Autry, D.; Cope, J.; Kono, T.; Klie, R.; Hu, Y.-J.; Barsoum, M. W., On the Structure of One-Dimensional TiO_2 Lepidocrocite. *Matter* **2023**, in press.

17. Badr, H. O.; El-Melegy, T.; Carey, M.; Natu, V.; Hassig, M. Q.; Johnson, C.; Qian, Q.; Li, C. Y.; Kushnir, K.; Colin-Ulloa, E.; Titova, L. V.; Martin,

J. L.; Grimm, R. L.; Pai, R.; Kalra, V.; Karmakar, A.; Ruffino, A.; Masiuk, S.; Liang, K.; Naguib, M.; Wilson, O.; Magenau, A.; Montazeri, K.; Zhu, Y.; Cheng, H.; Torita, T.; Koyanagi, M.; Yanagimachi, A.; Ouisse, T.; Barbier, M.; Wilhelm, F.; Rogalev, A.; Björk, J.; Persson, P. O. Å.; Rosen, J.; Hu, Y.-J.; Barsoum, M. W., Bottom-Up, Scalable Synthesis of Anatase Nanofilament-Based Two-Dimensional Titanium Carbo-Oxide Flakes. *Mater. Today* **2022**, 54, 8–17.

18. Ulman, A., Formation and Structure of Self-Assembled Monolayers. *Chem. Rev*. **1996**, *96*, 1533–1554.

19. Subramanian, A.; Kennel, S. J.; Oden, P. I.; Jacobson, K. B.; Woodward, J.; Doktycz, M. J., Comparison of techniques for enzyme immobilization on silicon supports. *Enzyme and Microbial Technology* **1999**, *24*, 26-34.

20. Faucheux, N.; Schweiss, R.; Lützow, K.; Werner, C.; Groth, T., Self-assembled monolayers with different terminating groups as model substrates for cell adhesion studies. *Biomaterials* **2004**, *25*, 2721-02730.

21. Weetall, H. H., Preparation of immobilized proteins covalently coupled through silane coupling agents to inorganic supports. *Applied Biochemistry and Biotechnology* **1993**, *41*, 157-188.

22. McAlpine, M. C.; Ahmad, H.; Wang, D.; Heath, J. R., Highly ordered nanowire arrays on plastic substrates for ultrasensitive flexible chemical sensors. *Nature Materials* **2007**, *6*, 379-384.

23. Chaki, N. K.; Vijayamohanan, K., Self-assembled monolayers as a tunable platform for biosensor applications. *Biosens. Bioelectron.* **2002**, *17*, 1–12.

24. Li, Z.; Guo, J.; Li, Z.; Han, W.; Ren, G.; Liu, C.; Shen, L.; Guo, W., Incorporating self-assembled silane-crosslinked carbon dots into perovskite solar cells to improve efficiency and stability. *J. Mater. Chem. A* **2020**, *8*, 5629–5637.

25. Carl, A. D.; Grimm, R. L., Covalent Attachment and Characterization of Perylene Monolayers on Si(111) and TiO_2 for Electron-Selective Carrier Transport. *Langmuir* **2019**, *35*, 9352–9363.

26. Chen, H.; Wang, J.; Huo, Q., Self-assembled monolayer of 3-aminopropyltrimethoxysilane for improved adhesion between aluminum alloy substrate and polyurethane coating. *Thin Solid Films* **2007**, *515*, 7181–7189.

27. Yu, J.; Li, W.; Zhang, K.; Han, X., Performance enhancement of all-inorganic carbon-based CsPbI2Br solar cells by using silane modification. *Journal of Materials Science: Materials in Electronics* **2021**, *32*, 20936–020945.

28. Choi, K.; Choi, H.; Min, J.; Kim, T.; Kim, D.; Son, S. Y.; Kim, G.-W.; Choi, J.; Park, T., A Short Review on Interface Engineering of Perovskite Solar

Cells: A Self-Assembled Monolayer and Its Roles. *Solar RRL* **2020**, *4*, 1900251.

29. Colak, B.; Di Cio, S.; Gautrot, J. E., Biofunctionalized Patterned Polymer Brushes via Thiol–Ene Coupling for the Control of Cell Adhesion and the Formation of Cell Arrays. *Biomacromolecules* **2018**, *19*, 1445–1455.

30. Yoon, S.-H.; Mofrad, M. R. K., Cell adhesion and detachment on gold surfaces modified with a thiol-functionalized RGD peptide. *Biomaterials* **2011**, *32*, 7286–7296.

31. Tähkä, S.; Sarfraz, J.; Urvas, L.; Provenzani, R.; Wiedmer, S. K.; Peltonen, J.; Jokinen, V.; Sikanen, T., Immobilization of proteolytic enzymes on replica-molded thiol-ene micropillar reactors via thiol-gold interaction. *Anal. BioAnal. Chem.* **2019**, *411*, 2339–2349.

32. Afrin, R.; Shah, N. A., Room temperature gas sensors based on carboxyl and thiol functionalized carbon nanotubes buckypapers. *Diamond Relat. Mater.* **2015**, *60*, 42–49.

33. Peng, H.; Chen, W.; Cheng, Y.; Hakuna, L.; Strongin, R.; Wang, B. Thiol Reactive Probes and Chemosensors. *Sensors* **2012**, 10.3390/s121115907.

34. Zhao, X.; Zhou, L.; Zhang, W.; Hu, C.; Dai, L.; Ren, L.; Wu, B.; Fu, G.; Zheng, N., Thiol Treatment Creates Selective Palladium Catalysts for Semihydrogenation of Internal Alkynes. *Chem* **2018**, *4*, 1080–1091.

35. Hagberg, E. C.; Malkoch, M.; Ling, Y.; Hawker, C. J.; Carter, K. R., Effects of Modulus and Surface Chemistry of Thiol-Ene Photopolymers in Nanoimprinting. *Nano Lett*. **2007**, *7*, 233–237.

36. Carlborg, C. F.; Haraldsson, T.; Öberg, K.; Malkoch, M.; van der Wijngaart, W., Beyond PDMS: off-stoichiometry thiol–ene (OSTE) based soft lithography for rapid prototyping of microfluidic devices. *Lab Chip* **2011**, *11*, 3136–3147.

37. Notsu, H.; Kubo, W.; Shitanda, I.; Tatsuma, T., Super-hydrophobic/super-hydrophilic patterning of gold surfaces by photocatalytic lithography. *J. Mater. Chem.* **2005**, *15*, 1523–1527.

38. Nakashima, N.; Taguchi, T., pH-Sensitive phosphate lipid self-assembled monolayers on gold. *Colloids Surf., A* **1995**, *103*, 159–165.

39. Gao, W.; Dickinson, L.; Grozinger, C.; Morin, F. G.; Reven, L., Self-Assembled Monolayers of Alkylphosphonic Acids on Metal Oxides. *Langmuir* **1996**, *12*, 6429–6435.

40. Spori, D. M.; Venkataraman, N. V.; Tosatti, S. G. P.; Durmaz, F.; Spencer, N. D.; Zürcher, S., Influence of Alkyl Chain Length on Phosphate Self-Assembled Monolayers. *Langmuir* **2007**, *23*, 8053–8060.

41. Li, M.; Chen, H.; Li, S.; Wang, G.; Wei, F.; Guo, X.; Tu, H., Active Self-Assembled Monolayer Sensors for Trace Explosive Detection. *Langmuir* **2020**, *36*, 1462–1466.

42. Wang, G.; Li, M.; Wei, Q.; Xiong, Y.; Li, J.; Li, Z.; Tang, J.; Wei, F.; Tu, H., Design of an AIE-Active Flexible Self-Assembled Monolayer Probe for Trace Nitroaromatic Compound Explosive Detection. *ACS Sensors* **2021**, *6*, 1849–1856.

43. Kaufmann, C.; Mani, G.; Marton, D.; Johnson, D.; Agrawal, C. M., Long-term stability of self-assembled monolayers on electropolished L605 cobalt chromium alloy for stent applications. *J. Biomed. Res., B* **2011**, *98B*, 280–289.

44. DiBenedetto, S. A.; Facchetti, A.; Ratner, M. A.; Marks, T. J., Molecular Self-Assembled Monolayers and Multilayers for Organic and Unconventional Inorganic Thin-Film Transistor Applications. *Adv. Mater*. **2009**, *21*, 1407–1433.

45. Liu, Y.; Zhou, J.; Zhang, X.; Liu, Z.; Wan, X.; Tian, J.; Wang, T.; Chen, Y., Synthesis, characterization and optical limiting property of covalently oligothiophene-functionalized graphene material. *Carbon* **2009**, *47*, 3113–3121.

46. Yu, D.; Yang, Y.; Durstock, M.; Baek, J. B.; Dai, L., Soluble P3HT-grafted graphene for efficient bilayer-heterojunction photovoltaic devices. *ACS Nano* **2010**, *4*, 5633–5640.

47. Greene, J. E., Review Article: Tracing the recorded history of thin-film sputter deposition: From the 1800s to 2017. *J. Vac. Sci. Technol. A* **2017**, *35*, 05C204.

48. Georgakilas, V.; Otyepka, M.; Bourlinos, A. B.; Chandra, V.; Kim, N.; Kemp, K. C.; Hobza, P.; Zboril, R.; Kim, K. S., Functionalization of Graphene: Covalent and Non-Covalent Approaches, Derivatives and Applications. *Chem. Rev.* **2012**, *112*, 6156-6214.

49. Zhang, J. L.; Ye, X.; Gu, C.; Han, C.; Sun, S.; Wang, L.; Chen, W., Non-covalent interaction controlled 2D organic semiconductor films: Molecular self-assembly, electronic and optical properties, and electronic devices. *Surf. Sci. Rep.* **2020**, *75*, 100481.

50. Shafi, M. A.; Bouich, A.; Fradi, K.; Guaita, J. M.; Khan, L.; Mari, B., Effect of deposition cycles on the properties of ZnO thin films deposited by spin coating method for CZTS-based solar cells. *Optik* **2022**, *258*, 168854.

51. Choy, W. C. H.; Zhang, D., Solution-Processed Metal Oxides as Efficient Carrier Transport Layers for Organic Photovoltaics. *Small* **2016**, *12*, 416–431.

52. Hertz, H., Electric Waves; Macmillan: S.L., 1893.

53. Hofmann, S.; Auger- and X-Ray Photoelectron Spectroscopy in Materials Science: A User-Oriented Guide, 1st ed.; Springer Berlin Heidelberg, Imprint: Springer: Berlin, Heidelberg, **2013**.

54. Hofmann, S., Sputter depth profiling: past, present, and future. *Surf. Interface Anal.* **2014**, *46*, 654–662.

55. Tarng, M. L.; Wehner, G. K., Alloy Sputtering Studies with in situ Auger Electron Spectroscopy. *J. Vac. Sci. Technol.* **1971**, *8*, 23–23.

56. Dupoisson, B.; Dumas, P.; Steinbrunn, A.; Colson, J. C., Single crystal cleavage device adaptable to a UHV vessel. *J. Phys. E* **1976**, *9*, 266.

57. Forssell, J.; Persson, B., Growth and Structure of Thin Chromium Films Condensed on Ultra-High Vacuum Cleaved NaCl and KCl Crystals. *J. Phys. Soc. Japan* **1970**, *29*, 1532-1545.

58. Huijser, A.; van Laar, J.; van Rooy, T. L., Electronic surface properties of UHV-cleaved III–V compounds. *Surf. Sci.* **1977**, *62*, 472–486.

59. Mendes, J. L.; Gao, W.; Martin, J. L.; Carl, A. D.; Deskins, N. A.; Granados-Focil, S.; Grimm, R. L., Interfacial States, Energetics, and Atmospheric Stability of Large-Grain Antifluorite Cs_2TiBr_6. *J. Phys. Chem. C* **2020**, *124*, 24289–24297.

60. Greczynski, G.; Hultman, L., Towards reliable X-ray photoelectron spectroscopy: Sputter-damage effects in transition metal borides, carbides, nitrides, and oxides. *Appl. Surf. Sci.* **2021**, *542*, 148599.

61. Reinert, F.; Hüfner, S., Photoemission spectroscopy—from early days to recent applications. *New J. Phys.* **2005**, *7*, 97.

62. Berglund, C. N., Photoemission studies of copper and silver; University Microfilms: Ann Arbor, **1960**.

63. Zhang, F.; Silver, S. H.; Noel, N. K.; Ullrich, F.; Rand, B. P.; Kahn, A., Ultraviolet Photoemission Spectroscopy and Kelvin Probe Measurements on Metal Halide Perovskites: Advantages and Pitfalls. *Adv. Energy Mater.* 2020, 10, 1903252.

64. Menzel, D.; Tejada, A.; Al-Ashouri, A.; Levine, I.; Guerra, J. A.; Rech, B.; Albrecht, S.; Korte, L., Revisiting the Determination of the Valence Band Maximum and Defect Formation in Halide Perovskites for Solar Cells: Insights from Highly Sensitive Near–UV Photoemission Spectroscopy. *ACS Appl. Mater. Interfaces* **2021**, *13*, 43540–43553.

65. Heber, M.; Grünert, W., Application of ultraviolet photoelectron spectroscopy (UPS) in the surface characterisation of polycrystalline oxide

catalysts. I. Methodics and analytical potential. *Top. Catal.* **2001**, *15*, 3–11.

66. Mansfeldova, V.; Zlamalova, M.; Tarabkova, H.; Janda, P.; Vorokhta, M.; Piliai, L.; Kavan, L., Work Function of TiO_2 (Anatase, Rutile, and Brookite) Single Crystals: Effects of the Environment. *J. Phys. Chem. C* **2021**, *125*, 1902–1912.

67. Heber, M.; Grünert, W., Application of Ultraviolet Photoelectron Spectroscopy in the Surface Characterization of Polycrystalline Oxide Catalysts. 2. Depth Variation of the Reduction Degree in the Surface Region of Partially Reduced V_2O_5. *J. Phys. Chem. B* **2000**, *104*, 5288–5297.

68. Olthof, S., The Impact of UV Photoelectron Spectroscopy on the Field of Organic Optoelectronics—A Retrospective. *Adv. Opt. Mater.* **2021**, *9*, 2100227.

69. King, D. A., Thermal desorption from metal surfaces: A review. *Surf. Sci.* **1975**, *47*, 384–402.

70. Redhead, P. A., Thermal desorption of gases. *Vacuum* **1962**, *12*, 203–211.

71. Cullity, B. D., Elements of X-ray diffraction, 2nd ed.; Addison-Wesley Publishing Company, Inc: Reading, MA, **1978**.

72. Mangir Murshed, M.; Mendive, C. B.; Curti, M.; Šehović, M.; Friedrich, A.; Fischer, M.; Gesing, T. M., Thermal expansion of mullite-type $Bi_2Al_4O_9$: A study by X-ray diffraction, vibrational spectroscopy and density functional theory. *J. Solid State Chem.* **2015**, *229*, 87–96.

73. Wang, S.; Wang, C.; Ji, X., Towards understanding the salt-intercalation exfoliation of graphite into graphene. *RSC Adv.* **2017**, *7*, 52252–52260.

74. Koh, H.-J.; Kim, S. J.; Maleski, K.; Cho, S.-Y.; Kim, Y.-J.; Ahn, C. W.; Gogotsi, Y.; Jung, H.-T., Enhanced Selectivity of MXene Gas Sensors through Metal Ion Intercalation: In Situ X-ray Diffraction Study. *ACS Sensors* **2019**, *4*, 1365–1372.

75. Pollock, H. C., The discovery of synchrotron radiation. *Am. J. Phys.* **1983**, *51*, 278–280.

76. Evans, L., The Large Hadron Collider. *New J. Phys.* **2007**, *9*, 335.

77. U.S. Department of Energy: Stanford Synchrotron Radiation Light Source (SSRL). (accessed February 5, 2023).

78. Salmeron, M.; Schlögl, R., Ambient Pressure Photoelectron Spectroscopy: A New Tool for Surface Science and Nanotechnology. *Surf. Sci. Rep.* **2008**, *63*, 169-199.

79. Mattevi, C.; Wirth, C. T.; Hofmann, S.; Blume, R.; Cantoro, M.; Ducati, C.; Cepek, C.; Knop-Gericke, A.; Milne, S.; Castellarin-Cudia, C.; Dolafi, S.;

Goldoni, A.; Schloegl, R.; Robertson, J., In-situ X-ray Photoelectron Spectroscopy Study of Catalyst–Support Interactions and Growth of Carbon Nanotube Forests. *J. Phys. Chem. C* **2008**, *112*, 12207–12213.

80. Bluhm, H.; Hävecker, M.; Knop-Gericke, A.; Kleimenov, E.; Schlögl, R.; Teschner, D.; Bukhtiyarov, V. I.; Ogletree, D. F.; Salmeron, M., Methanol Oxidation on a Copper Catalyst Investigated Using in Situ X-ray Photoelectron Spectroscopy. *J. Phys. Chem. B* **2004**, *108*, 14340–14347.

81. Yamamoto, S.; Bluhm, H.; Andersson, K.; Ketteler, G.; Ogasawara, H.; Salmeron, M.; Nilsson, A., In situ x-ray photoelectron spectroscopy studies of water on metals and oxides at ambient conditions. *J. Phys.: Condensed Matter* **2008**, *20*, 184025.

82. Blomberg, S.; Hoffmann, M. J.; Gustafson, J.; Martin, N. M.; Fernandes, V. R.; Borg, A.; Liu, Z.; Chang, R.; Matera, S.; Reuter, K.; Lundgren, E., In Situ X-Ray Photoelectron Spectroscopy of Model Catalysts: At the Edge of the Gap. *Phys. Rev. Lett*. **2013**, *110*, 117601.

83. Knop-Gericke, A.; Pfeifer, V.; Velasco-Velez, J.-J.; Jones, T.; Arrigo, R.; Hävecker, M.; Schlögl, R., In situ X-ray photoelectron spectroscopy of electrochemically active solid-gas and solid-liquid interfaces. *J. Electron Spectrosc. Relat. Phenom*. **2017**, *221*, 10–17.

84. Zhang, C.; Grass, M. E.; McDaniel, A. H.; DeCaluwe, S. C.; Gabaly, F. E.; Liu, Z.; McCarty, K. F.; Farrow, R. L.; Linne, M. A.; Hussain, Z.; Jackson, G. S.; Bluhm, H.; Eichhorn, B. W., Measuring fundamental properties in operating solid oxide electrochemical cells by using in situ X-ray photoelectron spectroscopy. *Nat. Mater.* **2010**, *9*, 944-949.

85. Wi, S.; Shutthanandan, V.; Sivakumar, B. M.; Thevuthasan, S.; Prabhakaran, V.; Roy, S.; Karakoti, A.; Murugesan, V., In situ x-ray photoelectron spectroscopy analysis of electrochemical interfaces in battery: Recent advances and remaining challenges. *J. Vac. Sci. Technol. A* **2022**, *40*, 010808.

86. Jürgensen, A.; Esser, N.; Hergenröder, R., Near ambient pressure XPS with a conventional X-ray source. *Surf. Interface Anal*. **2012**, *44*, 1100–1103.

87. Mangolini, F.; Åhlund, J.; Wabiszewski, G. E.; Adiga, V. P.; Egberts, P.; Streller, F.; Backlund, K.; Karlsson, P. G.; Wannberg, B.; Carpick, R. W., Angle-resolved environmental X-ray photoelectron spectroscopy: A new laboratory setup for photoemission studies at pressures up to 0.4 Torr. *Rev. Sci. Instrum.* **2012**, *83*, 093112.

88. Tao, F., Design of an in-house ambient pressure AP-XPS using a benchtop X-ray source and the surface chemistry of ceria under reaction conditions. *Chem. Commun*. **2012**, *48*, 3812-3814.

89. Roy, K.; Gopinath, C. S., UV Photoelectron Spectroscopy at Near Ambient Pressures: Mapping Valence Band Electronic Structure Changes from Cu to CuO. *Anal. Chem.* **2014**, *86*, 3683-3687.

90. Roy, K.; Vinod, C. P.; Gopinath, C. S., Design and Performance Aspects of a Custom-Built Ambient Pressure Photoelectron Spectrometer toward Bridging the Pressure Gap: Oxidation of Cu, Ag, and Au Surfaces at 1 mbar O_2 Pressure. *J. Phys. Chem. C* **2013**, *117*, 4717–4726.

91. Eriksson, S. K.; Hahlin, M.; Kahk, J. M.; Villar-Garcia, I. J.; Webb, M. J.; Grennberg, H.; Yakimova, R.; Rensmo, H.; Edström, K.; Hagfeldt, A.; Siegbahn, H.; Edwards, M. O. M.; Karlsson, P. G.; Backlund, K.; Åhlund, J.; Payne, D. J., A versatile photoelectron spectrometer for pressures up to 30 mbar. *Rev. Sci. Instrum.* **2014**, *85*, 075119.

92. Jackman, M. J.; Thomas, A. G.; Muryn, C., Photoelectron Spectroscopy Study of Stoichiometric and Reduced Anatase TiO2(101) Surfaces: The Effect of Subsurface Defects on Water Adsorption at Near-Ambient Pressures. *J. Phys. Chem. C* **2015**, *119*, 13682–13690.

93. Newberg, J. T.; Åhlund, J.; Arble, C.; Goodwin, C.; Khalifa, Y.; Broderick, A., A lab-based ambient pressure X-ray photoelectron spectrometer with exchangeable analysis chambers. *Rev. Sci. Instrum.* **2015**, *86*, 085113.

94. Jeong, C.; Yun, H.; Lee, H.; Muller, S.; Lee, J.; Mun, B. S., Performance test of new near-ambient-pressure XPS at Korean Basic Science Institute and its application to CO oxidation study on Pt3Ti polycrystalline surface. *Cur. Appl. Phys.* **2016**, *16*, 73–78.

95. Roy, K.; Artiglia, L.; van Bokhoven, J. A., Ambient Pressure Photoelectron Spectroscopy: Opportunities in Catalysis from Solids to Liquids and Introducing Time Resolution. *Chemcatchem* **2018**, *10*, 666–682.

96. Carl, A. D. Soft, Organic, Carrier-Selective Contacts at Inorganic Semiconductor Interfaces Enabled by Low-Defect Covalent Bonding. Doctoral Dissertation, Worcester Polytechnic Institute, Worcester, MA, **2020**.

97. Michalak, D. J.; Gstrein, F.; Lewis, N. S., The Role of Band Bending in Affecting the Surface Recombination Velocities for Si(111) in Contact with Aqueous Acidic Electrolytes. *J. Phys. Chem. C* **2008**, *112*, 5911–5921.

98. Yablonovitch, E.; Allara, D. L.; Chang, C. C.; Gmitter, T.; Bright, T. B., Unusually Low Surface-Recombination Velocity on Silicon and Germanium Surfaces. *Phys. Rev. Lett.* **1986**, *57*, 249–252.

99. Brattain, W. H.; Garrett, C. G. B., Combined Measurements of Field Effect, Surface Photo-Voltage and Photoconductivity. *Bell Sys. Tech. J.* **1956**, *35*, 1019–1040.

100. Laibinis, P. E.; Stanton, C. E.; Lewis, N. S., Measurement of Barrier Heights of Semiconductor/Liquid Junctions Using a Transconductance Method: Evidence for Inversion at n-Si/CH_3OH-1,1′-Dimethylferrocene$^{+/0}$ Junctions. *J. Phys. Chem*. **1994**, *98*, 8765–8774.

101. Yu, H.; Webb, L. J.; Ries, R. S.; Solares, S. D.; Goddard, W. A.; Heath, J. R.; Lewis, N. S., Low-Temperature STM Images of Methyl-Terminated Si(111) Surfaces. *J. Phys. Chem. B* **2005**, *109*, 671–674.

102. Webb, L. J.; Nemanick, E. J.; Biteen, J. S.; Knapp, D. W.; Michalak, D. J.; Traub, M. C.; Chan, A. S. Y.; Brunschwig, B. S.; Lewis, N. S., High-Resolution X-ray Photoelectron Spectroscopic Studies of Alkylated Silicon(111) Surfaces. *J. Phys. Chem. B* **2005**, *109*, 3930–3937.

103. Nemanick, E. J.; Hurley, P. T.; Brunschwig, B. S.; Lewis, N. S., Chemical and Electrical Passivation of Silicon (111) Surfaces through Functionalization with Sterically Hindered Alkyl Groups. *J. Phys. Chem. B* **2006**, *110*, 14800–14808.

104. Hunger, R.; Fritsche, R.; Jaeckel, B.; Jaegermann, W.; Webb, L. J.; Lewis, N. S., Chemical and electronic characterization of methyl-terminated Si(111) surfaces by high-resolution synchrotron photoelectron spectroscopy. *Phys. Rev. B* **2005**, *72*, 045317.

105. Nemanick, E. J.; Hurley, P. T.; Webb, L. J.; Knapp, D. W.; Michalak, D. J.; Brunschwig, B. S.; Lewis, N. S., Chemical and Electrical Passivation of Single-Crystal Silicon(100) Surfaces through a Two-Step Chlorination/Alkylation Process. *J. Phys. Chem. B* **2006**, *110*, 14770-14778.

106. Webb, L. J.; Lewis, N. S., Comparison of the Electrical Properties and Chemical Stability of Crystalline Silicon(111) Surfaces Alkylated Using Grignard Reagents or Olefins with Lewis Acid Catalysts. *J. Phys. Chem. B* **2003**, *107*, 5404-5412.

107. Boucher, D. G.; Speller, J. R.; Han, R.; Osterloh, F. E.; Rose, M. J., Decoupling Effects of Surface Recombination and Barrier Height on p-Si(111) Photovoltage in Semiconductor—Liquid Junctions via Molecular Dipoles and Metal Oxides. *ACS Appl. Energy Mater*. **2019**, *2*, 66–79.

108. Chen, M.; Hack, J. H.; Lin, X.; Janotti, A.; Opila, R. L. Electronic Structure Characterization of Hydrogen Terminated n-type Silicon Passivated by Benzoquinone-Methanol Solutions. *Coatings* **2018**, DOI: 10.3390/coatings8030108.

109. Har-Lavan, R.; Yaffe, O.; Joshi, P.; Kazaz, R.; Cohen, H.; Cahen, D., Ambient organic molecular passivation of Si yields near-ideal, Schottky-Mott limited, junctions. *AIP Adv.* **2012**, *2*, 012164.

110. O'Leary, L. E.; Johansson, E.; Brunschwig, B. S.; Lewis, N. S., Synthesis and Characterization of Mixed Methyl/Allyl Monolayers on Si(111). *J. Phys. Chem. B* **2010**, *114*, 14298–14302.

111. Kim, K.; Park, C.; Kwon, D.; Kim, D.; Meyyappan, M.; Jeon, S.; Lee, J.-S., Silicon nanowire biosensors for detection of cardiac troponin I (cTnI) with high sensitivity. *Biosens. Bioelectron.* **2016**, *77*, 695–701.

112. Vu, C.-A.; Chen, W.-Y.; Yang, Y.-S.; Chan, H. W.-H., Improved biomarker quantification of silicon nanowire field-effect transistor immunosensors with signal enhancement by RNA aptamer: Amyloid beta as a case study. *Sens. Actuators, B* **2021**, *329*, 129150.

113. Syedmoradi, L.; Ahmadi, A.; Norton, M. L.; Omidfar, K., A review on nanomaterial-based field effect transistor technology for biomarker detection. *Microchim. Acta* **2019**, *186*, 739.

114. Gao, A.; Chen, S.; Wang, Y.; Li, T., Silicon Nanowire Field-effect-transistor-based Biosensor for Biomedical Applications. *Sens. Mater.* **2018**, *30*, 1619.

115. Cao, A.; Sudhölter, E. J. R.; De Smet, L. C. P. M. Silicon Nanowire-Based Devices for Gas-Phase Sensing. *Sensors* **2014**, DOI: 10.3390/s140100245.

116. Ni, L. Silicon nanowires synthesized by VLS growth mode for gas sensing applications. Doctoral Dissertation. **2012**.

117. Wang, B.; Haick, H., Effect of Functional Groups on the Sensing Properties of Silicon Nanowires toward Volatile Compounds. *ACS Appl. Mater. Interfaces* **2013**, *5*, 2289–2299.

118. Wang, B.; Haick, H., Effect of Chain Length on the Sensing of Volatile Organic Compounds by means of Silicon Nanowires. *ACS Appl. Mater. Interfaces* **2013**, *5*, 5748–5756.

119. Weil, T.; Vosch, T.; Hofkens, J.; Peneva, K.; Müllen, K., The Rylene Colorant Family—Tailored Nanoemitters for Photonics Research and Applications. *Angew. Chem. Int. Ed*. **2010**, *49*, 9068–9093.

120. Shin, W. S.; Jeong, H.-H.; Kim, M.-K.; Jin, S.-H.; Kim, M.-R.; Lee, J.-K.; Lee, J. W.; Gal, Y.-S., Effects of functional groups at perylene diimide derivatives on organic photovoltaic device application. *J. Mater. Chem*. **2006**, *16*, 384–390.

121. Choi, W.; Lahiri, I.; Seelaboyina, R.; Kang, Y. S., Synthesis of Graphene and Its Applications: A Review. *Crit. Rev. Solid State Mater. Sci.* **2010**, *35*, 52–71.

122. Craciun, M. F.; Russo, S.; Yamamoto, M.; Tarucha, S., Tuneable electronic properties in graphene. *Nano Today* **2011**, *6*, 42–60.

123. Wang, L.; Sofer, Z.; Pumera, M., Will Any Crap We Put into Graphene Increase Its Electrocatalytic Effect? *ACS Nano* **2020**, *14*, 21–25.

124. Kosynkin, D. V.; Higginbotham, A. L.; Sinitskii, A.; Lomeda, J. R.; Dimiev, A.; Price, B. K.; Tour, J. M., Longitudinal unzipping of carbon nanotubes to form graphene nanoribbons. *Nature* **2009**, *458*, 872–876.

125. Sinitskii, A.; Dimiev, A.; Corley, D. A.; Fursina, A. A.; Kosynkin, D. V.; Tour, J. M., Kinetics of Diazonium Functionalization of Chemically Converted Graphene Nanoribbons. *ACS Nano* **2010**, *4*, 1949–1954.

126. Niyogi, S.; Bekyarova, E.; Itkis, M. E.; Zhang, H.; Shepperd, K.; Hicks, J.; Sprinkle, M.; Berger, C.; Lau, C. N.; deHeer, W. A.; Conrad, E. H.; Haddon, R. C., Spectroscopy of covalently functionalized graphene. *Nano Lett.* **2010**, *10*, 4061–4066.

127. Sree, S.; Gupta, J.; Zhang, Y.; Xu, G.; Valiyaveettil, S., Functionalization of surfactant wrapped graphenenanosheets with alkylazides for enhanced dispersibility. *Nanoscale* **2010**, *3*, 303–308.

128. Park, S.; Dikin, D. A.; Nguyen, S. T.; Ruoff, R. S., Graphene Oxide Sheets Chemically Cross-Linked by Polyallylamine. *J. Phys. Chem. C* **2009**, *113*, 15801–15804.

129. Sun, X.; Liu, Z.; Welsher, K.; Robinson, J. T.; Goodwin, A.; Zaric, S.; Dai, H., Nano-Graphene Oxide for Cellular Imaging and Drug Delivery. *Nano Res.* **2008**, *1*, 203–212.

130. Hong, H.; Yang, K.; Zhang, Y.; Engle, J. W.; Feng, L.; Yang, Y.; Nayak, T. R.; Goel, S.; Bean, J.; Theuer, C. P.; Barnhart, T. E.; Liu, Z.; Cai, W., In Vivo Targeting and Imaging of Tumor Vasculature with Radiolabeled, Antibody-Conjugated Nanographene. *ACS Nano* **2012**, *6*, 2361–2370.

131. Tian, B.; Wang, C.; Zhang, S.; Feng, L.; Liu, Z., Photothermally Enhanced Photodynamic Therapy Delivered by Nano-Graphene Oxide. *ACS Nano* **2011**, *5*, 7000–7009.

132. Yang, K.; Feng, L.; Liu, Z., Stimuli responsive drug delivery systems based on nano-graphene for cancer therapy. *Adv. Drug Delivery Rev.* **2016**, *105*, 228–241.

133. Yu, X.; Gao, D.; Gao, L.; Lai, J.; Zhang, C.; Zhao, Y.; Zhong, L.; Jia, B.; Wang, F.; Chen, X.; Liu, Z., Inhibiting Metastasis and Preventing Tumor Relapse by Triggering Host Immunity with Tumor-Targeted Photodynamic Therapy Using Photosensitizer-Loaded Functional Nanographenes. *ACS Nano* **2017**, *11*, 10147–10158.

134. Peng, C.; Hu, W.; Zhou, Y.; Fan, C.; Huang, Q., Intracellular Imaging with a Graphene-Based Fluorescent Probe. *Small* **2010**, *6*, 1686–1692.

135. Rong, P.; Yang, K.; Srivastan, A.; Kiesewetter, D. O.; Yue, X.; Wang, F.; Nie, L.; Bhirde, A.; Wang, Z.; Liu, Z.; Niu, G.; Wang, W.; Chen, X., Photosensitizer loaded nano-graphene for multimodality imaging guided tumor photodynamic therapy. *Theranostics* **2014**, *4*, 229–239.

136. Akhavan, O.; Ghaderi, E.; Emamy, H., Nontoxic concentrations of PE-Gylated graphene nanoribbons for selective cancer cell imaging and photothermal therapy. *J. Mater. Chem.* **2012**, *22*, 20626–20633.

137. Basu, S.; Bhattacharyya, P., Recent developments on graphene and graphene oxide based solid state gas sensors. *Sens. Actuators, B* **2012**, *173*, 1-21.

138. Kang, M.-A.; Ji, S.; Kim, S.; Park, C.-Y.; Myung, S.; Song, W.; Lee, S. S.; Lim, J.; An, K.-S., Highly sensitive and wearable gas sensors consisting of chemically functionalized graphene oxide assembled on cotton yarn. *RSC Adv.* **2018**, *8*, 11991-11996.

139. Liu, Y.; Yu, D.; Zeng, C.; Miao, Z.; Dai, L., Biocompatible Graphene Oxide-Based Glucose Biosensors. *Langmuir* **2010**, *26*, 6158–6160.

140. Majhi, S.; Mirzaei, A.; Kim, S., Reduced Graphene Oxide (rGO)-Loaded Metal-Oxide Nanofiber Gas Sensors: An overview. *Sensors* **2021**, *21*.

141. Han, R.; Liu, F.; Wang, X.; Huang, M.; Li, W.; Yamauchi, Y.; Sun, X.; Huang, Z., Functionalised Hexagonal Boron Nitride for Energy Conversion and Storage. *J. Mater. Chem. A* **2020**, *8*.

142. Dickinson, R. G.; Pauling, L., The crystal structure of molybdenite. *J. Am. Chem. Soc.* **1923**, *45*, 1466–1471.

143. Manzeli, S.; Ovchinnikov, D.; Pasquier, D.; Yazyev, O. V.; Kis, A., 2D transition metal dichalcogenides. *Nat. Rev. Mater.* **2017**, *2*, 17033.

144. Vazirisereshk, M. R.; Martini, A.; Strubbe, D.; Baykara, M., Solid Lubrication with MoS_2: A Review, *Lubricants* **2019**, *7*(7), 57.

145. Samy, O.; El Moutaouakil, A., A Review on MoS_2 Energy Applications: Recent Developments and Challenges. *Energies* **2021**, *14*, 4586.

146. Presolski, S.; Pumera, M., Covalent functionalization of MoS_2. *Mater. Today* **2016**, *19*, 140-145.

147. Wang, T.; Zhu, R.; Zhuo, J.; Zhu, Z.; Shao, Y.; Li, M., Direct Detection of DNA below ppb Level Based on Thionin-Functionalized Layered MoS2 Electrochemical Sensors. *Anal. Chem.* **2014**, *86*, 12064-12069.

148. Chou, S. S.; De, M.; Kim, J.; Byun, S.; Dykstra, C.; Yu, J.; Huang, J.; Dravid, V. P., Ligand Conjugation of Chemically Exfoliated MoS_2. *J. Am. Chem. Soc.* **2013**, *135*, 4584-4587.

149. Jiang, Y. R.; Chou, S. Y.; Chang, J. L.; Huang, S. T.; Lin, H. P.; Chen, C. C., Hydrothermal Synthesis of Bismuth Oxybromide-Bismuth Oxyiodide

Composites with High Visible Light Photocatalytic Performance for the Degradation of CV and Phenol. *RSC Adv*. **2015**, *5*, 30851-30860.

150. Luo, S. Q.; Chen, J. W.; Huang, Z. H.; Liu, C.; Fang, M. H., Controllable Synthesis of Titania-Supported Bismuth Oxyiodide Heterostructured Nanofibers with Highly Exposed (110) Bismuth Oxyiodide Facets for Enhanced Photocatalytic Activity. *Chemcatchem* **2016**, *8*, 3780-3789.

151. Chou, S. Y.; Chen, C. C.; Dai, Y. M.; Lin, J. H.; Lee, W. W., Novel Synthesis of Bismuth Oxyiodide/Graphitic Carbon Nitride Nanocomposites with Enhanced Visible-Light Photocatalytic Activity. *RSC Adv*. **2016**, *6*, 33478-33491.

152. Sharma, K.; Dutta, V.; Sharma, S.; Raizada, P.; Hosseini-Bandegharaei, A.; Thakur, P.; Singh, P., Recent Advances in Enhanced Photocatalytic Activity of Bismuth Oxyhalides for Efficient Photocatalysis of Organic Pollutants in Water: A Review. *J. Ind. Eng. Chem*. **2019**, *78*, 1-20.

153. Liu, Q. C.; Ma, D. K.; Hu, Y. Y.; Zeng, Y. W.; Huang, S. M., Various Bismuth Oxyiodide Hierarchical Architectures: Alcohothermal-Controlled Synthesis, Photocatalytic Activities, and Adsorption Capabilities for Phosphate in Water. *ACS Appl. Mater. Interfaces* **2013**, *5*, 11927-11934.

154. Kwolek, P.; Szaciłowski, K., Photoelectrochemistry of n-Type Bismuth Oxyiodide. *Electrochim. Acta* **2013**, *104*, 448-453.

155. Lei, Y.; Wang, G.; Song, S.; Fan, W.; Pang, M.; Tang, J.; Zhang, H., Room Temperature, Template-Free Synthesis of BiOI Hierarchical Structures: Visible-Light Photocatalytic and Electrochemical Hydrogen Storage Properties. *Dalton Trans*. **2010**, *39*, 3273–3278.

156. Chang, X.; Huang, J.; Cheng, C.; Sui, Q.; Sha, W.; Ji, G.; Deng, S.; Yu, G., BiOX (X=Cl, Br, I) Photocatalysts Prepared Using NaBiO3 as the Bi Source: Characterization and Catalytic Performance. *Catal. Commun*. **2010**, *11*, 460–464.

157. Zhang, X.; Zhang, L., Electronic and Band Structure Tuning of Ternary Semiconductor Photocatalysts by Self Doping: The Case of BiOI. *J. Phys. Chem. C* **2010**, *114*, 18198–18206.

158. Korichi, R.; Tranchant, J.-F., Decorative Products. In Handbook of Cosmetic Science and Technology, 3rd ed.; Barel, A. O.; Paye, M.; Maibach, H. I., Eds. CRC Press: **2009**.

159. Hoye, R. L. Z.; Lee, L. C.; Kurchin, R. C.; Huq, T. N.; Zhang, K. H. L.; Sponseller, M.; Nienhaus, L.; Brandt, R. E.; Jean, J.; Polizzotti, J. A.; Kursumović, A.; Bawendi, M. G.; Bulović, V.; Stevanović, V.; Buonassisi, T.; MacManus-Driscoll, J. L., Strongly Enhanced Photovoltaic Performance and Defect Physics of Air-Stable Bismuth Oxyiodide (BiOI). *Adv. Mater*. **2017**, *29*, 1702176.

160. Lee, W. W.; Lu, C.-S.; Chuang, C.-W.; Chen, Y.-J.; Fu, J.-Y.; Siao, C.-W.; Chen, C.-C., Synthesis of Bismuth Oxyiodides and Their Composites: Characterization, Photocatalytic Activity, and Degradation Mechanisms. *RSC Adv*. **2015**, *5*, 23450-23463.

161. Lee, Y.-H.; Dai, Y.-M.; Fu, J.-Y.; Chen, C.-C., A Series of Bismuth-Oxychloride/Bismuth-Oxyiodide/Graphene-Oxide Nanocomposites: Synthesis, Characterization, and Photcatalytic Activity and Mechanism. *Mol. Catal*. **2017**, *432*, 196–209.

162. Huang, Y.; Li, H.; Fan, W.; Zhao, F.; Qiu, W.; Ji, H.; Tong, Y., Defect Engineering of Bismuth Oxyiodide by IO3- Doping for Increasing Charge Transport in Photocatalysis. *ACS Appl. Mater. Interfaces* **2016**, *8*, 27859–27867.

163. Ye, K. H.; Chai, Z. S.; Gu, J. W.; Yu, X.; Zhao, C. X.; Zhang, Y. M.; Mai, W. J., BiOI-$BiVO_4$ Photoanodes with Significantly Improved Solar Water Splitting Capability: p-n Junction to Expand Solar Adsorption Range and Facilitate Charge Carrier Dynamics. *Nano Energy* **2015**, *18*, 222–231.

164. Zhao, Z.-Y.; Dai, W.-W., Electronic Structure and Optical Properties of BiOI Ultrathin Films for Photocatalytic Water Splitting. *Inorg. Chem*. **2015**, *54*, 10732–10737.

165. Shan, L. W.; He, L. Q.; Suriyaprakash, J.; Yang, L. X., Photoelectrochemical (PEC) Water Splitting of BiOI001 Nanosheets Synthesized by a Simple Chemical Transformation. *J. Alloy Compd*. **2016**, *665*, 158–164.

166. Tang, Z. K.; Yin, W. J.; Zhang, L.; Wen, B.; Zhang, D. Y.; Liu, L. M.; Lau, W. M., Spatial Separation of Photo-generated Electron-Hole Pairs in BiOBr/BiOI Bilayer to Facilitate Water Splitting. *Sci. Rep*. **2016**, *6*.

167. Wang, J. J.; Zhang, M.; Meng, J.; Li, Q. X.; Yang, J. L., Single- and Few-Layer BiOI as Promising Photocatalysts for Solar Water Splitting. *RSC Adv*. **2017**, *7*, 24446–24452.

168. Di, J.; Xia, J.; Li, H.; Guo, S.; Dai, S., Bismuth Oxyhalide Layered Materials for Energy and Environmental Applications. *Nano Energy* **2017**, *41*, 172–192.

169. Hahn, N. T.; Hoang, S.; Self, J. L.; Mullins, C. B., Spray Pyrolysis Deposition and Photoelectrochemical Properties of n-Type BiOI Nanoplatelet Thin Films. *ACS Nano* **2012**, *6*, 7712–7722.

170. Barsoum, M. W.; Brodkin, D.; El-Raghy, T., Layered machinable ceramics for high temperature applications. *Scripta Materialia* **1997**, *36*, 535–541.

171. Barsoum, M. W.; El-Raghy, T., Synthesis and Characterization of a Remarkable Ceramic: Ti_3SiC_2. *J. Am. Ceram. Soc*. **1996**, *79*, 1953–1956.

172. Sokol, M.; Natu, V.; Kota, S.; Barsoum, M. W., On the Chemical Diversity of the MAX Phases. *Trend. Chem.* **2019**, *1*, 210–223.

173. Nowotny, V. H., Strukturchemie einiger Verbindungen der Übergangsmetalle mit den Elementen C, Si, Ge, Sn. *Prog. Sol. State Chem.* **1971**, *5*, 27–70.

174. Goto, T.; Hirai, T., Chemically vapor deposited Ti_3SiC_2. *Mater. Res. Bull.* **1987**, *22*, 1195–1201.

175. Zhou, A.; Liu, Y.; Li, S.; Wang, X.; Ying, G.; Xia, Q.; Zhang, P., From structural ceramics to 2D materials with multi-applications: A review on the development from MAX phases to MXenes. *J. Adv. Ceram.* **2021**, *10*, 1194–1242.

176. Naguib, M.; Kurtoglu, M.; Presser, V.; Lu, J.; Niu, J.; Heon, M.; Hultman, L.; Gogotsi, Y.; Barsoum, M. W., Two-Dimensional Nanocrystals Produced by Exfoliation of Ti_3AlC_2. *Adv. Mater.* **2011**, *23*, 4248–4253.

177. Naguib, M.; Mashtalir, O.; Carle, J.; Presser, V.; Lu, J.; Hultman, L.; Gogotsi, Y.; Barsoum, M. W., Two-Dimensional Transition Metal Carbides. *ACS Nano* **2012**, *6*, 1322–1331.

178. Chen, W. Y.; Lai, S.-N.; Yen, C.-C.; Jiang, X.; Peroulis, D.; Stanciu, L. A., Surface Functionalization of $Ti_3C_2T_x$ MXene with Highly Reliable Superhydrophobic Protection for Volatile Organic Compounds Sensing. *ACS Nano* **2020**, *14*, 11490–11501.

179. Ho, D. H.; Choi, Y. Y.; Jo, S. B.; Myoung, J.-M.; Cho, J. H., Sensing with MXenes: Progress and Prospects. *Adv. Mater.* **2021**, *33*, 2005846.

180. Pei, Y.; Zhang, X.; Hui, Z.; Zhou, J.; Huang, X.; Sun, G.; Huang, W., $Ti_3C_2T_x$ MXene for Sensing Applications: Recent Progress, Design Principles, and Future Perspectives. *ACS Nano* **2021**, *15*, 3996–4017.

181. Bhardwaj, R.; Hazra, A., MXene-based gas sensors. *J. Mater. Chem. C* **2021**, *9*, 15735–15754.

182. Sinha, A.; Dhanjai; Zhao, H.; Huang, Y.; Lu, X.; Chen, J.; Jain, R., MXene: An emerging material for sensing and biosensing. *TrAC, Trends Anal. Chem.* **2018**, *105*, 424–435.

183. Zhu, S.; Wang, D.; Li, M.; Zhou, C.; Yu, D.; Lin, Y., Recent advances in flexible and wearable chemo- and bio-sensors based on two-dimensional transition metal carbides and nitrides (MXenes). *J. Mater. Chem. B* **2022**, *10*, 2113–2125.

184. Halim, J.; Persson, I.; Eklund, P.; Persson, P. O. Å.; Rosen, J., Sodium hydroxide and vacuum annealing modifications of the surface terminations of a Ti_3C_2 (MXene) epitaxial thin film. *RSC Adv.* **2018**, *8*, 36785–36790.

185. Li, J.; Du, Y.; Huo, C.; Wang, S.; Cui, C., Thermal stability of two-dimensional Ti_2C nanosheets. *Ceram. Int.* **2015**, *41*, 2631–2635.

186. Persson, I.; Halim, J.; Hansen, T. W.; Wagner, J. B.; Darakchieva, V.; Palisaitis, J.; Rosen, J.; Persson, P. O. Å., How Much Oxygen Can a MXene Surface Take Before It Breaks? *Adv. Func. Mater*. **2020**, *30*, 1909005.

187. Persson, I.; Halim, J.; Lind, H.; Hansen, T. W.; Wagner, J. B.; Näslund, L.-Å.; Darakchieva, V.; Palisaitis, J.; Rosen, J.; Persson, P. O. Å., 2D Transition Metal Carbides (MXenes) for Carbon Capture. *Adv. Mater*. **2019**, *31*, 1805472.

188. Zhang, Z.; Yao, Z.; Zhang, X.; Jiang, Z., 2D Carbide MXene under postetch low-temperature annealing for high–performance supercapacitor electrode. *Electrochim. Acta* **2020**, *359*, 136960.

189. Wu, X.; Wang, Z.; Yu, M.; Xiu, L.; Qiu, J., Stabilizing the MXenes by Carbon Nanoplating for Developing Hierarchical Nanohybrids with Efficient Lithium Storage and Hydrogen Evolution Capability. *Adv. Mater*. **2017**, *29*, 1607017.

190. Kamysbayev, V.; Filatov, A. S.; Hu, H.; Rui, X.; Lagunas, F.; Wang, D.; Klie, R. F.; Talapin, D. V., Covalent surface modifications and superconductivity of two-dimensional metal carbide MXenes. *Science* **2020**, *369*, 979–983.

191. Ji, J.; Zhao, L.; Shen, Y.; Liu, S.; Zhang, Y., Covalent stabilization and functionalization of MXene via silylation reactions with improved surface properties. *FlatChem* **2019**, *17*, 100128.

192. Riazi, H.; Anayee, M.; Hantanasirisakul, K.; Shamsabadi, A. A.; Anasori, B.; Gogotsi, Y.; Soroush, M., Surface Modification of a MXene by an Aminosilane Coupling Agent. *Adv. Mater. Interfaces* **2020**, *7*, 1902008.

193. Naguib, M.; Unocic, R. R.; Armstrong, B. L.; Nanda, J., Large-scale delamination of multi-layers transition metal carbides and carbonitrides "MXenes". *Dalton Trans*. **2015**, *44*, 9353-9358.

194. Zhao, J.; Yang, Y.; Yang, C.; Tian, Y.; Han, Y.; Liu, J.; Yin, X.; Que, W., A hydrophobic surface enabled salt-blocking 2D Ti_3C_2 MXene membrane for efficient and stable solar desalination. *J. Mater. Chem. A* **2018**, *6*, 16196–16204.

195. Cao, W.-T.; Feng, W.; Jiang, Y.-Y.; Ma, C.; Zhou, Z.-F.; Ma, M.-G.; Chen, Y.; Chen, F., Two-dimensional MXene-reinforced robust surface superhydrophobicity with self-cleaning and photothermal-actuating binary effects. *Mater. Horizons* **2019**, *6*, 1057–1065.

196. Lim, S.; Park, H.; Yang, J.; Kwak, C.; Lee, J., Stable colloidal dispersion of octylated Ti_3C_2-MXenes in a nonpolar solvent. *Colloids Surf., A* **2019**, *579*, 123648.

197. Kumar, S.; Lei, Y.; Alshareef, N. H.; Quevedo-Lopez, M. A.; Salama, K. N., Biofunctionalized two-dimensional Ti_3C_2 MXenes for ultrasensitive detection of cancer biomarker. *Biosens. Bioelectron.* **2018**, *121*, 243-249.

198. Yan, G.; Chen, G.; Peng, Z.; Shen, Z.; Tang, X.; Sun, Y.; Zeng, X.; Lin, L., The Cross-Linking Mechanism and Applications of Catechol–Metal Polymer Materials. *Adv. Mater. Interfaces* **2021**, *8*, 2100239.

199. Heckler, J. E.; Neher, G. R.; Mehmood, F.; Lioi, D. B.; Pachter, R.; Vaia, R.; Kennedy, W. J.; Nepal, D., Surface Functionalization of $Ti_3C_2T_x$ MXene Nanosheets with Catechols: Implication for Colloidal Processing. *Langmuir* **2021**, *37*, 5447–5456.

200. Ko, T. Y.; Kim, D.; Kim, S. J.; Kim, H.; Nissimagoudar, A. S.; Lee, S.-C.; Lin, X.; Cummings, P. T.; Doo, S.; Park, S.; Hassan, T.; Oh, T.; Chae, A.; Lee, J.; Gogotsi, Y.; In, I.; Koo, C. M., Universal Ligands for Dispersion of Two-Dimensional MXene in Organic Solvents. *ACS Nano* **2023**, *17*, 1112–1119.

201. Natu, V.; Sokol, M.; Verger, L.; Barsoum, M. W., Effect of Edge Charges on Stability and Aggregation of Ti3C2Tz MXene Colloidal Suspensions. *J. Phys. Chem. C* **2018**, *122*, 27745–27753.

202. Ghidiu, M.; Lukatskaya, M. R.; Zhao, M.-Q.; Gogotsi, Y.; Barsoum, M. W., Conductive two-dimensional titanium carbide 'clay' with high volumetric capacitance. *Nature* **2014**, *516*, 78+.

203. Sorrentino, A. L.; Serrano, G.; Poggini, L.; Cortigiani, B.; El-Kelany, K. E.; D'Amore, M.; Ferrari, A. M.; Atrei, A.; Caneschi, A.; Sessoli, R.; Mannini, M., Quasi-Hexagonal to Lepidocrocite-like Transition in TiO_2 Ultrathin Films on Cu(001). *J. Phys. Chem. C* **2021**, *125*, 10621–10630.

204. (a) Wang, S. L.; Luo, X.; Zhou, X.; Zhu, Y.; Chi, X.; Chen, W.; Wu, K.; Liu, Z.; Quek, S. Y.; Xu, G. Q., Fabrication and Properties of a Free-Standing Two-Dimensional Titania. *J. Am. Chem. Soc.* **2017**, *139*, 15414–15419.

(b) Nowotny, M. K.; Sheppard, L. R.; Bak, T.; Nowotny, J., Defect Chemistry of Titanium Dioxide. Application of Defect Engineering in Processing of TiO_2-Based Photocatalysts. *J. Phys. Chem. C* **2008**, *112*, 5275–5300.

205. Schneider, J.; Matsuoka, M.; Takeuchi, M.; Zhang, J.; Horiuchi, Y.; Anpo, M.; Bahnemann, D. W., Understanding TiO_2 Photocatalysis: Mechanisms and Materials. *Chem. Rev.* **2014**, *114*, 9919–9986.

206. Fujishima, A.; Rao, T. N.; Tryk, D. A., Titanium Dioxide Photocatalysis. *J. Photochem. Photobiol., C* **2000**, *1*, 1–21.

207. Kuvarega, A. T.; Mamba, B. B., TiO_2-based Photocatalysis: Toward Visible Light-Responsive Photocatalysts Through Doping and Fabrication of Carbon-Based Nanocomposites. *Crit. Rev. Solid State Mater. Sci.* **2016**, *42*, 295–346.

208. Wang, H.; Lewis, J. P., Effects of Dopant States on Photoactivity in Carbon-Doped TiO_2. *J. Phys.: Condens. Matter* **2005**, *17*, L209–L213.

209. Irie, H.; Watanabe, Y.; Hashimoto, K., Carbon-Doped Anatase TiO_2 Powders as a Visible-Light Sensitive Photocatalyst. *Chem. Lett.* **2003**, *32*, 772–773.

210. Di Valentin, C.; Pacchioni, G.; Selloni, A., Theory of Carbon Doping of Titanium Dioxide. *Chem. Mater.* **2005**, *17*, 6656–6665.

211. Chaparro, A. M.; Salvador, P.; Peter, L. M., The Role of Surface Defects in the Photooxidation of Iodide at n-$MoSe_2$: Evidence for a Local "Autocatalytic" Effect. *J. Phys. Chem.* **1995**, *99*, 6677–6683.

212. Chaparro, A. M.; Salvador, P.; Tabernero, A.; Navarro, R.; Coll, B.; Caselles, V., Charge recombination imaging at the WSe_2/I^- interface. *Surf. Sci.* **1993**, *295*, 457–461.

213. Hill, J. W.; Hill, C. M., Directly Mapping Photoelectrochemical Behavior within Individual Transition Metal Dichalcogenide Nanosheets. *Nano Lett.* **2019**, *19*, 5710–5716.

214. Van Erdewyk, M.; Lorenz, D. B.; Sambur, J. B., Answering old questions with new techniques: Understanding performance-limiting factors in transition metal dichalcogenide photoelectrochemical solar cells. *Current Opinion in Electrochemistry* **2023**, *37*, 101173.

215. Erdewyk, M. V.; Sambur, J. B., Molecular Reaction Imaging of a Surface Recombination Process Explains Performance Variation Among Smooth MoS2 Photoelectrodes. *J. Electrochem. Soc.* **2022**, *169*, 096519.

216. Lewerenz, H. J.; Gerischer, H.; Lübke, M., Photoelectrochemistry of WSe_2 Electrodes: Comparison of Stepped and Smooth Surfaces. *J. Electrochem. Soc.* **1984**, *131*, 100.

217. Parkinson, B. A.; Furtak, T. E.; Canfield, D.; Kam, K.-K.; Kline, G., Evaluation and reduction of efficiency losses at tungsten diselenide photoanodes. *Faraday Discuss. Chem. Soc.* **1980**, *70*, 233–245.

218. Qi, Y.; Liu, J.; Dong, Y.; Feng, X.-Q.; Li, Q., Impacts of environments on nanoscale wear behavior of graphene: Edge passivation vs. substrate pinning. *Carbon* **2018**, *139*, 59–66.

219. Qi, Y.; Liu, J.; Zhang, J.; Dong, Y.; Li, Q., Wear Resistance Limited by Step Edge Failure: The Rise and Fall of Graphene as an Atomically Thin Lubricating Material. *ACS Appl. Mater. Interfaces* **2017**, *9*, 1099–1106.

220. Ma, P.; Fang, D.; Liu, Y.; Shang, Y.; Shi, Y.; Yang, H. Y., MXene-Based Materials for Electrochemical Sodium-Ion Storage. *Adv. Sci.* **2021**, *8*, 2003185.

221. Hou, C.; Huang, C.; Yu, H.; Shi, S., Surface-Engineered $Ti_3C_2T_x$ with Tunable Work Functions for Highly Efficient Polymer Solar Cells. *Small* **2022**, *18*, 2201046.

222. Huang, C.; Shi, S.; Yu, H., Work Function Adjustment of Nb_2CT_x Nanoflakes as Hole and Electron Transport Layers in Organic Solar Cells by Controlling Surface Functional Groups. *ACS Energy Lett.* **2021**, *6*, 3464–3472.

223. Schultz, T.; Frey, N. C.; Hantanasirisakul, K.; Park, S.; May, S. J.; Shenoy, V. B.; Gogotsi, Y.; Koch, N., Surface Termination Dependent Work Function and Electronic Properties of $Ti_3C_2T_x$ MXene. *Chem. Mater.* **2019**, *31*, 6590–6597.

224. Moulder, J. F.; Stickle, W. F.; Sobol, P. E.; Bomben, K. D., Handbook of X-ray Photoelectron Spectroscopy; Physical Electronics Division: Perkin-Elmer Corporation, **1992**.

225. Jablonski, A.; Powell, C. J., The electron attenuation length revisited. *Surf. Sci. Rep.* **2002**, *47*, 33–91.

226. Seah, M. P.; Dench, W. A., Quantitative electron spectroscopy of surfaces: A standard data base for electron inelastic mean free paths in solids. *Surf. Interface Anal.* **1979**, *1*, 2–11.

227. Cumpson, P. J.; Seah, M. P., Elastic Scattering Corrections in AES and XPS. II. Estimating Attenuation Lengths and Conditions Required for their Valid Use in Overlayer/Substrate Experiments. *Surf. Interface Anal.* **1997**, *25*, 430–446.

228. Seah, M. P., Quantification of AES and XPS. In Practical Surface Analysis: Auger and X-ray Photoelectron Spectroscopy, Briggs, D.; Seah, M. P., Eds. John Wiley & Sons Ltd.: **1990**.

229. Carl, A. D.; Kalan, R. E.; Obayemi, J. D.; Kana, M. G. Z.; Soboyejo, W. O.; Grimm, R. L., Synthesis and Characterization of Alkylamine-Functionalized Si(111) for Perovskite Adhesion With Minimal Interfacial Oxidation or Electronic Defects. *ACS Appl. Mater. Interfaces* **2017**, *9*, 34377-034388.

230. Fairley, N. Peak Fitting in XPS. http://www.casaxps.com/help_manual/manual_updates/peak_fitting_in_xps.pdf.

231. Jansson, C.; Hansen, H. S.; Yubero, F.; Tougaard, S., Accuracy of the Tougaard method for quantitative surface analysis. Comparison of the Universal and REELS inelastic cross sections. *J. Electron Spectrosc. Relat. Phenom.* **1992**, *60*, 301–319.

232. Yamaguchi, M.; Takamoto, T.; Araki, K.; Ekins-Daukes, N., Multi-Junction III–V Solar Cells: Current Status and Future Potential. *Sol. Energy* **2005**, *79*, 78–85.

233. Bertness, K. A.; Kurtz, S. R.; Friedman, D. J.; Kibbler, A. E.; Kramer, C.; Olson, J. M., 29.5%-Efficient GaInP/GaAs Tandem Solar Cells. *App. Phys. Lett*. **1994**, *65*, 989–991.

234. Takamoto, T.; Ikeda, E.; Kurita, H.; Ohmori, M., Over 30% Efficient InGaP/GaAs Tandem Solar Cells. *Appl. Phys. Lett*. **1997**, *70*, 381–383.

235. Essig, S.; Allebé, C.; Remo, T.; Geisz, J. F.; Steiner, M. A.; Horowitz, K.; Barraud, L.; Ward, J. S.; Schnabel, M.; Descoeudres, A.; Young, David L.; Woodhouse, M.; Despeisse, M.; Ballif, C.; Tamboli, A., Raising the One-Sun Conversion Efficiency of III–V/Si Solar Cells to 32.8% for Two Junctions and 35.9% for Three Junctions. *Nat. Energy* **2017**, *2*, 17144.

236. Department of Energy EERE Exchange. DE-FOA-0002064: Solar Energy Technologies Office Fiscal Year 2019 Funding Program. https://eere-exchange.energy.gov/FileContent.aspx?FileID=d2f56f78-decb-4cc1-9a88-0f6241708508.

237. Bush, K. A.; Palmstrom, A. F.; Yu, Z. J.; Boccard, M.; Cheacharoen, R.; Mailoa, J. P.; McMeekin, D. P.; Hoye, R. L. Z.; Bailie, C. D.; Leijtens, T.; Peters, I. M.; Minichetti, M. C.; Rolston, N.; Prasanna, R.; Sofia, S.; Harwood, D.; Ma, W.; Moghadam, F.; Snaith, H. J.; Buonassisi, T.; Holman, Z. C.; Bent, S. F.; McGehee, M. D., 23.6%-Efficient Monolithic Perovskite/Silicon Tandem Solar Cells with Improved Stability. *Nat. Energy* **2017**, *2*, 17009.

238. Werner, J.; Weng, C.-H.; Walter, A.; Fesquet, L.; Seif, J. P.; De Wolf, S.; Niesen, B.; Ballif, C., Efficient Monolithic Perovskite/Silicon Tandem Solar Cell with Cell Area >1 cm^2. *J. Phys. Chem. Lett.* **2016**, *7*, 161–166.

239. Wyckoff, R. W. G., Crystal Structures; Interscience Publishers: New York, **1963**; Vol. 1.

240. Comey, A. M.; Hahn, D. A., A Dictionary of Chemical Solubilities: Inorganic, 2nd ed.; The MacMillan Company, **1921**.

241. Yoo, B.; Ding, D.; Marin-Beloqui, J. M.; Lanzetta, L.; Bu, X.; Rath, T.; Haque, S. A., Improved Charge Separation and Photovoltaic Performance of BiI_3 Absorber Layers by Use of an In Situ Formed BiSI Interlayer. *ACS Appl. Mater. Interfaces* **2019**, *2*, 7056–7061.

242. Hamdeh, U. H.; Nelson, R. D.; Ryan, B. J.; Bhattacharjee, U.; Petrich, J. W.; Panthani, M. G., Solution-Processed BiI_3 Thin Films for Photovoltaic Applications: Improved Carrier Collection via Solvent Annealing. *Chem. Mater*. **2016**, *28*, 6567–6574.

243. Walker, P.; Tarn, W. H., Handbook of Metal Etchants; CRC Press, **1991**.

244. Judge, J. S., A Study of the Dissolution of SiO_2 in Acidic Fluoride Solutions. *J. Electrochem. Soc*. **1971**, *118*, 1772.

245. Hoshino, T.; Nishioka, Y., Etching process of SiO_2 by HF molecules. *J. Chem. Phys*. **1999**, *111*, 2109-2114.

246. Kang, J. K.; Musgrave, C. B., The Mechanism of HF/H_2O Chemical Etching of SiO_2. *J. Chem. Phys*. **2001**, *116*, 275–280.

247. Takishita, I.; Nara, M.; Homma, T., Electrochemical Analyses of Metal Ions in HF and H_2SiF_6 Aqueous Solution for Recycling Silicate Glasses of Cathode-Ray Tube by Liquid-Phase Deposition. *Resources Processing* **2010**, *57*, 114–119.

248. Gouda, P., Arsenic, Selenium, Antimony Ultra-Trace Analysis; iUniverse: Bloomington, Indiana, **2012**.

249. Gao, W.; Zielinski, K.; Drury, B. N.; Carl, A. D.; Grimm, R. L., Elucidation of Chemical Species and Reactivity at Methylammonium Lead Iodide and Cesium Tin Bromide Perovskite Surfaces via Orthogonal Reaction Chemistry. *J. Phys. Chem. C* **2018**, *122*, 17882–17894.

250. Fadley, C. S., Solid state—and Surface—Analysis by Means of Angular-Dependent X-Ray Photoelectron Spectroscopy. *Prog. Sol. State Chem*. **1976**, *11*, 265-343.

251. Dai, W.-W.; Zhao, Z.-Y., Structural and Electronic Properties of Low-Index Stoichiometric BiOI Surfaces. Mater. *Chem. Phys*. **2017**, *193*, 164-176.

252. Kong, T.; Wei, X.; Zhu, G.; Huang, Y., First-Principles Studies on Facet-Dependent Photocatalytic Properties of BiOI 001 Surface. *J. Mater. Sci*. **2017**, *52*, 5686–5695.

253. Schmidt, P.; Binnewies, M.; Glaum, R.; Schmidt, M., Chemical Vapor Transport Reactions–Methods, Materials, Modeling. In Advanced Topics on Crystal Growth, Ferreira, S. O., Ed. **2013**.

254. Russell, M. A.; Kalan, R. E.; Pugliese, A. J.; Carl, A. D.; Masucci, C. P.; Strandwitz, N. C.; Grimm, R. L., Dual Liquid Junction Photoelectrochemistry: Part II. Open-Circuit Photovoltage Variations Due to Surface Chemistry, Interfacial Dipoles, and Non-Ohmic Junctions at Back Contacts. *J. Electrochem. Soc*. **2019**, *166*, H6080–H614.

255. Fairley, N. Peak Fitting in XPS. http://www.casaxps.com/help_manual/manual_updates/peak_fitting_in_xps.pdf.

256. Shirley, D. A., High-Resolution X-Ray Photoemission Spectrum of the Valence Bands of Gold. *Phys. Rev. B* **1972**, *5*, 4709–4714.

257. Tougaard, S., Formalism for Quantitative Surface Analysis by Electron Spectroscopy. **J. Vac. Sci. Technol., A 1990**, *8*, 2197–2203.

258. Jansson, C.; Hansen, H. S.; Yubero, F.; Tougaard, S., Accuracy of the Tougaard Method for Quantitative Surface Snalysis. Comparison of the Universal and REELS Inelastic Cross Sections. *J. Electron Spectrosc. Relat. Phenom.* **1992**, *60*, 301–319.

259. Gleason-Rohrer, D. C.; Brunschwig, B. S.; Lewis, N. S., Measurement of the Band Bending and Surface Dipole at Chemically Functionalized Si(111)/Vacuum Interfaces. *J. Phys. Chem. C* **2013**, *117*, 18031–18042.

260. Greczynski, G.; Hultman, L., X-ray photoelectron spectroscopy: Towards Reliable Binding Energy Referencing. *Prog. Mater. Sci.* **2020**, *107*, 100591.

261. Zhao, Z. Y.; Dai, W. W., Structural, Electronic, and Optical Properties of Eu-Doped BiOX (X = F, Cl, Br, I): A DFT+U Study. *Inorg. Chem.* **2014**, *53*, 13001–13011.

262. Seah, M. P., XPS Reference Procedure for the Accurate Intensity Calibration of Electron Spectrometers— Results of a BCR Intercomparison Co-Sponsored by the VAMAS SCA TWA. *Surf. Interface Anal.* **1993**, *20*, 243–266.

263. Walton, J.; Fairley, N., Transmission-Function Correction for XPS Spectrum Imaging. *Surf. Interface Anal.* **2006**, *38*, 388–391.

264. Muir, M. M. P., Additional Observations on the Halogen Salts of Bismuth. *Pharm. J. Trans.* **1881**, *12*, 411.

265. Trucks, G. W.; Raghavachari, K.; Higashi, G. S.; Chabal, Y. J., Mechanism of HF Etching of Silicon Surfaces: A Theoretical Understanding of Hydrogen Passivation. *Phys. Rev. Lett.* **1990**, *65*, 504–507.

266. Knotter, D. M., Etching Mechanism of Vitreous Silicon Dioxide in HF-Based Solutions. *J. Am. Chem. Soc.* **2000**, *122*, 4345–4351.

267. Mikeska, K. R.; Bennison, S. J., Corrosion of Alumina in Aqueous Hydrofluoric Acid. *J. Am. Ceram. Soc.* **1999**, *82*, 3561–3566.

268. Kandi, D.; Martha, S.; Thirumurugan, A.; Parida, K. M., Modification of BiOI Microplates with CdS QDs for Enhancing Stability, Optical Property, Electronic Behavior toward Rhodamine B Decolorization, and Photocatalytic Hydrogen Evolution. *J. Phys. Chem. C* **2017**, *121*, 4834–4849.

269. Zhang, X.; Li, B. H.; Wang, J. L.; Yuan, Y.; Zhang, Q. J.; Gao, Z. Z.; Liu, L. M.; Chen, L., The Stabilities and Electronic Structures of Single-Layer Bismuth Oxyhalides for Photocatalytic Water Splitting. *Phys. Chem. Chem. Phys.* **2014**, *16*, 25854–25861.

270. Tang, Z.-K.; Yin, W.-J.; Le, Z.; Wen, B.; Zhang, D.-Y.; Liu, L.-M.; Lau, W.-M., Spatial Separation of Photo-Generated Electron-Hole Pairs in BiOBr/BiOI Bilayer to Facilitate Water Splitting. *Sci. Rep.* **2016**, *6*, 32764.

271. Radisavljevic, B.; Radenovic, A.; Brivio, J.; Giacometti, V.; Kis, A., Single-layer MoS2 transistors. *Nature Nanotechnology* **2011**, *6*, 147-150.

272. Choi, W.; Choudhary, N.; Han, G.; Park, J.; Akinwande, D.; Lee, Y. H., Recent development of two-dimensional transition metal dichalcogenides and their applications. *Mater. Today* **2017**, *20*.

273. Shinde, P. A.; Patil, A. M.; Lee, S.; Jung, E.; Chan Jun, S., Two-dimensional MXenes for electrochemical energy storage applications. *J. Mater. Chem. A* **2022**, *10*, 1105–1149.

274. Nan, J.; Guo, X.; Xiao, J.; Li, X.; Chen, W.; Wu, W.; Liu, H.; Wang, Y.; Wu, M.; Wang, G., Nanoengineering of 2D MXene-Based Materials for Energy Storage Applications. *Small* **2021**, *17*, 1902085.

275. Zhang, X.; Zhang, Z.; Zhou, Z., MXene-based materials for electrochemical energy storage. *J. Energy Chem.* **2018**, *27*, 73-85.

276. Cao, M.-S.; Cai, Y.-Z.; He, P.; Shu, J.-C.; Cao, W.-Q.; Yuan, J., 2D MXenes: Electromagnetic property for microwave absorption and electromagnetic interference shielding. *Chem. Eng. J.* **2019**, *359*, 12650–1302.

277. Kuo, C.-H.; Liu, C.-P.; Lee, S.-H.; Chang, H.-Y.; Lin, W.-C.; You, Y.-W.; Liao, H.-Y.; Shyue, J.-J., Effect of surface chemical composition on the work function of silicon substrates modified by binary self-assembled monolayers. *Phys. Chem. Chem. Phys.* **2011**, *13*, 15122–15126.

278. Roscioni, O. M.; Muccioli, L.; Mityashin, A.; Cornil, J.; Zannoni, C., Structural Characterization of Alkylsilane and Fluoroalkylsilane Self-Assembled Monolayers on SiO_2 by Molecular Dynamics Simulations. *J. Phys. Chem. C* **2016**, *120*, 14652–14662.

279. Szwajca, A.; Koroniak, H., Fluorinated SAMs on Si(001) surface: Surface electronic properties and structural aspects. *Phosphorus, Sulfur, and Silicon and the Related Elements* **2016**, *191*, 502–506.

280. Celle, C.; Suspène, C.; Ternisien, M.; Lenfant, S.; Guérin, D.; Smaali, K.; Lmimouni, K.; Simonato, J. P.; Vuillaume, D., Interface dipole: Effects on threshold voltage and mobility for both amorphous and poly-crystalline organic field effect transistors. *Organic Electronics* **2014**, *15*, 729–737.

281. Huang, C.; Katz, H. E.; West, J. E., Solution-Processed Organic Field-Effect Transistors and Unipolar Inverters Using Self-Assembled Interface Dipoles on Gate Dielectrics. *Langmuir* **2007**, *23*, 13223–13231.

282. Khaderbad, M. A.; Roy, U.; Yedukondalu, M.; Rajesh, M.; Ravikanth, M.; Rao, V. R., Variable Interface Dipoles of Metallated Porphyrin Self-

Assembled Monolayers for Metal-Gate Work Function Tuning in Advanced CMOS Technologies. *IEEE Trans. Nanotechnol.* **2010**, *9*, 335–337.

283. Reichel, C.; Würfel, U.; Winkler, K.; Schleiermacher, H.-F.; Kohlstädt, M.; Unmüssig, M.; Messmer, C. A.; Hermle, M.; Glunz, S. W., Electron-selective contacts via ultra-thin organic interface dipoles for silicon organic heterojunction solar cells. *J. Appl. Phys.* **2018**, *123*, 024505.

284. Natu, V.; Benchakar, M.; Canaff, C.; Habrioux, A.; Celerier, S.; Barsoum, M., A critical analysis of the X-ray photoelectron spectra of $Ti_3C_2T_z$ MXenes. *Matter* **2021**, *4*.

285. Persson, I.; Näslund, L.-Å.; Halim, J.; Barsoum, M. W.; Darakchieva, V.; Palisaitis, J.; Rosen, J.; Persson, P. O. Å., On the organization and thermal behavior of functional groups on Ti_3C_2 MXene surfaces in vacuum. *2D Materials* **2017**, *5*, 015002.

286. Benchakar, M.; Loupias, L.; Garnero, C.; Bilyk, T.; Morais, C.; Canaff, C.; Guignard, N.; Morisset, S.; Pazniak, H.; Hurand, S.; Chartier, P.; Pacaud, J.; Mauchamp, V.; Barsoum, M. W.; Habrioux, A.; Célérier, S., One MAX phase, different MXenes: A guideline to understand the crucial role of etching conditions on $Ti_3C_2T_x$ surface chemistry. *Appl. Surf. Sci.* **2020**, *530*, 147209.

287. Halim, J.; Cook, K. M.; Naguib, M.; Eklund, P.; Gogotsi, Y.; Rosen, J.; Barsoum, M. W., X-ray photoelectron spectroscopy of select multilayered transition metal carbides (MXenes). *Appl. Surf. Sci.* **2016**, *362*, 406–417.

288. Badr, H. O.; Montazeri, K.; El-Melegy, T.; Natu, V.; Carey, M.; Gawas, R.; Phan, P.; Qian, Q.; Li, C. Y.; Wiedwald, U.; Farle, M.; Colin-Ulloa, E.; Titova, L. V.; Currie, M.; Ouisse, T.; Barbier, M.; Rogalev, A.; Wilhelm, F.; Hans, M.; Schneider, J. M.; Tandoc, C.; Hu, Y.-J.; Snyder, J.; Barsoum, M. W., Scalable, Inexpensive, One Pot, Synthesis of Crystalline Two-dimensional Birnessite Flakes. *Matter* **2022**, *4*, 2365–2381.

289. Liao, T.; Sun, Z.; Dou, S. X., Theoretically Manipulating Quantum Dots on Two-Dimensional TiO_2 Monolayer for Effective Visible Light Absorption. *ACS Appl. Mater. Interfaces* **2017**, *9*, 8255–8262.

290. Sheng, L.; Liao, T.; Kou, L.; Sun, Z., Single-Crystalline Ultrathin 2D TiO_2 Nanosheets: A Bridge Towards Superior Photovoltaic Devices. *Mater. Today Energy* **2017**, *3*, 32–39.

291. Wang, A. S. D.; Sasaki, T., Titanium Oxide Nanosheets: Graphene Analogues with Versatile Functionalities. Chem. Rev. 2014, 114, 9455–9486.

292. Monticone, S.; Tufeu, R.; Kanaev, A. V.; Scolan, E.; Sanchez, C., Quantum size effect in TiO_2 nanoparticles: does it exist? *Appl. Surf. Sci.* **2000**, *162–163*, 565–570.

293. Varsano, D.; Giorgi, G.; Yamashita, K.; Palummo, M., Role of Quantum-Confinement in Anatase Nanosheets. *J. Phys. Chem. Lett*. **2017**, *8*, 3867-3873.

294. Migas, D. B.; Filonov, A. B.; Borisenko, V. E.; Skorodumova, N. V., Orientation Effects in Morphology and Electronic Properties of Anatase TiO_2 One-Dimensional Nanostructures. I. Nanowires. *Phys. Chem. Chem. Phys.* **2014**, *16*, 9479–9489.

295. Migas, D. B.; Filonov, A. B.; Borisenko, V. E.; Skorodumova, N. V., Orientation Effects in Morphology and Electronic Properties of Anatase TiO_2 One-Dimensional Nanostructures. II. Nanotubes. *Phys. Chem. Chem. Phys*. **2014**, *16*, 9490–9498.

296. Tosoni, S.; Pacchioni, G., Hydrogen Adsorption on Free-Standing and Ag–Pt Supported TiO_2 Thin Films. *J. Phys. Chem. C* **2019**, *123*, 7952–7960.

297. Rajaraman, T. S.; Parikh, S. P.; Gandhi, V. G., Black TiO_2: A Review of its Properties and Conflicting Trends. *Chem. Eng. J*. **2020**, *389*, 123918.

298. Carl, A. D.; Kalan, R. E.; Obayemi, J. D.; Zebaze Kana, M. G.; Soboyejo, W. O.; Grimm, R. L., Synthesis and Characterization of Alkylamine-Functionalized Si(111) for Perovskite Adhesion With Minimal Interfacial Oxidation or Electronic Defects. *ACS Appl. Mater. Interfaces* **2017**, *9*, 34377–34388.

299. Nyholm, R.; Martensson, N.; Lebugle, A.; Axelsson, U., Auger and Coster-Kronig Broadening Effects in the 2p and 3p Photoelectron Spectra From the Metals ^{22}Ti–^{30}Zn. *J. Phys. F: Met. Phys*. **1981**, *11*, 1727-1733.

300. Scanlon, D. O.; Dunnill, C. W.; Buckeridge, J.; Shevlin, S. A.; Logsdail, A. J.; Woodley, S. M.; Catlow, C. R. A.; Powell, M. J.; Palgrave, R. G.; Parkin, I. P.; Watson, G. W.; Keal, T. W.; Sherwood, P.; Walsh, A.; Sokol, A. A., Band alignment of rutile and anatase TiO_2. *Nat. Mater*. **2013**, *12*, 798-801.

301. Walter, M. G.; Warren, E. L.; McKone, J. R.; Boettcher, S. W.; Mi, Q.; Santori, E. A.; Lewis, N. S., Solar Water Splitting Cells. *Chem. Rev*. **2010**, *110*, 6446-6473.

302. Yamada, Y.; Kanemitsu, Y., Determination of electron and hole lifetimes of rutile and anatase TiO_2 single crystals. *Appl. Phys. Lett*. **2012**, *101*, 133907.

303. Tamaki, Y.; Furube, A.; Katoh, R.; Murai, M.; Hara, K.; Arakawa, H.; Tachiya, M., Trapping dynamics of electrons and holes in a nanocrystalline TiO_2 film revealed by femtosecond visible/near-infrared transient absorption spectroscopy. *C. R. Chim*. **2006**, *9*, 268-274.

304. Tamaki, Y.; Furube, A.; Murai, M.; Hara, K.; Katoh, R.; Tachiya, M., Dynamics of efficient electron–hole separation in TiO_2 nanoparticles revealed by femtosecond transient absorption spectroscopy under the weak-excitation condition. *Phys. Chem. Chem. Phys*. **2007**, *9*, 1453–1460.

305. Katoh, R.; Murai, M.; Furube, A., Transient absorption spectra of nanocrystalline TiO_2 films at high excitation density. *Chem. Phys. Lett*. **2010**, *500*, 309–312.

306. Schneider, J.; Bahnemann, D., Strong Transient Absorption of Trapped Holes in Anatase and Rutile TiO_2 at High Laser Intensities. *J. Phys. Chem. C* **2018**, *122*, 13979–13985.

307. Samsudin, E. M.; Abd Hamid, S. B., Effect of Band Gap Engineering in Anionic-Doped TiO_2 Photocatalyst. *Appl. Surf. Sci*. **2017**, *391*, 326–336.

308. Choudhury, B.; Choudhury, A., Oxygen Defect Dependent Variation of Band Gap, Urbach Energy and Luminescence Property of Anatase, Anatase–Rutile Mixed Phase and of Rutile Phases of TiO_2 Nanoparticles. *Phys. E (Amsterdam, Neth.)* **2014**, *56*, 364–371.

309. Sakai, N.; Ebina, Y.; Takada, K.; Sasaki, T., Electronic Band Structure of Titania Semiconductor Nanosheets Revealed by Electrochemical and Photoelectrochemical Studies. *J. Am. Chem. Soc*. **2004**, *126*, 5851–5858.

310. Trasatti, S., The Absolute Electrode Potential: An Explanatory Note (Recommendations 1986). *Pure Appl. Chem*. **1986**, *58*, 955-966.

311. Seah, M. P., Background subtraction: I. General behaviour of Tougaard-style backgrounds in AES and XPS. *Surf. Sci*. **1999**, *420*, 285–294.

312. Seah, M. P., Post-1989 calibration energies for X-ray photoelectron spectrometers and the 1990 Josephson constant. *Surf. Interface Anal*. **1989**, *14*, 488–488.

A

CH. 4 SUPPORTING INFORMATION: QUANTIFICATION OF SURFACE REACTIVITY AND STEP-SELECTIVE ETCHING CHEMISTRY ON SINGLE-CRYSTAL BiOI(001)

A.1 Materials and Chemicals

All reagents were used as received unless otherwise stated. A Millipore Milli-Q system provided 18 MΩ cm resistivity water for all water requirements. Synthesis procedures for single-crystal BiOI(001) utilized BiOI (98%, Alfa Aesar), Bi (99.5%, Alfa Aesar), Bi_2O_3 (99.9%, Strem Chemicals), BiI_3 (99%, Sigma-Aldrich), I_2 (99.99%Alfa Aesar). Specific preparation methods utilized quartz growth ampoules formed from quartz fused silica tubing (19 mm O.D., 17 mm I.D., 4' long, Technical Glass Products, Inc., Painesville, Ohio) with particular cleaning steps prior to synthesis. Cleaning and preparation of

quartz tubes preceding syntheses alternatively utilized NaOH (98.5%, Acros Organics) or KOH (86.6%, Fisher Chemical). Prior to chemical loading, stock quartz tubes were cut to ~40 cm lengths, sealed at one end under an oxypropane flame, and submerged in a 10 wt % $KOH_{(aq)}$ or $NaOH_{(aq)}$ bath for at least one week. Following this base-bath submersion, tubes were rinsed copiously with water and stored in a ¿100 °C oven until use.

Solutions for etching studies of single-crystal BiOI(001) included water, acetone, aqueous hydrofluoric acid, and aqueous hydrochloric acid. ***Caution:*** *Aqueous hydrogen fluoride is an acute poison that is toxic at even small amounts and limited exposures.* The $HF_{(aq)}$ was diluted to 5.8 M (9.8%) in water from a commercial stock solution (49%, electronic grade, Transene Company Inc., Danvers, Massachusetts). Cleaning and preparation of glass test tubes preceding organic rinsing procedures utilized piranha solution. ***Caution:*** *piranha solution is a strong acid and a strong oxidant that reacts highly exothermically with organic matter.* Piranha solution consisted of a freshly prepared 3:1 mixture of concentrated sulfuric acid (98%, Fisher Chemical) and $H_2O_{2(aq)}$ (35 wt %, Alfa Aesar).

A.2 Synthesis of Single-Crystal and Large-Grain BiOI

Etching chemistry and surface analyses of BiOI(001) utilized single-crystal and large-grain BiOI samples synthesized via high-temperature in vacuo vapor transport. We delineate the employed crystal growth to include physical vapor transport (PVT, or sublimation) of the single-source material, and chemical vapor transport (CVT) from multiple reagents with additional molecular iodine as a transport agent.

Prior to growth reactions, the base-bath-cleaned and oven-based ~40 cm quartz growth ampoules were cooled and loaded with reagents. For BiOI(001) growth via physical vapor transport, the sole reagent was 1–2 g of BiOI. For chemical vapor transport, stoichiometric combinations of Bi + I_2 + Bi_2O_3, or BiI_3 + Bi_2O_3, or BiOI that totaled 1–2 g were combined with 300–500 mg I_2. Each loaded ampoule was sealed in a rotary evacuator connected to a diffusion-pump-equipped Schlenk line with a base pressure below 1×10^{-3} Torr.

Figure A.1 illustrates the tube-sealing apparatus. The tube sealing apparatus is based around connecting 1″ or 3/4″ O.D. glass tubes to a repurposed BÜCHI Rotavapor R 110. In place of a standard vapor tube, we machined an aluminum 6061 piece to fit into the tapered motor fitting, seal against a KD–22 gasket, and terminate in a KF 16 fitting for adapting to an ampoule rather than a traditional 24/40 ₹ fitting. (The aluminum piece demonstrates pitting over prolonged use, and replacing this with a glass vapor tube that terminates in a glass KF 16 fitting – à la EVAC AG, Grabs, Switzerland – would obviate this issue.) Ampoules connect to the KF 16 fitting through

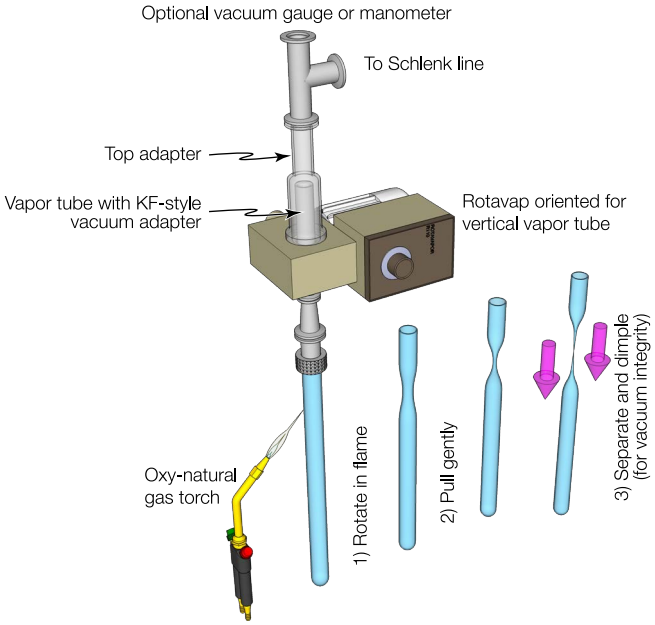

Figure A.1. The tube sealing setup is based around a solvent-removing rotary evaporator that has been modified with KF-style fittings to a chemical ampoule via a KF-to-ultra-torr adapter, and further modified to remove a condenser in favor of a direct connection to a vacuum line. The even heat distribution on the rotating glass or quartz obviates the need for complicated and potentially dangerous torch work.

an ultra-torr-style compression fitting such as the KF16-CP075 from Duniway Stockroom (Freemont, California) that adapts to the 19 mm or 3/4" O.D. quartz employed in the present study. On the vacuum (top) side, we replaced the outer glass piece around the KD–22 gasket (that is typically a condenser of some sort) based on a glass fitting (based on a 50 mm Rotavap flange adapter, part #946054 Adams & Chittenden Scientific Glass Coop., Berkeley, California) to a vacuum adapter that is in turn connected to a vacuum manifold or Schlenk line with an intervening liquid nitrogen cryotrap.

To minimize sublimation of iodine or other components, the bottom of the ampoule containing the source material was cooled in a liquid-nitrogen bath for two minutes preceding evacuation as well as throughout the sealing procedure. An oxygen-natural gas torch sealed the growth ampoules to ~20–25 cm lengths under evacuation to <50 mTorr. For CVT growth trials, the resulting lengths yielded a molecular iodide loading of 3–5 mg per mL of ampoule internal volume.

All syntheses utilized horizontally mounted 5-cm-I.D. tube furnaces that were constructed from two abutting tubular ceramic heaters (CRFC-series, Omega

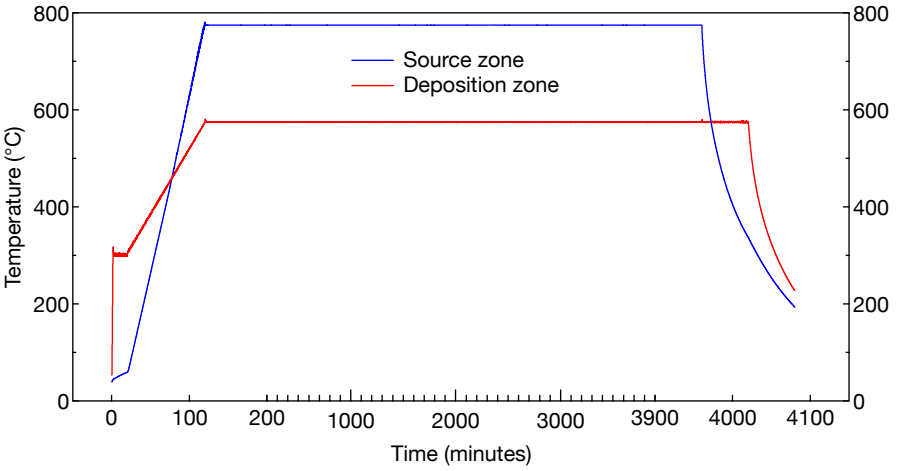

Figure A.2. Actual temperature profiles for a (blue) source zone and a (red) deposition zone for a characteristic growth run of BiOI(001). Note the variable *x*-axis scaling. 1 minor tick = 100 minutes.

Engineering, Norwalk, CT). A 30-cm-long and a 15-cm-long heater defined the independently controlled source zone and deposition zone, respectively. Temperature controllers (Love 32B, Dwyer Instruments, Michigan City, IN) recorded temperatures at K-type thermocouples (Nextel ceramic braid insulation, Omega Engineering, spot welded in house) that were positioned at the center of each zone. An in-house-written LabVIEW program interfaced with the temperature controllers for conducting temperature programs. In a typical program, the deposition zone was heated directly to 300 °C, after which both zones were ramped to their soak temperature over 2 h. The initial heating of the deposition zone resulted in that zone remaining at a higher temperature than the source zone for the initial ~1 h of the heating ramp to clean out the deposition zone. Following a soak period that was typically 64 h, heating ceased at the source zone, while the deposition zone maintained its soak temperature for an additional 1 h to prevent deleterious condensation on any crystals in the deposition zone during cooling. Upon stopping the deposition zone heating, the source zone was <350 °C and remained at a lower temperature than the deposition zone for the remainder of the cooling period to maximize deposition *away* from the crystals during cooling. Temperature ranges for the source zone soak ranged from 725–775 °C with 775 °C representing a typical soak temperature. Temperature ranges for the deposition zone soak ranged from 525–575 ° C with 550 °C representing a typical soak temperature. Figure A.2 displays typical T vs t data for both the source zone (blue) and the deposition zone (red). Note the non-linear time axis in Fig. A.2 that highlights the ramp regions at the expense of the long soak times.

Grown crystals remained stored in their respective growth ampoules in the dark until use.

In our experience, growth ampoules that were opened directly in an air ambient were severely broken by the turbulent equilibration with the atmosphere and the delicate BiOI crystals were often concomitantly destroyed. To obviate sample destruction during atmospheric pressure equilibration, the ampoules for BiOI that comprised all data under consideration in this manuscript were scored in between the source and deposition regions, loaded into a wire-reinforced flexible vacuum hose, and evacuated on the Schlenk line. Ampoules were cracked open by flexing the vacuum hose at the score point under a passive vacuum then subsequently and slowly returned to ambient pressure for crystal removal. The samples that were not used directly were stored in plastic petri dishes that were wrapped in aluminum foil and stored in the dark until use.

A.3 Etching and surface reactivity

Under an air ambient, samples were individually subjected to etchants, solvent cleaning, or both. Such treatments included sonication in water; sonication in acetone; immersion for 10 s in 6 M $HF_{(aq)}$ and a subsequent water rinse; or to sequential steps of immersion for 10 s in 6 M $HF_{(aq)}$, a water rinse, and sonication in acetone. All $HF_{(aq)}$ etching procedures consisted of single-side exposure with a disposable plastic tweezer,[S1] while rinses with water or organic solvents immersed the entire sample. Water rinses following $HF_{(aq)}$ etching did not employ sonication unless explicitly stated. Plastic tweezers underwent sequential sonication in acetone, IPA, and water prior to any cleaning or etching protocol.

For sonication in water or acetone, samples in a piranha-cleaned test tube filled alternatively with water or acetone that were submerged directly in the sonicator bath were significantly broken from the high-frequency ultrasonic waves. To obviate sample destruction, the sonication in water or acetone consisted of "padding" the water- or acetone-filled test tubes from the sonicator bath with various vessels filled with water. A beaker filled with water was submerged in the sonicator bath water. Then, a test tube filled with water was immersed halfway in the water-filled beaker. Lastly, a piranha-cleaned glass test tube was filled alternatively with either water or acetone and immersed halfway in the test tube of water. The samples were held with plastic tweezers, submerged completely in the water- or acetone-filled test tube for 30 s, and then dried on a cloth wipe.

For the $HF_{(aq)}$ etch and subsequent water rinse, samples were held with plastic tweezers and the 6 M $HF_{(aq)}$ was added drop-wise to the upward-facing sample surface with a plastic Pasteur pipette until the entire surface

was covered (surface tension was sufficient to ensure single-side exposure).[S1] The respective dilute acid solution remained on the surface for 10 s, was carefully removed ensuring no exposure to the bottom face, rinsed copiously with water, and dried on a cloth wipe.

For sequential HF etching, a water rinse, and sonication in acetone, samples were held with tweezers, subjected to a single-side 6 M $HF_{(aq)}$ etch as described prior, rinsed copiously with water, and then subjected to sonication in acetone as described previously. Directly following acetone sonication, the sample was dried etched-face-up on a cloth wipe. Importantly, following HF exposure, careful attention was paid throughout subsequent rinsing stages to keep track of the etched face for later analysis.

A.4 Photoelectron spectroscopy

A.4.1 XPS experimental methods

A PHI 5600 XPS system with a third-party data acquisition system (RBD Instruments, Bend Oregon) acquired all photoelectron spectra as detailed previously.[S2] Analysis chamber base pressures were $<1 \times 10^{-9}$ Torr. A hemispherical energy analyzer that is positioned at 90° with respect to the incoming monochromated Al Kα X-radiation and 54.7° with respect to a non-monochromated source of Al Kα X-rays collected the photoelectrons. Analyses of chemical composition, and Bi:O:I ratios as found in Figs. 4 and 7, and Tables 1 and 2 in the main text utilized monochromated Al K_α X-radiation. Angle-resolved XPS experiments that yielded the data in Fig. 8 in the main manuscript utilized the non-monochromated Al K_α X-ray source. The angle-resolved photoelectron experiments[S3] utilized angles of 15–75° between the analyzer and the sample normal angle, while all other X-ray-based experiments utilized 45° angles between the sample normal angle and both the x-ray source and the analyzer. In all experiments, survey spectra utilized a 117 eV pass energy, a 0.5 eV step size, and a 50-ms-per-step dwell time. All high-resolution XP spectra employed a 23.5 eV pass energy, 0.025 eV step size, and a 50 ms dwell time per step. Consistent positions of I 3d and Bi 4f features ascribed to the BiOI samples obviated a need for charge neutralization.

For samples subjected to any of the aforementioned rinsing and/or etching procedures, samples were mounted on steel XPS pucks and evacuated in the loading chamber of the instrument directly following chemical processing. For tape-cleaved samples, flakes were mounted on a freshly-cleaned steel puck with carbon tape, mechanically exfoliated with VWR laboratory tape under an air ambient, and evacuated in the loading chamber <15 s following cleaving.

Post-acquisition fitting utilized an in-house-developed LabVIEW-based program. Data fitting employed baseline-corrected, pseudo-Voigt, GL(x)-style

functions where x non-linearly scales from a pure Gaussian ($x = 0$) to a pure Lorentzian ($x = 100$).[S4] Baseline functions were either of a linear type, a Shirley type,[S5] or a Tougaard style with $B = 2900$ eV^2 and $C = 1643$ eV^2 within a universal function that is scaled to the height of the photoelectron data.[S6–8] Optimization routines utilize the built-in LabVIEW implementation of the Levenberg-Marquardt algorithm for multiparameter fitting.

Fitting of the Cl 2p, C 1s, and O 1s features utilized a linear background and GL(30) functional peak shapes. When fitting of the C 1s or O 1s regions necessitated multiple fit peaks, they were constrained to have identical full width at half max values. For some samples, the C 1s region contained neighboring K 2p features. In such cases, the linear background was fit spanning both the C 1s and K 2p features. K 2p and Cl 2p doublets were individually constrained to have identical full-width-at-half-max (fwhm) values with the $2p_{1/2}$ peaks containing 50% of the area of the $2p_{3/2}$ peaks. Bi 4f regions fit with a single Shirley-shaped background were not representative of the true spectral background of the data. As such, fitting of the Bi 4f region necessitated two abutting Shirley-shaped backgrounds sharing a common boundary at ~161 eV. One Shirley-shaped background spanned the lower binding energy portion of the region to fit the background of the Bi $4f_{7/2}$ peak and a second Shirley-shaped background spanned the higher binding energy portion of the region to fit the background of the Bi $4f_{5/2}$ peak. All Bi 4f features were fit with GL(70) functional peak shapes and the Bi doublets were constrained to have identical fwhm values with $4f_{5/2}$ peaks containing 75% of the area of $4f_{7/2}$ peaks. The I 3d features utilized a Tougaard-shaped background and GL(80) functional peak shapes. The F 1s region of the spectrum contains an overlapping Bi 4p feature. Thus, fitting of the F 1s region employed a Shirley-shaped background spanning both the F 1s and Bi 4p features. In the F 1s region, the Bi 4p and the F 1s features were respectively fit with GL(80) and GL(30) functional peak shapes and the fwhm values were left unconstrained. Figure A.3 represents a combined F 1s + Bi $4p_{3/2}$ region for BiOI(001) following a prolonged HF etch.

Quantification of Bi 4p-to-I 3d, Bi 4f-to-O 1s, I 3d-to O-1s, C 1s-to-Bi 4f, and Bi 4f-to-F 1s ratios utilized sensitivity-factor-corrected peak areas which were defined as the quotient of the raw peak area and the respective sensitivity factor. We employed instrument-specific sensitivity factors for photoelectron collection at 90° with respect to the incident X-ray beam. Factors for Bi 4f, C 1s, O 1s, I 3d, and F 1s were 7.632, 0.296, 0.711, 5.337, and 1.000 respectively.[S9] For quantification of Bi 4f-to-O 1s and I 3d-to-O 1s ratios, only O 1s features ascribed to oxygen in the BiOI lattice at ~529 eV were considered. Features ascribed to adventitious oxygen species did not factor into calculated ratios. For quantification of C 1s-to-Bi 4f ratios that serve as an approximate measure of sample cleanliness, the sole contributor to the C 1s peak area was that corresponding to the feature centered near 284.8 eV ascribed to adventitiously adsorbed carbon species. However, as described in

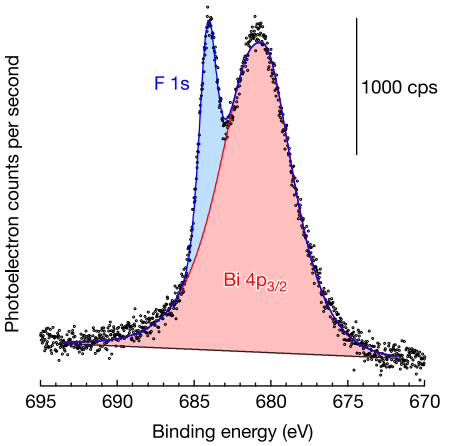

Figure A.3. The sharp F 1s feature at 684.13 eV (blue) is straightforwardly deconvolved from the broad Bi $4p_{3/2}$ feature at 680.59 eV (red). Thus the shape of the Bi $4p_{3/2}$ feature itself effectively serves as the background for fitting and quantifying F 1s in HF-treated BiOI(001) samples.

the results section, the position of the adventitious C 1s feature demonstrated small surface-treatment-dependent shifts in energy position by as much as 1 eV that was quantified by a binding-energy invariance of Bi 4f and I 3d features with surface treatment.

A.4.2 UPS experimental methods

A gas-discharge light source (UVS 40A2, Prevac, Rogów, Poland) mounted in the PHI 5600 instrument provided He I radiation at $\mathbf{E}_{\mathrm{He\,I}}$ = 21.218 eV (58.433 nm) from research-grade helium (Airgas). We utilize a –35 V substrate bias and collect photoelectrons at the sample normal angle to both isolate and maximize the desired spectral contributions of secondary electrons both from the sample and from the analyzer. To verify analyzer transmission and detection linearity across the ~25 eV acquisition window for the low kinetic energy electrons from ultraviolet photoemission, we collected UP spectra on Au for a range of substrate biases. UP spectra that were collected for substrate biases between –20 eV and –50 eV revealed no observable difference in shape or energy positions, and no observable signal attenuation on either the Fermi or the secondary-electron cutoff side of the spectra. This validated the use of –35 V substrate biases for all collected UP spectra.

Off-line analyses of freshly evaporated and a freshly argon-sputter-cleaned gold sample verified instrumental calibration. Both X-ray and UV photoelectron spectra were calibrated using freshly Argon-ion-sputtered samples of Cu and Au foils to establish the scaling factor and work function of the

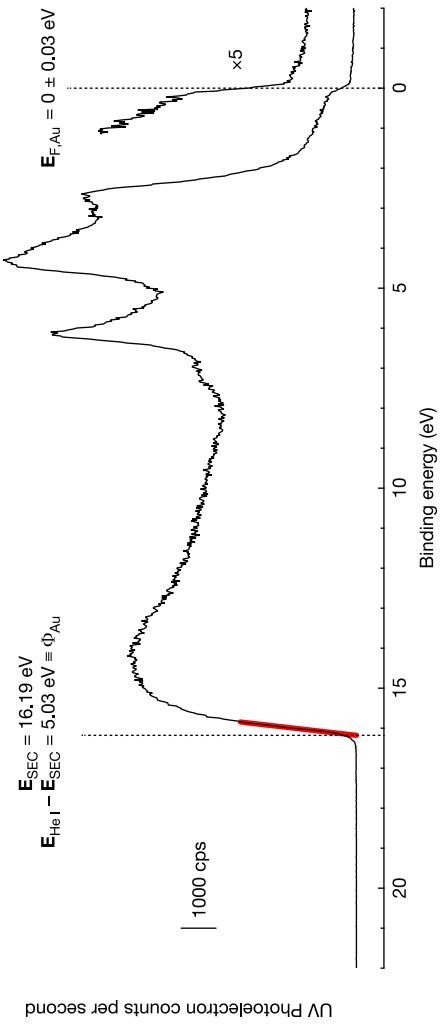

Figure A.4. He I UV photoelectron spectrum of freshly sputtered polycrystalline Au foil indicating a Fermi level, $E_{F,Au} = 0.00 \pm 0.03$ eV. The difference of the energy of the incoming radiation, $E_{He\,I} = 21.218$ eV minus the x-axis intercept of a linear fit to the secondary-electron cutoff, $E_{SEC} = 16.187$ eV yields a work function of $\Phi_{Au} = 5.03 \pm 0.03$ eV.

instrument. Calibration revealed energy positions of $\mathbf{E}_{\mathrm{Cu\ 2p_{3/2}}} = 932.67$ eV and $\mathbf{E}_{\mathrm{Au\ 4f_{7/2}}} = 84.00$ eV for the respective Cu or Au sample.[S10] Figure A.4 presents a UP spectrum for a freshly-evaporated and freshly argon-sputter-cleaned Au sample following X-ray photoelectron calibration. The spectrum in Fig. A.4 verifies a spectrometer calibration of binding energy values to the Fermi level energy of gold, $\mathbf{E}_{\mathrm{F,Au}} = 0.00 \pm 0.05$ eV. From plots of photoelectron counts vs bias-corrected binding energy, the x-axis intercept of linear regressions quantifies a secondary-electron-cutoff energy, $\mathbf{E}_{\mathrm{SEC}}$, and a valence-band-edge (maximum) energy, $\mathbf{E}_{\mathrm{VBM}}$. Considering the binding energy calibration of the instrument, we report sample work function values, Φ, as the difference between $\mathbf{E}_{\mathrm{He\ I}}$ and the secondary electron cutoff energy, or $\Phi = \mathbf{E}_{\mathrm{He\ I}} - \mathbf{E}_{\mathrm{SEC}}$. For the semiconductor samples of interest, the onset of photoelectron counts near the Fermi region corresponds to the valence band maximum energy, $\mathbf{E}_{\mathrm{VBM}}$. We report Fermi level energies relative to valence band maximum energies, or $\mathbf{E}_{\mathrm{F}} - \mathbf{E}_{\mathrm{VBM}}$ where a regression fit to the x-axis determines $\mathbf{E}_{\mathrm{VBM}}$, and $\mathbf{E}_{\mathrm{F}} = 0$ eV in the photoelectron spectra as the sample Fermi level is equilibrated to the Fermi level of gold, $\mathbf{E}_{\mathrm{F,Au}} \equiv 0$ eV. As ultrahigh vacuum bakeouts can yield a small perturbation in instrument calibration that would deleteriously affect data analyses, both calibration and BiOI data acquisition were collected in the same "bakeout window."

A.4.3 Angle-resolved overlayer model

We utilized a combination of angle-resolved X-ray photoelectron spectroscopy and overlayer models to support descriptions of particular surface termination on BiOI(001) as a function of chemical treatment (or "nascent" surfaces from a freshly cracked vapor-transport growth tube).[S3,11] In these instances, we utilize the exponential attenuation of photoelectron current as a function of depth below the surface. For high take-off angles relative to the surface normal angle, photoelectron signals are particularly sensitive to the chemical speciation of the top few atomic layers. Ratios of one photoelectron counts arising from chemical species to counts from another, say, from bismuth and from iodine, will demonstrate a strong take-off-angle dependence based on which atomic species is closer to the surface. For species "A", eq A.1 describes the partial contribution of photoelectron intensity, I_{A}, from an infinitesimally thick layer at depth z below the surface.

$$\frac{\partial I_{\mathrm{A}}}{\partial z} \propto \rho_{\mathrm{A}}(z) \exp\left(\frac{-z}{\lambda_{\mathrm{A,\,self}} \cos\theta}\right) \tag{A.1}$$

Equation A.1 relies on terms including the number density per unit volume of species A as a function of depth $\rho_{\mathrm{A}}(z)$, the photoelectron takeoff angle θ vs the sample normal angle, and the photoelectron attenuation length λ. We present λ as $\lambda_{\mathrm{A,\,self}}$ to indicate that we are considering photoemission

of electrons from species A traveling only through the material from which they originated, that is to say, the material itself. We present the derivative of intensity as being proportional to the given terms to indicate a reliance on additional terms such as the x-ray photon flux in photons per area per time, the photoionization cross section in area per atom, the instrument-specific angular detection efficiency, the efficiency of photoelectron production, the sample detection area, and an instrument-specific photoelectron detection efficiency. We ignore these terms based on utilizing experimentally acquired intensity ratios, say $I_{\mathrm{Bi\,4f}} \div I_{\mathrm{I\,3d}}$ that are collected for several photoelectron take-off angles, θ, between 15 and 75°, and normalizing each ratio to the ratio at $\theta = 45°$. This effectively yields a ratio of ratios, $\frac{I_{\mathrm{Bi\,4f}}}{I_{\mathrm{I\,3d}}} \div \frac{I^{\theta=45°}_{\mathrm{Bi\,4f}}}{I^{\theta=45°}_{\mathrm{I\,3d}}}$, in which the spectrometer, ionization, and transmission terms cancel out and further obviates the need to consider sensitivity factors.

Commonly, eq A.1 is integrated so as to yield eq A.2 that is commonly applied over a depth interval [*a*,*b*] that is related to the thickness of an overlayer or its substrate.

$$I_{\mathrm{A}} \propto \int_a^b \rho_{\mathrm{A}}(z) \exp\left(\frac{-z}{\lambda_{\mathrm{A,\,self}} \cos\theta}\right) \mathrm{d}z \tag{A.2}$$

Typically, the number density term is brought outside of the integral as the species of interest is uniformly or sufficiently uniformly distributed through the layer of interest, but that is not the best description in the present study. We consider single-crystal BiOI(001) flakes with a [001] vector that is parallel both to the defined z depth into the material as well as to the c-axis of the crystal. Considering the layered atomic arrangement in BiOI and the direction under study, $\rho_{\mathrm{A}}(z)$ is not a constant function but rather is a function of depth and is quantized. (There are no bismuth atoms in an iodine layer of BiOI, so $\rho_{\mathrm{Bi}}(z)$ would be 0 in that layer.)

Figure A.5 presents the unit cell of BiOI with cell-relative layer spacing and differential spacing in nanometers. Based on the cell in Fig. A.5, we think about layer stacking in the [001] direction as two half-unit cells that are stacked head-to-head and tail-to-tail (as well as rotated by 90° along a [001] vector). Importantly for the terminations considered below, each of the half-unit cells is charge neutral, and contain one atom each of Bi^{3+}, O^{2-}, and I^{-} for a complete charge-neutral unit-cell stoichiometry of $Bi_2O_2I_2$. The last point of note is that the unit cell in Fig. A.5 draws the strongly polar covalent bonds that exist between oxygen and bismuth and between bismuth and iodide atoms in the BiOI lattice. The weak van der Wall bonds that hold individual layers together are implicit and reside between the adjacent (001)-parallel iodide layers in the middle of the Fig. A.5 cell.

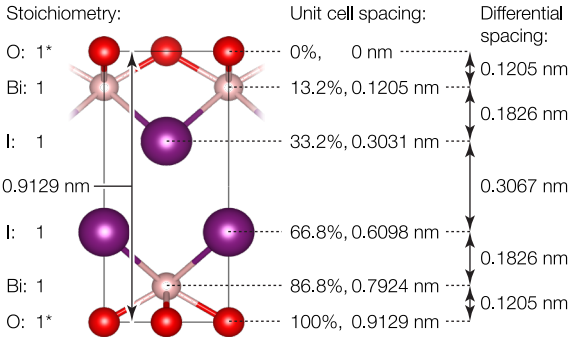

Figure A.5. Unit cell of BiOI with cell-relative layer spacing and differential spacing in nanometers. The indicated 0.9129 nm distance refers to the *c*-axis unit cell length that is parallel to the crystal [001] vector. Sphere sizes are based on a red O^{2-} with a 0.126 nm crystal ionic radius, a 0.206 nm radius for purple I^{-}, and a 0.117 pm radius for peach Bi^{3+}.

Thus, representing the photoelectron intensity for species A an integral as presented in eq A.2 may not be as useful for interpreting BiOI(001) XPS data as a summation with terms given for layers in which $\rho_A(z) \neq 0$. In such a summation of atomic layer contributions, a volume density such as $\rho_A(z)$ makes less sense than a number density of atoms of A per unit area slice at depth z, or $\sigma_A(z)$. Equation A.3 defines photoelectron intensity of species A as the resulting contribution of the i^{th} distinct atomic layer.

$$I_A \propto \sum_i \sigma_{A,i}(z_i) \exp\left(\frac{-z_i}{\lambda_{A,\,\text{self}} \cos\theta}\right) \tag{A.3}$$

With eq A.3 and Fig. A.5, specific terminations define the bismuth-oxide-terminated BiOI(001) (frame **A**) and iodide-terminated BiOI(001) (frame **B**) surfaces in Fig. A.6. Figure A.6 repeats Fig. 1 in the main text with the addition of lengths, distances, and unit cell indices relevant to the numerical model.

Although displayed second, we will describe the iodine-terminated photoelectron model in Fig. A.6**B** first. From an infinitely thick BiOI(001) crystal, we assume iodine termination takes the form of figuratively slicing the BiOI unit cell in a (001)-parallel slice between the two Van-der-Waals-bonded iodide layers shown in Fig. A.5 and otherwise typical unit cell stacking. We represent the unit cell stacking with an indexing variable n that starts at 0, which is to say that the top-most unit cell is indexed as the 0^{th} unit cell while the next unit cell below it is the 1^{st} and so forth. Considering the atomic layer distances and spacing given in Fig. A.5, we define the topmost atomic layer to be the surface at $z = 0$ and subsequent atomic layers below the surface as a function of interatomic-layer distances in A.5, the cell index n, and the

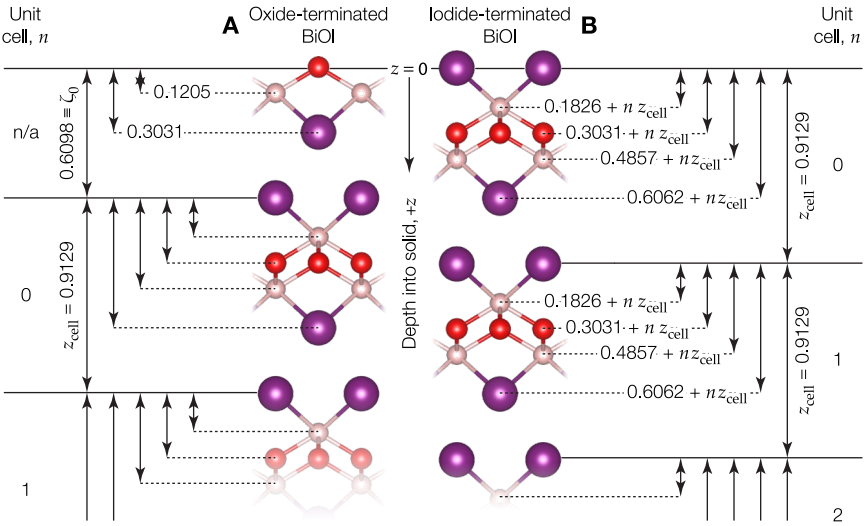

Figure A.6. Both **A** bismuth-oxide terminated, and **B** I-terminated BiOI(001) surfaces with relative atomic layer spacing and unit-cell spacing relative to a top layer that we define as $z = 0$. Cell periodicity enables atomic layer spacing definitions as a function of unit cell number below the surface, n, and the unit cell height itself, $z_{\text{cell}} = 0.9129$ nm. The oxide-terminated surface contains an additional half-unit cell that we exclude from the layer periodicity. All distance values are in nm.

unit cell height z_{cell}. From these heights, we can derive expressions of iodide-terminated BiOI(001) for $I_{\text{Bi 4f}}$, $I_{\text{O 1s}}$, and $I_{\text{Br 3d}}$. As mentioned above, we need not worry about the sensitivity factors since we are presenting experimental results as a ratio of ratios. Since we are representing the experimental data as a ratio, the number density for the i^{th} atomic layer per surface area term in eq A.3, $\sigma_{\text{A},i}(z_i)$, is simplified by considering that as long as the areas for each intensity term is the same (*i.e.* not capricious) then that area can be arbitrary. So, we arbitrarily choose the $a \times b = 0.1588$ nm^2 area of the BiO unit cell that yields $\sigma_{\text{Bi}}(z_i) = 1$ area^{-1}, $\sigma_{\text{O}}(z_i) = 2$ area^{-1}, and $\sigma_{\text{I}}(z_i) = 1$ area^{-1} for all atomic layers i. Below, we do not include the units on σ values as they cancel out in considering identical $a \times b$ unit cell areas. We can define the X-ray photoelectron intensities for the Bi 4f, O 1s, and I 3d features for iodide-terminated BiOI(001) as in eqs A.4–A.6. These equations rely on the sum $\sum_{n=0}^{\infty} \exp -qn = \frac{\exp q}{\exp q - 1}$, and we drop the "self" from each λ term as the photoelectrons are all traveling through BiOI itself with no consideration for an attenuation due to interfacial contamination.

For bismuth-oxide-terminated BiOI(001) as in Fig. A.6**A**, we envision a termination that includes one additional half-unit cell stacked on top of an iodide-terminated BiOI(001) cell. As mentioned above, each half-unit cell is charge neutral, and in this case terminated with oxygen. Notably, this

bismuth-oxide termination in Fig. A.6**A** carries a 1:1 bismuth-to-oxygen stoichiometry in contrast to the Bi_2O_3 stoichiometry of the variously-structured compounds that are named bismuth oxide.

$$\begin{aligned} I_{\text{Bi 4f,I-term}} &\propto \sum_{n=0}^{\infty}\left[\exp\left(\frac{-0.1826\,\text{nm} - n\,z_{\text{cell}}}{\lambda_{\text{Bi}}\cos\theta}\right) + \exp\left(\frac{-0.4857\,\text{nm} - n\,z_{\text{cell}}}{\lambda_{\text{Bi}}\cos\theta}\right)\right] \\ &\propto \left[\exp\left(\frac{-0.1826\,\text{nm}}{\lambda_{\text{Bi}}\cos\theta}\right) + \exp\left(\frac{-0.4857\,\text{nm}}{\lambda_{\text{Bi}}\cos\theta}\right)\right]\sum_{n=0}^{\infty}\exp\left(\frac{-n\,z_{\text{cell}}}{\lambda_{\text{Bi}}\cos\theta}\right) \\ &\propto \left[\exp\left(\frac{-0.1826\,\text{nm}}{\lambda_{\text{Bi}}\cos\theta}\right) + \exp\left(\frac{-0.4857\,\text{nm}}{\lambda_{\text{Bi}}\cos\theta}\right)\right]\frac{\exp\left(\frac{z_{\text{cell}}}{\lambda_{\text{Bi}}\cos\theta}\right)}{\exp\left(\frac{z_{\text{cell}}}{\lambda_{\text{Bi}}\cos\theta}\right)-1} \end{aligned} \tag{A.4}$$

$$\begin{aligned} I_{\text{O 1s,I-term}} &\propto 2\sum_{n=0}^{\infty}\exp\left(\frac{-0.3031\,\text{nm} - n\,z_{\text{cell}}}{\lambda_{\text{O}}\cos\theta}\right) \\ &\propto 2\exp\left(\frac{-0.3031\,\text{nm}}{\lambda_{\text{O}}\cos\theta}\right)\sum_{n=0}^{\infty}\exp\left(\frac{-n\,z_{\text{cell}}}{\lambda_{\text{O}}\cos\theta}\right) \\ &\propto 2\exp\left(\frac{-0.3031\,\text{nm}}{\lambda_{\text{O}}\cos\theta}\right)\frac{\exp\left(\frac{z_{\text{cell}}}{\lambda_{\text{O}}\cos\theta}\right)}{\exp\left(\frac{z_{\text{cell}}}{\lambda_{\text{O}}\cos\theta}\right)-1} \end{aligned} \tag{A.5}$$

$$\begin{aligned} I_{\text{I 3d,I-term}} &\propto \sum_{n=0}^{\infty}\left[\exp\left(\frac{-n\,z_{\text{cell}}}{\lambda_{\text{I}}\cos\theta}\right) + \exp\left(\frac{-0.6062\,\text{nm} - n\,z_{\text{cell}}}{\lambda_{\text{I}}\cos\theta}\right)\right] \\ &\propto \left[1 + \exp\left(\frac{-0.6062\,\text{nm}}{\lambda_{\text{I}}\cos\theta}\right)\right]\sum_{n=0}^{\infty}\exp\left(\frac{-n\,z_{\text{cell}}}{\lambda_{\text{I}}\cos\theta}\right) \\ &\propto \left[1 + \exp\left(\frac{-0.6062\,\text{nm}}{\lambda_{\text{I}}\cos\theta}\right)\right]\frac{\exp\left(\frac{z_{\text{cell}}}{\lambda_{\text{I}}\cos\theta}\right)}{\exp\left(\frac{z_{\text{cell}}}{\lambda_{\text{I}}\cos\theta}\right)-1} \end{aligned} \tag{A.6}$$

Having the half-unit cell on top of the bismuth-oxide-terminated BiOI(001) yields important simplifications for the remainder of the full unit cells that may be expressed as a function of the iodide-terminated BiOI(001). As the first iodide-terminated unit cell is displaced from the surface by a distance $\zeta_0 \equiv 0.6098$ nm as shown in Fig. A.6, we express photoelectron intensities as a function of the contribution from the top half-unit cell plus ζ_0 offset to the respective iodide-terminated surface photoelectron intensity. Equations A.7–A.9 respectively present the Bi 4f, O 1s, and I 3d photoelectron intensities for bismuth-oxide-terminated BiOI(001).

$$I_{\text{Bi 4f,Ox-term}} \propto \exp\left(\frac{-0.1205\,\text{nm}}{\lambda_{\text{Bi}}\cos\theta}\right) + \sum_{n=0}^{\infty}\left[\exp\left(\frac{-\zeta_0 - 0.1826\,\text{nm} - n\,z_{\text{cell}}}{\lambda_{\text{Bi}}\cos\theta}\right) + \exp\left(\frac{-\zeta_0 - 0.4857\,\text{nm} - n\,z_{\text{cell}}}{\lambda_{\text{Bi}}\cos\theta}\right)\right]$$
$$\propto \exp\left(\frac{-0.1205\,\text{nm}}{\lambda_{\text{Bi}}\cos\theta}\right) + \exp\left(\frac{-\zeta_0}{\lambda_{\text{Bi}}\cos\theta}\right) I_{\text{Bi 4f,I-term}} \tag{A.7}$$

$$I_{\text{O 1s,Ox-term}} \propto \exp\left(\frac{-0\,\text{nm}}{\lambda_{\text{O}}\cos\theta}\right) + 2\sum_{n=0}^{\infty}\exp\left(\frac{-\zeta_0 - 0.3031\,\text{nm} - n\,z_{\text{cell}}}{\lambda_{\text{O}}\cos\theta}\right)$$
$$\propto 1 + \exp\left(\frac{-\zeta_0}{\lambda_{\text{O}}\cos\theta}\right) I_{\text{O 1s,I-term}} \tag{A.8}$$

$$I_{\text{I 3d,Ox-term}} \propto \exp\left(\frac{-0.3031\,\text{nm}}{\lambda_{\text{I}}\cos\theta}\right) + \sum_{n=0}^{\infty}\left[\exp\left(\frac{-\zeta_0 - n\,z_{\text{cell}}}{\lambda_{\text{I}}\cos\theta}\right) + \exp\left(\frac{-\zeta_0 - 0.6062\,\text{nm} - n\,z_{\text{cell}}}{\lambda_{\text{I}}\cos\theta}\right)\right]$$
$$\propto \exp\left(\frac{-0.3031\,\text{nm}}{\lambda_{\text{I}}\cos\theta}\right) + \exp\left(\frac{-\zeta_0}{\lambda_{\text{I}}\cos\theta}\right) I_{\text{I 3d,I-term}} \tag{A.9}$$

To solve for the desired intensities, and the ratio of intensities that we consider in the manuscript, we further need photoelectron attenuation length values, λ_{Bi}, λ_{O}, and λ_{I}. To our knowledge, photoelectron attenuation lengths have not been established for BiOI. The empirical model in eq A.10 from Cumpson and Seah estimates attenuation lengths in nanometers based on **E**, the photoelectron kinetic energy; $\langle A\rangle$, the average atomic mass of species in the material in g mol^{-1}; ρ, the material density in kg m^{-3}; N, Avogadro's number, and $\langle Z\rangle$, the average atomic number of the atoms in the material.[S12]

$$\lambda = 0.316\times 10^{12}\left(\frac{\langle A\rangle}{\rho N}\right)^{1/2}\left[\frac{\mathbf{E}}{\langle Z\rangle^{0.45}\left(3 + \ln\frac{\mathbf{E}}{27}\right)} + 4\right] \tag{A.10}$$

For single crystal BiOI, $\langle A\rangle$ = 117.3 g mol^{-1}, and $\langle Z\rangle$ = 48. Since each 0.14497 nm^{-3} unit cell contains 2 atoms each of bismuth, oxygen, and iodine, ρ = 8061.08 kg m^{-3}. For Bi 4f photoelectrons with a binding energy of ~159 eV, an instrument work function of ~4 eV, and illumination with 1486.6 eV Al Kα X-radiation, **E** = 1324 eV, which yields λ_{Bi} = 1.85 nm. For O 1s

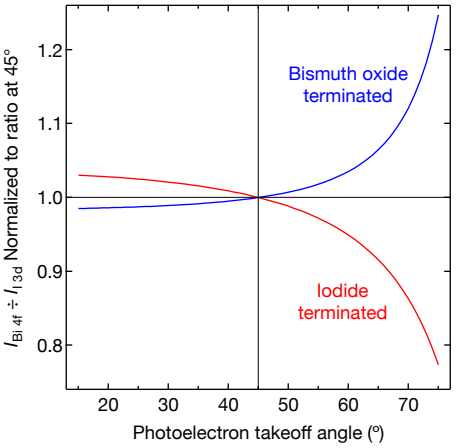

Figure A.7. Normalized Bi 4f-to-I 3d photoelectron intensity ratios from the overlayer model results for bismuth-oxide-terminated (blue) and for iodide-terminated (red) BiOI(001). The divergence between the two intensity ratios, particularly at high takeoff angles, validates the use of angle-resolved photoelectron spectroscopy for revealing surface terminations on nascent and solution processed BiOI(001).

photoelectrons with a binding energy of ~529 eV, **E** = 954 eV that yields λ_O = 1.45 nm. Lastly, I 3d photoelectrons with binding energy of ~619 eV, would have a kinetic energy, **E**, of 864 eV, and a λ_I of 1.35 nm. Each of the calculated attenuation length values are smaller than we expected, and we attribute the small values to the high mass density of the material.

A.4.4 Angle-resolved overlayer model results

As mentioned above, we are interested in exploring the intensity *ratios* both because experimentally this eliminates challenges with absolute alignment, and numerically for the simplifications afforded by the ratios. We further normalize our bismuth-to-iodide intensity ratios to that ratio at $\theta = 45°$ to best align experimental and numerical results.

Figure A.7 displays bismuth-to-iodide intensity ratios that are normalized to that ratio at $\theta = 45°$, $\frac{I_{\text{Bi 4f,I-term}}}{I_{\text{I 3d,I-term}}} \div \frac{I^{\theta=45°}_{\text{Bi 4f,I-term}}}{I^{\theta=45°}_{\text{I 3d,I-term}}}$, for iodide-terminated BiOI(001) in the red trace derived from eqs A.4 and A.6 and for oxide-terminated BiOI(001) in the blue trace that are derived from eqs A.7 and A.9. Relevant to experimental comparisons, both bismuth-oxide-terminated and iodide-terminated BiOI(001) demonstrate strong dependencies on photoelectron take-off angle, and each show vastly diverging trends in their angle-dependent intensity ratios relative to each other. As takeoff angles approach the surface normal angle, photoelectrons reach the detector that originated from *several* nanome-

Table A.1. Model-determined photoelectron intensities for Bi 4f, O 1s, and I 3d for iodide-terminated BiOI(001), as well as a Bi 4f / I 3d intensity ratio normalized to the ratio at $\theta = 45°$ to compare with experimental results.

Angle (°)	$I_{\text{Bi 4f,I-term}}$	$I_{\text{O 1s,I-term}}$	$I_{\text{I 3d,I-term}}$	$\frac{I_{\text{Bi 4f,I-term}}}{I_{\text{I 3d,I-term}}} \div \frac{I^{\theta=45°}_{\text{Bi 4f,I-term}}}{I^{\theta=45°}_{\text{I 3d,I-term}}}$
15	4.159	3.356	3.225	1.030
30	3.752	3.034	2.936	1.021
45	3.103	2.519	2.478	≡ 1.000
60	2.250	1.834	1.894	0.949
75	1.227	0.975	1.268	0.773

ters deep into a surface. As the bismuth-oxide-terminated and the iodide-terminated BiOI(001) are similar for $z \geq \zeta_0 = 0.6098$ nm, and this yields $\frac{I_{\text{Bi 4f}}}{I_{\text{I 3d}}}$ ratios that change very little in the range $15° < \theta < 45°$. The small angle dispersion in the intensity ratios yields $\frac{I_{\text{Bi 4f}}}{I_{\text{I 3d}}} \div \frac{I^{\theta=45°}_{\text{Bi 4f}}}{I^{\theta=45°}_{\text{I 3d}}}$ values that are very close to 1 for both bismuth-oxide-terminated and iodide-terminated BiOI(001) in this "bulk-sensitive" range $15° < \theta < 45°$. In contrast to small angles, large takeoff angles relative to the surface normal angle yields photoelectron signals that dramatically favor just the top few atomic layers. Our ratio of interest $\frac{I_{\text{Bi 4f}}}{I_{\text{I 3d}}} \div \frac{I^{\theta=45°}_{\text{Bi 4f}}}{I^{\theta=45°}_{\text{I 3d}}}$ demonstrates a significant dispersion with takeoff angles above 45°, and importantly the ratio deviates significantly for bismuth-oxide-terminated vs iodide-terminated surfaces. Indeed, $\frac{I_{\text{Bi 4f,Ox-term}}}{I_{\text{I 3d,Ox-term}}} \div \frac{I^{\theta=45°}_{\text{Bi 4f,Ox-term}}}{I^{\theta=45°}_{\text{I 3d,Ox-term}}} = 1.247$ for the bismuth-oxide-terminated BiOI(001) as in Fig. A.6**A**, and the ratio $\frac{I_{\text{Bi 4f,I-term}}}{I_{\text{I 3d,I-term}}} \div \frac{I^{\theta=45°}_{\text{Bi 4f,I-term}}}{I^{\theta=45°}_{\text{I 3d,I-term}}} = 0.773$ for iodide-terminated BiOI(001) as in Fig. A.6**B**. The divergence between the ratio for bismuth-oxide-terminated and for iodide-terminated BiOI(001) supports the use of angle-resolved photoelectron spectroscopy for the analysis of surface termination of BiOI(001).

Tables A.1 and A.2 present the results of the overlayer model for the angles under experimental consideration in the main manuscript. Equations A.4–A.9 yield the data for each respective intensity column. Tables A.1 and A.2 each present a column of intensity normalized data, $\frac{I_{\text{Bi 4f,I-term}}}{I_{\text{I 3d,I-term}}} \div \frac{I^{\theta=45°}_{\text{Bi 4f,I-term}}}{I^{\theta=45°}_{\text{I 3d,I-term}}}$ to best compare to the experimental data.

A.5 X-ray Diffraction

A Bruker-AXS D8 focus powder X-ray diffractometer with Cu K_α radiation collected X-ray diffraction (XRD) traces in the range of 5–45° (2θ) at a step

Table A.2. Model-determined photoelectron intensities for Bi 4f, O 1s, and I 3d for bismuth-oxide-terminated BiOI(001), as well as a Bi 4f / I 3d intensity ratio normalized to the ratio at $\theta = 45°$ to compare to experimental results.

Angle (°)	$I_{\text{Bi 4f,Ox-term}}$	$I_{\text{O 1s,Ox-term}}$	$I_{\text{I 3d,Ox-term}}$	$\frac{I_{\text{Bi 4f,Ox-term}}}{I_{\text{I 3d,Ox-term}}} \div \frac{I^{\theta=45°}_{\text{Bi 4f,Ox-term}}}{I^{\theta=45°}_{\text{I 3d,Ox-term}}}$
15	3.891	3.169	2.810	0.985
30	3.491	2.865	2.511	0.989
45	2.858	2.387	2.033	≡ 1.000
60	2.041	1.789	1.403	1.035
75	1.121	1.191	0.639	1.247

size of 0.05° and a dwell time of 5 s per step. X-ray tube operating conditions were 40 kV and 40 mA. For samples subjected to any of the aforementioned chemical rinsing and/or etching procedures, samples were freely situated on a sample stage and analyzed directly following chemical processing. Analyses of tape-cleaved samples utilized double-sided tape to mechanically adhere a BiOI sample to the XRD substrate followed by mechanical exfoliation tape under an air ambient and XRD analysis directly afterwards. As expected for the large-grain, single-crystal BiOI material synthesized, the {001}, {002}, {003}, . . . family of reflections from the literature trace is well represented in the experimental traces.

As mentioned in the manuscript, we compared the experimentally acquired XRD traces to database references. Figure A.8 presents the XRD trace for the tape-cleaved sample in Fig. 4.3C from Chapter 4 with both a logarithmic and a linear y-axis scaling as well as the card for tetragonal BiOI from powder data file 00-010-0445. While the logarithmic y axis highlights the trace contributions to each reflection, the linear scaling reinforces the dominance of the {001}, {002}, {003}, . . . family of reflections that is consistent with the production of single crystal BiOI(001) material.

A.6 Scanning Electron Microscopy

A Tescan Analytics Vega3 (Tescan Orsay Holding, A.S., Brno-Kohoutovice, Czechia) scanning electron microscope with a tungsten cathode operating at a 10 kV acceleration potential and a secondary electron detector acquired the images in Fig. 4.6A. A Phenom Pro SEM (Phenom-World BV, Eindhoven, Netherlands) equipped with a back-scatter detector (BSD) and a CeB_6 cathode collected all SEM images in Fig. 4.6B.

A.7 Appendix A References

S1. Russell, M. A.; Kalan, R. E.; Pugliese, A. J.; Carl, A. D.; Masucci, C. P.; Strandwitz, N. C.; Grimm, R. L., Dual Liquid Junction Photoelectrochemistry: Part II. Open-Circuit Photovoltage Variations Due to Surface Chemistry, Interfacial Dipoles, and Non-Ohmic Junctions at Back Contacts. *J. Electrochem. Soc.* **2019**, *166*(13), H608–H614. 10.1149/2.1351712jes

S2. Carl, A. D.; Kalan, R. E.; Obayemi, J. D.; Zebaze Kana, M. G.; Soboyejo, W. O.; Grimm, R. L. Synthesis and Characterization of Alkylamine-Functionalized Si(111) for Perovskite Adhesion with Minimal Interfacial Oxidation or Electronic Defects. *ACS Appl. Mater. Interfaces* **2017**, *9*(39), 34377–34388. 10.1021/acsami.7b07117

S3. Fadley, C. S., Solid State-and Surface-Analysis by Means of Angular-Dependent X-ray Photoelectron Spectroscopy. *Prog. Solid State Chem.* **1976**, *11*, 265–343. 10.1016/0079-6786(76)90013-3

S4. Fairley, N. Peak Fitting in XPS. `http://www.casaxps.com/help_manual/manual_updates/peak_fitting_in_xps.pdf` (accessed Aug. 2015).

S5. Shirley, D. A., High-Resolution X-Ray Photoemission Spectrum of the Valence Bands of Gold. *Phys. Rev. B* **1972**, *5*(12), 4709–4714. 10.1103/PhysRevB.5.4709

S6. Tougaard, S. Formalism for quantitative surface analysis by electron spectroscopy. *J. Vac. Sci. Technol.* **1990**, *8*(3), 2197–2203. 10.1116/1.577037

S7. Jansson, C.; Hansen, H. S.; Yubero, F.; Tougaard, S. Accuracy of the Tougaard method for quantitative surface analysis. Comparison of the Universal and REELS inelastic cross sections. *J. Electron Spectrosc. Relat. Phenom.* **1992**, *60*(4), 301–319. 10.1016/0368-2048(92)80025-4

S8. Seah M. P. Background subtraction: I. General behaviour of Tougaard-style backgrounds in AES and XPS. *Surf. Sci.* **1999**, *420*(2–3), 285–294. 10.1016/S0039-6028(98)00852-8

S9. Moulder, J. F.; Chastain, J., Handbook of X-ray Photoelectron Spectroscopy: A Reference Book of Standard Spectra for Identification and Interpretation of XPS Data; Physical Electronics Division, Perkin-Elmer Corporation, 1992.

S10. Seah M. P. Post-1989 calibration energies for X-ray photoelectron spectrometers and the 1990 Josephson constant. *Surf. Interf. Anal.* **1989**, *14*(8), 488. 10.1002/sia.740140813

S11. Seah, M. P., Quantification of AES and XPS. *In* Practical Surface Analysis Volume 1: Auger and X-ray Photoelectron Spectroscopy, 2nd ed.; Briggs, D.; Seah, M. P., Eds. John Wiley & Sons: 1990; 201–255.

S12. Cumpson, P. J.; Seah, M. P. Elastic Scattering Corrections in AES and XPS. II. Estimating Attenuation Lengths and Conditions Required for their Valid Use in Overlayer/Substrate Experiments. *Surf. Interface Anal.* **1997**, *25*, 430–446.10.1002/(SICI)1096-9918(199706)25:6<430::AID-SIA254>3.0.CO;2-7

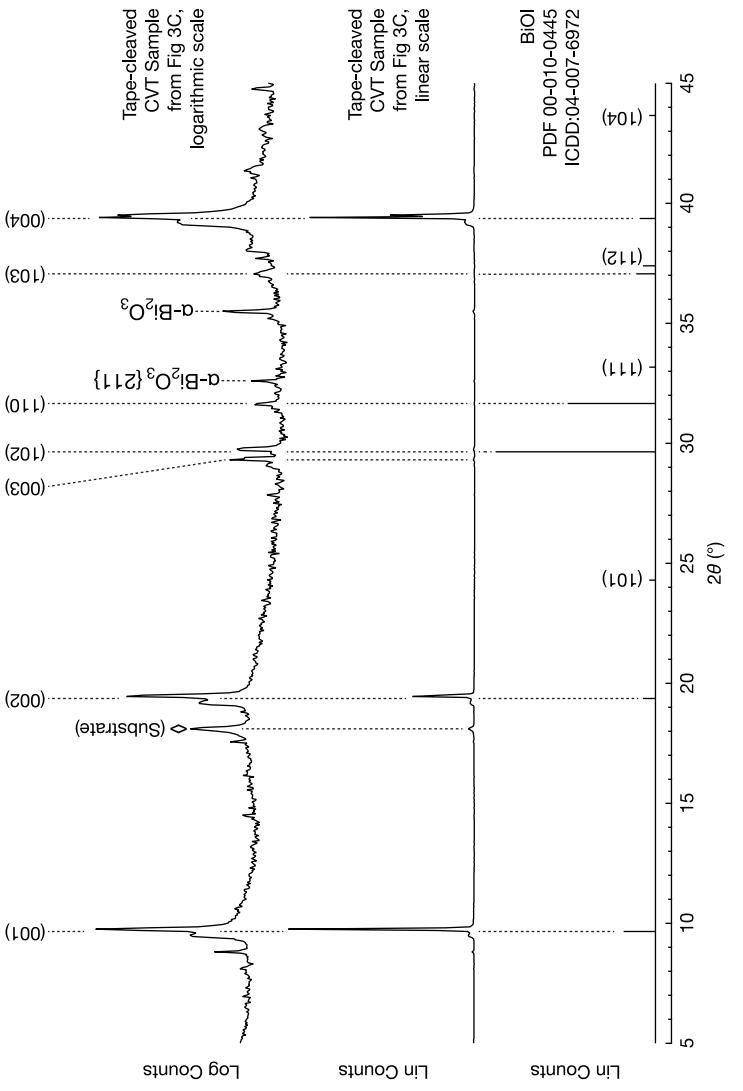
Tape-cleaved
CVT Sample
from Fig 3C,
logarithmic scale
Tape-cleaved
CVT Sample
from Fig 3C,
linear scale
BiOI
PDF 00-010-0445
ICDD:04-007-6972
Log Counts
Lin Counts
Lin Counts
(001)
◇ (Substrate)
(002)
(003)
(102)
(110)
α-Bi2O3 {211}
α-Bi2O3
(103)
(004)
(101)
(111)
(112)
(104)
5
10
15
20
25
30
35
40
45
2θ (°)

Figure A.8. XRD trace from Fig. 6.3C in Chapter 6 reproduced in (top) logarithmic y-axis scaling and (middle) linear y-axis scaling along with the (bottom) literature powder diffraction file 00-010-0445 card for BiOI. The {001}, {002}, etc. family of features from the literature trace are well represented in the experimental data, as we expect for the large-grain, single-crystal BiOI(001) synthesized herein. The absence of other features in the experimentally acquired trace are also due to the synthesis of large grain material that is dominated by {001} terraces rather than nanoscale powdered material. A notable presence in the experimental data is scattering signal off of the {003} reflections with a 1:2000 intensity ratio as compared to the {001} reflections. This highly attenuated feature shows up well in the logarithmic representation in the top but would not appear in the literature powder data file that cuts off intensities at 1% of the largest peak in the trace.

B

CH. 5 SUPPORTING INFORMATION: CHEMICAL AND OPTOELECTRONIC CONTROL OF $Ti_3C_2T_X$ MXENE VIA COVALENTLY-TETHERED ORGANIC MONOLAYERS

B.1 Photoelectron Spectroscopy

A PHI 5600 XPS system with a third-party data acquisition system (RBD Instruments, Bend Oregon) acquired all X-ray photoelectron spectra as detailed previously.[229] Analysis chamber base pressures were $<1 \times 10^{-9}$ Torr. A hemispherical energy analyzer that is positioned at 90◦ with respect to the incoming monochromated Al K_α X-radiation and 54.7° with respect to a non-monochromated source of Al K_α X-rays collected the photoelectrons. All X-ray measurements utilized 45° angles between the sample normal angle and both the X-ray source and the analyzer. In all experiments, survey

spectra utilized a 117 eV pass energy, a 0.5 eV step size, and a 50-ms-per-step dwell time. All high-resolution XP spectra employed a 23.5 eV pass energy, 0.025 eV step size, and a 50 ms dwell time per step. Consistent positions of Ti 2p features ascribed to the $Ti_3C_2T_x$ samples obviated a need for charge neutralization.

For all $Ti_3C_2T_x$ material, samples were mounted on steel XPS pucks and evacuated in the loading chamber of the instrument directly following chemical processing. The films were deposited by a gravity-feed, compressed-gas-propelled commercial airbrush (Master Airbrush, G233). Spray depositions for nascent $Ti_3C_2T_x$ material utilized <0.5 mL of the aqueous $Ti_3C_2T_x$ colloid while depositions for functionalized $Ti_3C_2T_x$ material utilized <0.5 mL of the ethanolic $Ti_3C_2T_x$ suspension. Films were sufficiently thick such that the analysis depth for typical XPS and UPS experiments excluded photoelectron contributions from the silicon substrate. Routine cleaning of the airbrush body and components utilized dilute, aqueous glacial acetic acid (AcOH, 99.7%, Alfa Aesar). Components in frequent contact with $Ti_3C_2T_x$ material including the needles, fluid tips, and reservoir were sonicated in the aqueous, dilute acetic acid and rinsed with copious amounts of water in between subsequent depositions.

Post-acquisition fitting utilized an in-house-developed LabVIEW-based program. Data fitting employed baseline-corrected, pseudo-Voigt, GL(x)-style functions where x nonlinearly scales from a pure Gaussian (x = 0) to a pure Lorentzian (x = 100).[255] Baseline functions were either of a linear type, a Shirley type,[256] or a Tougaard style with B = 2900 eV^2 and C = 1643 eV^2 within a universal function that is scaled to the height of the photoelectron data.[257–258,311] Optimization routines utilize the built-in LabVIEW implementation of the Levenberg-Marquardt algorithm for multiparameter fitting.

Fitting of the O 1s and F 1s features utilized a linear background and GL(30) functional peak shapes. When fitting of the F 1s or O 1s regions necessitated multiple fit peaks, they were constrained to have identical full-width-at-half-max (fwhm) values. The Si 2p, C 1s, and N 1s features were fit with a Tougaard-shaped background. The Si 2p regions were well fit by one doublet with GL(30) functional peak shapes. The Si 2p doublet peaks were constrained to have identical fwhm with the $2p_{1/2}$ peak containing 50% of the area of the $2p_{3/2}$ peak. The C 1s and N 1s regions were described by multiple peaks with GL(30) functional peak shapes. Additionally, the lowest-binding-energy peak in the C 1s region was best fit with a tail function, GL(30)T(2). When fitting of the C 1s or N 1s regions necessitated multiple fit peaks, they were constrained to have identical fwhm values. The Ti 2p region is best described with an Offset-Shirley with 30% linear character and GL(30) functional peak shapes. The Ti 2p region was fit by four doublets with GL(30) functional peak shapes. The four Ti $2p_{3/2}$ peaks were constrained to have identical fwhm values and the four Ti $2p_{1/2}$ peaks were constrained to have a

fwhm value 20% larger than that of the $2p_{3/2}$ peaks. All of the areas for the Ti 2p features were left unconstrained, except the highest-binding-energy $2p_{1/2}$ peak at 459 eV was constrained to have 30% the area of the corresponding $2p_{3/2}$ peak.

For UPS experiments, a gas-discharge light source (UVS 40A2, Prevac, Rogów, Poland) mounted in the PHI 5600 instrument provided He I radiation at $\mathbf{E}_{\mathrm{He\,I}}$ = 21.218 eV (58.433 nm) from research-grade helium (Airgas). We utilize a –35 V substrate bias and collect photoelectrons at the sample normal angle to both isolate and maximize the desired spectral contributions of secondary electrons both from the sample and from the analyzer. To verify analyzer transmission and detection linearity across the ~25 eV acquisition window for the low kinetic energy electrons from ultraviolet photoemission, we collected UP spectra on Au for a range of substrate biases. UP spectra that were collected for substrate biases between –20 eV and –50 eV revealed no observable difference in shape or energy positions, and no observable signal attenuation on either the Fermi or the secondary-electron cutoff side of the spectra. This validated the use of –35 V substrate biases for all collected UP spectra.

Off-line analyses of freshly evaporated and a freshly argon-sputter-cleaned gold sample verified instrumental calibration. Both X-ray and UV photoelectron spectra were calibrated using freshly Argon-ion-sputtered samples of Cu and Au foils to establish the scaling factor and work function of the instrument. Calibration revealed energy positions of $\mathbf{E}_{\mathrm{Cu\,2p_{3/2}}}$ = 932.67 eV and $\mathbf{E}_{\mathrm{Au\,4f_{7/2}}}$ = 84.00 eV for the respective Cu or Au sample.[312] Fig. B.1 presents a UP spectrum for a freshly-evaporated and freshly argon-sputtercleaned Au sample following X-ray photoelectron calibration. The spectrum in Fig. 5.3 verifies a spectrometer calibration of binding-energy values to the Fermi-level energy of gold, $\mathbf{E}_{\mathrm{f,Au}}$ = 0.00 ± 0.05 eV. From plots of photoelectron counts vs bias-corrected binding energy, the x-axis intercept of linear regressions quantifies a secondary-electron-cutoff energy, $\mathbf{E}_{\mathrm{SEC}}$, and a valence-band-edge (maximum) energy, $\mathbf{E}_{\mathrm{VBM}}$. Considering the binding energy calibration of the instrument, we report sample work function values, Φ, as the difference between $\mathbf{E}_{\mathrm{He\,I}}$ and the secondary electron cutoff energy, or $\Phi = \mathbf{E}_{\mathrm{He\,I}} - \mathbf{E}_{\mathrm{SEC}}$.

For the semiconductor samples of interest, the onset of photoelectron counts near the Fermi region corresponds to the valence-band-maximum energy, $\mathbf{E}_{\mathrm{VBM}}$. We report Fermi-level energies relative to valence-band-maximum energies, or $\mathbf{E}_{\mathrm{f}} - \mathbf{E}_{\mathrm{VBM}}$, where a regression fit to the x-axis determines $\mathbf{E}_{\mathrm{VBM}}$, and $\mathbf{E}_{\mathrm{f}}$ = 0 eV in the photoelectron spectra as the sample Fermi-level is equilibrated to the Fermi level of gold, $\mathbf{E}_{\mathrm{f,\,Au}} \equiv 0$ eV. As ultrahigh-vacuum bakeouts can yield a small perturbation in instrument calibration that would deleteriously affect data analyses, both calibration and BiOI data acquisition were collected in the same "bakeout window."

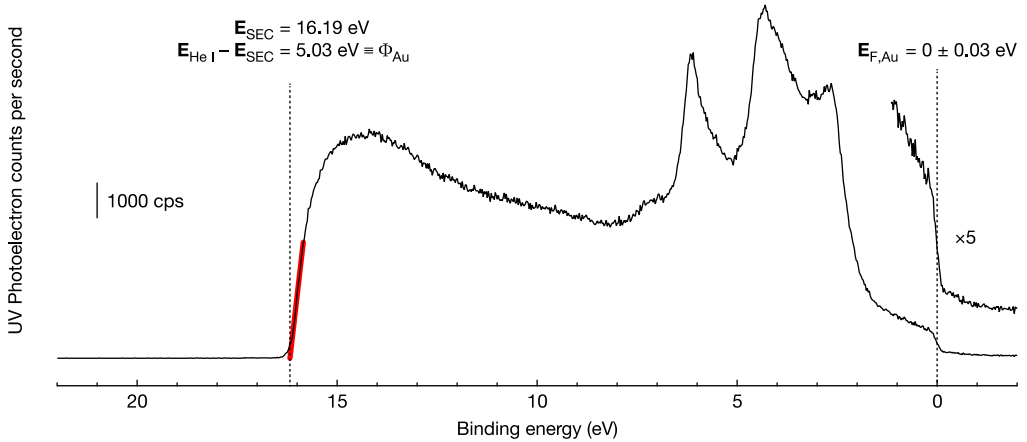

Figure B.1. He I UV photoelectron spectrum of freshly sputtered polycrystalline Au foil indicating a Fermi level, $\mathbf{E}_{\mathrm{F,Au}} = 0.00 \pm 0.03$ eV. The difference of the energy of the incoming radiation, $\mathbf{E}_{\mathrm{He\,I}} = 21.218$ eV minus the x-axis intercept of a linear fit to the secondary-electron cutoff, $\mathbf{E}_{\mathrm{SEC}} = 16.187$ eV yields a work function of $\Phi_{\mathrm{Au}} = 5.03 \pm 0.03$ eV.

C

CH. 6 SUPPORTING INFORMATION: ELECTRONIC STRUCTURE OF 1D LEPIDOCROCITE TiO_2 AS REVEALED BY OPTICAL ABSORPTION AND PHOTOELECTRON SPECTROSCOPY

C.1 Raw Absorbance Spectrum and Band-Gap Interpretation

Figure C.1 presents the raw absorbance spectrum (top left) for the indirect-gap Tauc plot (top right) in Fig. C.1C in Chapter 6. We further include a direct-gap Tauc plot in the lower left and a Cody plot of $(A/(h\nu))^{1/2}$ vs $h\nu$ that support a band gap in excess of 4 eV.

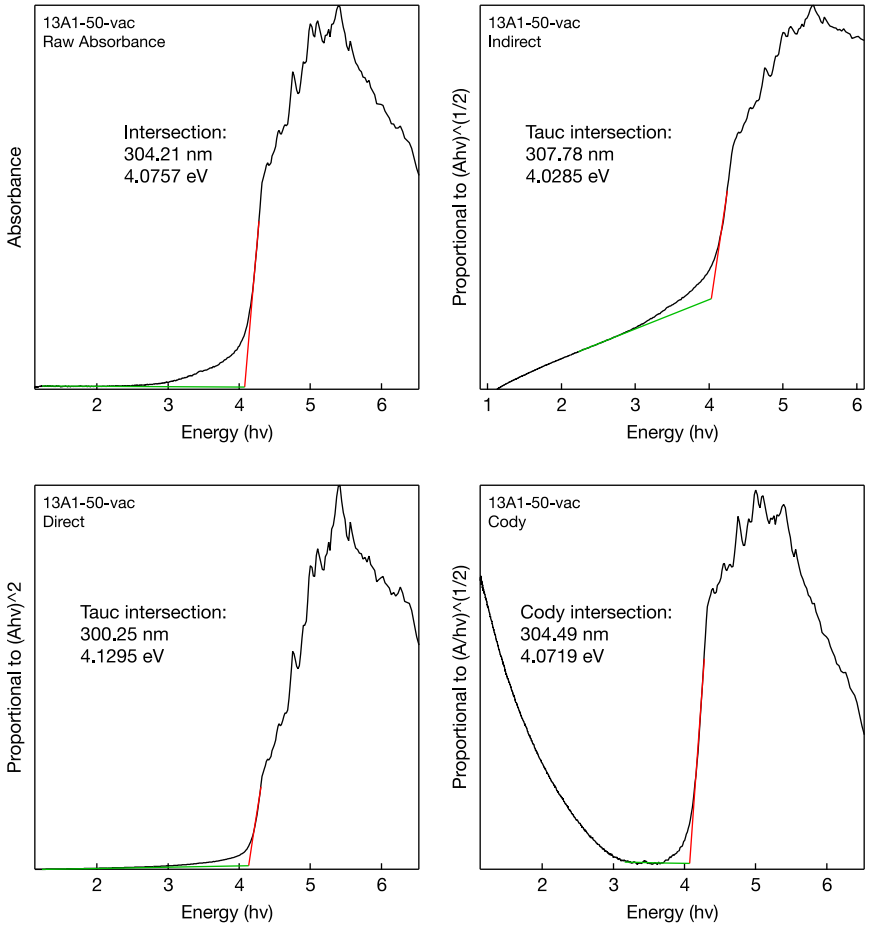

Figure C.1. Raw absorbance spectrum, direct- and indirect-gap Tauc plots, and Cody plot for the 1DL TiO_2 material.

C.2 Fits of Ultraviolet Photoelectron Spectra

In Chapter 6, we present band edge positioning based on a fit of ultraviolet photoelectron spectra but concede that other interpretations may exist. Figure C.2 presents competing cases for fitting the photoelectron count structure in the valence region (i.e. binding energies between 5 and 0 eV vs the Fermi level). Frame A in Fig. C.2 presents the data as shown in Figure 6.4 in Chapter 6 in which a red-dashed fit to the secondary-electron-cutoff region yields a work-function energy, $\Phi = h\nu - \mathbf{E}_{SEC} = 4.03$ eV. Further, the 16× inset in Fig. C.2A demonstrates a green-dashed fit to the photoelectron count structure

that predicts a valence-band edge that is 3.74 eV below the Fermi energy, or $\mathbf{E}_f - \mathbf{E}_{VBM} = 3.74$ eV. In concert with a 4.0 eV band gap energy from Tauc plots of UV–Vis absorbance data yields valence and conduction edges at –7.8 eV and –3.8 eV vs the vacuum energy level, $\mathbf{E}_{vac}$.

Revealed in the near-valence-edge data in the 16× inset in Fig. C.2A, when $\mathbf{E}_f - \mathbf{E}_{VBM} = 3.74$ eV, gray-shaded photoelectron counts exist at binding energies between –3.74 vs $\mathbf{E}_f$ and $\mathbf{E}_f$ itself. With the valence-edge fit as in Case 1, the gray-shaded photoelectron count region in Case 1 would be assigned to photoemission of electrons from defect states directly above the valence band. Case 2 in Fig. C.2B considers whether these gray-shaded photoelectron counts do not represent defects, but rather represent the valence-band edge itself. In Fig. C.2B, the assigned valence structure implies a small density of states near the valence band edge and a significantly larger density of states deeper within the valence band. With the same data in Case 1 in Fig. C.2A on the left and Case 2 on the right in Fig. C.2B, the 128× inset indeed reveals a linear region that may be fit down to the baseline with $\mathbf{E}_f - \mathbf{E}_{VBM} = 1.65$ eV. In conjunction with $\Phi = 4.03$ eV and $\mathbf{E}_g = 4.0$ eV, a fit of $\mathbf{E}_f - \mathbf{E}_{VBM} = 1.65$ eV respectively positions the valence and conduction band edges at –5.7 eV and –1.7 eV.

Considering two competing fits of the photoelectron data as in Case 1 and Case 2 in Fig. C.2 and in concert with the fitted Tauc plot of the UV–Vis absorbance data, we consider Case 1 to be the most realistic fit. With a 4.0 eV band edge, the fit in Case 2 positions the conduction band edge very close to the vacuum energy, or a small electron affinity of $\chi = \sim 1.7$ eV. This small electron affinity poorly resembles other TiO_2 materials. Conversely, the band edge positioning in Case 1 well resembles expected band edge positions for highly quantum-confined titanium oxide material.

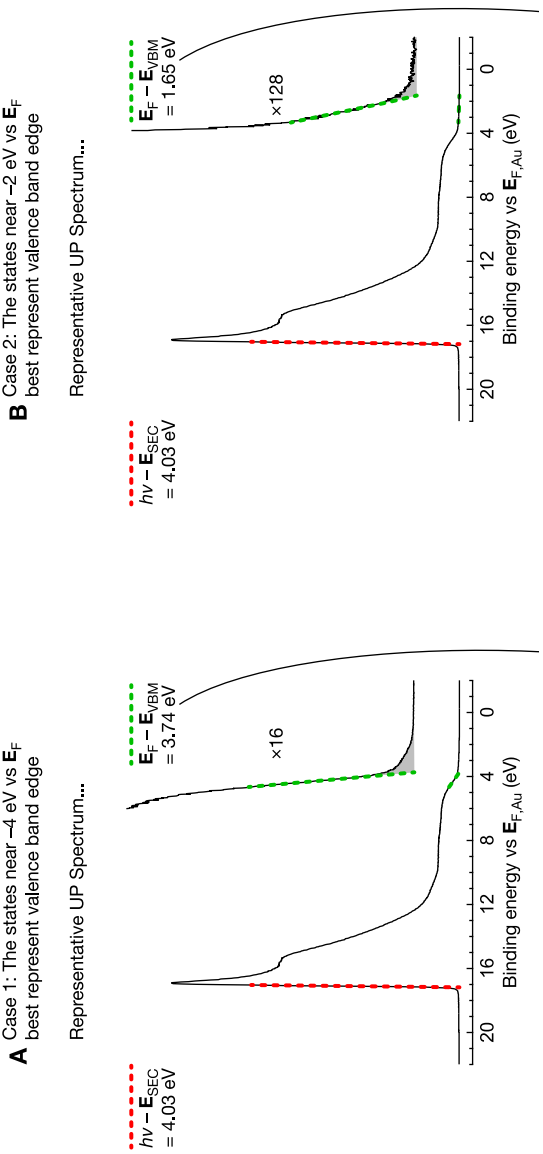
A Case 1: The states near –4 eV vs E_F
best represent valence band edge
Representative UP Spectrum...
$h\nu - E_{SEC}$ = 4.03 eV
$E_F - E_{VBM}$ = 3.74 eV
×16
20
16
12
8
4
0
Binding energy vs $E_{F,Au}$ (eV)
B Case 2: The states near –2 eV vs E_F
best represent valence band edge
Representative UP Spectrum...
$h\nu - E_{SEC}$ = 4.03 eV
$E_F - E_{VBM}$ = 1.65 eV
×128
20
16
12
8
4
0
Binding energy vs $E_{F,Au}$ (eV)

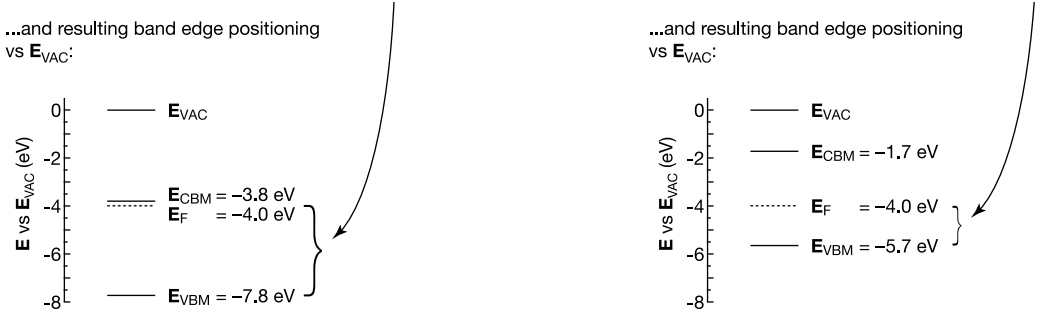

Figure C.2. Different fits of the valence structure of the ultraviolet photoelectron spectra for titanium-based 1DL yield differences in the predicted band edge positioning on an absolute energy scale.

D

MODIFICATIONS TO THE XPS

D.1 Hijacking mono filament to power twin filament 1

Since the connections to filament 1 (A and B) are not working correctly, we decided to hijack the filament 2 connections (C and D) from the mono (J10) to power the twin anode (J3) filament 1. We desoldered A, B, C, and D from J10 and covered up A and B with heat shrink. We desoldered A and B from J3 which are also not working and covered them up with heat shrink. Then we soldered C (white/ orange striped wire) from J10 to ”B” port on J3. We soldered D (yellow wire) from J10 to ”A” port on J3. See Figs. D.1, D.2, and D.3 for details.

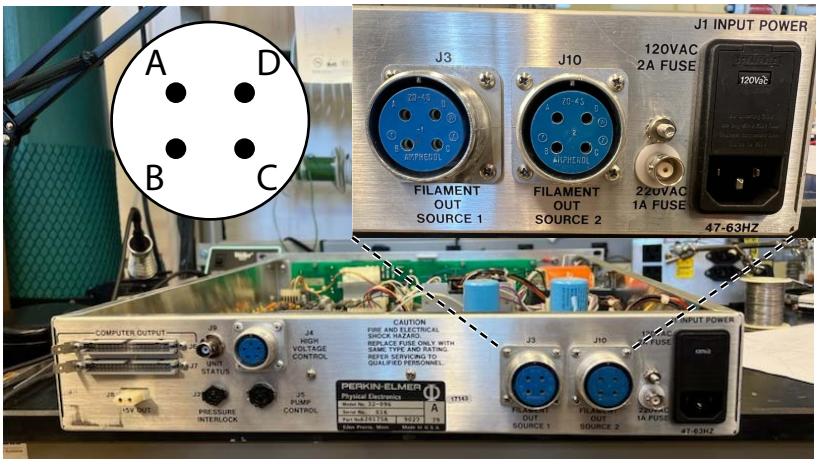

Figure D.1. Exterior view of the back of the 32-096 X-ray control box where the filament cable pin connections for both J10 and J3 are A-D clockwise respectively.

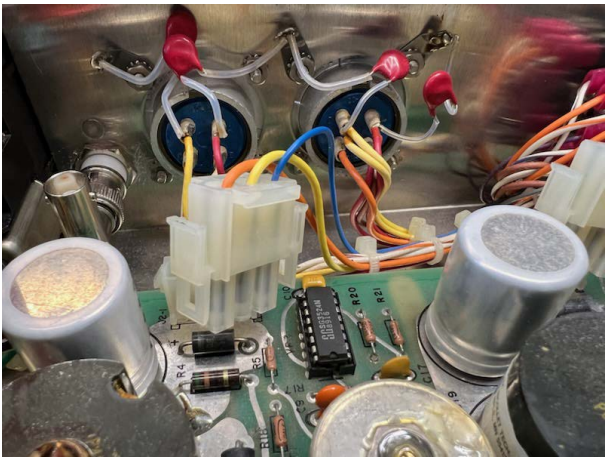

Figure D.2. Interior view of the 32-096 X-ray control box where J10 and J3 control the monochromated and twin sources respectively.

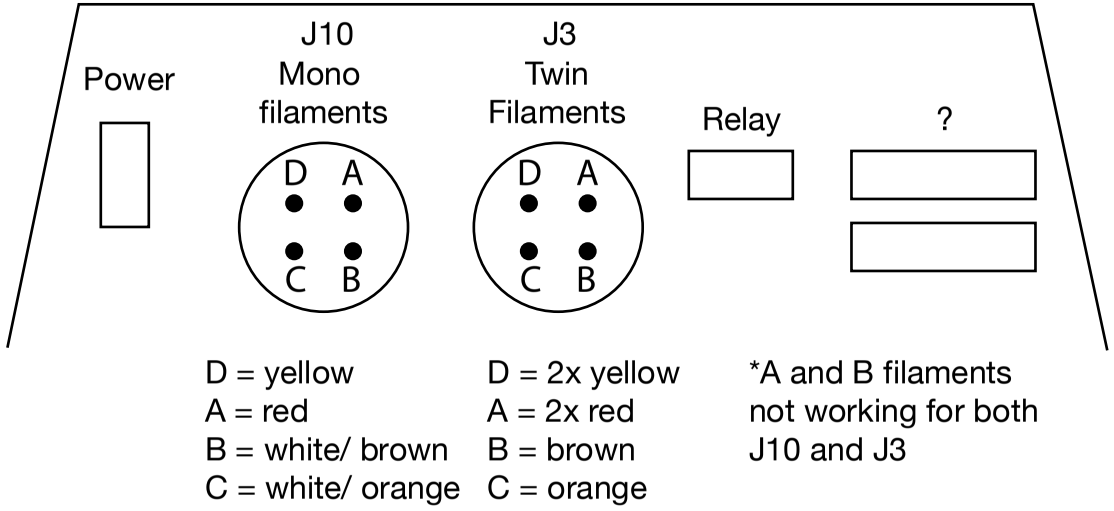

Figure D.3. Diagram of the filament connections for the J10 and J3 amphenols from an interior view of the 32-096 X-ray control box. Currently, A and B which correspond to "filament 1" in both cases are not working correctly and don't send power to mono or twin filament 1.

Figure D.4. Photo of the original XPS valve manifold for which we clipped the cable connections and took offline.

D.2 Second ion gauge

We acquired a second DIG III ion gauge controller from Ebay and got it connected to our second ion gauge to read the pressure on the load lock and TPD side. It was working beautifully for a while. Eventually, we did have an issue during which the filament wouldn't stay lit and upon removing the ion gauge sensor, we noticed one of the filaments got bent and was shorting through the body. We bent it back into place and it fixed the issue. Note that the two different ion gauge tubes (main chamber versus load lock side) have different filament connections connections and filament replacement styles.

D.3 Valve rebuild

Given the scarcity and cost of the original-style pneumatic control valves for PHI5600 (Fig. D.4), we decided to upgrade the manifold to a newer style featuring the same MAC 34C style pneumatic valves we used in the ALD. Currently, the new pneumatic control values as shown in Fig. D.5 are live powering V1 open, V1 close, V2, V3, and V4 manually with a +24 V power supply. We envision interfacing with the computer and a tablet running a custom LabVIEW to enable automation and simultaneous recording of loadlock pressures. The rebuild will continue in the hands of RLG and RJG.

D.4 Notes about J13 and J14 cables coming unplugged

At some point in time, we suspected the analyzer voltages were not behaving correctly as evidenced by total photoelectron counts not changing much across different software area settings. Recall that in switching between "micro", "minimum", "small", and "large" areas in the software, a distinct set of voltages are applied to the electrostatic condensing lenses. To test the theory, we (ADC, JLM, RLG) used the high voltage probe to measure the voltages applied to the lenses (FCL, CTL) at various area settings. In measuring at each area setting multiple times, we saw that –407 V was applied in each

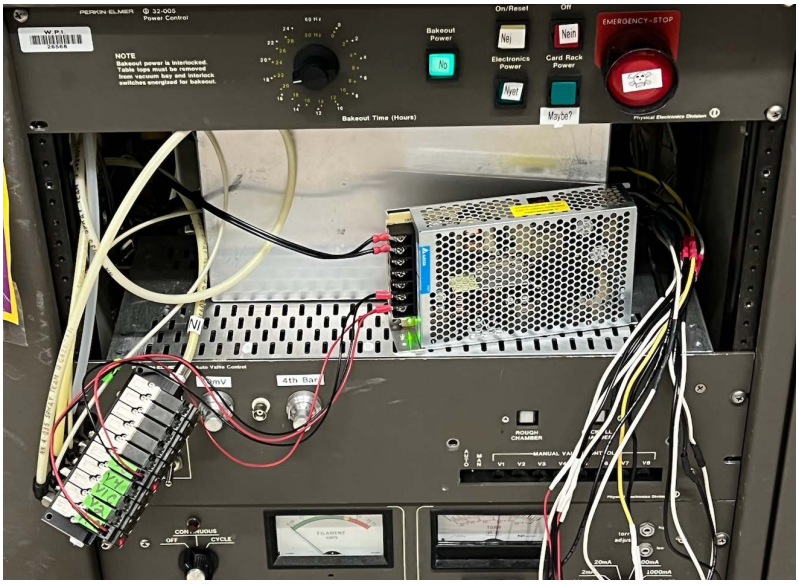

Figure D.5. Newer pneumatic MAC 34C valves that are currently live with manual control from a +25 V power supply. Ultimately, we envision interfacing with a touchscreen tablet running LabVIEW programs that enable automation.

case which is incorrect. After some correspondence with Randy on the RBD portal, we realized that two cables, J13 and J14, that should be plugged into the A252 board were unplugged and dangling. These cables connect the RBD 147 box and the card rack motherboards. We aren't sure when this happened. We plugged them back into A252 and tested across area settings and correctly saw changes in total CPS with magnitudes as expected based on prior behavior when things were working. This lasted for a while but during a bakeout in October 2022, JLM suspected the voltages were not behaving correctly again and sure enough, J13 and J14 cables were unplugged again. JLM re-plugged in and voltages behaved as expected. Then, March 2023 we noticed they yet again became unplugged. JLM and RJG marked a few-inch segment of the cables with bright green tape as a visual indicator for users walking behind the instrument to mitigate running with them unplugged unknowingly. We carefully tucked the heavy-ish loop of slack gray cable deeper inside the birds' nest in a way that should lessen tugging of the delicate J13 and J14 connections to hopefully help them from getting yanked out. In the process, another cable got unplugged... this is detailed in §D.5 plus the instrument logbook 2 from March 2023 (JLM notes) and logbook 1 from June 2016 (ADC notes) contain additional illustrations and explanations. The evidence that this cable is unplugged is the multiplier CPS being locked >20 million counts.

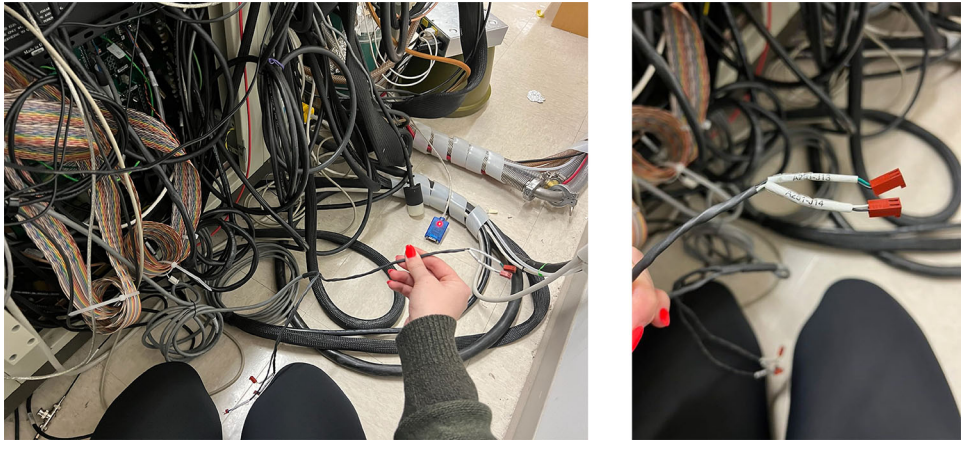

Figure D.6. A252-J13 and A252-J14 cables unplugged. The other ones in the bundle remain unplugged (except J36 2-pin male connector discussed in §9.4.4), while J13 and J14 plug into board A252.

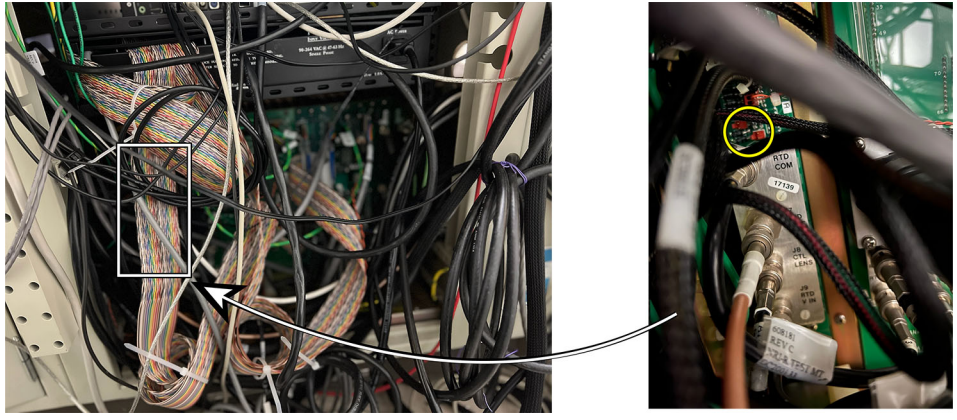

Figure D.7. The white box highlights very roughly where board A252 is positioned behind the bird's nest. The yellow circle highlights the connections on board A252 for J13 and J14 which are labeled accordingly.

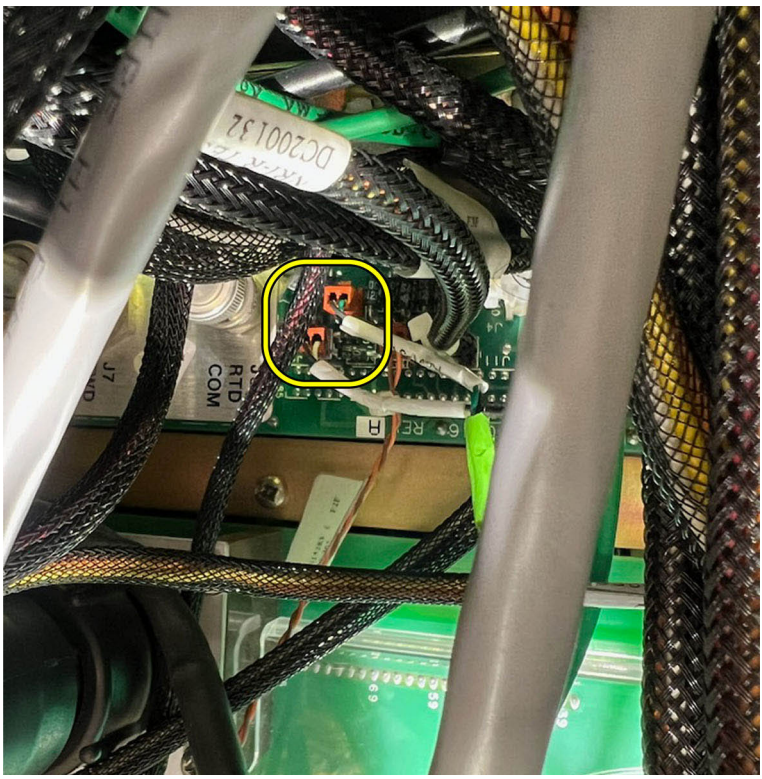

Figure D.8. J13 and J14 plugged in correctly. Keep an eye on the green tape to monitor the status of the cable.

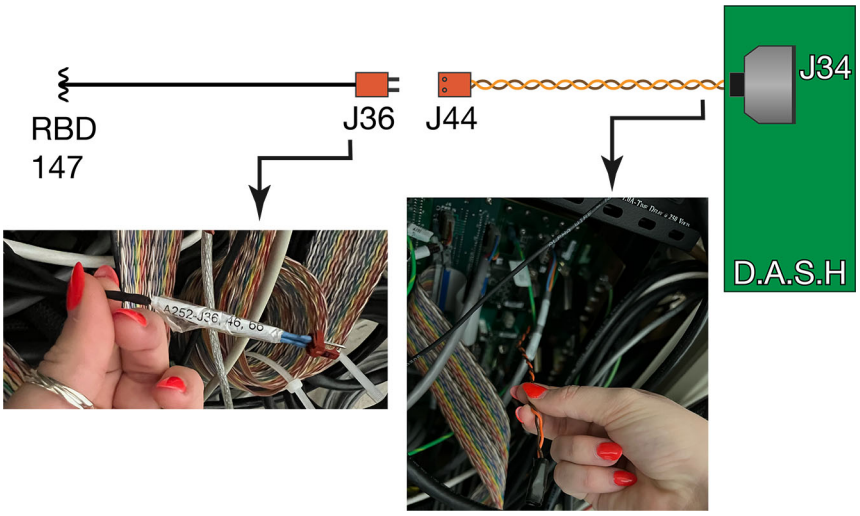

Figure D.9. Diagram of J36 and J44/J34 connections between the RDB 147 box and the DASH card rack board.

D.5 Notes about J36 and J44/34 getting unplugged from each other

There is a 2-pin male connector (labeled A252–J36) that comes out from the RBD 147 box and is living in the same bundle of cables as A252–J13 and A252–J14. It's the only other cable in that bundle besides J13 and J14 that actually plugs into something. It plugs into a female connector (J44, twisted brown/orange wires) that comes out from the DASH at a site on the board labeled J34. Not sure why each end of this cable are labeled differently and manuals don't mention it. In 2016, Alex noticed this cable got unplugged as evidenced by the multiplier CPS being locked >20 million counts. He plugged it back in and wrapped pin connection with electrical tape for some extra support as the wires get accidentally tugged on. During this last bakeout March 2023, in the process of plugging back in J13 and J14, this J36/J44 connecton accidentally came unplugged. We re-plugged in, CPS behaved normally after, and below shows photos and a diagram of this connection.

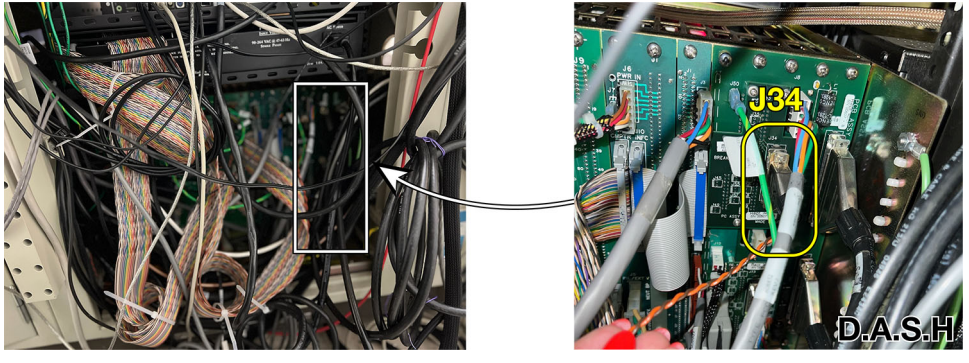

Figure D.10. The white box indicates roughly where the DASH is located behind the birds nest. The yellow box indicates where the other end of the J44 cable plugs into the DASH board, the connection site for which is labeled J34 for whatever reason. The other end of that (female 2 pin) cable which is labeled J44 connects to the 2-pin male connector A252-J36 coming out the RDB 147 box in the same bundle of cables as A252-J13 and A252-J14.

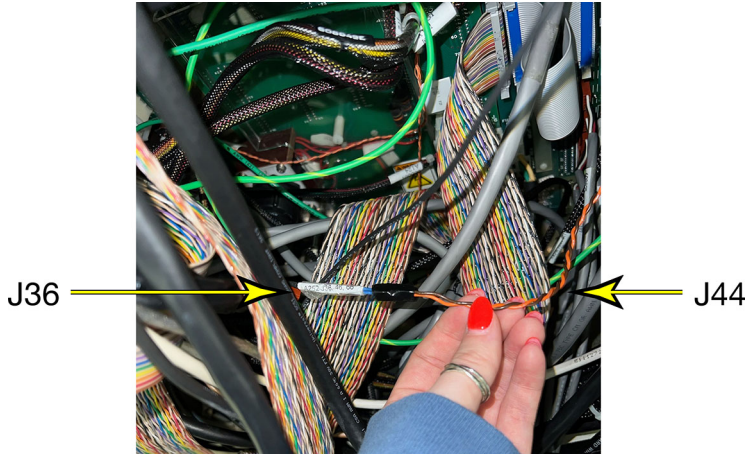

Figure D.11. A252-J36 from RBD 147 and J44 from DASH card rack board (other end is plugged into the DASH at connection site labeled J34) connected properly with electrical tape for support.

E

AIR-FREE MXene PROCEDURES

All $Ti_3C_2T_x$ material was synthesized by Barsoum and colleagues and shipped to WPI from Drexel in its multilayered form as it is most suitable for long term storage in terms of oxidative stability. The multilayered $Ti_3C_2T_x$ was stored as received in a nitrogen-purged flush box and small aliquots were removed as needed prior to functionalization experiments. A stash of piranha-cleaned dram vials were dried in a >100 °C oven overnight and stored inside the flush box for ready use in silane solution preparation and small aliquots of the $Ti_3C_2T_x$ were weighed into 15 mL centrifuge tubes inside the box and removed as needed.

E.1 Preparation of delaminated MXene

Delamination procedures were employed for small aliquots of the multilayered $Ti_3C_2T_x$ prior to all functionalization experiments. Sonication and subsequent separations via centrifugation yielded delaminated $Ti_3C_2T_x$ material based on established procedures with slight modifications. In our hands, sonication of the $Ti_3C_2T_x$ material under an air ambient deleteriously oxidized the material as evidenced by a large Ti^{4+} feature dominating the Ti 2p region of high-resolution XP spectra as well as loss of characteristic optical behavior in THz and TA spectroscopy. As such, all delamination and functionalization

procedures were carried out via air-free methods with active bubbling with UHP N_2 throughout all steps, especially sonication.

For each delamination procedure, 10 mL of water was degassed in a piranha-cleaned 5 dram glass vial with ~1 bubble per second N_2 (ultrahigh purity, Airgas) flow for 15 minutes. The dram vials were sealed with custom dram vial caps that we modified with custom glass tubing ports to enable simultaneous N_2 bubbling and silane addition.

Throughout all delamination steps preceding separation via centrifugation, active N_2 bubbling was maintained and the flow rate remained relatively constant. Following, 100 mg of multilayered $Ti_3C_2T_x$ was weighed out in the flush box, removed, and added to the degassed water and left to "soak" for 3 hr with continued N_2 bubbling. After the soak period, the material was sonicated with N_2 bubbling in an ice-cooled water bath for 1 hr. The ice was added to the bath during the degassing step so that it was sufficiently melted prior to the start of sonication. Following sonication, the $Ti_3C_2T_x$ colloid in water was transferred to a 15 mL polypropylene centrifuge tube and filled with water up to the 10 mL graduation line to account for water loss from evaporation. Centrifugation at 3000*g* for 10 min initially separated delaminated $Ti_3C_2T_x$ material from the comparatively larger particulates. This initial round of centrifugation yielded a black pellet and a dark green-black supernatant. The supernatant liquid was decanted and transferred to a separate, clean 50 mL centrifuge tube and the pellet was discarded. For this step, we used 50 mL tubes rather than 15 mL due to the rotor constraints of the 4th floor ultracentrifuge compared to the Olsen group's system. Due to the volume constraints of ultracentrifugation (the tube should be filled at least halfway to avoid collapsing under high speeds and vacuum), enough volume of water was added to the colloid in the 50 mL tube to bring the total volume to the 30 mL line. To ultimately separate the solid material from the water, the colloid of delaminated $Ti_3C_2T_x$ (the initial supernatant liquid) was further purified by centrifugation at 5000*g* for 10 min which yielded a pellet containing a fractional percentage of the $Ti_3C_2T_x$ solid material and a supernatant which comprised a colloidal suspension of a fractional percentage of the $Ti_3C_2T_x$ material in water. This was done using the Gateway 1 4th floor Beckmann ultracentrifuge with Paula Moravek's permission and training. Following decanting and discarding of the supernatant liquid, the $Ti_3C_2T_x$ material in the pellet was resuspended in 7 mL of fresh ethanol via physical agitation and sonication for 2 min with N_2 bubbling as described prior. The resulting $Ti_3C_2T_x$-containing suspension in ethanol was then subjected to functionalization as described in the proceeding sections.

E.2 Functionalization of MXene with organosilanes

Preparation of silane solutions for functionalization experiments was carried out inside the flush box using dry solvents (ethanol or toluene). The solvents were stored in the flush box over activated sieves. To yield molar ratios of 2:1 organosilane:MXene, solutions of organosilane in dry ethanol were prepared to 239 mM concentrations. As such, solutions of trimethoxypropylsilane, trimethoxy(3,3,3-trifluoropropyl)silane, 3-aminopropyltrimethoxysilane, and cyanopropyltrimethoxysilane were prepared in 5 mL dry ethanol from 210, 228, 212, and 189 μL respectively. The solution was left capped inside the flush box during all MXene delamination and preparation steps until immediately preceding use.

Following delamination and solvent exchange from water to ethanol as described earlier, 1 mL of 0.1 M acetic acid in water was added to the 7 mL suspension of delaminated $Ti_3C_2T_x$ in ethanol. The resulting acidified $Ti_3C_2T_x$-containing suspension was degassed for 15 min with N_2 bubbling as described prior. Throughout the functionalization procedure, the N_2 flow persisted and the flow rate was maintained at ~1 bubble min^{-1}. Following, the suspension was sonicated in an ice-cooled water bath for 15 minutes with N_2 bubbling. Concurrently, silane solutions were prepared in the flushbox with ethanol dried over activated sieves as described prior. The ethanolic silane solution was then added to the closed system by syringe at a rate of 1 mL per 15 min over the course of 75 min until the full 5 mL were delivered. The silane solutions were prepared in a 2:1 molar ratio of silane: $Ti_3C_2T_x$ MXene as described in §5.3.1. The silane-containing $Ti_3C_2T_x$ solution was sonicated for 4 hr total from the first silane addition in an ice-cooled water bath with N_2 bubbling.

Following the 4 hr reaction, the $Ti_3C_2T_x$ solution was quantitatively transferred to a 15 mL centrifuge tube rinsing with small volumes of ethanol to reach a final volume of 15 mL. Centrifugation at 3000g for 2 min initially separated the solid $Ti_3C_2T_x$ material from the silane reaction solution. Following decanting and discarding of the supernatant liquid, the $Ti_3C_2T_x$ material was resuspended in 6 mL of fresh ethanol via physical agitation and sonication. Three cycles of centrifugation as above, decanting, and re-suspension further purified the material left in the pellet after each stage of rinsing and centrifugation in ethanol. Through each stage of ethanolic centrifugation, the supernatant showed no signs of suspended material and progressively transitioned from light gray to a clear solution. With the final decanting of the clear ethanolic supernatant, the $Ti_3C_2T_x$ centrifugation pellet was suspended in 10 mL ethanol and thoroughly sonicated. This suspension of functionalized $Ti_3C_2T_x$ in ethanol was stored inside a nitrogen-purged flush box until further use.

F

MXene XPS DATA DUMP

The following spectra are random text dumps with stuff.

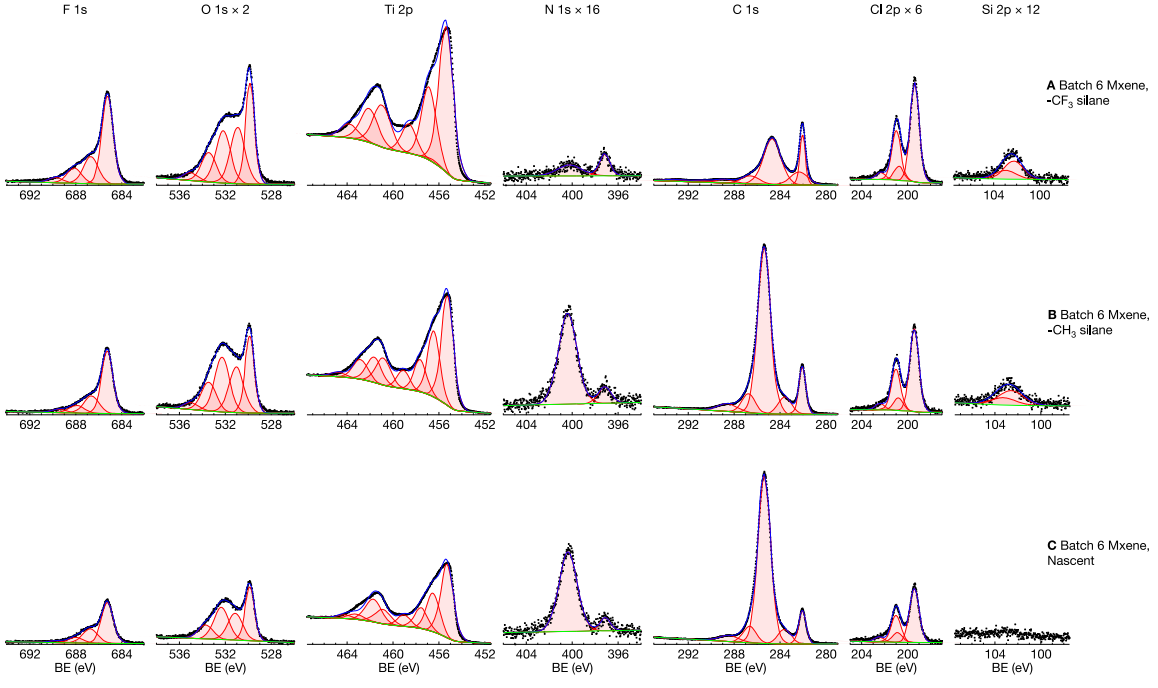

Figure F.1. First round of XPS on Batch 6 $Ti_3C_2T_x$ MXene made by Mary at Drexel following Kiana's recipe (MX6041, 42, 43). Carbide contributions to C 1s and Ti 2p are lower than is typical for nascent material. There is also significant N 1s signal shich should not be present for any of the three samples. Optical data for these samples on quartz also did not look characteristically MXene. This is when we started wondering about our delamination procedures. We've historically been delaminating in ethanol directly preceding silanization procedures. Shortly after this we had a MXene meeting with Drexel and Natick about this. Varun claims you need to do the delamination in water as larger solvent molecules are not small enough to intercalate between the layers to sufficiently delaminate. Shortly after this we switched to water delamination with a 2–3 h soak in degassed water then 1 h sonication with degassing. Interestingly for A –CF_3 functionalized MXene the N 1s signal is much lower compared to B and C. Not sure what's up with that without knowing where the nitrogen is coming from. In "PHI5600/kngo/2023-02-10 MX6041-42-43 pure propyl CF3 control".

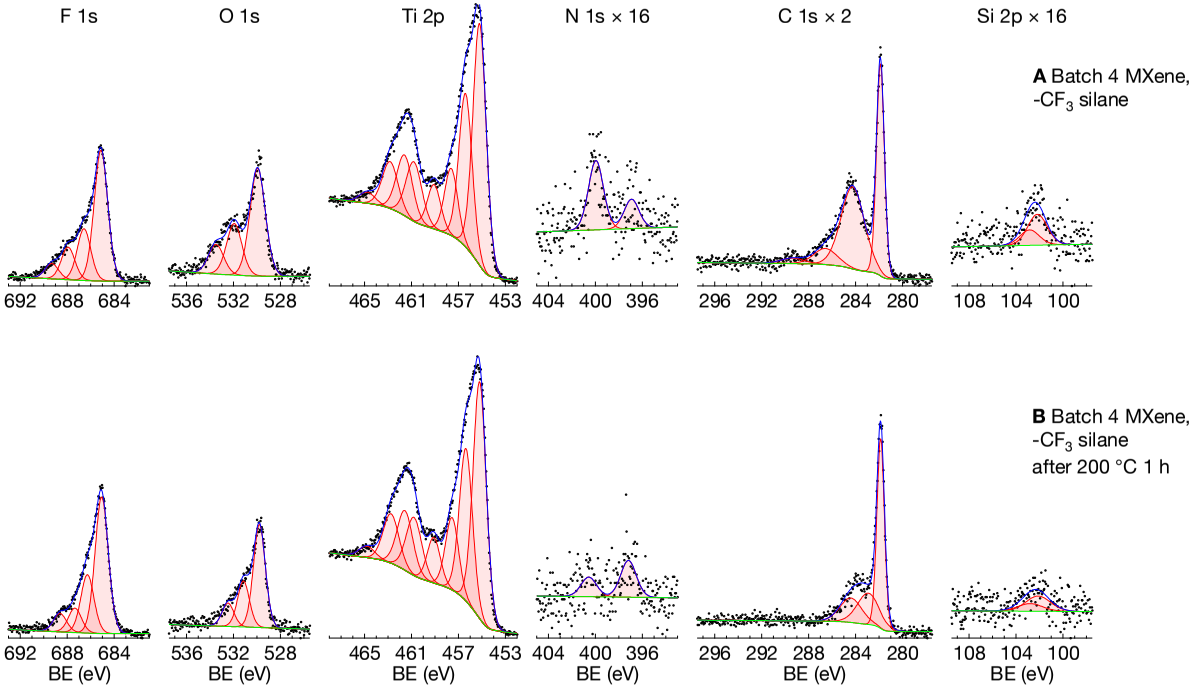

Figure F.2. MX23 Batch 4 MXene made by Kiana at Drexel functionalized with trimethoxy(3,3,3-trifluoropropyl)silane. A shows initial multiplex and B shows multiplex after heating at 200 °C for 1 h. Organic F 1s looks largely consistent, although decreased a bit relative to fluoride. N 1s signal looks smaller. Likely covalently attached but low coverage, way below one monolayer. In "PHI5600/jmartin2/2022/2022-12-14 MX23 MXene batch 4 plus CF3".

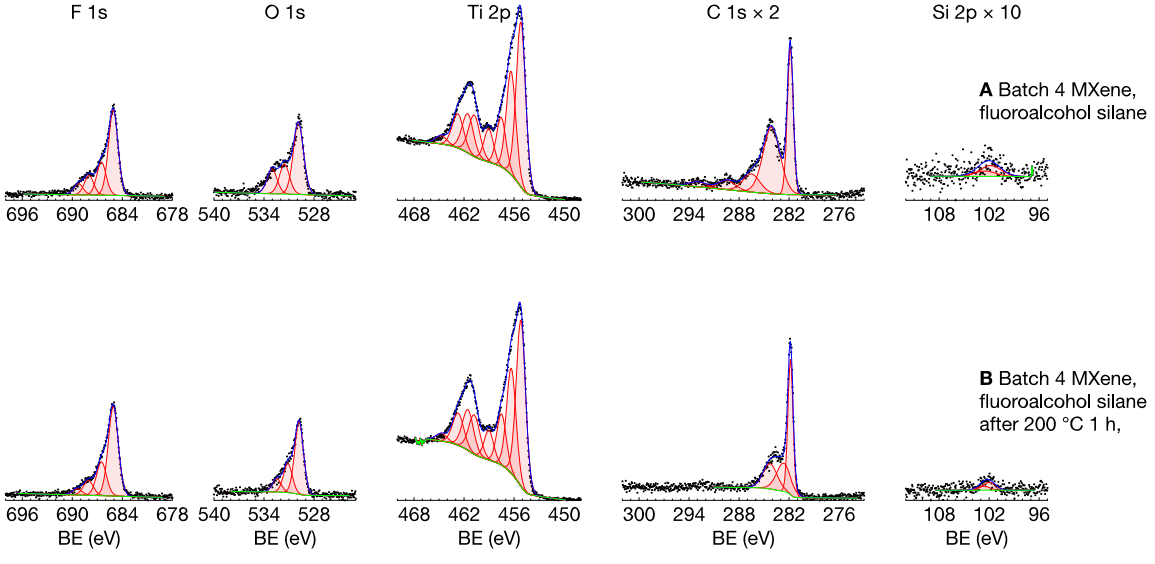

Figure F.3. MX24 batch 4 MXene made by Kiana at Drexel functionalized with the fluoroalcohol silane synthesized by RJG and AH. A shows initial multiplex and B shows multiplex after heating at 200 °C for 1 h. Organic F 1s looks largely consistent, although decreased a bit relative to fluoride. Likely covalently attached but low coverage, way below one monolayer. In "PHI5600/jmartin2/2022/2022-12-12 MX24 MXene batch 4 plus fluoroalcohol round 2".

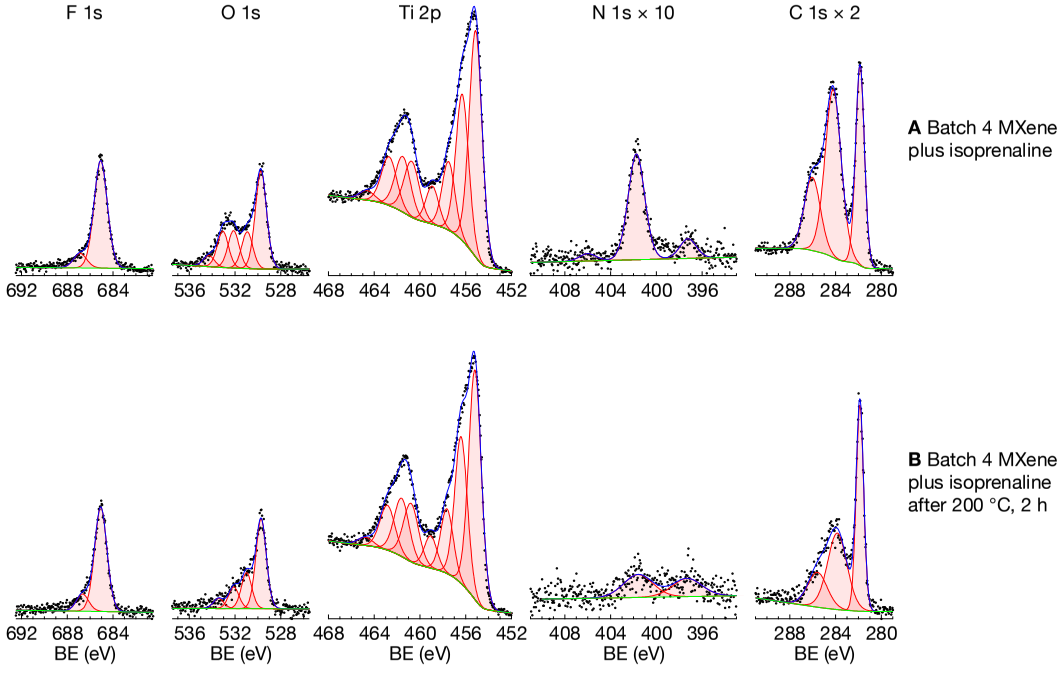

Figure F.4. MX20 Batch 4 MXene made by Kiana at Drexel functionalized with isoprenaline (reagent borrowed from Scarlata lab). A shows initial multiplex and B shows multiplex after heating at 200 °C for 2 h. In "PHI5600/jmartin2/2022/2022-11-15 MXene batch 4 plus isoprenaline 3 hrs sonicated air free".

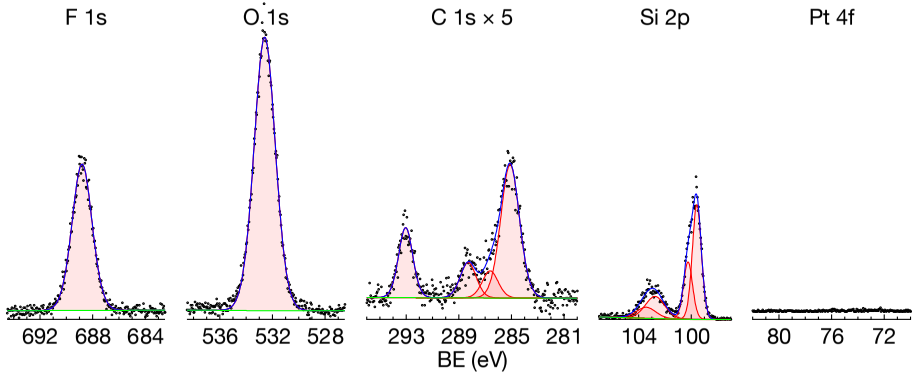

Figure F.5. Fluoroalcohol silane synthesized by RJG and AH on a Si(111) wafer. In "PHI5600/jmartin2/2022/2022-11-08 becca fluorosilane on Si dirty and R3 TiC QDN 80".

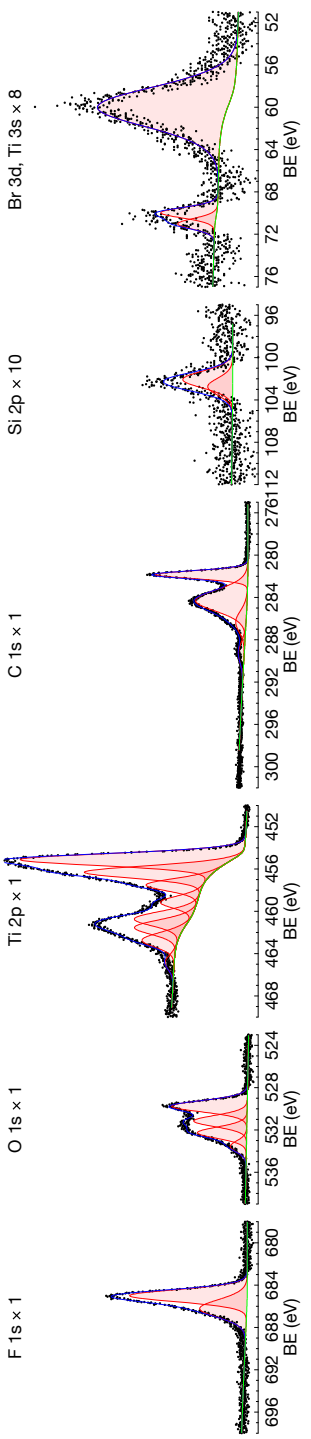

Figure F.6. MX07 Batch 2 MXene plus 3-(bromopropyl)trimethoxysilane. In "PHI5600/jmartin2/2022/2022-04-27 MX07 mxene plus bromopropylsilane on n+ Si ox drop cast dried RT".

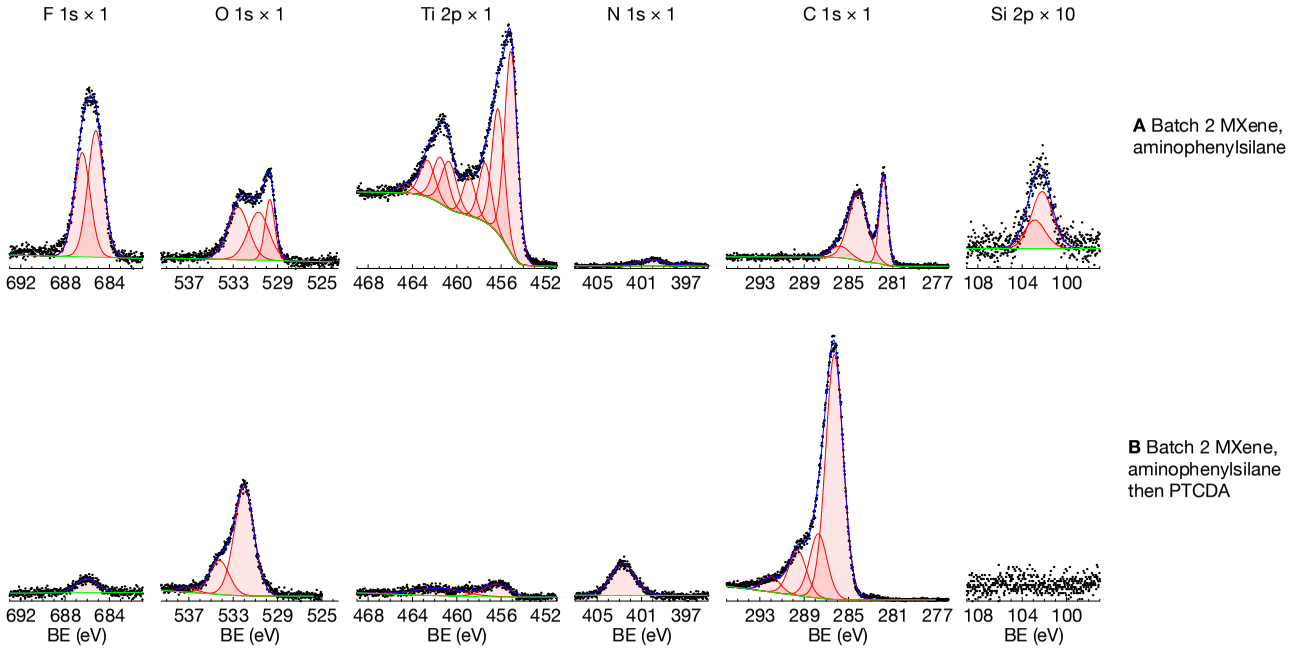

Figure F.7. MX08 Batch 2 MXene plus p-aminophenyltrimethoxysilane and B MX09 which was MX08 plus ring-opened PTCDA room temp. Way too much coverage, peaks shifted up 1 eV. Need to dial PTCDA loading way down. Also very difficult to rinse out all of the unreacted PTCDA during workup. Needs parameterizing. In "PHI5600/jmartin2/2022/2022-05-05 MX08 mxene plus aminophenylsilane RT 8hrs drop cast".

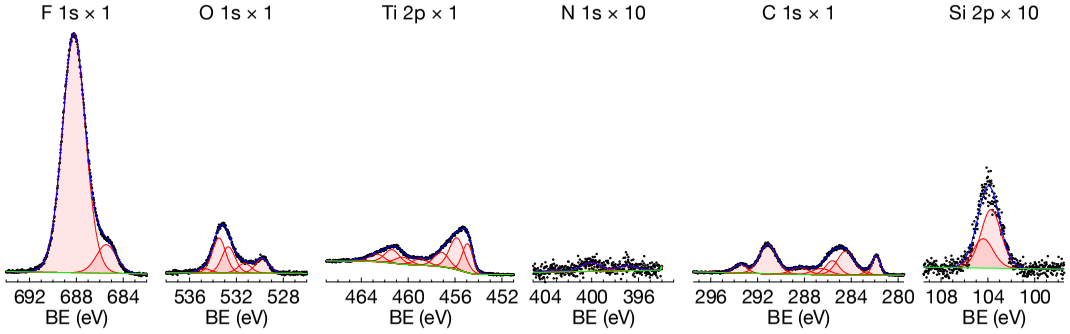

Figure F.8. MX02 Batch 2 MXene plus trichloro(1H,1H,2H,2H-perfluoroocyl)silane. Way too much coverage, F 1s dominating. Needs parameterizing.

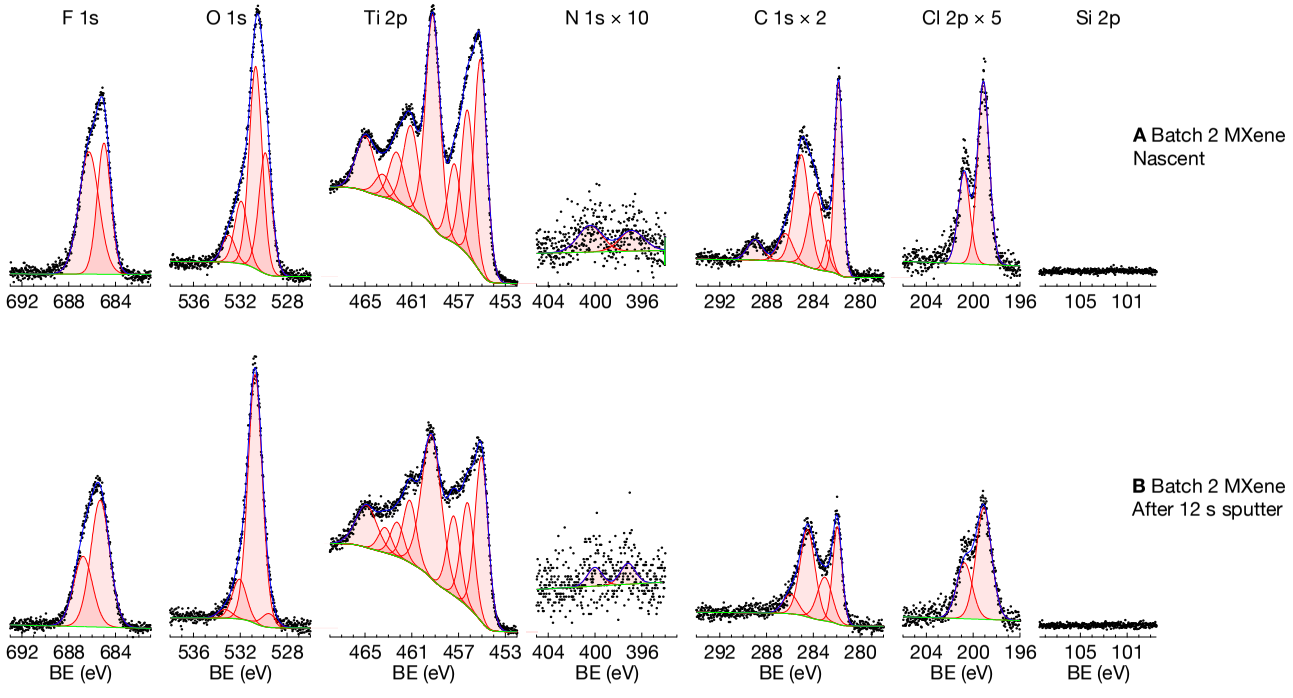

Figure F.9. Batch 2 MXene on SiO^x wafer non-functionalized A before and B after 12 s Ar^+ sputter.

G

MXene UPS DATA DUMP

This incomplete story maps UP spectra of following MX23 Batch 4 MXene functionalized with trimethoxy(3,3,3-trifluoropropyl)silane as a function of heating temperature. This may become a story in the future.

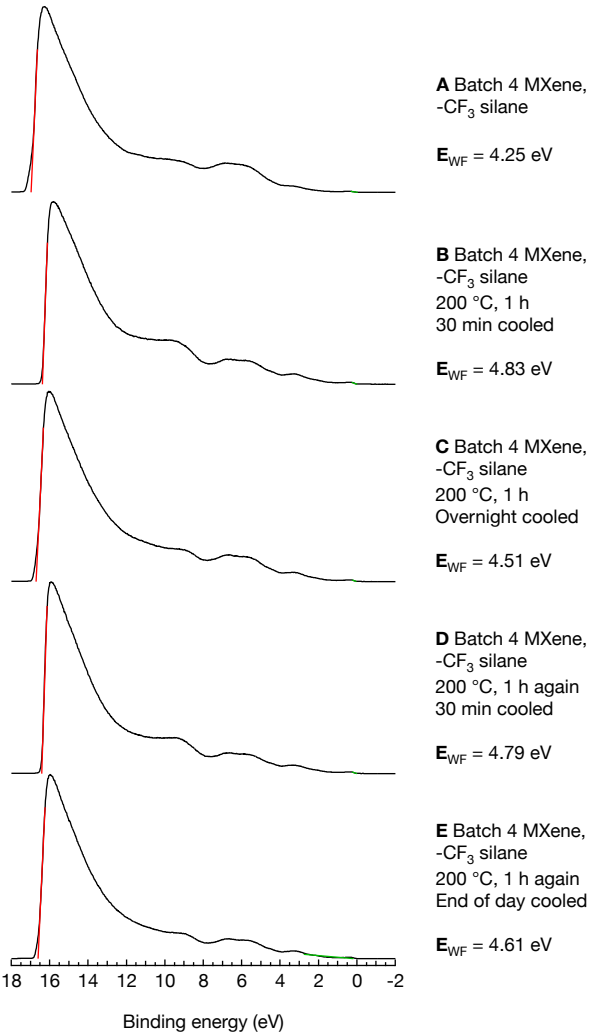

Figure G.1. Above data shows UP spectra for MX23 Batch 4 MXene functionalized with trimethoxy(3,3,3-trifluoropropyl)silane at various stages of sample heating. We did isothermal heating at 200 °C for 1 h to probe covalent attachment versus physisorption. We noticed that the work functions for samples scanned shortly after heating were erroneously high. To test this theory, we scanned again after the sample was substantially cooler (overnight as in C) and the resulting work function was closer to that of the original as in A before any heating. We heated again to see if the work function increased again, and it did. You can see the work functions for B and D which were acquired only 30 min after heating are close in value to each other while the work functions acquired after 10+ h of cooling as in C and E are close in value to each other and are closer to the "nascent" as in A which was acquired prior to any heating.

H

CUSTOM IGOR SCRIPTS

H.1 BEShift(shiftval)

Located in "Grimmgroup Photoelectron/RLG_shiftUPS.ipf"

`BEShift(shiftval)` operates on UP spectra that have been direclty imported into IGOR Pro as a .vms data file. This corrects the binding-energy axis when a bias voltage is applied to the stage that would linearly shift all binding energies. For instance, if a –35 V bias is used, type `BEShift(35)` in the IGOR Pro command window to execute the shift on the data in the topmost window.

```
// 7 August 2019 rlgii
//this procedure shifts the baseline to account for an arbitrary bias
     in finding the stuff

Function BEShift(shiftval)
   Variable shiftval

   DFREF originalDFR, blockDFR
   Variable data_found=0, graphtracenum, waves_in_a_table = 0,
    cols_in_a_table, i, j
   String graphname = "", tablename = "", table_list = "",
    temp_wave_path_string, counts_trace_name = ""
   Wave Counts, BE, tempwave_in_table

```

```
11    // do this no matter what
12    originalDFR = GetDataFolderDFR()
13
14    // Get list of traces in topmost graph that start with "Counts"
15    graphname = WinName(0,1)
16    String fulltracelist = TraceNameList(graphname,";",1)
17    String countsonlytracelist = ListMatch(fulltracelist,"Count*")
18
19    if (ItemsInList(countsonlytracelist) > 1)
20       Prompt graphtracenum, "Choose a trace:", popup
      countsonlytracelist
21       DoPrompt "Which trace should I work on?", graphtracenum
22       if (V_Flag)
23          data_found = 0 // user cancelled
24       else
25          data_found = 1
26          // save the trace name for data
27          counts_trace_name = StringFromList(graphtracenum-1,
      countsonlytracelist)
28          // assign the wave references for that y counts trace, the x
       BE trace, and the data folder
29          Wave/Z Counts = TraceNameToWaveRef(graphname,StringFromList(
      graphtracenum-1, countsonlytracelist))
30          Wave/Z BE = XWaveRefFromTrace(graphname,StringFromList(
      graphtracenum-1, countsonlytracelist))
31          blockDFR = GetWavesDataFolderDFR(Counts)
32       endif
33    elseif (ItemsInList(countsonlytracelist) < 1)
34       Print "I am sorry, but I can not find a trace named \"Counts\".
         I can not help you."
35       data_found = 0
36    else
37       // there is only one "Counts" trace on the graph.  this is easy
38       data_found = 1
39       counts_trace_name = "Counts"
40       Wave/Z Counts = TraceNameToWaveRef(graphname,"Counts")
41       Wave/Z BE = XWaveRefFromTrace(graphname,"Counts")
42       blockDFR = GetWavesDataFolderDFR(WaveRefIndexed(graphname,0,1))
43    endif
44
45    if(data_found)
46       SetDataFolder blockDFR
47
48       Wave BE_Orig=blockDFR:BE_Orig
49       Variable diff_shift, diff_shift_orig
50
51       // make a backup of the data wave in BE_Orig if it doesn't
       already exist
52       if (!(WaveExists(BE_Orig)))
53          Duplicate/O BE, BE_Orig
54       endif
55       // do the shift and save numbers for shifting the SEC and fermi
       fit stuff
56       diff_shift_orig = BE[0]
57       BE = BE_Orig + shiftval
58       diff_shift = BE[0] - diff_shift_orig
```

```
59
60      // check to see if there was a fermi/SEC fit by looking for the
        wave fermi_edge_Y
61      Wave fermi_edge_Y = blockDFR:fermi_edge_Y
62      if (WaveExists(fermi_edge_Y))
63         // it exists so let's recompute the lines and the fermi/SEC
        values as they've moved!
64         Wave sec_elect_cutoff_X = blockDFR:sec_elect_cutoff_X
65         sec_elect_cutoff_X += diff_shift
66         Wave fermi_edge_X = blockDFR:fermi_edge_X
67         fermi_edge_X += diff_shift
68         String annotationstring = "\\f01E\\f00\\BSEC\\M = " +
        num2str(sec_elect_cutoff_X[2]) + "eV\r\\f01E\\f00\\BWF\\M = " +
        num2str(21.22-sec_elect_cutoff_X[2]) + "eV\r\\f01E\\f00\\BF\\M =
        " + num2str(fermi_edge_X[2]) + " eV"
69         TextBox/C/N=intercept_summary annotationstring
70      endif
71      SetDataFolder originalDFR
72   endif
73   return 1
74 End
```

H.2 CountsShift(shiftval)

Located in "Grimmgroup Photoelectron/RLG_shiftUPS.ipf"

CountsShift(shiftval) operates on UP spectra that have been directly imported into IGOR Pro as a *.vms data file. This shifts the counts axis for some reason.

```
0  Function CountsShift(shiftval)
1     Variable shiftval
2
3     DFREF originalDFR, blockDFR
4     Variable data_found=0, graphtracenum, waves_in_a_table = 0,
       cols_in_a_table, i, j
5     String graphname = "", tablename = "", table_list = "",
       temp_wave_path_string, counts_trace_name = ""
6     Wave Counts, BE, tempwave_in_table
7
8     // do this no matter what
9     originalDFR = GetDataFolderDFR()
10
11    // Get list of traces in topmost graph that start with "Counts"
12    graphname = WinName(0,1)
13    String fulltracelist = TraceNameList(graphname,";",1)
14    String countsonlytracelist = ListMatch(fulltracelist,"Count*")
15
16    if (ItemsInList(countsonlytracelist) > 1)
17       Prompt graphtracenum, "Choose a trace:", popup
       countsonlytracelist
18       DoPrompt "Which trace should I work on?", graphtracenum
19       if (V_Flag)
20          data_found = 0 // user cancelled
```

```
21        else
22           data_found = 1
23           // save the trace name for data
24           counts_trace_name = StringFromList(graphtracenum-1,
     countsonlytracelist)
25           // assign the wave references for that y counts trace, the x
      BE trace, and the data folder
26           Wave/Z Counts = TraceNameToWaveRef(graphname,StringFromList(
     graphtracenum-1, countsonlytracelist))
27           Wave/Z BE = XWaveRefFromTrace(graphname,StringFromList(
     graphtracenum-1, countsonlytracelist))
28           blockDFR = GetWavesDataFolderDFR(Counts)
29        endif
30     elseif (ItemsInList(countsonlytracelist) < 1)
31        Print "I am sorry, but I can not find a trace named \"Counts\".
        I can not help you."
32        data_found = 0
33     else
34        // there is only one "Counts" trace on the graph.  this is easy
35        data_found = 1
36        counts_trace_name = "Counts"
37        Wave/Z Counts = TraceNameToWaveRef(graphname,"Counts")
38        Wave/Z BE = XWaveRefFromTrace(graphname,"Counts")
39        blockDFR = GetWavesDataFolderDFR(WaveRefIndexed(graphname,0,1))
40     endif
41
42     if(data_found)
43        Wave Counts_Orig=blockDFR:Counts_Orig
44
45        SetDataFolder blockDFR
46        if (!(WaveExists(Counts_Orig)))
47           Duplicate/O Counts, Counts_Orig
48        endif
49        Counts = Counts_Orig - shiftval
50
51        // check to see if the UPS is being fit for SEC and for fermi
      positions
52        // if exists, replot the things.  if not, don't do anything
      else.
53        Wave/Z UPS_cursor_positions = blockDFR:UPS_cursor_positions
54        if (WaveExists(UPS_cursor_positions))
55           UPS_find_intercepts()
56        else
57           // do nothing
58        endif
59
60        SetDataFolder originalDFR
61     endif
62     return 1
63  End
```

H.3 Juliacasatab()

`Juliacasatab()` operates on multiplexed XP data loaded into IGOR Pro in the form of `*.casatab` data files exported from Casa XPS. It executes some graph preferences that JLM likes for XP spectra including making line colors black, deleting graph mirroring, etc.

```
// 28 April 2021 Julia Martin
// These functions format the the import casatabs in a way Julia likes them
// Casatab Graph properties
Function Juliacasatab()
   ModifyGraph expand=2

   #ifdef MACINTOSH
      // Mac
      ModifyGraph gFont="Helvetica Neue"
   #else
      #ifdef WINDOWS
         // Win
         ModifyGraph gFont="Arial"
      #else
         Print "Unknown OS, not doing anything with the default fontyness..."
      #endif
   #endif

   ModifyGraph mirror(bottom)=0
   ModifyGraph axThick(left)=0
   ModifyGraph manTick(bottom)={0,2,0,0},manMinor(bottom)={0,0}
   ModifyGraph rgb(Envelope)=(0,0,0),rgb(Background)=(0,0,0)
End
```

H.4 Juliasurvey()

`Juliasurvey()` is intended to operate on XP survey spectra loaded into IGOR Pro in the form of .casatab data files exported from Casa XPS. It executes some graph preferences that JLM likes for XP surveys including making line colors black, deleting graph mirroring, changing tick increments, etc.

```
Function Juliasurvey()
   #ifdef MACINTOSH
      // Mac
      ModifyGraph gFont="Helvetica Neue"
   #else
      #ifdef WINDOWS
         // Win
         ModifyGraph gFont="Arial"
      #else
         Print "Unknown OS, not doing anything with the default fontyness..."
      #endif
```

```
    #endif
    ModifyGraph nticks(left)=0, axThick(left)=0
    Label left "Counts "
    ModifyGraph mirror(bottom)=0
    ModifyGraph manTick(bottom)={0,200,0,0},manMinor(bottom)={9,0}
End
```

H.5 JuliaUPS()

`JuliaUPS()` operates on full UP spectra loaded into IGOR Pro in the form of .vms data files exported from Casa XPS following execution of BEShift() for bias correction. It executes some graph preferences that JLM likes for UP spectra including making line colors black, deleting graph mirroring, etc. Note that this function is intended for UP spectra of semiconductors as it sets upper and lower BE values based on Fermi-edge positioning that is one or more eV above zero.

```
// 28 April 2021 Julia Martin
// These functions format the the import casatabs in a way Julia likes them
//UPS Graph Properties for semiconductors
Function JuliaUPS()
    #ifdef MACINTOSH
        // Mac
        ModifyGraph gFont="Helvetica Neue"
    #else
        #ifdef WINDOWS
            // Win
            ModifyGraph gFont="Arial"
        #else
            Print "Unknown OS, not doing anything with the default fontyness..."
        #endif
    #endif
    ModifyGraph nticks(left)=0, axThick(left)=0
    Label left "Counts "
    ModifyGraph mirror(bottom)=0
    ModifyGraph manTick(bottom)={0,2,0,0},manMinor(bottom)={3,2}
    SetAxis/R bottom 20,0
    ModifyGraph width=288
    ModifyGraph margin(left)=18,margin(bottom)=18,margin(right)=7,margin(top)=7
End
```

H.6 JuliaFermi()

`JuliaFermi()` should be executed directly following JuliaUPS() on a duplicate window of that same graph. To use this function, load in a full UP spectrum in the form of .vms data file, execute BEShift() and JuliaUPS() on

that graph, duplicate that graph, and execute JuliaFermi() on that duplicated window. This function is intended to produce a magnified zoom of the Fermi region with the same eV per inch spacing as the full spectrum. After executing the steps above, change the Y-axis limits to the desired magnification. Note that this function is intended for UP spectra of semiconductors as it sets upper and lower BE values based on Fermi-edge positioning that is one or more eV above zero.

```
// 28 April 2021 Julia Martin
// These functions format the the import casatabs in a way Julia likes them
// UPS Graph Properties for semiconductors
Function JuliaFermi()
   ModifyGraph width=72,height=72
   SetAxis/R bottom 5,0
   TextBox/K/N=intercept_summary
   ModifyGraph noLabel(left)=2
   ModifyGraph noLabel=2
   TextBox/C/N=text0/F=0/B=1/X=20.00/Y=40.00 "\\Z06x"
End
```

H.7 JuliaUPSppt()

`JuliaUPSppt()` operates on full UP spectra loaded into IGOR Pro in the form of .vms data files exported from Casa XPS following execution of `BEShift()` for bias correction. This function is intended to increase text size to 14 pt and modify tick increments accordingly to enable direct import to PPT for informal meetings. For the default aspect ratio for UP spectra, 7 pt font doesn't scale up as much as JLM likes for readability on slides.

```
// 28 April 2021 Julia Martin
// 15 December 2022 Julia Martin
// These functions format the the import casatabs in a way Julia likes them
// UPS Graph Properties increase text size and modify ticks for direct import to ppt for informal meetings
Function JuliaUPSppt()
   ModifyGraph gfSize=14
   ModifyGraph margin(bottom)=36
   ModifyGraph lblPos(bottom)=35
End
```

H.8 JuliaUPSmetal()

`JuliaUPSmetal()` operates on full UP spectra loaded into IGOR Pro in the form of .vms data files exported from Casa XPS following execution of `BEShift()` for bias correction. It executes some graph preferences that JLM likes for UP spectra including making line colors black, deleting graph mirroring, etc. Note that this function is intended for UP spectra of metals as it

sets upper and lower BE values based on Fermi-edge positioning that is very close to zero. That is to say, the main difference between this function and `JuliaUPS()` is that there are a few extra eV below zero for `JuliaUPSmetal()`.

```
// 28 April 2021 Julia Martin
/ 15 December 2022 Julia Martin
// These functions format the the import casatabs in a way Julia likes them
//UPS Graph Properties for metals w shelf at zero (MXene)
Function JuliaUPSmetal()
   #ifdef MACINTOSH
      // Mac
      ModifyGraph gFont="Helvetica Neue"
   #else
      #ifdef WINDOWS
         // Win
         ModifyGraph gFont="Arial"
      #else
         Print "Unknown OS, not doing anything with the default fontyness..."
      #endif
   #endif
   ModifyGraph nticks(left)=0, axThick(left)=0
   Label left "Counts "
   ModifyGraph mirror(bottom)=0
   ModifyGraph manTick(bottom)={0,2,0,0},manMinor(bottom)={3,2}
   SetAxis/R bottom 18,-2
   ModifyGraph width=288
   ModifyGraph margin(left)=18,margin(bottom)=18,margin(right)=7,margin(top)=7
End
```

H.9 JuliaFermimetal()

`JuliaFermimetal()` is executed directly following `JuliaUPSmetal()` on a duplicate window of that same graph. To use this function, load in a full UP spectrum in the form of .vms data file, execute `BEShift()` and `JuliaUPS()` on that graph, duplicate that graph, and execute JuliaFermi() on that duplicated window. This function is intended to produce a magnified zoom of the Fermi region with the same eV per inch spacing as the full spectrum. After executing the steps above, change the Y-axis limits to the desired magnification. Note that this function is intended for UP spectra of metals as it sets upper and lower BE values based on Fermi-edge positioning that is very close to zero. That is to say, the main difference between this function and `JuliaUPS()` is that there are a few extra eV below zero for `JuliaUPSmetal()`.

```
// 28 April 2021 Julia Martin
// 15 December 2022 Julia Martin
// These functions format the the import casatabs in a way Julia likes them
// UPS Graph Properties for metals w shelf at zero (MXene)
```

```
Function JuliaFermimetal()
   ModifyGraph width=57.6,height=72
   SetAxis/R bottom 2,-2
   TextBox/K/N=intercept_summary
   ModifyGraph noLabel(left)=2
   ModifyGraph noLabel=2
   TextBox/C/N=text0/F=0/B=1/X=20.00/Y=40.00 "\\Z06x"
End
```

H.10 JuliaPL()

JuliaPL() operates on full PL spectra imported into IGOR Pro in the form of .pl files which are tab-delimited text files exported from Titova lab PL software. Simply change the file extension of the raw data to .pl. This graph executes some graph preferences that JLM likes for PL spectra including changing the marker shapes for the raw data points, specifying line colors, adding graph labels, etc.

```
// 28 April 2021 Julia Martin
// These functions format the the import casatabs in a way Julia
    likes them
//PL Graph Properties
Function JuliaPL()
   ModifyGraph mode=3,marker=8,lsize=0.5,rgb=(0,0,0)
   ModifyGraph width=144,expand=3
   ModifyGraph tick=2,axThick(bottom)=0.5,btLen=2,stLen=1,manTick(
    left)={0,20,0,0},manMinor(left)={1,0},manTick(bottom)={0,50,0,0},
    manMinor(bottom)={4,0}
   ModifyGraph axThick=0.5
   ModifyGraph rgb=(1,16019,65535)
   ModifyGraph lblPosMode(bottom)=3,lblPos(bottom)=20;DelayUpdate
   Label bottom "time (s)"
   ModifyGraph lblPosMode=3,lblPos(left)=40;DelayUpdate
   Label left "Photoluminescence Intensity (arb)"
End
```